VYSOKÉ UČENÍ
TECHNICKÉ
V BRNĚ

CEITEC
Central European Institute of Technology
BRNO | CZECH REPUBLIC

BRNO UNIVERSITY OF TECHNOLOGY
VYSOKÉ UČENÍ TECHNICKÉ V BRNĚ

CENTRAL EUROPEAN INSTITUTE OF TECHNOLOGY BUT
STŘEDOEVROPSKÝ TECHNOLOGICKÝ INSTITUT VUT

CELLULAR POLYMER NANOCOMPOSITES
CELULÁRNÍ POLYMERNÍ NANOKOMPOZITY

DOCTORAL THESIS TOPIC
POJEDNÁNÍ KE STÁTNÍ DOKTORSKÉ ZKOUŠCE

AUTHOR AUTOR PRÁCE	Ing. KLÁRA ZÁRYBNICKÁ
SUPERVISOR VEDOUCÍ PRÁCE	prof. RNDr. JOSEF JANČÁŘ, CSc.
CO-SUPERVISORS ŠKOLITELÉ SPECIALISTI	Ing. FRANTIŠEK ONDREÁŠ, Ph.D. Ing. PETR LEPCIO, Ph.D.

BRNO 2021

ABSTRACT

This dissertation thesis deals with the preparation and characterization of polymer nanocomposite foams with a focus on means to control their structure at multiple length scales and application in 3D printing in their fabrication. The aim of this work is to investigate polymer nanocomposite with hierarchical structure – from the nano-, through the micro to macro scale. The structural properties of polymer nanocomposites prepared from glassy polymers by the solvent-casting method were investigated in the first part of the work. It has been shown that the difference in the solubility parameters of the polymer and the solvent plays a crucial role. This finding has been verified for systems containing various nanoparticles, polymers, and solvents. With the knowledge of the general principles controlling the structure of nanocomposites, impact polystyrene filled with nanosilica was investigated in greater detail. These nanocomposites were used for the preparation of nanocomposite foams. The porous structure was achieved using a thermal chemical blowing agent azodicarbonamide. The filaments were extruded and the material was processed by 3D printing into the required shapes and foamed. The result was a hierarchical system with the organization of the structure from nano (organization of nanoparticles), through micro (two-component polymer blend structure and foam structure) to macro scale (foam structure and 3D printed design). The effect of nanoparticles on the structure and the thermal and mechanical properties of polymeric foams were observed. The nanoparticles operate as a nucleating agent in the formation of the foam. Pores are easily formed on their surface so that with the content of nanoparticles in the system smaller pores have been formed, which helped to make the foam fine and homogeneous. The presence of nanoparticles changed the surface energy of the blowing agent grains, thanks to which it decomposed at lower temperatures and foaming was even faster. At the same time, nanoparticles have the potential to reinforce foam walls and thus improve mechanical properties. 3D printing is a popular and widespread technique, due to its simplicity it is in many laboratories and test institutions, therefore the demand for filaments with special properties is growing. The material developed in this dissertation is essentially a finished and characterized product that could contribute to the satisfaction of this claim.

KEYWORDS

Polymer nanocomposites, foams, nanoparticle organization, cellular composites, hierarchical systems, 3D printing, structure, mechanical properties, HIPS, azodicarbonamide, nanosilica.

ABSTRAKT

Tato dizertační práce se zabývá přípravou a charakterizací nanokompozitních polymerních pěn se zaměřením na strukturu materiálu a aplikaci v 3D tisku. Cílem práce je studium materiálu s vysoce organizovanou hierarchickou strukturou – od nanoměřítka, přes mikroskopickou strukturu po makroskopická tělesa. V první části práce byly řešeny strukturní vlastnosti nanokompozitů připravených z polymerních skel roztokovou metodou. Byl hledán obecně platný trend, pomocí kterého by bylo možné předpovídat disperzi nanočástic v kompozitu. Ukázalo se, že řídícím faktorem může být závislost na rozdílu parametrů rozpustnosti polymeru a rozpouštědla. Tento poznatek byl ověřen na systémech obsahujících různé nanočástice, polymery a rozpouštědla. Se znalostí principů pro řízení struktury nanokompozitů byly připraveny nanokompozity impaktního polystyrenu plněného nanosilikou. Tyto nanokompozity posloužily jako základ pro přípravu polymerních nakompozitních pěn. Porézní struktury bylo dosaženo pomocí termálního chemického nadouvadla azodikarbonamidu. Z těchto materiálů byly extrudovány filamenty, které byly následně zpracovány pomocí 3D tisku do požadovaných tvarů a vypěněny. Výsledkem byla hierarchická struktura s organizací struktury od nano (organizace nanočástic), přes mikro (struktura dvoukomponentní polymerní směsi a struktura pěny) po makroměřítko (struktura pěny a design 3D tisku). Byl pozorován vliv nanočástic na strukturu a termální a mechanické vlastnosti polymerních pěn. Nanočástice fungují při tvorbě pěny jako nukleační činidlo, na jejich povrchu snadno dochází k tvorbě pórů, takže s obsahem nanočástic v materiálu bylo vytvořeno více menších pórů, což napomohlo k homogenitě pěnové struktury. Přítomnost nanočástic změnila povrchovou energii zrn nadouvadla, díky čemuž docházelo k jeho rozkladu za nižích teplot a pěnění bylo i rychlejší. Nanočástice mají zároveň potenciál vyztužit stěny pěny a zlepšit tak mechanické vlastnosti. 3D tisk je oblíbená a hojně rozšířená technika, díky své jednoduchosti je v mnoha laboratořích a zkušebnách, proto roste poptávka po filamentech se speciálními vlastnostmi. Materiál vyvinutý v této dizertační práci je v podstatě hotovým a charakterizovaným produktem, který by mohl přispět k uspokojení této pohledávky.

KLÍČOVÁ SLOVA

Polymerní nanokompozity, pěny, organizace nanočástic, celulární kompozity, hierarchické systémy, 3D tisk, struktura, mechanické vlastnosti, HIPS, azodikarboamid, nanosilika.

ZÁRYBNICKÁ, K. Celulární polymerní nanokompozity. Brno: Vysoké učení technické v Brně, Středoevropský technolický institut VUT, 2021. 140 s. Vedoucí diplomové práce prof. RNDr. Josef Jančář, CSc.

DECLARATION

I declare that this thesis has been composed solely by myself under the supervision of prof. RNDr. Josef Jančář, CSc. and that all quotations of the literary sources are accurate and complete. The presented results are the property of Central European Institute of Technology at Brno University of Technology and all commercial uses are allowed only if approved by both the supervisor and the director of the Central European Institute, BUT. The thesis includes copyrighted content which further use may require permission from the copyright owner.

Brno ………………………………. ……………………………….
author's signature

ACKNOWLEDGMENT

I would like to express thanks to my supervisor prof. RNDr. Josef Jančář, CSc. for mediating internship in the USA and support in project activities. I would also like to express my thanks to Ing. František Ondreáš, Ph.D. and Ing. Petr Lepcio, Ph.D. for their professional guidance, help in the laboratory, and for teaching me the most of what I know. Thanks to Ing. Michal Kalina, Ph.D. for zeta potential measurement. I would like to thank all my fellow Ph.D. students – Juraj, Martina, Janča, Kika, Klárka, Matěj, Katka, Martina, Evča, Johanka, and doctor Marek – for helping me survive the hard times.

TABLE OF CONTENTS

Abstract 1
Keywords 1
Abstrakt 2
Klíčová slova 2
Declaration 3
Acknowledgment 3
Table of contents 4
1 Introduction to polymer nanocomposite foams 6
2 Literature review 8
  2.1 Nanocomposites 8
    2.1.1 Nanoparticles dispersion in polymer matrix 8
    2.1.2 Nanocomposite preparation 9
    2.1.3 Theoretical models for prediction nanoparticle dispersion 11
    2.1.4 Nanoparticles in block copolymers 14
    2.1.5 Interaction of nanocomposite components during solvent-casting 16
      2.1.5.1 Polymer-solvent interactions 16
      2.1.5.2 Particle-solvent interaction in solution 18
      2.1.5.3 Polymer-particle interactions 19
    2.1.6 Mechanical properties of copolymers and polymer nanocomposites 21
      2.1.6.1 Mechanical properties of high-impact polystyrene 21
      2.1.6.2 Mechanical properties of polymer nanocomposites 21
  2.2 Polymer foams 25
    2.2.1 Foaming agents methods 27
    2.2.2 Other foaming methods – syntactic foams, phase separation, leaching, etching, and electrospinning 28
    2.2.3 Foaming mechanism 31
    2.2.4 Foam processing technology 32
    2.2.5 3D printed foams 34
      2.2.5.1 Selective laser sintering (SLS) 34
      2.2.5.2 Inject-based printing 34
      2.2.5.3 Stereolithography (SLA) 34
      2.2.5.4 Fused deposition modeling (FDM) 35
    2.2.6 Mechanical properties of foams 37
  2.3 Nanocomposite polymer foams 40
3 Aims of thesis 44
4 Materials, preparation protocol, and methods 45
  4.1 Materials 45
    4.1.1 Polymer matrices 45
      4.1.1.1 Polymer glasses 45
      4.1.1.2 High impact polystyrene (HIPS) 45
    4.1.2 Nanoparticles 46
    4.1.3 Foaming agent – azodicarbonamide 46
    4.1.4 Solvents 48
  4.2 Preparation protocol 49
    4.2.1 Solvent-casting 49
    4.2.2 Foams preparation 50
  4.3 Methods 53
    4.3.1 Structural analysis 53
    4.3.2 Thermal analysis 55
    4.3.3 Zeta potential 55
    4.3.4 Mechanical properties 55

5 Results and discussion 57
  5.1 Controlling nanocomposite structure 57
    5.1.1 Nanocomposites with homopolymer matrices 57
      5.1.1.1 ξ-potential of spherical nanosilica in solvents 57
      5.1.1.2 Nanocomposite with spherical nanosilica 58
      5.1.1.3 General laws controlling morphogenesis in glassy nanocomposites 64
      5.1.1.4 Nanocomposites with functional nanoparticles 69
      5.1.1.5 Relaxation properties of polymer nanocomposites 72
    5.1.2 Nanocomposites with HIPS matrix 76
      5.1.2.1 Solvent-casted HIPS nanocomposites 76
      5.1.2.2 Melt-blended HIPS and PS nanocomposites 81
  5.2 Structural and thermal analysis of foams 83
    5.2.1 Structure evolution during preparation 83
    5.2.2 Thermal decomposition of the foaming agent 86
    5.2.3 Effect of nanoparticles on the foaming process 87
    5.2.4 Effect of silica content on the foam porosity 89
    5.2.5 Spatial distribution of nanoparticles within the foam structure 93
    5.2.6 Structure of the 3D printed foams 94
  5.3 Mechanical properties of foams 97
    5.3.1 Tensile properties of filaments 97
    5.3.2 Compressive behaviour of 3D printed foams 101
6 Conclusion 107
7 Appendix – Raw data 109
8 Bibliography 117
9 List of abbreviations 129
10 List of figures 133
11 List of tables 138
12 Author publications and other outputs 139
  12.1 Publications 139
    12.1.1 First author papers 139
    12.1.2 Co-author papers 139
    12.1.3 Utility model 139
    12.1.4 First author abstracts 139
  12.2 Projects 140
    12.2.1 Principal investigator 140
    12.2.2 Co-investigator 140
    12.2.3 Collaborator 140

1 INTRODUCTION TO POLYMER NANOCOMPOSITE FOAMS

Future materials and fabrication technologies will need to integrate unprecedented combinations of stiffness, strength, and toughness at low density and environmental friendliness with end-use specific functions, such as super-hydrophobicity, self-cleaning, mechanical and chemical sensing, shape memory, etc. Even the most advanced synthetic composites do not exhibit the desired structural and functional hierarchy that is found in nature´s load-bearing structures. Structures of natural materials are created by self-assembling processes from relatively simple components. For example, nacre is made of stiff but fragile aragonite and tough but weak protein. These components are organized in a precisely defined hierarchical structure (*bricks and mortar*) from nano to macro-scale which can make the final material of nacre stiff and tough simultaneously. [1] Nature materials with a cellular structure are widespread and include wood, cork, plant parenchyma, glass sponge, and even certain bones, such as a vertebra, femoral head, or skull are filled with a spongy structure called trabecular bone. Exceptional mechanical properties of these materials are believed to be due to a functional adaptation of the structure at levels of hierarchy. For example, the honeycomb-like microstructure of wood gives it a high-performance index for resisting bending and buckling. The radial and longitudinal density gradients and fiber-reinforced composite structure make bamboo strong and stiff with significantly low density. The mineralized cylindrical cage skeleton of a deep-sea glass sponge is structured over at least six levels of hierarchy – biogenic silica reduces its stiffness but an architecture provides substantial toughening that overcomes that of technical glass thanks to structuring at the nanometer and at the micrometer level. [2; 3; 4; 5]

Understanding the role of preparation protocol in the morphogenesis of hierarchical nanocomposites is vitally important for the future applications of polymer nanocomposites in high value-added engineering components. The key obstacle in transforming polymer nanocomposites into industrially viable materials lies in our current inability to directly control the nanoparticle organization over multiple length scales on reasonably short production time and with an industrially viable throughput. Numerous polymer nanocomposites have achieved complex structural hierarchy, from the nanometer to micrometer length scales. However, all of these examples are limited in their ability to organize into larger structures, lacking the necessary combination of simple fabrication and mechanical robustness that span length scales greater than tens of microns.

One possible way how to improve the organization to a higher hierarchical level is to use block copolymers (Figure 1). Block copolymer consists of at least two different monomer blocks that can organize into distinct domains consisting of the constituting homopolymers. For example, two-component polymer blend high impact polystyrene (HIPS) consists of microscale polybutadiene rubber (PBR) particles dispersed in a homopolymer polystyrene (PS) matrix. Adding nanoparticles in such a system will result in their different distribution in the different domains enabling a new level of structural organization. [6; 7]

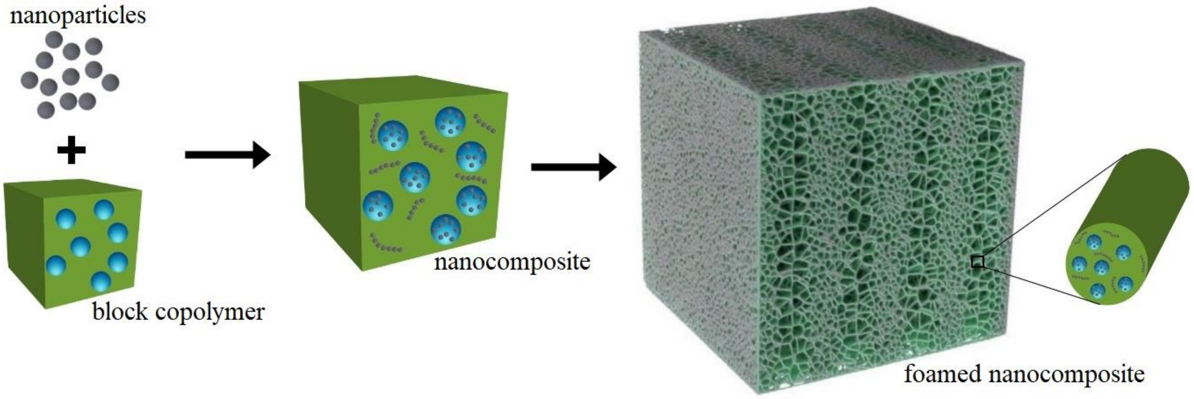

Figure 1: Scheme of foam material with multiple hierarchical levels of structural organization. The state of nanoparticle (grey) dispersion in a polymer matrix (green) represents an organization of material on a nano-scale level. An arrangement of domains (blue) in a block copolymer (e.g., rubber particles in the PS matrix) exhibits the organization of structure on a micro-scale. A micro-to-macro-scale organization is determined by a structure of walls and cells forming polymer foam. The final macroscopic shape of a product could be organized via 3D printing.

Polymer foams are used in many applications because of their excellent thermal and sound insulation properties or because of the flexibility of generating desired morphologies to meet specific applications. On the other hand, foam applications are in many ways limited because of their inferior mechanical strength, poor surface quality and low resistance to high temperatures, and poor dimensional stability. Recently, polymer nanocomposite foams have received increasing attention in both scientific and industrial communities. The combination of functional nanoparticles and foaming technology has a high potential to generate a new class of materials that are lightweight, high strength, and multifunctional. Nano-scaled particles are suitable for microscaled reinforcement (reinforcing of walls of bubble cells), thus achieving the macroscopic mechanical enhancement of foam. Moreover, a small amount of well-dispersed nanoparticles in the polymer may serve as nucleation centers for forming bubbles during the foaming process. Pore nucleation is facilitated and a more homogenous and fine structure of the foam is produced. [8; 9; 10] It has already been shown that nanoparticles can significantly enhance the strength and stiffness of polymer foams and introduce additional functions such as electrical conductivity (with carbon or semiconductive nanoparticles), fire resistance (magnesium hydroxide), hydrophobicity, etc. [11; 12; 13]

Recently, a breakthrough in the 3D printing of versatile, compressible solids with programmable microstructure, customizable shapes, and a tunable mechanical response has been reported. [14; 15] However, the success of 3D printed materials possessing regular cellular architecture as viable replacements for traditional stochastic foams [16; 17; 18] critically depends on their mechanical performance and stability of their micro-architecture under long-term mechanical stress and temperature oscillations. By using polymer nanocomposites instead of neat polymers in this process, it could be envisioned to rapidly fabricate hierarchical, lightweight, functional engineering components possessing the desired balance of stiffness, strength, and toughness.

2 LITERATURE REVIEW

2.1 Nanocomposites

Polymer nanocomposites are two-component solid systems in which one component is continuous (polymeric matrix) and the discrete second component (filler) is dispersed in the matrix wherein the filler has at least one dimension on the nanometer scale. If the filler is in the form of sheets, there is only one dimension in nanometers - e.g. graphene [19] or silicate-layered nanocomposites [20] (exfoliated montmorillonite or smectite). In the case of nanofibers, there are two dimensions in nanometers – e.g. carbon nanotubes [21] or cellulose nanofibers [22]. This dissertation thesis is focused on nanoparticle composites, which has all three filler dimensions in the nanometer scale.

2.1.1 Nanoparticles dispersion in polymer matrix

Nowadays, it is well known that the addition of inorganic nanoparticles into the organic polymeric matrix results in the production of polymeric nanocomposites with improved macroscopic properties. Many experiments have shown that these improvements are influenced by the spatial organization of nanoparticles, so optimal dispersion of nanoparticles may vary depending on what property is required. [23] Changes in material properties are also influenced by the shape of nanoparticles – platelets, slices, nanotubes, or polyhedral particles. This may affect both the surface energy of the particles and the surface-volume ratio. [11] Individual nanoparticles tend to aggregate into formations that may have dimensions up to the order of microns. [24] In this case, the active surface of the nanoparticles is greatly reduced, only a small amount of the polymeric matrix is affected by the nanoparticles, and the modification of the properties is negligible.

In a polymer matrix, the nanoparticles can be arranged into three limiting structures – nanoparticle aggregates, nanoparticle clusters in which the nanoparticles are bonded by polymer chains, or dispersion of individual particles (Figure 2). Nanoparticles in aggregates interact directly with each other, thanks to an attractive particle-particle interaction that is stronger than other interfacial interactions in the system. Thus, the aggregate is a separate large inclusion consisting of many nanoparticles bound together by physical interparticle interactions. In polymer nanocomposites with aggregated nanoparticles, the nanoparticle-chain interfacial region is restricted, the layer of coils influenced by the surface of the particles is reduced. Aggregates can easily be broken even with small deformations, so the composite becomes brittle. In the case of individually dispersed particles, the nanoparticle-chain interfacial region is maximized, the surface of the particles affects the maximum of the polymer chains. Nanocomposites with good particle dispersion show the most significant modification of properties (e.g., a higher elastic modulus). In the case of chain-bound clusters, the particles are separated by a single polymer chain that mediates interactions between particles. Thus, clusters behave like internally structured inclusions having properties dependent on their composition and dispersion in the polymer matrix. Clusters, in the opposite of aggregates, are deformable and at the same size of inclusions, there are fewer nanoparticles in the cluster than in the aggregate. Polymer nanocomposites with clusters could be considered as a two-level hierarchical structure. [25]

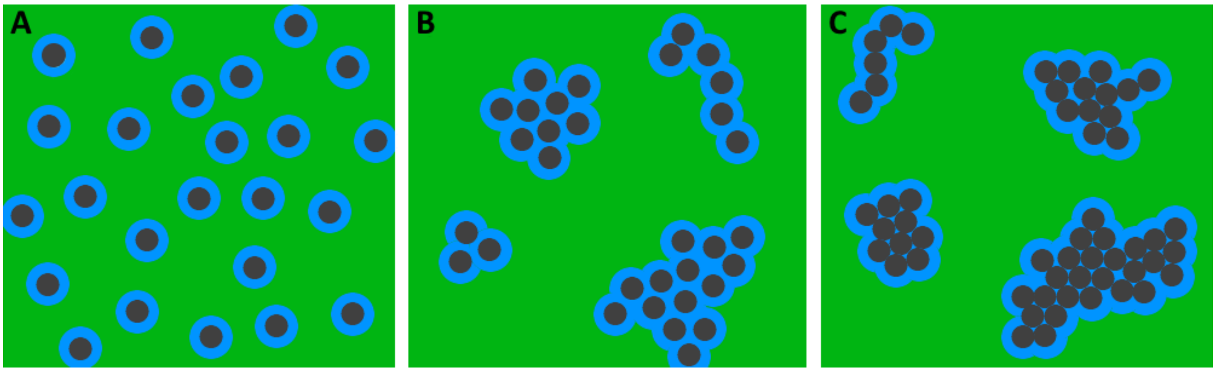

Figure 2: Schematic depiction of nanoparticles (grey) dispersed in a polymer matrix (green) and the amount of affected polymer matrix (blue). **A** – Individually dispersed particles, **B** – chain bound clusters, and **C** – contact aggregates.

2.1.2 Nanocomposite preparation

During the nanocomposite preparation, it is usually required to achieve controlled nanoparticle dispersion and distribution in a polymer matrix, which is not a trivial task and is still a largely unaccomplished task. Strategies proposed to accomplish good dispersion include the use of ultrasonication, high shear mixing, surfactants, and functionalization of particle surface (grafting). Most commonly, three main self-assembly methods are used for nanocomposite preparation – melt-blending, solvent-casting, and in situ polymerization. [10]

In the melt-blending method, which is usually carried out in a mixer or extruder at elevated temperature, a molten polymer and the powdered nanoparticles are mixed directly. The advantage of this process is that it is relatively inexpensive and simple but in the case of bare nanoparticles with an untreated surface, it is very difficult to achieve a good dispersion, generally, aggregation occurs. Care has to be taken to cohere particle surface chemistry to increase compatibility with the polymer matrix. Melt-blending is often used for the preparation of intercalated silicate layers nanocomposites. Due to the incompatibility of the hydrophobic polymer matrix and hydrophilic inorganic particles, the particle surface is modified with polar ligands (e.g. alkyl ammonium or phosphonium ion) or grafted directly with polymer chains. Polymers (e.g. polypropylene; PP) are modified with a polar compatibilizer such as maleic anhydride. [10; 26; 27; 28] Multiple extrusion of the nanocomposite also increases the proportion of good dispersion due to intensive repeated mixing [29], but further degradation of the polymer matrix happens at each cycle.

In the solution-blending (solvent-casting) method, both the nanoparticles and the polymer are dissolved and mixed in the same solvent, usually followed by the step of rapid drying to fix the dispersion pre-organized in solution. Slow removal of the solvent could lead to sedimentation and particle aggregation. A good solvent can prevent particle aggregation and a perfect dispersion of the individual particles can be achieved. The advantage of this method is that good dispersion can be relatively easily achieved with a bare particle surface (without grafting). The disadvantage is that a large amount of solvent and its energy-consuming removal is required, which makes the process expensive and time-consuming. Jouault et al. [30] investigated the influence of solution blending of spatial dispersion of silica nanoparticles with the partially treated surface but with silanol groups still available at the surface and of poly(2-vinyl pyridine) (PVP). They cast nanocomposites from two different solvents –

ethyl methyl ketone (MEK) and pyridine. In MEK (Figure 3A), they showed that PVP strongly adsorbed onto the silica surface and stabilized particles against aggregation, and thus good nanoparticle dispersion in composite was always achieved, independent of PVP molecular weight, concentration, or nanoparticle volume fraction. On the contrary, in pyridine (Figure 3B), PVP interacted preferentially with solvent molecules and did not adsorb on the nanoparticles, which collided. Jouault et al. [31] also showed that silica could be well dispersed in PS via the solvent-casting method. It is difficult to obtain a good dispersion of polar silica at the nanometer scale because it forms in most cases large compact aggregates (of the order of a hundred nanometers or larger) in a non-polar PS matrix. The key for good dispersion is to use a high boiling solvent with hydrogen bonds, in Jouault's case dimethylacetamide (DMAC), and a controlled evaporation procedure. Silica in PS aggregated at nanometer size only and was well dispersed at all large sizes (Figure 3C).

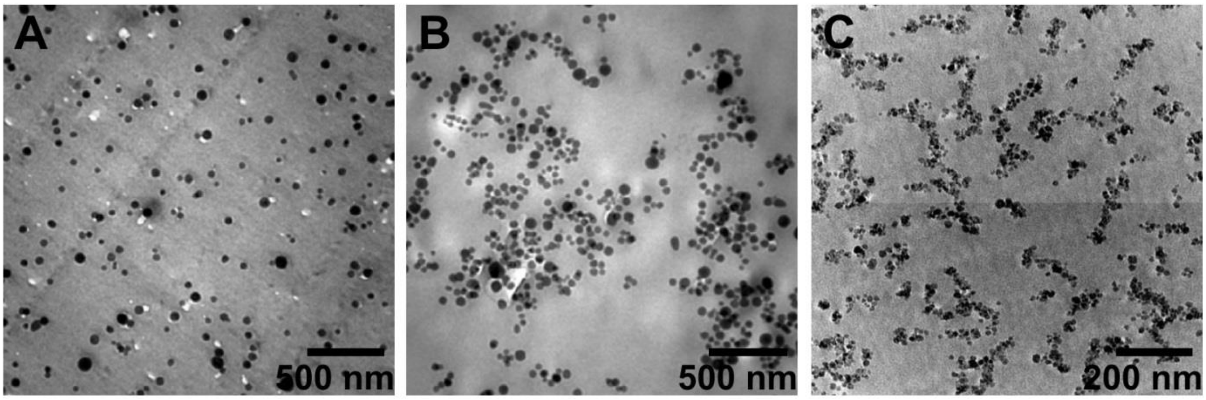

Figure 3: Transmission electron microscopy (TEM) images of nanocomposites with solvent-casted silica. **A** – With PVP prepared in MEK. **B** – With PVP prepared in pyridine. *Reprinted with permission from* [30]. *Copyright 2014 American Chemical Society*. **C** – With PS prepared in DMAC. *Reprinted with permission from* [31]. *Copyright 2009 American Chemical Society.*

In situ polymerization finds application in the preparation of nanocomposites made of thermoset polymers because it is for them the only viable method to prepare nanocomposites. Free radical polymerization has also been employed to synthesize many thermoplastic nanocomposites. Because of the low monomer viscosity, it is much easier to achieve uniform mixing of particles using a high shear mixing. It is also often used for exfoliation of silicate layers (montmorillonite) because the low viscosity and high diffusivity result in a higher rate of monomer diffusion into the interlayer region. [10; 32]

In general, great dispersion of particles can be achieved most often in systems where hydrogen bonds exist between nanoparticles and polymer matrix (e.g. hydrogen bonding between hydroxyl group on PVP and nitrogen on ligand grafted onto nanoparticles). Even bare non-grafted silica, due to its hydroxyl groups, forms hydrogen bonds with PVP, poly(methyl methacrylate) (PMMA), or poly(vinyl acetate) (PVAc). [23]

2.1.3 Theoretical models for prediction nanoparticle dispersion

A considerable effort has been recently focused on the development of a reliable and generally applicable model for the prediction of nanoparticles spatial organization in polymer nanocomposites but no completely reliable model has been published yet.

Hooper and Schweizer [33; 34; 35] proposed a theoretical model of possible arrangements of nanoparticles in a dense homopolymer melt using the potential of mean force between two rigid spherical particles. They included the effect of particle-monomer size ratio, degree of polymerization, strength and spatial range of attraction forces between monomer and particle, and direct van der Waals interactions between particles in the model. Based on these parameters, they developed the PRISM theory (polymer reference interaction site model), which can predict the structure, effective forces, and thermodynamics in entropy-controlled athermal mixtures. According to the PRISM theory, four basic types of polymer-mediated nanoparticle organization (Figure 4) can occur for rigid spherical particles: contact aggregation due to depletion attraction (low attraction between polymer and particle), steric stabilization due to the thermodynamically stable absorbed polymer layer, tight particle bridging by polymer segment and tele-bridging, where layers of adsorbed polymer coexist with long-range bridging.

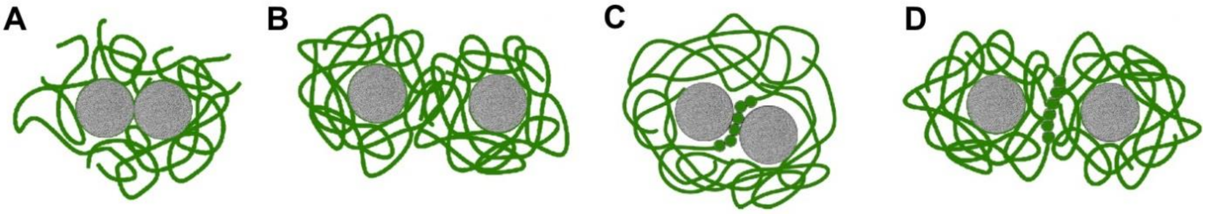

Figure 4: Basic types of nanoparticle organization in polymer melt according to PRISM theory. **A** – Contact aggregation. **B** – Steric stabilization. **C** – Polymer segment level tight particle bridging. **D** – Tele-bridging. *Adapted with permission from* [33]. *Copyright 2005 American Chemical Society.*

The disadvantage of PRISM theory is that it considers the interaction of a small number of particles and not the entire system with an unlimited number of particles. But such considerations would be very challenging for the mathematical model. The state of the dispersion is often dependent on the volume fraction of the filler and with its increasing fraction, the dispersion may collapse. Another disadvantage of this theory is that it considers the interaction of only the polymer and the particle and not the solvent in which the nanocomposites are often prepared. Therefore, the model cannot be applied to any nanocomposite system.

Mackay et al. [36] showed that thermodynamically stable dispersion of nanoparticles in a polymeric liquid is enhanced for systems where the radius of gyration R_g of the linear polymer is greater than the radius of the nanoparticles (Figure 5). They verified this hypothesis by experimental data of nanocomposites with a linear PS matrix. They used three different types of nanoparticles: crosslinked polystyrene nanoparticles, where monomer-monomer contacts were the same for all of its constituents in this system, fullerene C_{60} to demonstrate that good dispersion of fullerenes in polymers could be reached, and branched polyethylene (PE) particles to compare the system of two standardly phase-separating linear polymers. For example, dendritic PE particles (radius 10–15 nm) were miscible with 393 kg·mol^{-1} PS (R_g = 17.3 nm) but the miscibility did not occur with 155 kg·mol^{-1} PS (R_g = 10.5 nm). They also emphasized that even when the dispersed state is thermodynamically stable, the correct processing strategy needs to be adopted (especially in the case of fullerenes). However, Mackay's theory was proved not to be the case for solvent-casted polymer nanocomposites [25], where good dispersion could be reached even when nanoparticles are larger than R_g of polymer coil.

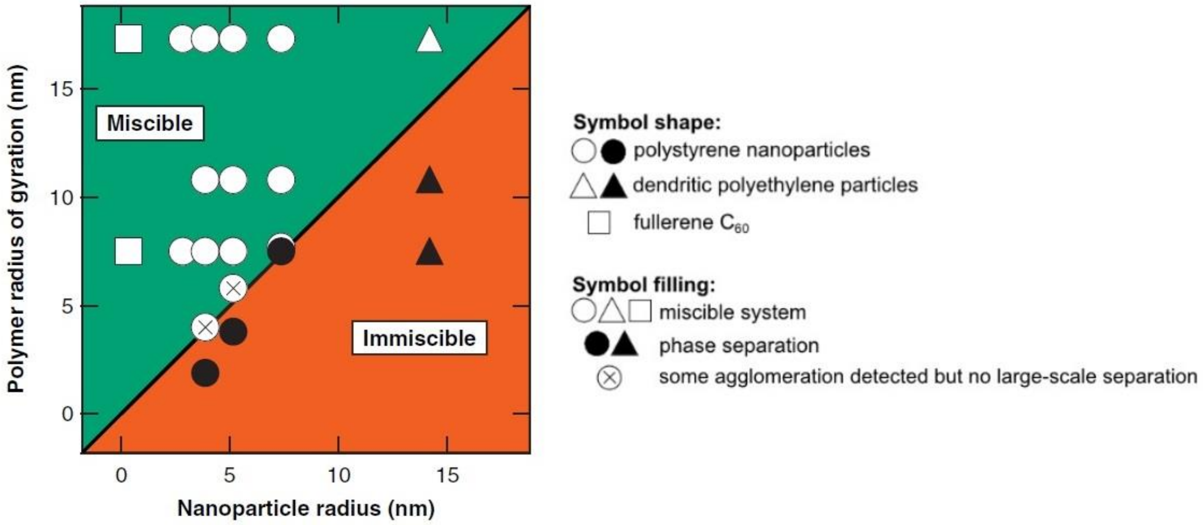

Figure 5: A polymer radius of gyration to nanoparticle radius phase diagram with the area of miscible systems (good dispersion of nanoparticles) and the area of immiscible systems (aggregates). Each nanocomposite was with PS matrix and with 2 wt. % of nanoparticles. *From* [36]. *Reprinted with permission from AAAS.*

However, neither of the above-mentioned models (Hooper-Schweizer and Mackay) consider the presence of a solvent and its impact on the organization. In solution, the stability of nanoparticle dispersion is affected by the presence of the solvent which alters forces in nanoparticle systems, e.g. short-range van der Waals attraction, long-range electrostatic repulsion, or steric repulsion. Hence, the polymer nanocomposite structure can be effectively controlled by the selection of the dispersing solvent since the solid-state structure is preserved from the solution for sufficiently fast drying. [25; 30; 31]

In our previous paper [25], we attributed the key role in nanoparticle spatial organization of solution blended polymer nanocomposites to acid-base competition for adsorption sites between nanoparticle surface, polymer segments, and solvent molecules. This concept was originally used to interpret polymer adsorption on the surface of inorganic microparticles by Fowkes et al., [37; 38; 39] who extended Drago's model [40] for enthalpies of the acid-base interactions between a donor and an acceptor pair of solvents. This model counts interfacial interaction enthalpy $-\Delta H$ in the donor-acceptor system from semi-empirical constant and takes the form of a four-parameter equation:

$$-\Delta H = E_A E_B + C_A C_B, \tag{1}$$

where subscript A denotes acceptor (acid) and B denotes donor (base). Empirically determined parameters were suggested to represent the susceptibility of a functional group to undergo electrostatic interactions (E_A, E_B) and to form covalent bonds (C_A, C_B). Fowkes et al. [37; 38; 39] found that acidic functional groups on the filler surface are competed for by the basic functional groups of solvent and polymer. Alternatively, acidic solvents and acidic groups on particle surface compete for basic functional groups of the polymer. However, their research was limited because of the small specific surface area of microparticles, for which the observed effects were relatively small compared to our recent study with nanoparticles (Figure 6). [25] Depending on the dispersing solvent used during the preparation, it is possible to calculate the interaction enthalpy –Δ*H* of the silica-polymer pair (black color in the graph) and the silica-solvent pair (other colors in the graph) to determine the preferred interactions in the system and to predict the stability of the dispersion of the nanosilica in the solidified nanocomposite.

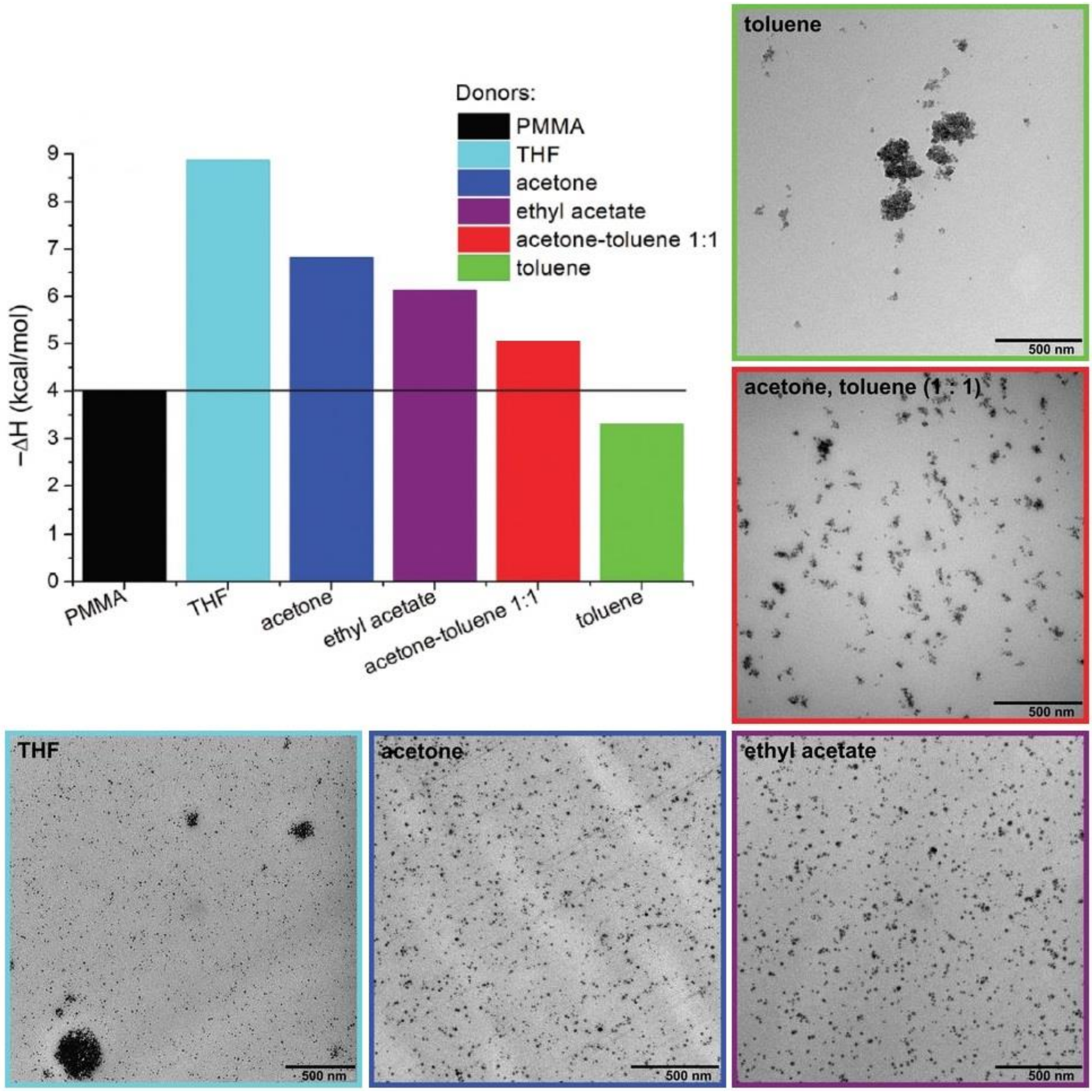

Figure 6: Bar diagram of donor-acceptor interaction enthalpies of silanol groups on nanosilica surface (acceptor) and PMMA and various solvents (donors). TEM images of PMMA nanocomposites filled with 1 vol. % of nanosilica prepared in an appropriate solvent. [25]

At sufficiently high values −Δ*H* the solvent is capable to form a solvation shell around the silica particle that stabilizes the good dispersion (acetone, ethyl acetate). At even higher values of −Δ*H* (tetrahydrofuran; THF), such a strong solvating shell is formed that the solvent displaces the polymer from the interphase around the particles (depletion attraction) so that, when the solvent is removed during drying, particles may collide to form aggregates. However, the aggregates are accompanied by a good dispersion of the individual particles. In the case of toluene, the values of $-\Delta H$ are lower than for PMMA, therefore toluene is not able to form a sufficient solvation shell capable of stabilizing the good dispersion and contact aggregation occurs. In the case of the acetone-toluene mixture (volume ratio 1:1), the compromise between good dispersion in acetone and aggregates in toluene was established and good dispersion of clusters was formed. [25; 41; 42]

Despite the promising results, the prediction capability of the donor-acceptor model is limited by the lack of empirical Drago-Fowkes constants E_A, $E_{B,}$ and C_A, C_B available in the literature – they are determined just for silica and a few of polymers (PMMA, polyoxyethylene POE, and phenoxy resins) and they are not determined even for many commonly used solvents. [37; 38; 39; 40] Therefore, it has to be continued to elaborate a more practical method for the prediction of nanoparticle spatial arrangement in polymer nanocomposites.

2.1.4 Nanoparticles in block copolymers

Block copolymer consists of at least two macromolecular domains – majority domain (component A) and minority domain (component B). Depending on the type of polymer and the ratio of components, domains can be arranged in different structures because of the microphase separation – component B forms discrete spheres or cylinders in component A, lamellar structure, in which the layers of components A and B alternate regularly, or bicontinuous gyroid structure (Figure 7A). [43; 44]

When nanoparticles are added, they can self-assemble in the preferred wetting domain of the block copolymer selectively (Figure 7B). To provide a more selective arrangement of nanoparticles into the preferenced domains, functional small molecules and polymers can be attached to nanoparticles by physical adsorption or covalent attachment (grafting of particles). The ligands on the surface of the particles favorably interact with the favored polymer domain. [45; 46]

The presence of nanoparticles affects the microphase separation or orientation of block copolymer domains (Figure 7C) whereas the morphology of the composite depends on particle concentration. [6; 47; 48] For example, PS and PVP are highly incompatible, the PS-PVP phase separates very quickly during annealing and the microstructure is less ordered in poor packing of the cylinders. When Au nanoparticles (30 wt. %) assemble in the block copolymer, particles reduce the degree of segregation resulting in better ordering of the microdomains. [48]

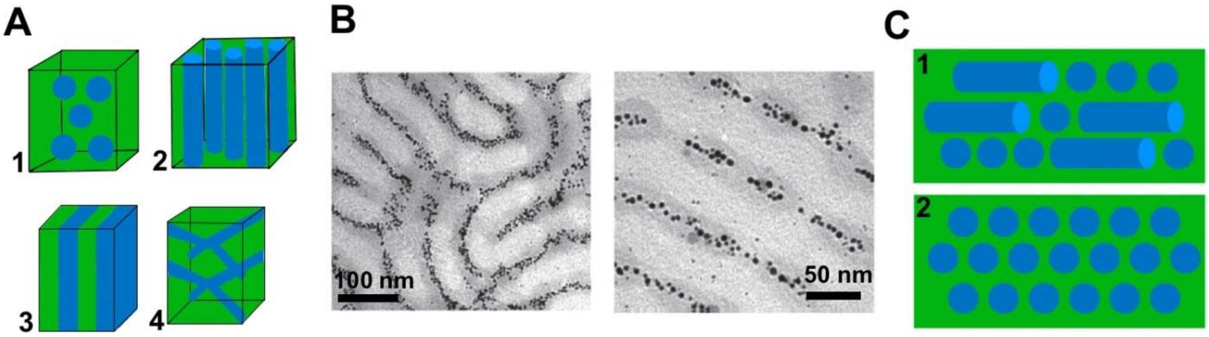

Figure 7: **A** – Phase separation models in diblock copolymers: spheres (**1**), cylinders (**2**), lamellar (**3**), and gyroid structure (**4**). *Reuse from* [44]. *Copyright 2009 Technical University of Liberec.* **B** – TEM image of the PS-PVP block copolymer with Au particles localized in PVP domains. *Reprinted with permission from* [47]. *Copyright 2008 Wiley Materials.* **C** – Schematic picture showing the microphase separation of neat block copolymer (**1**) and the same copolymer with nanoparticles (**2**). *Reprinted with permission from* [48]. *Copyright 2012 Wiley Materials.*

Theoretical approaches reveal that both entropy and enthalpy contributions from nanoparticles induce phase transformation. Previous observation implies that the spatial distribution of nanoparticles in the microphase-separated morphologies can be controlled by nanoparticle chemistry (bare surface or tailoring by ligands; i.e., enthalpic effects) and the size of the nanoparticles (i.e., entropic effects). Large particles localize at the center of the domains to maintain an energetically more favorable status. In contrast, small particles self-organize at the polymer interface or are more uniformly dispersed within domains to gain maximum entropy. The addition of nanoparticles balances the discrepancy of surface energy between the two domains and reduces the degree of segregation of the system that slows down microphase separation. [45; 48; 49]

Huh et al. [49] used Monte Carlo simulations and scaling theory in the strong segregation limit to investigate the influence of hard nanoparticles in the phase behaviour of diblock copolymers. They considered enthalpic interactions between the nearest neighbors – ε_{AB} represents interaction energy between A (majority monomers) and B (minority monomers) and ε_{PA} represents particle-monomer A interaction. Here,

$$\varepsilon_{\mathrm{AB}} = \varepsilon_{\mathrm{PA}} = \varepsilon > 0 \qquad (2)$$

and all other interaction parameters were set to zero. Thus, the particles had an affinity toward the B-block. They obtained the phase diagram as a function of the nanoparticle concentration Φ and diblock composition f (Figure 8A).

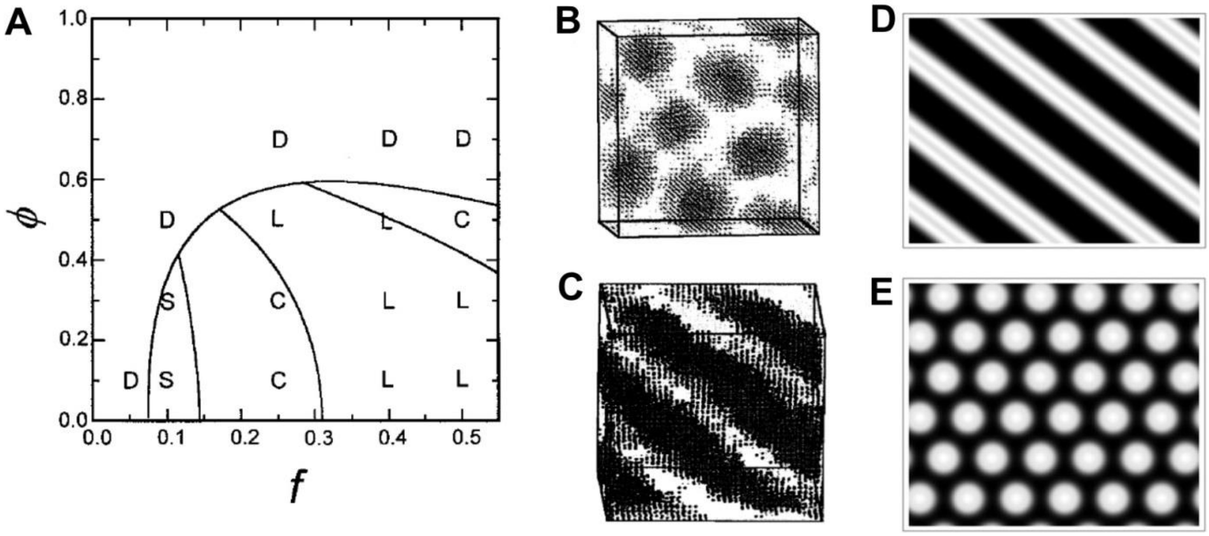

Figure 8: **A** – Approximate phase diagram for diblock copolymer filled with nanoparticles defining areas of different block structures – disordered (D), spherical (S), cylindrical (C), and lamellar (L). **B** – Snapshot of diblock copolymer without nanoparticles (cylindric structure). **C** – Block copolymer with 50 vol. % of small nanoparticles (lamellar). *Reprinted with permission from* [49]. *Copyright 2000 American Chemical Society.* **D** – Block copolymer with 20 vol. % of larger nanoparticles (lamellar). **E** – Block copolymer with 20 vol. % of smaller nanoparticles (cylindrical). *Reproduced by permission of The Royal Society of Chemistry from* [50].

Figure 8B shows a neat block copolymer with 25 % of component B with the cylindrical structure. When 50 vol. % of small nanoparticles with a size smaller than R_g of minority B-block was added, the structure of the block copolymer was modified to lamellar (Figure 8C). Thus by controlling the volume fraction of particles, the structure of the copolymers can be changed to another. [45; 49] Lee et al. [10] showed the influence of entropic interactions by changing particle size on diblock copolymer morphology through theoretical modeling. The enthalpic interaction between A and B segments was described by the dimensionless Flory-Huggins parameter χ_{AB}. Sphere hard particles were preferentially wetted by the A-blocks. They used two types of nanoparticles – a larger one with size $R_p = 0.2\,R_0$, where R_0 is the size of the diblock copolymer, and smaller particles with $R_p = 0.1\,R_0$. Entropic effects played a role in the observed transition from the lamellar structure with larger particles (Figure 8D) to the cylindrical phase with smaller particles (Figure 8E) at the same volume fraction of particles. Smaller particles gained translation entropy by delocalizing and migrating into the unfavorable B-phase, leading to a microphase separation in the system.

2.1.5 Interaction of nanocomposite components during solvent-casting

2.1.5.1 Polymer-solvent interactions

Depending on the constitution of the polymer chain and the solvent, two cases can occur in their solution: the chain segments try to gather together into the intramolecular aggregates to avoid contact with the solvent, the polymer coils are packed as tightly as possible, in this case, it is the so-called poor solvent. Or, conversely, the segments try to get in contact with the solvent and the coils expand (in good solvent). The process of the dissolving of the polymer depends on the cohesive energy of the solvent and on the cohesive forces between polymer chains.

When the solid polymer is dissolved, the secondary bonds between the structural units of the chain are replaced by secondary bonds between the structural units of the chain and the solvent molecules. Only when all the segments belonging to the same chain are solved, the whole macromolecule can move freely from the interface of the phases. In most cases, the polymer chain is entangled with other chains. To release the chain, the surrounding macromolecules must also be dissolved. Solvent molecules first penetrate from the interface inside to the solid polymer and cause partial solvation of polymer chains. Because of the slow diffusion process, the solvent molecules have enough time to penetrate into the polymer bulk, so the polymer initially swells. In good solvents, each individual polymer molecule is surrounded by solvent molecules and can move in the solution freely. [51]

The basic law for assessing the solubility of the polymer in the solvent is the Flory-Huggins equation. This relationship expresses the change in Gibbs energy of mixing ΔG_M based onchanges in enthalpy and blend entropy depending on the representation of individual components:

$$\Delta G_{\mathrm{M}} = RT(n_1 \ln \varphi_1 + n_2 \ln \varphi_2 + \chi n_1 \varphi_2), \tag{3}$$

where R is the universal gas constant ($\mathrm{J \cdot K^{-1} \cdot mol^{-1}}$), T is the absolute temperature (K), n is the amount of the substance (mol), φ volume fraction, and χ is interaction parameter ($\mathrm{m^2 \cdot kg \cdot s^{-2} \cdot K^{-1}}$). Index 1 refers to the solvent, index 2 to the polymer. The dissolution occurs when the change of Gibbs energy is negative. The first two terms in brackets on the right side of the equation are entropic, their value is always negative. The third term in brackets is the enthalpy part of the equation and its value is usually positive. The sign of Gibbs energy, as well as the miscibility, depends on whether the influence of the thermal movement (represented by the entropic term) and the influence of the change of the cohesive energy in the formation of polymer-solvent bonds. The large positive value of the parameter χ may result in limited miscibility or immiscibility of the solvent-containing polymer. [52; 53]

Interaction parameter χ characterizes the difference of interaction energies of two components in the mixture divided by kT (k is the Boltzmann constant):

$$\chi = \frac{z\Delta\varepsilon}{2kT} = \frac{z \cdot (\varepsilon_{11} + \varepsilon_{22} - 2\varepsilon_{12})}{2kT}, \tag{4}$$

where z is the number of solvent molecules surrounding one polymer molecule (coordination number) and $\Delta\varepsilon$ is the difference in molecular interaction energy (J) – ε_{11} and ε_{22} represent energies of agglomeration of individual systems to form phase separation, and ε_{12} represents the mixing energy of both components. For non-polar mixtures with species interacting mainly by dispersion forces, the interaction parameter could be also expressed as a dependence of square of the difference in Hildebrant solubility parameters δ:

$$\chi = \frac{V_{\mathrm{m1}}}{RT}(\delta_1 - \delta_2)^2 + \beta, \tag{5}$$

where V_m is the molar volume ($cm^3 \cdot mol^{-1}$) and β is empiric constant, its value is usually 0.35. As mentioned above, a low value of the χ parameter is needed to dissolve the polymer. As evident from equation (5), the value of the difference of Hildebrandt parameters δ must be also low to reach good miscibility of components. Unlike the interaction parameter χ that considers the interaction between two substances, the Hildebrandt solubility parameter δ characterizes only one substance and is defined as the square root of cohesive density:

$$\delta = \sqrt{\frac{E_m{}'}{V_m}}. \tag{6}$$

$E_m{}'$ is the energy needed to remove a unit of molecules to infinite separation. [53; 54]

2.1.5.2 Particle-solvent interaction in solution

Aggregation of particles in a colloidal solution can occur when the surfaces of both particles approach due to long-distance physical processes, and the short-distance thermodynamic interaction allows the particles to join. For particles smaller than 100 nm, long-distance forces between particles are mediated by diffusion and Brown motion, which then cause the approaching of particles. If particle contact occurs, the particles can either be attracted or repelled. The summation of attractive and repulsive forces then determines the resulting interaction.

Two types of short-distance forces are dominated by colloidal particles: the van der Waals forces that are caused by electron interactions in the particles (adsorption forces), and the electrostatic double-layer forces. The electrical double layer is formed by the charge on the surface of the particles and is also influenced by the chemical structure of the solvent surrounding the particles. [24]

There is a difference in electrical potential between the charged particle surface and the volume solvent phase. The sign of the surface potential is the same as the sign of the surface charge. When the particles move through the solution, the adsorbed solvent molecules move with the particle. The potential between moving solid phase and solution is called electrokinetic potential (ζ-potential), it is the potential between the adhering solvent layer and the other liquid. The electrical bilayer is very important for the formation and stability of colloidal nanoparticle solutions. Particles with a ζ-potential greater than +30 mV or more negative than −30 mV are normally considered as stable. [55; 56]

In the case of very small particles (nanoparticles), the curvature of the surface is so distinctive that a classical planar electric double layer cannot be considered. It has been experimentally found that small particles have a less tendency to surface charge than larger particles of the same type. This leads to the formation of a weaker electric double layer and thus weaker repulsion forces between the particles. Smaller colloidal particles tend to contact aggregation more. The aggregation of smaller particles also contributes to the fact that larger particles have a larger specific surface and thus smaller particles aggregate to reduce surface energy. [24] The overall charge and concentration of active functional groups on the nanoparticle surface can significantly influence the tendency to aggregate or stay in a stable state without phase separation. [57]

2.1.5.3 Polymer-particle interactions

Polymer chain can be physisorbed to nanoparticle surface due to attractive intermolecular forces such as van der Waals forces with one or more polymer segments. Macromolecules usually adsorb irreversibly to surfaces and it is difficult to remove them after adsorption, thus desorption is often negligible. Polymer binds onto the surface with many atoms, even when one bond is released (binding energy is below thermal energy *kT*, where *k* is Boltzman constant and *T* is thermodynamic temperature) other bonds easily exceed the thermal energy. [58] Polymer chain can adsorb onto nanoparticle surface in different ways - one segment or a series of consecutive segments, multiple detached segments (forming a loop), or one polymer chain can interconnect multiple nanoparticles and form a bridge molecule (Figure 9). [33]

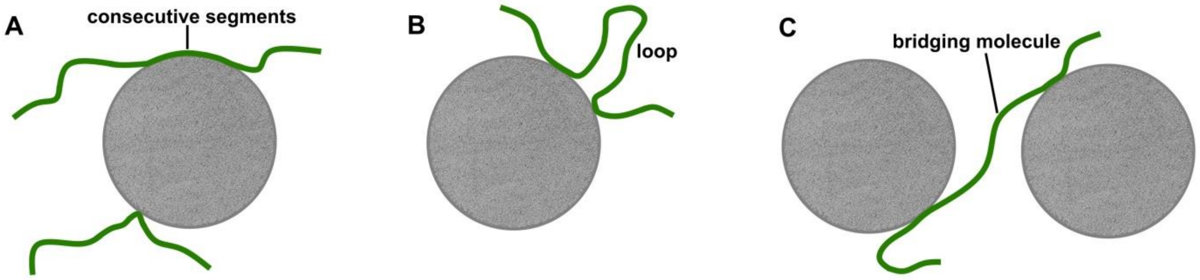

Figure 9: Adsorption of polymer chain onto the nanoparticle surface. **A** – Adsorption with one polymer segment and with a series of consecutive segments. **B** – Adsorption with multiple detached segments. **C** – Interconnecting of multiple nanoparticles.

The strength and spatial range of the interaction between the polymer segment and theparticle surface control the microstructure and nanoparticle dispersion (phase diagram in Figure 10A). The degree of particle aggregation is a function of the attraction force of the polymer segment and the particle, ε_{pc}. The three regions of the different phase behaviour in the polymer-particle system are defined in the diagram of the dependence of the volume fraction of particles Φ on ε_{pc}. If ε_{pc} is small compared to the average thermal energy of the system (*kT*), the decline in attractive forces results in nanoparticle aggregation into compact formations (contact aggregates). In the range of large ε_{pc}, polymer chains form bridges between nanoparticles resulting in phase separation or formation of a non-equilibrium polymer-particle network (clusters formation). In mean ε_{pc} values, the polymer is adsorbed onto the nanoparticles to form a thin bound layer which results in steric stabilization and miscibility of the polymer-particles system (individually dispersed particles). The area of good dispersion is broadest at low Φ values, and with increasing Φ, the area narrows as the probability of particle contact with each other increases with more particles. [59]

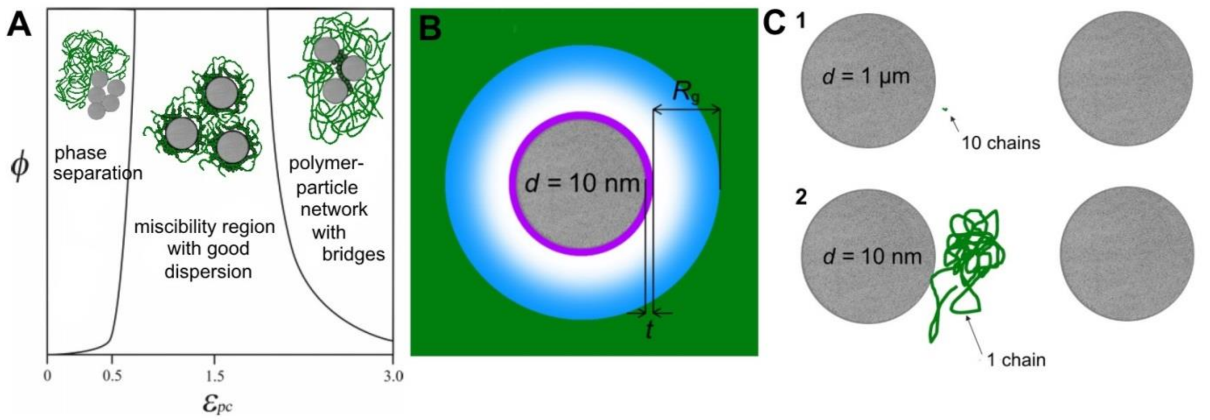

Figure 10: **A** – Attraction polymer-particle force phase diagram. *Reprinted with permission from* [35]. *Copyright 2007 Americal Chemical Society*. **B** – Nanoparticle (grey) with absorbed immobilized/accelerated layer of polymer segments (purple) with adjacent frustrated layer (blue) all incorporated in the original bulk polymer matrix (green). [42] **C** – Comparison of interparticle distance and polymer coil size in the case of microparticles (1) and nanoparticles (2). *Reprinted from* [11], *2010, with permission from Elsevier.*

Interactions at the rigid nanoparticle surface influence the relaxation behaviour of adsorbed polymers forming the interfacial layer. In the case of attractive polymer-particle force, the polymer chain exhibits retardation in direct contact with the particle, forming an immobilized layer of polymer chains. This phenomenon could be observed as increasing glass transition temperature T_g. In the case of polymer-particle repulsive forces, an accelerated layer is created in which the chains exhibit dynamic acceleration (T_g decreasing). [11; 42] Together with nanoparticles and the original bulk polymer matrix, there is also an immobilized/accelerated layer of chain segments of thickness t in the polymer nanocomposites and also an adjacent layer of chains with frustrated chain arrangement and dynamics. A schematic illustration of such a system is shown in Figure 10B. The volume and properties of the modified matrix depend on the specific surface area, amount, and dispersion state of the particles, and the strength, spatial extent, and type of interactions that are determined by the chemical composition of the polymer chains and functional groups on the surface of the particles. [42]

Nanoparticles have at least two orders of magnitude larger surface area than microparticles (at the same volume of particles), hence many more polymer chains are affected by nanoparticles. The effect of the modified matrix, which is negligible in microcomposites, plays a significant role in nanocomposites. A simplified view of the polymer chain with $R_g = 5$ nm in a micro and nanoparticle composite is depicted in Figure 10C. [11] Žídek [60] developed a model of the random spatial arrangement of solid spherical particles and found that the interparticle distance is equal to the diameter of one particle at a volume fraction of 2.6 vol. %. This means that the 1 μm diameter particle spacing is 1 μm. This distance is much larger than the size of the polymer coil so that only a negligible amount of chains interact with the particle surface. On the other hand, the interparticle distance of 10 nm particles is approximately as large as the polymer coil, so that each macromolecule is affected by the particle surface.

2.1.6 Mechanical properties of copolymers and polymer nanocomposites

2.1.6.1 Mechanical properties of high-impact polystyrene

Brittle PS can be substantially toughened by the addition of PBR particles. HIPS is usually produced by free radical polymerization of styrene containing dissolved butadiene rubber molecules or by mechanically mixing the PS with the rubber in a heated homogenizer. A condition of good adhesion between rubber particles and the glassy state matrix and crosslinking of the rubber phase is needed to obtain a toughening effect. Rubber particles can be divided into two types – the smaller (~1 µm) particles are solid rubber and the larger particles contain sub-inclusions of PS forming occluded rubber particles, this structure is also called salami type (Figure 11). Because of the inhomogeneity of occluded particles, the addition of 6 wt. % of rubber lead to the formation of 20–30 % larger particles with rubber surface and incorporated PS. As an occluded particle responds to the externally applied strain, the rubber elongates, whereas the PS occlusions remain undeformed because of a much higher value of Young modulus of the PS ($E_{\mathrm{PS}} \approx 3$ GPa, $E_{\mathrm{PBR}} \approx 2$ MPa). Locally the rubber is pulled into fibrils accompanied by energy dissipation and because of them, no large voids are formed. The response of a solid rubber particle is very different. As deformation proceeds, voids leading to craze break-down are formed at the edge of the solid particle. [61; 62; 63; 64; 65]

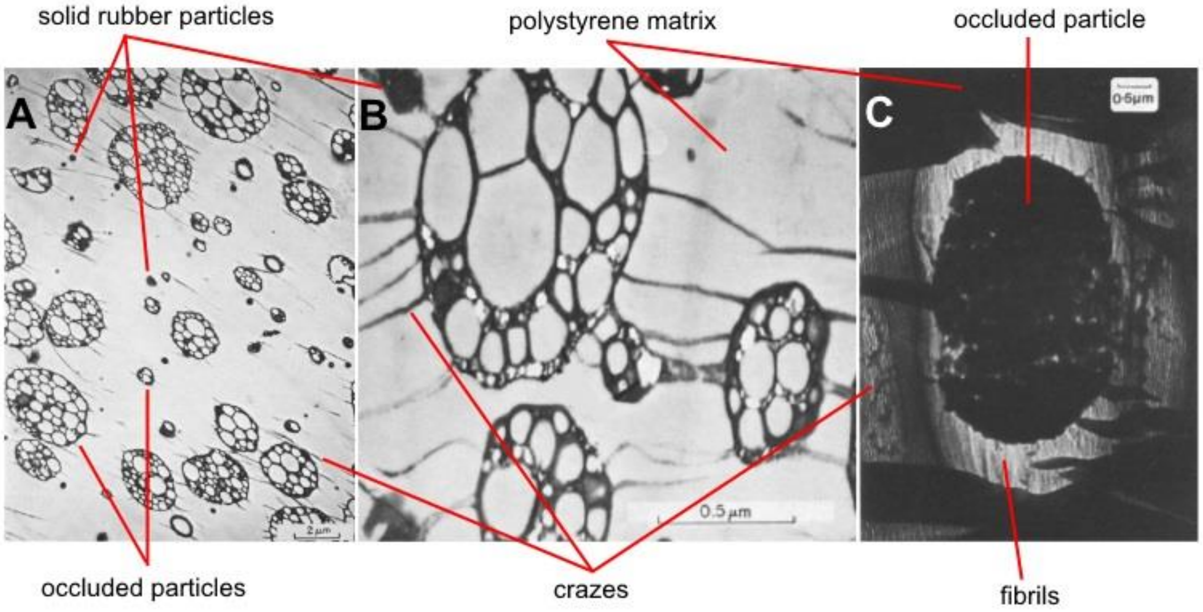

Figure 11: TEM images of HIPS structure. **A** – Crazes appearing on rubber particles after applying tension (**B** – detail). Stained with OsO_4. *Reprinted from* [63], *Copyright 1986, with permission from Elsevier.* **C** – Highly occluded particle almost totally engulfed by the surrounding craze. The outer rubber shell at the poles of the particle is highly extended and fibrillated. *Reprinted by permission from Springer Nature:* [61], *Copyright 1982.*

2.1.6.2 Mechanical properties of polymer nanocomposites

Conventional microcomposites generally require a large amount of filler (≥20 vol. %) to achieve enhanced stiffness and T_g, these improvements are usually offset by losses in ductility and toughness and weight excess. In contrast, nanoparticles facilitate significant improvement in both rigidity and toughness with a much smaller volume fraction, so that the low density of the composite and eventually its transparency is maintained. [11; 66]

Reinforcement of the polymer particle composites consists of a contribution related to the volume of the rigid filler, which is dominant for coarse particles, and a contribution due to the molecular stiffening caused by the interaction between the particle surface and matrix chains, which prevails for submicron particles. Jancar and Recman [67] investigated the size dependence of the elastic modulus of particulate-filled PMMA near its T_g (100 °C) since molecular stiffening is pronounced the most for highly mobile chains. They measured the elastic modulus of PMMA nanocomposites E_c with three different particles – fumed nanosilica (size of 20 nm), fused silica microbeads (3 µm), or glass beads (10 µm) via the solvent-casting method in acetone. The measurements were taken above T_g at 130 °C by oscillation measurement in rheometer and below T_g at 80 °C by tensile testing. The experimental E_c data were reduced using the Guth-Gold model for measurements above T_g and using the Kerner-Nielsen model for measurements below T_g to obtain modulus of the matrix in the presence of particles M_m^* which differs from that for the neat polymer. The dependence of M_m^* on the logarithm of the specific interface area S_f is plotted in Figure 12. [67]

Guth-Gold model used to determine the elastic modulus at temperatures above T_g:

$$E_{\mathrm{c,\,GG}} = 1 + 2.5\varphi + 14.1\varphi^2, \tag{7}$$

where φ is the volume fraction of the filler (silica). Kerner-Nielson model used to determine the elastic modulus at temperatures below T_g:

$$E_{\mathrm{c,\,KN}} = E_{\mathrm{m}} \frac{1 + AB\varphi}{1 - B\psi\varphi}, \tag{8}$$

in which the parameters A, B, and ψ are determined by equations:

$$A = \frac{7 - 5\nu}{8 - 10\nu}, \tag{9}$$

$$B = \frac{\frac{E_{\mathrm{f}}}{E_{\mathrm{m}}} - 1}{\frac{E_{\mathrm{f}}}{E_{\mathrm{m}}} + A}, \tag{10}$$

$$\psi = 1 + \frac{1 - v_{\mathrm{m}}}{v_{\mathrm{m}}^2}\varphi, \tag{11}$$

where ν is the Poisson ratio of the matrix, E_f is the elastic modulus of the filler, E_m is the elastic modulus of the matrix and v_m is the maximum possible volume fraction of the filler (for the monodisperse system with spherical particles $v_m = 0.637$). If the filler does not affect the extensibility of the matrix, then parameter A has a constant value, usually 1.2. If the system is filled with solid particles, then $E_f << E_m$ and B has a value of approximately equal to 1. [68]

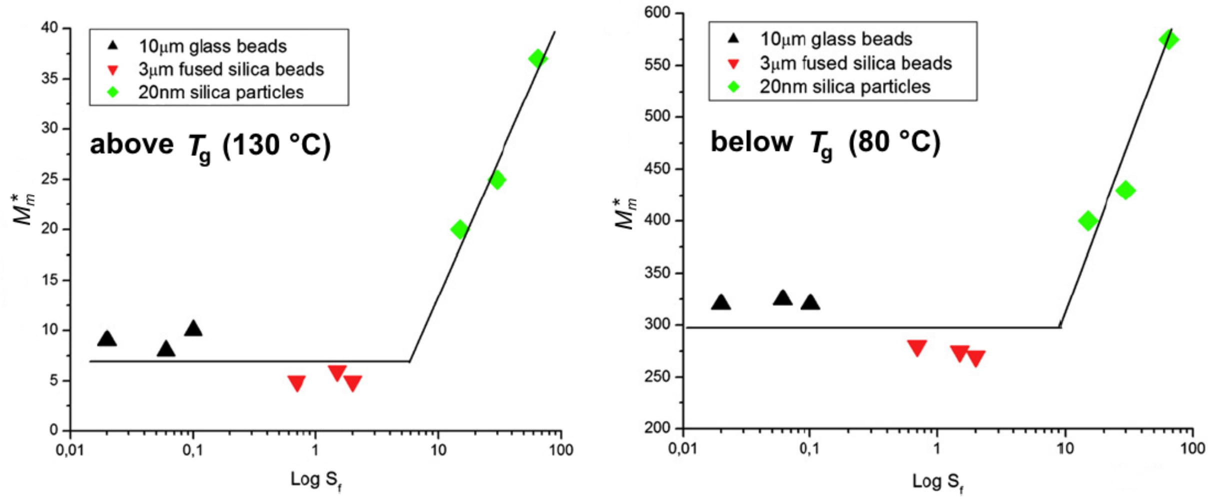

Figure 12: Dependence of the matrix modulus $M_m^* = E_c/f(\varphi)$ on the logarithm of the specific interface area S_f above T_g using the Guth-Gold model (**left**) and below T_g using Kerner-Lewis model (**right**). *Reprinted from* [67]. *Copyright 2010, with permission from Elsevier.*

It was found that for particles larger than 1 μm, the extent of molecular stiffening was negligible and, thus, matrix modulus was independent of φ or more precisely independent of S_f. For nanometer-sized particles, the extent of chain stiffening was larger resulting in a strong dependence of the matrix modulus on the filler content increasing approximately linearly with log(S_f) for both temperatures investigated. Needless to point out that the scale of matrix stiffening below T_g is only about 1/8 of that above T_g. [11; 67]

Moreover Mo and Xu [69] calculated the dependence of mechanical properties (Young modulus, shear modulus, bulk modulus, and Poisson ration) on the size of silica particles in nanometer scale (ranging from 1 to 1.5 nm) for polyimide (PI) composites by molecular dynamic simulation. For example Young modulus of composites with 5 vol. % of silica increased by 136.9 % when 10 Å large particles were used, by 135.2 % with 13 Å particles, and by 133.7 % with 15 Å particles.

Modification of mechanical properties is dependent also on interfacial interaction between polymer and silica. Yang and Nelson [70] prepared nanocomposites of PMMA, PS, and polycarbonate (PC) via single-screw extrusion. They observed that mechanical properties (tensile strength, Young modulus, and elongation at the break) were improved in all systems, especially for PMMA-based composites (Figure 13A). They explained the reinforcement by improved interfacial interactions in PMMA nanocomposites. Modulus of polymer composites and polymer blends is directly related to the strength of the interfacial interaction between matrix polymer and silica. A good interface restricts the shearing or deformation of the polymer chains around the particles, leading to a more difficult initial deformation of the material, therefore a higher modulus. [70; 71]

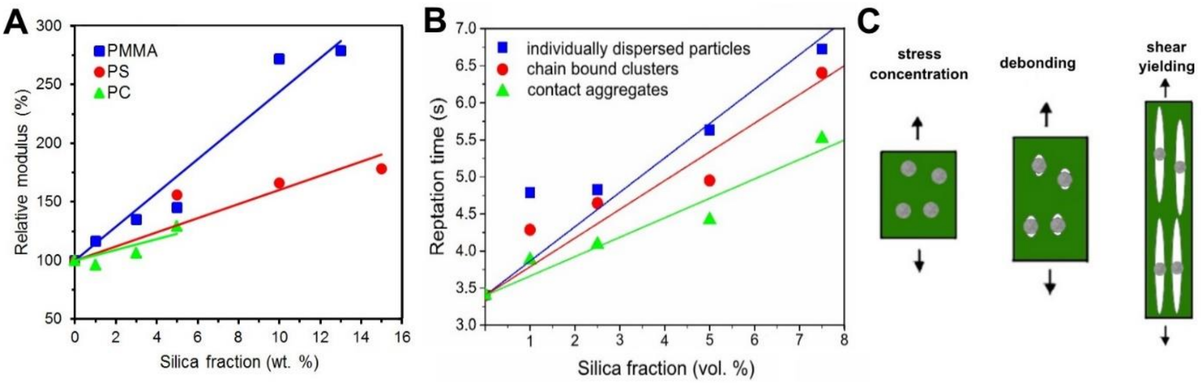

Figure 13: A – Dependence of relative elastic modulus on silica fraction of nanocomposites in three different matrices – PMMA, PS, and PC. [70] **B** – Dependence of reptation time on silica fraction of PMMA nanocomposites with a different state of nanoparticle dispersion. *Reprinted from* [42]. *Copyright 2018, Brno University of Technology.* **C** – Scheme of nanoparticle toughening mechanism. *Reprinted from* [72]. *Copyright 2003, with permission from Elsevier.*

Mechanical properties are also dependent on the state of dispersion in the nanocomposite. Ondreas [42] investigated PMMA composites filled with nanosilica prepared via solvent-casting with three different structures – individually dispersed particles (prepared in acetone), chain bound clusters (acetone, toluene mixture), and contact aggregates (toluene), TEM pictures are captured above in Figure 6. He observed thermomechanical properties (tensile and compressive behaviour, rheological measurements) of these three systems with the same chemical composition. In general, a more pronounced enhancement of properties compared to pure polymer occurred in a system with individual particles and the insignificant in the case of aggregates. Individual particles had the largest specific surface area in the composite and so the highest interactions between polymer and silica, dynamic of chains was retarded and reinforcement was maximized. Conversely, in the case of aggregates, the active surface of the particles was considerably reduced and the modification of properties of PMMA was therefore inhibited. An example is an increase in repetition time shown in Figure 13B.

Nanoparticles are considered to be similarly effective like rubber particles in toughened copolymers (e.g. HIPS). It is considered that the cavitation of nanoparticles and its successive shear yielding contribute to an improvement in the toughness of nanocomposites. Zuiderduin et al. [72] summarized the toughening process of rigid particles into three stages (Figure 13C):

1. Stress concentration – The rigid particles act as stress concentrators owing they have different elastic properties compared to the matrix polymer.
2. Debonding – Stress concentration gives rise to built triaxial stress around the particles, leading to debonding at the particle-polymer interface.
3. Shear yielding – The voids resulting from debonding alter the stress state in the polymer matrix surrounding the voids. This reduces the sensitivity towards crazing and promotes shear yielding. [66; 72]

Zhang et al. [73] prepared injection molded HIPS with TiO_2 nanoparticles and investigated the impact and tensile properties of the resulting nanocomposite to show toughening and reinforcing effect of the nanoparticles to HIPS. They find out that notched impact strength, tensile strength, and tensile modulus were maximalized with 2 wt. % of TiO_2. Up to the 2 wt. % TiO_2 content value, the properties increased. After this content value, the material properties decreased, which proves that the nanoparticles are very effective at lower filler volumes.

2.2 Polymer foams

Polymer foams, sometimes also called expanded, porous, or cellular polymers, are biphase systems that contain gas voids dispersed in denser thermoplastic or thermoset polymer matrix. It is a considerable group of polymeric materials that can be rigid or flexible depending on whether the T_g of the polymer is above or below the temperature at which it is applied. The most well-known polymer foams are PS, polyurethane (PU), or polyolefin materials. [44; 74] The properties of the expanded polymer depend on several different parameters. From the material point of view, the most important is the composition of the polymer phase, e.g. type of polymer and the content and type of additives. In structural terms, it is especially the type and distribution of pores. To accurately describe the structure of lightweight materials, it would be necessary to describe each pore (size, shape, location, etc.), which is practically impossible. Therefore, the structure is usually mostly characterized by an easily measurable volumetric mass density or average porosity and cell density. The density of the cellular material divided by the density of the same material without pores is the relative mass density. It is equivalent to the volume fraction of solid. [75; 76]

The low-density cellular materials can be classified into two groups – closed-cell or open-cell foams (Figure 14). If each pore is a discrete cell, it is a closed-cell material. In closed-cell foams, the pores are enclosed from all sides. Open-cell foams contain interconnected porosity made by an opening between cells. [18; 77]

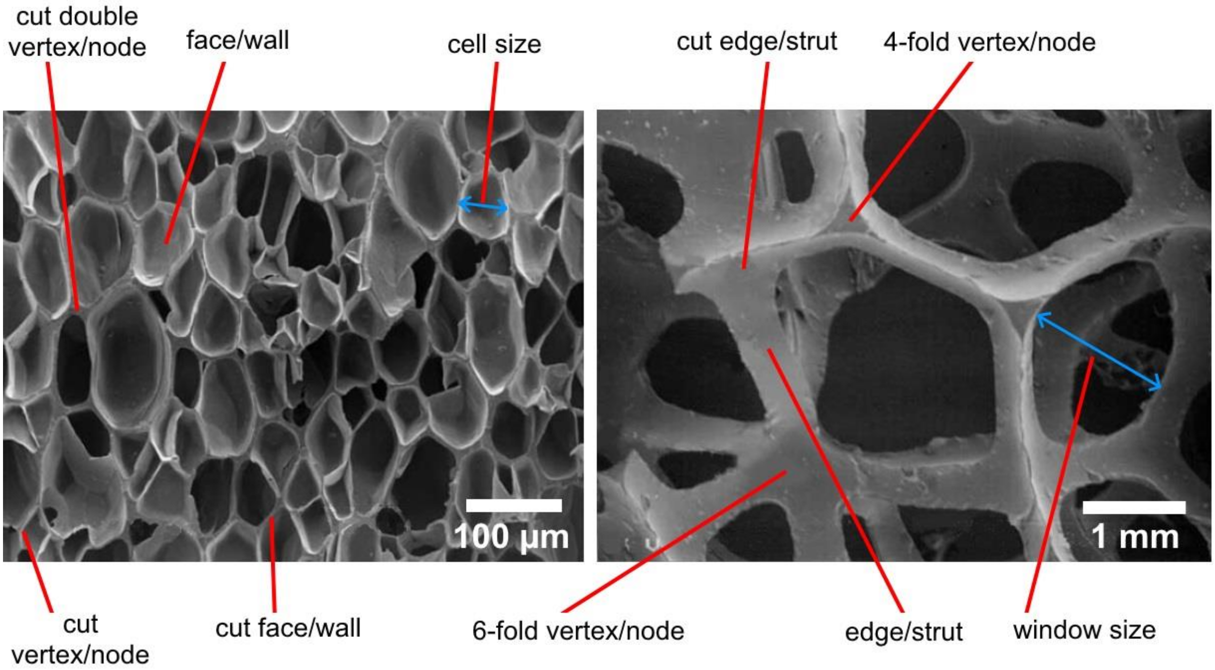

Figure 14: Morphology of closed-cell poly(ethylene-vinyl acetate) (EVA; **left**) and open-cell PU (**right**) foams. *Reprinted from* [78], *Copyright (2003), with permission from Elsevier.*

In general, that could be said that the closed-cell mechanical properties are always greater than are the open-cell properties. The closed-cell geometry is simply a more efficient use of the material. [79] Differences in pore size deteriorate mechanical properties, superior foams have homogenous distribution. [75] Closed-cell foams also exhibit lower permeability, thus they are a better thermal insulator. A heat-dissipating medium cannot flow through closed pores. [80] Open-cell foams show better absorptive capacity and they are better sound insulators because they are more difficult to spread vibration. [81]

Polymer foams can be also categorized based on their flexibility as rigid and flexible foams. These properties are dependent on the composition, cell morphology, and physical properties of the foam and usually also depend on whether the foams are used – above or below the T_g of the polymer. For example, flexible PU foams are usually open-cell, whereas rigid PU foams are made of closed-cell materials. [10; 77]

According to the size of the foam cells, polymer foams can be classified as macrocellular (>100 μm), microcellular (1–100 μm), ultramicrocellular (0.1–1 μm), and nanocellular (0.1–100 nm). Most commonly use polymer foams have a void size in the tens of micron. [10; 82]

Microcellular foams are characterized by foams with a cell size of less than 100 μm and cell density higher than 10^6 cells·cm^{-3}. They have shown many promising properties compared to conventional macrocellular foams with cell size higher than 100 μm and cell density less than 10^6 cells·cm^{-3}. Preparation of microcellular materials requires very strict conditions with a very narrow processing window (strict control of pressure conditions, extremely high pressure, temperature control, etc.), this also limits the attainable size of the foam products. [10] The idea of rating nanopores in polymeric materials is exciting and largely unexplored and the development of nanocellular foams now attracts great attention in research. Due to the unique structures, nanofoams are expected to have many properties that are superior to those of existing materials such as high strength-to-weight ratio or the ability of structural coloration. [82; 83]

Otsuka et al. [84] prepared nanocellular foams in PS-PMMA blend via CO_2 physical foaming. They put PS beads in a liquid methyl methacrylate (MMA) monomer so the MMA diffused into PS. The mixture was then cured at elevated temperatures to polymerize PMMA and to form highly dispersed PMMA domains in the continuous PS phase. The blend was blown by CO_2 batch foaming and because much more PMMA is CO_2-philic than PS, just PMMA domains were foamed selectively and porous of size 40–50 nm were formed. Similar work with nanoporosity production was done by Yokoyama et al. [85; 86] They used block copolymer poly(styrene-*block*-perfluorooctyethyl methacrylate) (PS-PFMA) and reached nanoporosite with cell size 10 nm (Figure 15) Yokoyama et al. used supercritical CO_2 as a foaming agent.

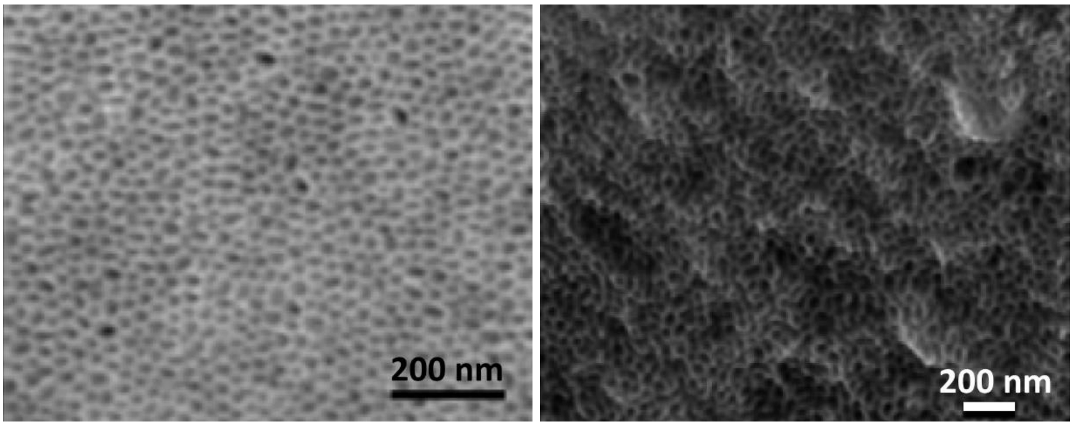

Figure 15: SEM images of nanocellular PS-PFMA. *Reprinted with permission from* [85]. *Copyright 2005 American Chemical Society*.

2.2.1 Foaming agents methods

The most widespread way to prepare porous polymer materials is the method based on the use of foaming agents which are substances capable to release gas into the polymer bulk to form pores. It could be divided into two groups – physical blowing agents that vaporize to enlarge their volume and chemical blowing agents that release gas by their thermal decomposition or by chemical reaction. Foaming agents should be affordable, easily dispersible in a polymer matrix, the decomposition of the thermal blowing agent should not be energetically intensive and should take place in the polymer processing temperature, the decomposition products should not affect the physical or chemical properties of the expanded material, the resulting gas should not be corrosive, toxic or smelly. [75]

Physical foaming is based on the release of inert gas (CO_2, N_2) or volatile liquid (pentane). It is suitable for the preparation of microcellular foams. In the case of inert gas foaming, the polymer is saturated with gas, usually at a higher pressure in an autoclave or pressure chamber. The gas is then released under normal pressure and by heating above T_g of the polymer matrix, the plastic becomes softer and allows the gas to vaporize and the whole polymer system to expand. [75; 87]

A typical polymer physically blown by low-boiling liquid is PS or polyvinyl chloride (PVC). PS is made by styrene polymerization in a suspension process in the presence of volatile aliphatic hydrocarbons (e.g. pentane 6–7 %) that are soluble in the monomer but insoluble in the polymer. PS granulates are turbid because of the content of dispersed hydrocarbon. They are pre-heated above the softening temperature of the polymer (approx. 100 °C), partially pre-expanded, cooled down and they are supplied as pre-expanded beads. They should be processed in a few days before the blowing agent migrates out from pre-puff and loses its ability to expand. The expanded products of the desired shapes are then finished by water-steam heating in the perforated molds. The bead can increase its volume up to forty times. The result is a foam with a closed-pore structure. The expanded PS can be produced in a wide volume density range (5–100 $kg \cdot m^{-3}$), but in practice, it is most often 20–35 $kg \cdot m^{-3}$. [65; 75; 77] Previously, chlorofluorocarbons by another name freons (e.g. trichlorofluoromethane), were used as low-boiling foaming agents, but their use has been severely restricted due to disruption of the ozone layer. [77; 87]

Chemical foaming by the reaction of the functional group during polymerization is typical for PU foams. The reaction of isocyanate groups with water or organic acids easily carries out and is accompanied by the releasing of CO_2 (reaction (12), forming oligomer/polymer expands and solidification of reaction mixture follows immediately. The heat released by the exothermic reaction is sufficient to solidify PU and cure the foam. [75; 87]

$$\text{R–N=C=O} + \text{H–O–H} \rightarrow \text{R–NH}_2 + \text{CO}_2 \tag{12}$$

Another method of chemical foaming is the decomposition of the blowing agent, namely thermal (citric acid, sodium bicarbonate, azodicarbonamide), radiation, or catalytic decomposition leading to the release of gaseous products. The blowing agent is dispersed in the polymer usually by kneading. In the case of thermal decomposition, the blowing agent decomposes at elevated temperature into gaseous products which form pores in the matrix. The temperature at which gas is released from the blowing agent determines its applicability to a certain polymer with its processing conditions. The structure of the expanded polymer material depends on the type of blowing agent, the viscosity of the polymer melt in the temperature range corresponding to the blowing agent decomposition, and the blowing temperature and time. [75]

2.2.2 Other foaming methods – syntactic foams, phase separation, leaching, etching, and electrospinning

Polymer foams can be prepared by a vast array of methods. In addition to foaming by the blowing agents described in the previous paragraph, this paragraph summarizes a quick overview of other widely used methods.

In the manufacture of expanded thermosetting plastics (e.g. urea-formaldehyde resin), whipping air into the resin reaction mixture and rapid curing or cooling the resin is applied. The reaction mixture of resin with hardener, emulsifier, and foam stabilizer is whipped, poured into a mold, and solidify. [75; 77]

Cellular polymers produced by blending microscopically (30 μm) small hollow balls of glass or plastics in a resin matrix binder are called syntactic foams (Figure 16). This produced a light closed-cell material which could be also classified as a particulate composite. [18; 77] Enclosing porosity inside thin stiff shells of particles provides a reinforcing effect to every void present in the microstructure of the material. Such composites can be tailored to have a higher specific modulus than the matrix resin and a high level of energy absorption under compression. [18]

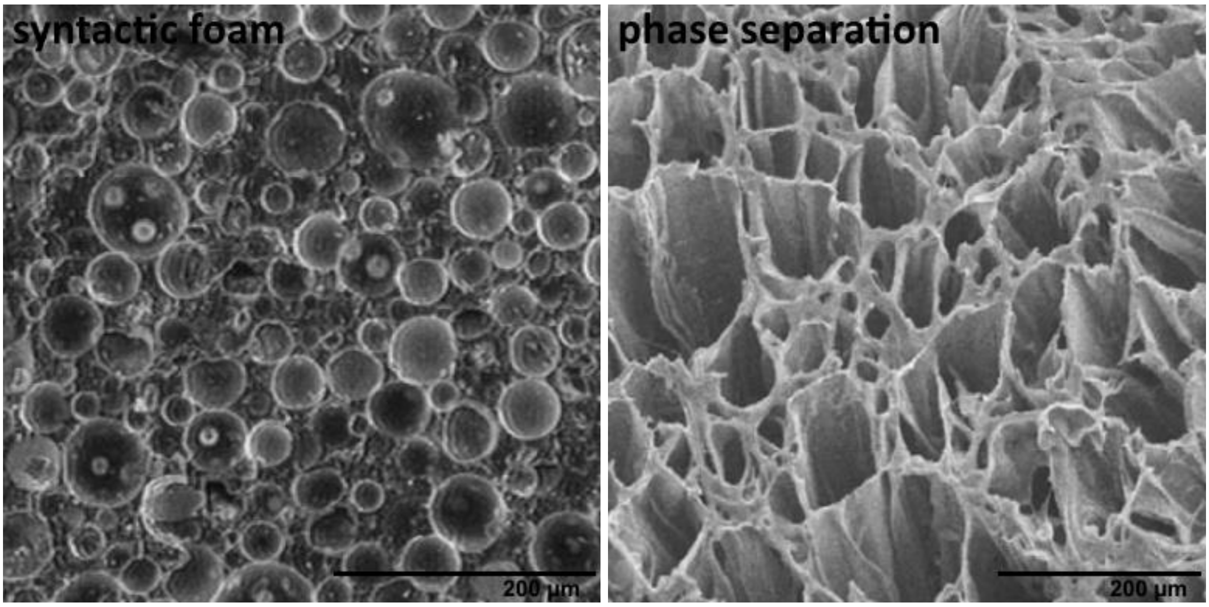

Figure 16: SEM images. **Left** – Syntactic foam structure composed of glass microballoons and epoxy resin. [88] – *Copyright 2009, Journal of Sandwich Structures and Materials.* **Right** – Phase separated biodegradable poly(ester urethane)urea scaffold. *Reprinted from* [89], *Copyright 2005, with permission from Elsevier*.

The phase separation technique [76; 82] is based on thermally or chemically induced separation of polymer and solvent from homogenous solution, followed by solvent removal and resulting in a porous polymer structure (Figure 16). This technique is widely used for scaffold preparation for tissue engineering. During thermal induction, the solution is cooled down to the lower temperature, solidified, and then at the constant temperature cryogenically dried. The structure of the porous material can be controlled, for example, by the cooling rate. In chemical induction, the solvent is gradually changed from a good solvent to a poor one, the deterioration of solubility conditions also leads to phase separation. An example of the materials used to create a porous structure by thermal induction is collagen-glycosaminoglycan, polylactide-dextran [90], or biodegradable PU [89], and by chemical induction for example epoxy resins [91].

Leaching is a method in which particles (inorganic salts or another polymer) are mixed into the polymer matrix and washed away. The particles can be incorporated into the polymer by solvent-casting from the solution (followed by drying the original solvent) or in the melt. Subsequently, a suitable solvent is used to dissolves the porogen particles, leach them away leaving pores in the polymer matrix. The foam structure, porosity, and pore size can be easily induced by changing the degree of filling and the size and shape of the particles. [76; 82] Mosadeh-Sedghi et al. [92] prepared low-density PE hollow fiber membranes by melt-extrusion with NaCl particles which were leached out in the water. Reignier and Huneault [93] combine polymer and salt particulate leaching. They prepared a blend of polycaprolactone (PCL) and POE with NaCl particles. After dissolving POE and NaCl in water, a fully interconnected porous structure with bimodal pore size distribution was created in the PCL scaffold (Figure 17).

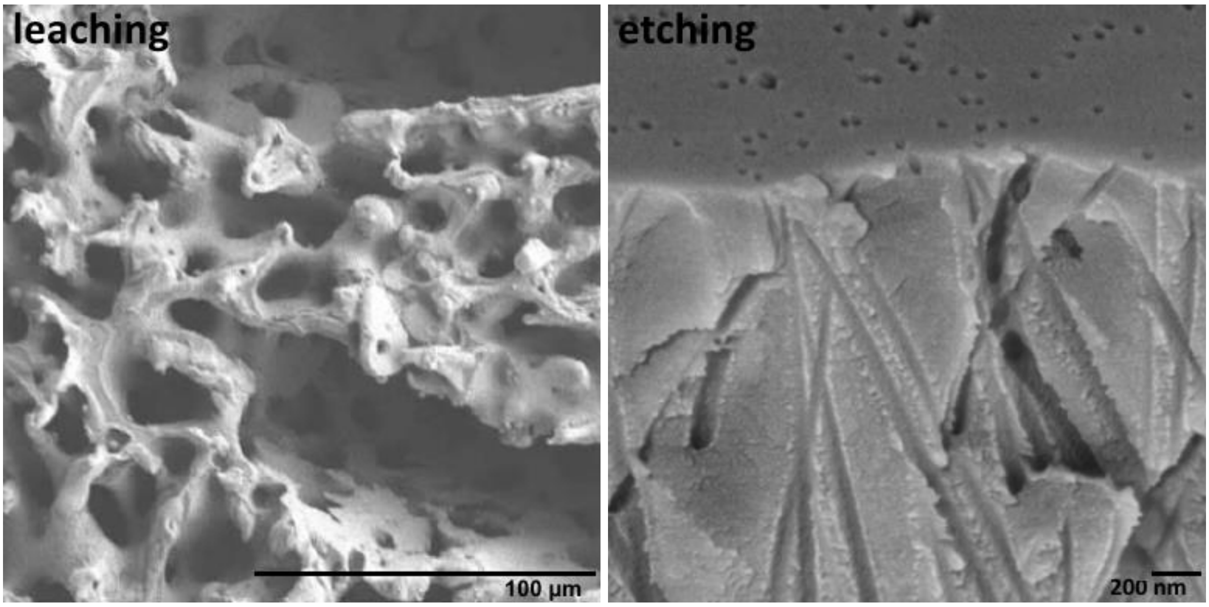

Figure 17: SEM images. **Left** – Bimodal porous structure of polycaprolactone (PCL) with smaller pores created by leaching NaCl and with two visible larger pores created by leaching POE. *Reprinted from* [93], *Copyright 2006, with permission from Elsevier.* **Right** – Structure of a PC membrane with a skin layer obtained using surfactant-controlled etching, the picture shows nanopores passing through the entire film material. *Reprinted from* [94], *Copyright 2008, with permission from Elsevier.*

The etching technique uses high-energy radiation to induce scission polymer chains of matrix or to break down inorganic particles in the polymer matrix. This first radiation step is followed by a second step – etching in an alkaline or acidic solution to wash out the loose parts of the system and thereby form a porous structure. The structure of the cellular material depends on the shape and size of the inorganic particles, the time of radiation, and the time of etching. [82] For example, Yamauchi and Apel [94; 95] etched PC or poly(ethylene terephthalate) (PET) films irradiated with heavy-ion for membrane applications (Figure 17) and investigated the effect of surfactants on the development of pores.

Electrospinning is a technique for the production of extremely long fibers from a polymeric solution or from melt liquid extruded through a thin nozzle by applying a high-voltage electric field to spin the fibers. The result is a macroporous interconnected network of micron-scale or nano-scale diameter fibers. Fiber diameter and pore size can be controlled through processing variables such as the polymer concentration, choice of solvent, applied voltage, and nozzle diameter. [76; 96] Liu [97] and McCann [98] developed modified electrospinning techniques for preparation fibers with inner porosity (Figure 18).

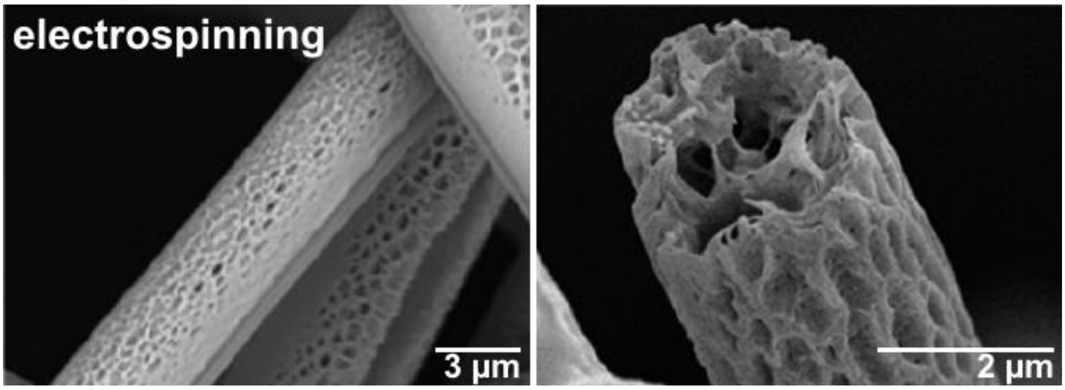

Figure 18: Highly porous electrospun PS fibers, SEM images. *Reprinted with permission from* [97]. *Copyright 2019, American Chemical Society.*

2.2.3 Foaming mechanism

Four stages during the foaming process and pore formation can be distinguished [77; 99; 100]:

1) Prenucleation.
2) Pore nucleation.
3) Pore growth.
4) Pore shrinkage.

The individual stages will be specified on the example when a chemical blowing agent is used for foam formation [99], i.e. a gas-releasing agent (chemical blowing agent used in practical experiments of this dissertation thesis).

During the prenucleation stage, particles of the blowing agent are being activated at elevated temperatures. In locations with a higher occurrence of blowing agent particles, small pores being to form, but they immediately shrink. The polymer matrix contains very little dissolved gas in this stage. The gas, which has been concentrated in the emerging pore, is dissolved in a polymer matrix due to the concentration gradient, pore disappears. The life span of these pores is very short (hundredths to tenths of a second). [99]

During bubble nucleation, the gas concentration in the matrix increases over time and reaches a saturation state. Once equilibrium is reached, the newly formed pore in the gas-rich region is not dissolved in the matrix, the pore can reach the critical diameter and becomes stable. [99; 101] Besides, particles of solid not yet decomposed blowing agent serve as nucleating agent [102] causing heterogeneous nucleation which originates from pre-existing microvoids on the solid particles. [103]

During pore growth, the gas released from blowing agent particles promotes the growth of the pores. The matrix is stretched out and the volume of pores increases. If the pores continue to grow, the pore coalescence may occur leading to the formation of larger closed pores or even to the formation of open porosity, i.e. the polymer walls between the individual cells begin to disappear and only edges and struts remain. [99] The growing pore process is also high viscosity [100; 104; 105], resp. temperature [99; 106] dependent because of diffusivity, bubble stabilization, and pore deformation, and blowing agent decomposition rate. The higher the viscosity of the melt, the more difficult is the polymer to foam, but on the other hand, the coalescence of the pores is easier at a low viscosity.

After decomposition of the remaining blowing agent, the concentration of the gas dissolved in the matrix begins to decrease, the gas migrates out of the system. The concentration profile around the pores is changed and the gas in the pores begins to dissolve into the matrix. At this point, the maximum diameter of pores is reached, the pores start to shrink. [99]

The formed porous structure can be stabilized either by cooling the polymer below its melting point or glass transition (in the case of thermoplastics) or by crosslinking (thermosets), resp. vulcanization (rubber compounds) and thus prevent a collapse of the resulting porosity. These processes must be harmonized so that stabilization does not occur too early, when the material is not yet lightened to the desired extend, or late, when the formed pores already have an undesired structure or even decrease in the volume of the resulting expanded product, for example, due to collapse of the melt. [75] Too short foaming time or low temperature do not ensure sufficient decomposition of the blowing agent or mobility of polymer matrix (e.g. below glass temperature in the case of thermoplastics), a small amount of pores is formed and the material does not expand effectively. Too long foaming time or a high temperature could cause small homogeneous pores to coalesce into large inhomogeneous pores, collapsing the polymer melt and thereby collapsing of the cellular structure, and degradation of the polymer itself. Therefore, it is necessary to find the optimum foaming temperature and time.

2.2.4 Foam processing technology

Various processes have been developed for expanding polymer materials preparation – non-continuous processes like batch foaming, injection molding, and continuous processes for melt-processible polymers like extrusion.

In batch foaming, a polymer is saturated with a gas foaming agent (e.g. CO_2) under a certain temperature and pressure, usually much higher than atmospheric pressure. CO_2 is dissolved in a polymer matrix, which increases the free volume between molecular chains and chain mobility. If the temperature is above T_g of polymer, the saturation must be fixed by cooling, otherwise, gas release, its nucleation, and bubble growth would occur. If the saturation temperature is below T_g, the cell is not able to nucleate and grow after the release of pressure because of the rigidity of the matrix. the second step of batch foaming is physical foaming at a higher temperature, usually in a liquid bath. Cell structure is again fixed by cooling. CO_2 at moderate critical temperature and pressure acquires supercritical properties. The combination of gas-like viscosity and liquid-like density makes supercritical CO_2 usable as a solvent and plasticizer in polymer foaming and advantageous morphology properties of the foam are obtained. [10; 82; 107] When CO_2 is used in its supercritical form, enhanced properties could be reached. [108; 109; 110]

Foam injection molding has the advantages to produce parts with complex geometry. The injection molding process usually leads to the formation of integral foams (self-skin foams with a solid shell and cellular core). [111; 112] The blowing agent is fed into a hooper (low-pressure processing) or directly into the molten plastic just before it enters the mold (high-pressure processing). The blowing agent expands after plastic injection into the mold cavity and pressure drops. The latest injection molding technology for porous polymers is MuCell. It is based on compressed inactive gases (N_2, CO_2) in the form of supercritical fluids with high solubility in the melted thermoplastic in the plasticizing part of the injection molding machine. The pores reach a size of 5–50 μm and compensate for shrinkage by their pressure. [77; 113; 114; 115]

Reaction injection molding (RIM) is widely used in the case of resins, for example, PU. Liquid monomer materials are injected into the mold cavity in a smaller amount that does not completely fill the mold. The mold is closed before the reaction occurs. The start of the chemical reaction causes the foaming of material and its expansion. Expanding material fulfills the mold and after curing, the product retains the shape of the mold. If the expanded plastic and the mold become together with the final product, the process is called expanding in place. [77; 116]

The thermal excitation of molecules of a blowing agent using high-frequency radio energy used to expand polymer beads is called dielectric molding. In the case of a technique called spraying, a special spraying device could be used to place expendable plastics in mold surfaces or walls and roofs for insulation, for example making a house shell. [77]

The most important foam process technology, in the terms of this dissertation thesis, is extrusion, because it is widely used for sample fabrication in the experimental part. Foam extrusion is a continuous process, where thermoplastic materials are processed together with a blowing agent in the melt state. [117]

Optimization of extrusion properties is crucial to achieving high-quality foam. For example, decreasing die temperature leads to an increase in melt viscosity, which prevents bubble coalescence and thus leads to higher cell density. Increasing the screw speed can establish high backpressure in the extruder, which is beneficial for the uniformity of pore structure [118] but can decrease void fraction due to better mixing and higher residual time [119]. An increase in foam cell density could be boosted by the choice of an appropriate nucleation agent [12] or by increasing the chemical blowing agent content [119].

Sahagún et al. [120] investigated the morphology of foamed HDPE (high-density polyethylene) and PP blends, they used azodicarbonamide as a blowing agent in low concentration (0.5 wt. %), which ensured the formation of a closed-cell porosity. They observed foam morphology in the longitudinal and transverse directions to the extrusion direction (Figure 19). The pores were elongated in the extrusion direction.

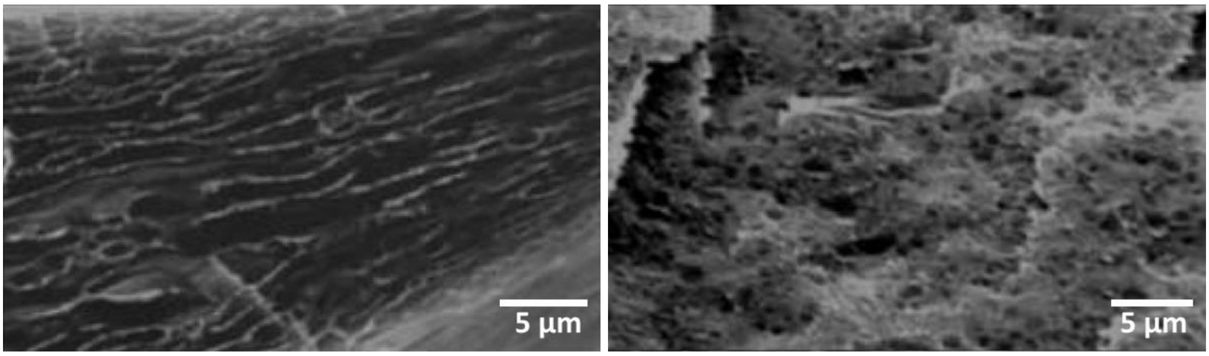

Figure 19: Morphology of extruded foam in longitudinal (**left**) and transverse (**right**) direction. *Reuse from* [120].

2.2.5 3D printed foams

3D printing is a modern progressive method for the preparation of porous structures. Its advantage is the possibility of preparing specific architecture and shapes that are accurately designed using software allowing to fine-tune porosity and mechanical parameters. In terms of processing of polymers by 3D printing, four techniques can be distinguished – selective laser sintering (SLS), inject-based printing, local polymerization of the photosensitive resin – stereolithography (SLA), and extrusion of molten thermoplastic filament layer-by-layer called fused deposition modeling (FDM). By conventional 3D printing techniques could be obtained macro-scale porosity. [76; 121] In nowadays, many advanced 3D printing techniques are used, for example, bioprinting of hydrogels for tissue engineering. [122; 123]

2.2.5.1 Selective laser sintering (SLS)

Lahtinen et al. [124] used SLS to prepare highly porous graphene electrodes, they homogenized powder graphene and powder polyamide (PA), PS, and PU. The powder mixture was then selectively melted by a laser and then cooled to bind into a solid durable cellular material with sufficient conductivity compared to the bulk graphite.

2.2.5.2 Inject-based printing

Wagner et. al. [125] introduced ink for direct injection 3D printing of porous structures consisting of acrylic components and blowing agent sulfonyl hydrazide, which was modified to be miscible with acrylate monomers and to form a stable solution. Their goal was to directly produce foam during the printing process in contrast to the other methods for 3D printing requiring post-processing foaming. They used a heat gun (near-infrared) to thermally decompose the foaming agent. They established a complex approach for foaming because the ink must be dimensionally stable in the printing plane and the resulting pores need to be stabilized immediately after the foaming process (photocuring with UV light) to create a stable foam.

Lee et al. [126] investigated cellulose nanofiber foam-based ink for direct ink writing 3D printing. More description is provided in chapter 2.3.

2.2.5.3 Stereolithography (SLA)

Mu et al. [127] combined 3D printing with salt leaching. Salt particles and photocurable resin were mixed and used as the ink. The liquid photosensitive monomer with salt was then selectively shined to polymerized it developing a scaffold with computer-designed macropores and micropores generated by salt leaching (Figure 20A).

Wirth et al. [128] developed a foaming prepolymer resin for lithographic additive manufacturing. Their material was based on 2-hydroxyethyl methacrylate photocurable monomer and di-*tert*-butyl dicarbonate as a blowing agent. They showed preparation, printability, controllable expansion, and controllable structure of highly expandable foam, which allows the production of large objects using small amounts of precursor resin, allowing the fabrication of structures that are significantly greater than the building place of the printer (Figure 20B). The foam expanded up to 40x in comparison with solid unfoamed material.

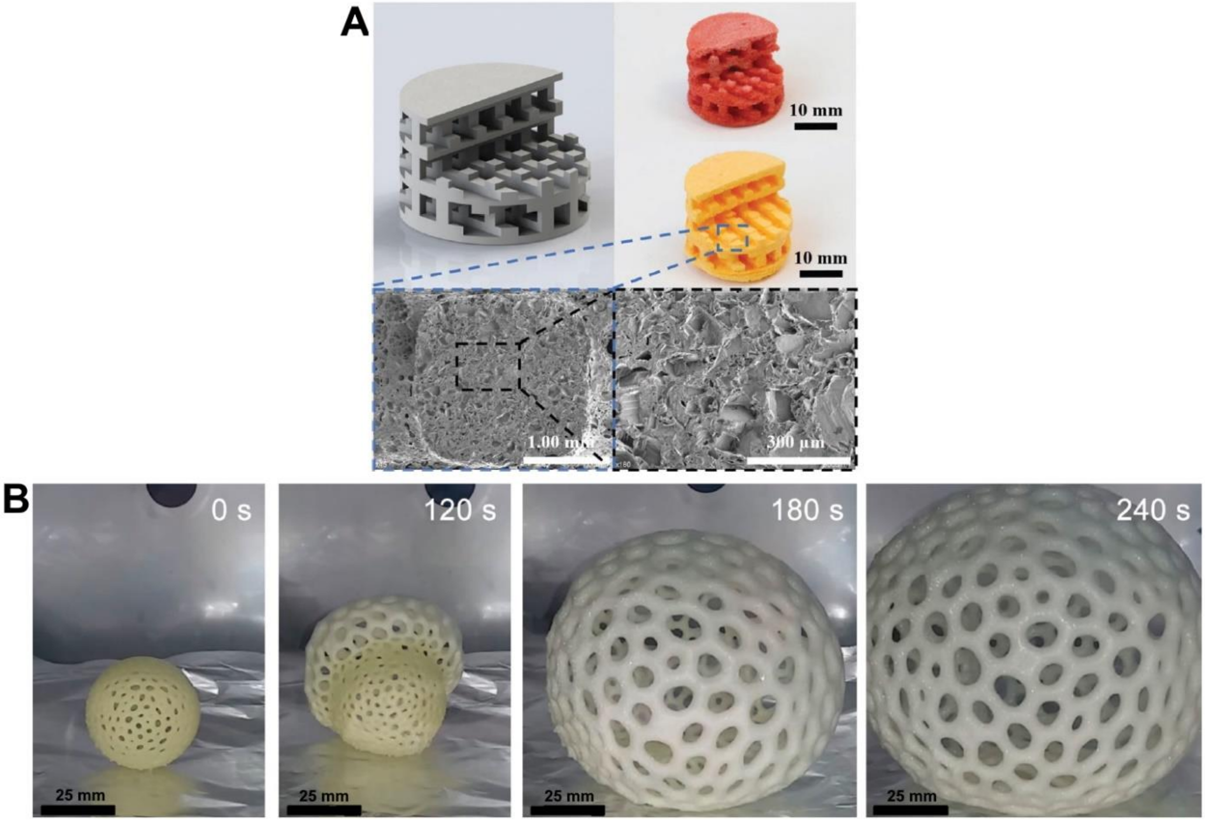

Figure 20: SLA 3D printed porous structures. **A** – 3D printed scaffold with computer-designed macropores and micropores generated by salt leaching, SEM images. *Reprinted from* [127], *Copyright 2017, with permission from Royal Society of Chemistry*. **B** – High expansion of 3D printable foaming polymer – photographic time frame images. *Reprinted with permission from* [128]. *Copyright 2020 American Chemical Society.*

2.2.5.4 Fused deposition modeling (FDM)

Gama et al. [129] used PU matrix filled with cork particles to produced 3D printed cellular structure. The addition of cork led to the presence of voids in the struts of the resulting PU foams. Due to the presence of cork as well as to the presence of voids, the resulting foam showed lower density, lower thermal conductivity, and proved more flexible. Yuen Ng et al. [130] chose the opposite process – they extruded the filament without voids from recycled PS foam and used it for 3D printing of solid products.

Another method how to 3D print porous structure, is to use hollow microballoon filaments (syntactic foams). Doddamani et al. extruded filament for 3D printing from HDPE and hollow glass microballoons [131] or environmental pollutant fly ash cenospheres (also hollow microballoons) [132] to produced lightweight composite foams eventually eco-friendly (Figure 21). In both cases, they used 20–60 vol. % filling and observed the similar impact of spheres to material properties. With increasing microballoon content, the coefficient of thermal expansion decreased, thereby lowered the thermal stresses in prints. The crystallinity of HDPE lowered with increasing spheres content. They also observed higher tensile (up to 48 % higher) and flexural modulus compared to neat HDPE. They compared 3D printed samples to injection and compression-molded samples with the same composition and found out that 3D printed samples showed about 80 % higher modulus.

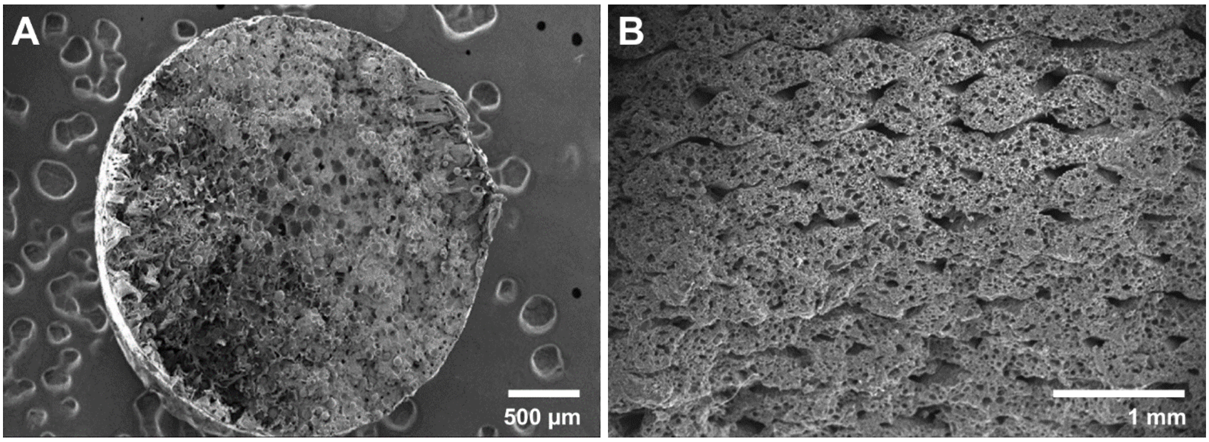

Figure 21: HDPE syntactic foams for 3D printing. **A** – filament for 3D printing with 20 vol. % of fly ash cenospheres. *Reprinted from* [132], *Copyright 2019, ACS Publications.* **B** – 3D printed body with 60 vol. % of glass hollow fibers with observable raster gabs. *Reprinted from* [131], *Copyright 2020, with permission from Elsevier.*

However, syntactic foams have a limited structure strictly given by choice and content of used spheres. Moreover, the spheres tend to break during processing. Preferred systems for 3D printing enabling variability of the structure by a simple variation of conditions are systems using blowing agents (physical – e.g. CO_2, or chemical – e.g. azodicarbonamide).

Yoo et al. [133] proposed a new CO_2 gas-based 3D printing technique. They used expanded PP beads with CO_2 to manufacture extruded hybrid filament for 3D printing (Figure 22A). It is necessary to mention that foaming of CO_2 cannot be inhibited during the whole processing and it could be released and bubbles could be generated during the process of extrusion. The filament for subsequent 3D printing was foamed before the final fabrication of the sample which could cause processing problems during 3D printing. In their other work [134] they developed a hybrid 3D printing filament with a chemical blowing agent (azodicarbonamide) mixed in PP in concentration 5 wt. % of azodicarbonamide. This filament was 3D printed with the traditional FDM method. They used the heater temperature of the printing nozzle to thermally decompose the foaming agent directly during the printing process to form a porous structure (Figure 22B). They investigated the dependence of porosity on nozzle temperature and found that increasing temperature means increasing the porosity likely to be due to a more efficient decomposition of the foaming agent whereas the temperature had to be higher than 200–205 °C otherwise decomposition of foaming agent and formation of pores did not occur. The size of formed pores ranged from 10 to 300 µm. It is worth mentioning that foaming directly during printing causes compression of forming pores by printer nozzle and the pores are therefore smaller due to mechanical compression before solidification.

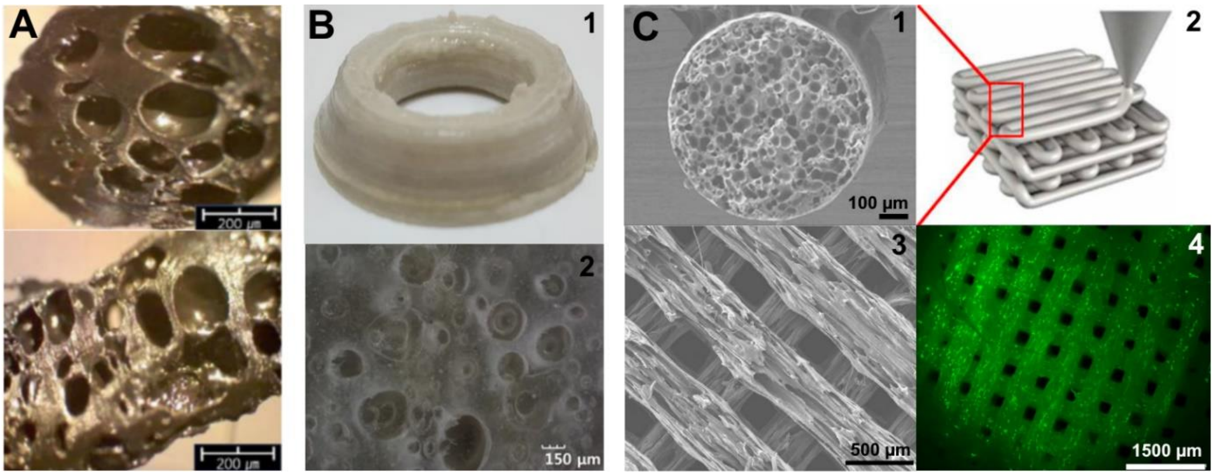

Figure 22: **A** – Porous CO$_2$ hybrid filament for 3D printing observed by optical microscopy. *Reuse from* [133], *Copyright 2017, Elsevier*. **B** – 3D printed samples from hybrid filament with chemical blowing agent – photo of 3D printed sample (**1**) and an internal cross-section of the foamed structure formed by 3D printing, optical microscopy (**2**). *Reuse from* [134], *Copyright 2017, Institute of Physics*. **C** – Dual porous 3D printed poly-lactic acid) (PLA) foams – detail of 3D printed monofilament (**1**), schematic of 3D printed structure (**2**), detail of dual porous printed porous scaffold (**3**), and green fluorescence staining image of living cells (**4**). *Reprinted from* [135], *Copyright 2020 with permission from Elsevier.*

Choi et al. [135] developed dual porous poly(lactic acid) (PLA) foam using FDM 3D printing for medical scaffold preparation (Figure 22C). They extruded filament for 3D printing from the compound of PLA, chemical blowing agent azodicarbonamide, and chain extender. The epoxy chain extender improved the rheological properties, morphology, and foamability of PLA. 3D printed scaffold was then fabricated with design freedom, one-step processing, it exhibited by dual porous structure – sub-macro pores caused by blowing agent (10–60 μm) and macro-sized pores caused by 3D printing (200–300 μm). The biocompatibility of this scaffold was confirmed through cytotoxicity.

2.2.6 Mechanical properties of foams

The deformation of three-dimensional polymer foams is a complex process. The mechanism by which foams deform and fail can be represented by compression stress-strain curve (Figure 23A), which is characterized by three regimes [76]:

1. Linear elastic regime – corresponding to cell edge bending or face stretching.
2. Stress plateau – corresponding to progressive cell collapse by elastic buckling, plastic yielding, or brittle crushing.
3. Densificitaion – corresponding to the collapse of the cells throughout the material and subsequent loading of the cell edges and faces against one another.

The tensile stress-strain curve can be described by three similar regimes:

1. Linear elasticity (bending).
2. Plastic yielding.
3. Cell wall alignment.

In the case of elastic-plastic foams, plastic yielding peak point and following the strain-softening regime could be observed. In the case of elastomeric foams, only strain hardening could be observed. [76]

Kader et al. [136] investigated mechanical properties and collapse mechanisms of different closed-cell structures through a combination of experimental validation and finite element simulations. They 3D printed structures from acrylonitrile butadiene styrene (ABS) and examined the dependence of their elastic and plastic responses (Figure 23B) and compared the results to the local stress simulation (Figure 23C).

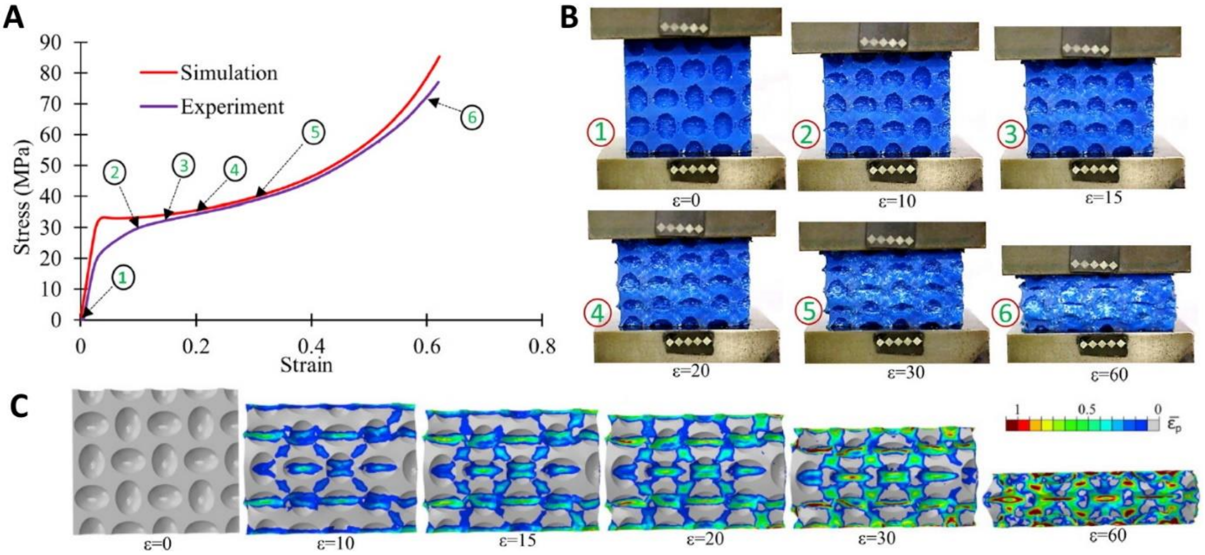

Figure 23: Compressive deformation of 3D printed ABS with elliptical pores. **A** – Compressive stress-strain curve (comparison of simulation and experimental measurement). **B** – Real 3D printed specimen during compression. **C** – Plastic strain contours from the numerical simulations. *Reprinted from* **[136]**, *with permission from Elsevier.*

The mechanical properties of cellular polymers are structure-dependent. An increase in foam density leads to a higher compression modulus of foams. When the material becoming more lightened, the fraction of solid matrix in the material is reduced, i.e. cell walls and cell struts are reduced and the quality of mechanical properties such as elastic modulus drop. This behaviour was explained by Gibson and Ashby. [137] According to the model, the stiffness of closed-cell foams results from three contributions:

- Cell struts and cell wall edge bending stiffness, which determined the elastic modulus.
- Cell wall elastic buckling, which causes elastic collapse.
- Internal gas pressure of the closed cells, which only plays a minor role in the atmospheric pressure. Under normal laboratory conditions (temperature, pressure, it can therefore be neglected.

The sum of the first two contributions can be expressed by the equation:

$$\frac{E_{\mathrm{fo}}}{E_{\mathrm{s}}} = \phi_{\mathrm{p}}^{2} \cdot \left(\frac{\rho_{\mathrm{f}}}{\rho_{\mathrm{s}}}\right)^{2} + \left(1 - \phi_{\mathrm{p}}\right) \cdot \frac{\rho_{\mathrm{f}}}{\rho_{\mathrm{s}}}, \tag{13}$$

where E_{fo} is the elastic modulus of the foam, E_{s} is the elastic modulus of the solid material, ρ_{f} is the foam density, ρ_{s} is the solid polymer density, ϕ_{p} is the fraction of the polymer contained in the cell struts, and $1 - \phi_{\mathrm{p}}$ is the solid fraction in the cell walls. The equation above could be simplified showing a power-law relationship describing the functional dependence of the modulus on the foam density:

$$E = \alpha \cdot \rho_{\mathrm{f}}^{x}, \tag{14}$$

where x is the density exponent of the foam and α is the preexponential factor. For bulk materials, the density exponent is 1, suggesting a linear relationship between the modulus and solid material density. Theoretically, the value of x should be between 1 and 2 for closed-cell foams. [12; 138]

The basic tool for assessing material properties is diagrams. They give an overview of properties in a compact way, reveal correlations between the properties when no direct measurements are available, and provide a tool for optimized selection of materials to meet given design requirements. New materials and hybrids could be displayed and compared with those of conventional materials, bringing out their novel characteristics and suggesting possible applications.

Bubble charts, which show the relationship between two selected engineering properties, are widely used. Figure 24 illustrates an example of a bubble chart with the correlation of the elastic modulus and density chart for engineering materials. Young's elastic modulus is one of the most self-evident of material properties, reflecting resistance of the material to being deformed non-permanently. Density represents weight requirements that are crucial for many applications (aviation, space). In the overall scale of the chart, the largest value of the chosen property is more than ten million times greater than the smallest – so axes are plot on logarithmic scales, not linear ones.

Data for a given family of materials are seen to cluster together on the chart, and each family is enclosed within an envelope in the diagram. Polymers lie in the dark blue envelope in the center, elastomers in the lighter blue envelope below, with moduli as low as 0.0001 GPa. Materials with a lower density than polymers are porous (light green): man-made foams and natural cellular structures like wood and cork.

Desired material properties lie in the white upper left region called the „search region“. Potential materials in this area would exhibit excellent mechanical properties (such as high stiffness, strength, and fracture toughness) while having a low density. [139; 140]

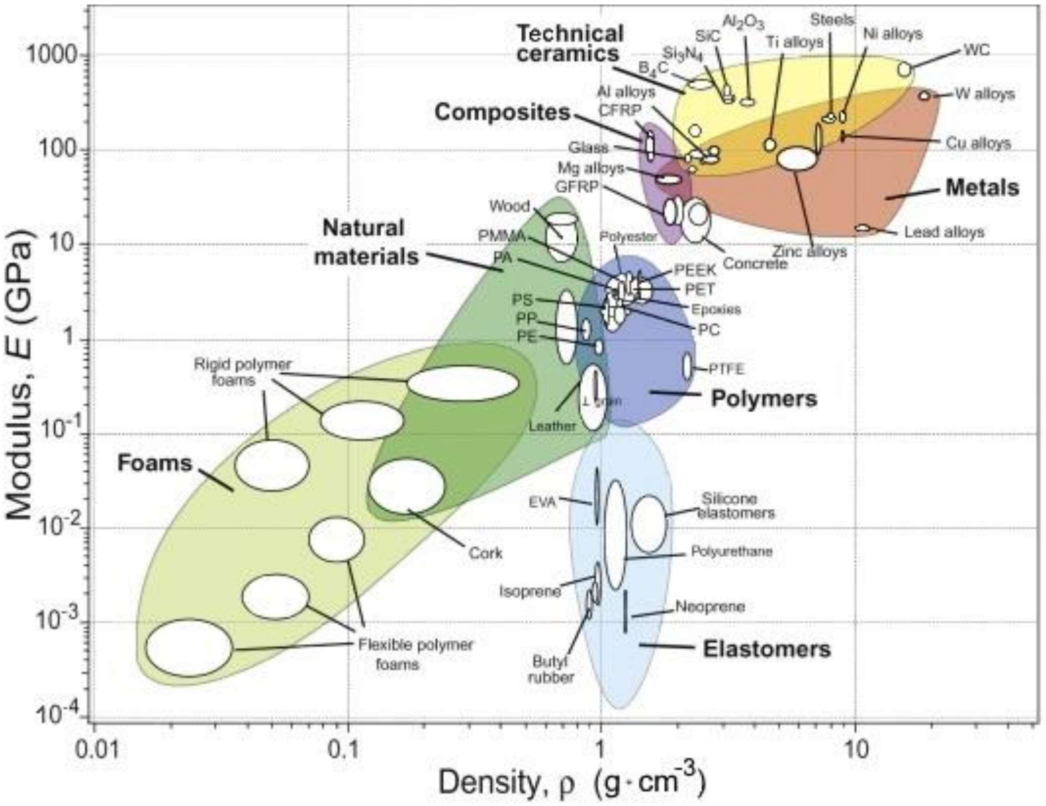

Figure 24: Ashby bubble chart relating elastic modulus and density of engineering materials. *Reuse from* [139].

2.3 Nanocomposite polymer foams

Reinforced cellular materials may be produced with particulate and fibrous reinforcement dispersed through the polymer matrix. Fibers tend to orient themselves parallel to cell walls, resulting in improved rigidity. [77] A small amount of well-dispersed nanoparticles in the polymer matrix may serve as the heterogeneous nucleation sites to facilitate the bubble nucleation process causes the growth of a higher amount of smaller bubbles leading to narrower pore size distribution and more homogenous material. Nanofiller serves as a rheology-modifying additive that supports strain hardening of the polymer matrix in the melt state. When this hardened melt is foamed, the coalescence of voids is reduced leading to foams with smaller cell size and greater cell density (Figure 25). Moreover, the nano-scaled particles are suitable for micro-scaled reinforcement of cell walls in foam structure, thus achieving macroscopic mechanical enhancement. Nanoparticles in polymer foams also cause enhancement of physical properties, heat distortion temperature, and fire resistance. [10; 14; 141; 142]

The size, shape, and chemical surface of nanoparticles influence foam morphology and thus properties of cellular material and add functionality. Surface chemistry can lower the energy barrier for bubble nucleation. A flat surface of the filler provides a better nucleating surface than curved surfaces. [142]

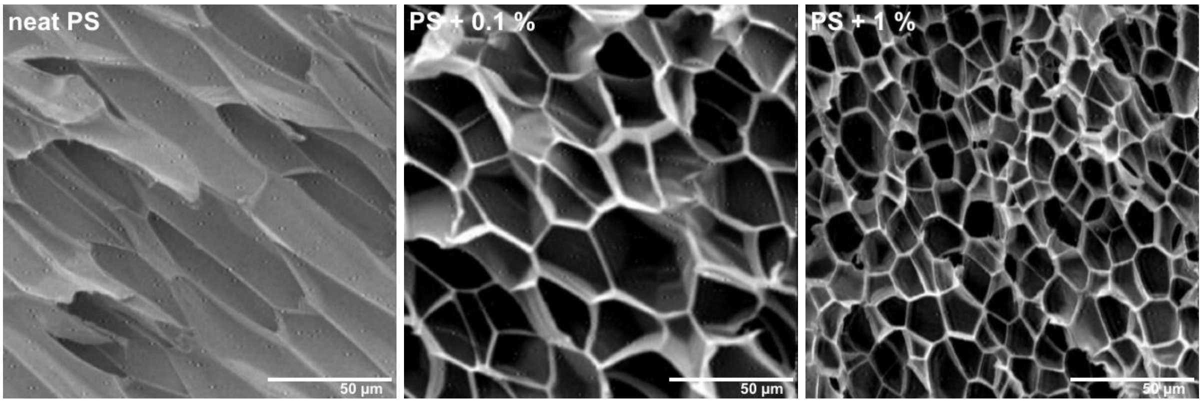

Figure 25: PS samples foamed with CO_2. **Left** – neat PS without nanoparticles. **Middle** – PS loaded with 0.1 wt. % of nanosilica. **Right** – PS with 2 wt. % of the nanosilica. *Reprinted with permission from Springer Nature*: [143], *Copyright 2014.*

Saha et al. [144] investigated the role of different nanoparticle types on foam structure and properties. They prepared PU foams with three different types of nanoparticles – spherical TiO_2, platelet nanoclay, and rod-shaped carbon nanofibers. They dispersed nanoparticles in two-part PU foam liquid and cured the foam in an aluminum mold. Carbon nanofibers showed maximum enhancement of the properties – an increase of tensile, compressive, and flexural strength, and modulus whereas foam with TiO_2 showed the minimum increase. They believed, that the large aspect ratio nanoparticles (carbon fibers) stretched the cell growth in the direction of the nanoparticle due to interaction between the polymer and nanoparticles during cell nucleation, growth, and stabilization stages.

Zakiyan et. al. [143] investigate the role of particle size, particle loading, and particle surface treatment on foam structure and properties. They used PS and nanosilica composite prepared in toluene expanded by batch foaming with supercritical CO_2. They used three nanosilica particles with the size of 12, 20, and 40 nm and three different loading content – 0.1, 1, and 2 wt. %. They observed that decreasing particle size or increasing particle content provides more nucleation centers, moreover decreasing filler size also led to a decrease in critical Gibbs free energy of nucleation causing increased cell density and decreased cell size. And finally, vinyltriethoxysilane was used as a particle surface modifier. The effect of surface chemistry caused better dispersion of nanoparticles with the modified surface in PS matrix, decreased the surface free energy of nanosilica, and changed silica interaction with CO_2 leading to increased cell density compared to the untreated silica.

Ling et al. [145] prepared polyetherimide (PEI) nanocomposite foam with graphene sheets via phase separation. They generated in situ extensional flow during the phase separation which enriched and oriented graphene sheets along the cell walls (Figure 26A, B). Lee et al. [146] incorporated thermally labile PEO-POSS nanoparticles (20 nm domains) in PI. These nanoparticles undergo thermolysis to leave voids (10–40 nm) and forming nanoporous foam. Materials like this have a lower dielectric constant and high thermal stability (Figure 26C, D).

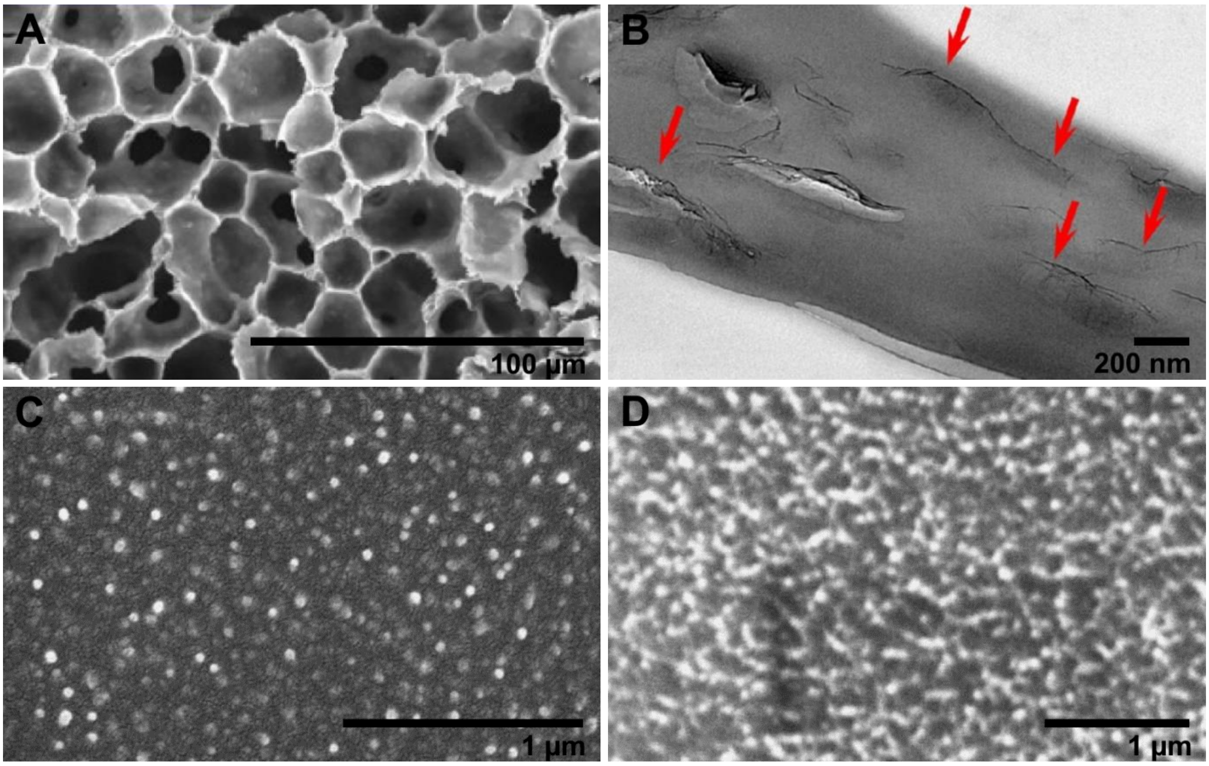

Figure 26: Microscopic photos of nanocomposite foams. **A** – PEI with 1 wt. % of graphene (overview). **B** – PEI with 1 wt. % of graphene (detail of cell wall, red arrows point to oriented graphene sheets. *Reprinted with permission from* [145]. *Copyright 2013 American Chemical Society.* **C** – PI with 5 wt. % of POSS particles before thermal treatment. **D** – PI after thermal treatment and decomposition of 5 wt. of POSS nanoparticles. *Reprinted from* [146], *Copyright 2005, with permission from Elsevier.*

The practical part of this thesis is focused on the preparation of nanocomposite foams via extrusion [141; 147; 148] and 3D printing [126], so the author would like to highlight works, in which cellular nanocomposites were prepared by these methods.

Chaudhary et al. [141] prepared extruded PP foam with organoclay. They used the chemical blowing agent azodicarbonamide for foaming. Clay sheets caused polymer matrix melt-extensional strain hardening and changed crystalization behaviour. Among nanocomposites that did not strain harden, a slower rate of crystalization led to foams with smaller cell size and higher cell density. With nanocomposites where significant strain hardening was observed in extensional flow, the extruded PP nanocomposite foams displayed the smallest cell sizes and the greatest cell density by reducing cell coalescence. Antunes et al. [148] used similar material (PP with montmorillonite and azodicarbonamide as a foaming agent). The compound was twin-screw extruded first and later foamed using a one-step compression-molding process. Han et al. [147] used extrusion to produced polystyrene nanocomposite foams expanded by supercritical CO_2.

Lee et al. [126] investigated cellulose nanofiber foam-based ink for direct ink writing 3D printing. The liquid cellulose nanofiber foam ink was produced by a simple stirring of cellulose nanofiber dispersion with sodium dodecyl sulfate (SDS) as an emulsifier, the porosity of the foam was influenced by the SDS content and the stirring rate. This liquid foam (Figure 27A, B) was printed using direct ink writing 3D printing. The 3D porous structure of a solid cellulose nanofiber foam (Figure 27C, D) was fabricated by the polymerization of pyrrole on freeze-dried foam.

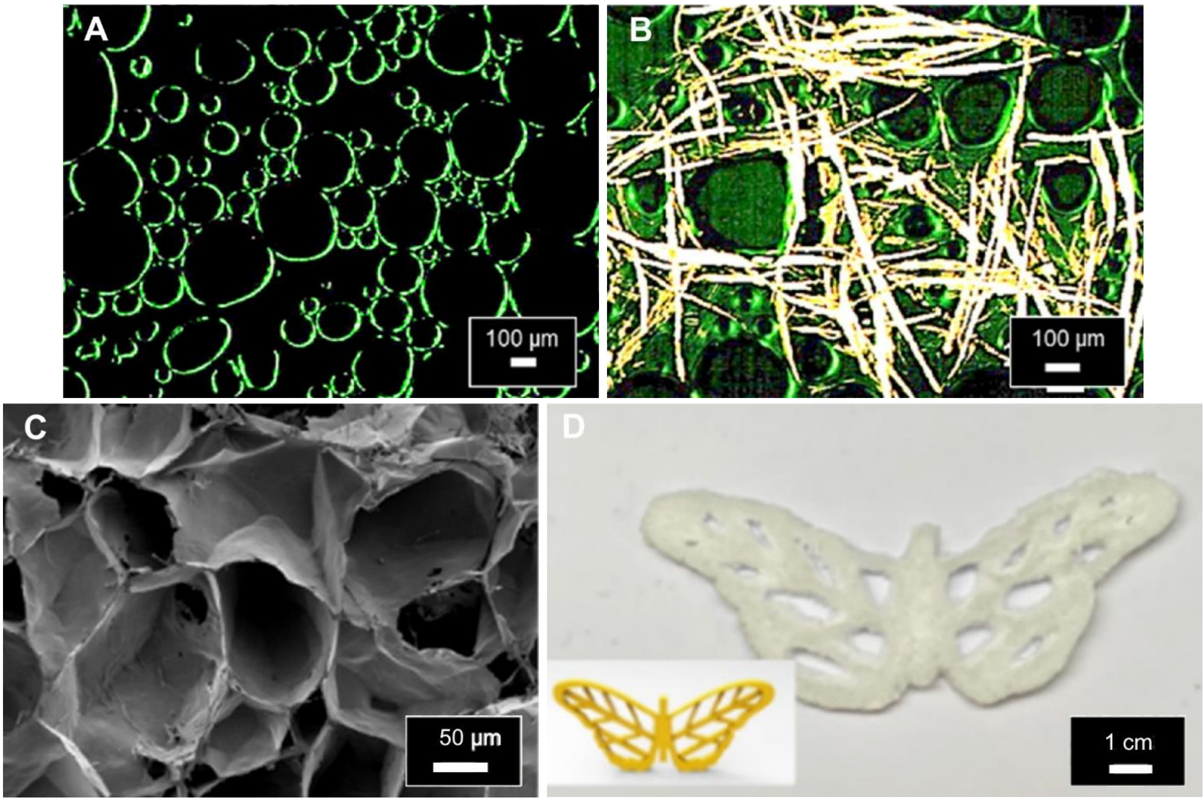

Figure 27: 3D printing with liquid cellulose nanofiber foam. **A** – Dark-field microscopy image of air bubbles in liquid foam ink. **B** – Distribution of cellulose nanofibers in liquid foam ink. **C** – Pore structure of the solid cellulose nanofiber foam. **D** – 3D printed structure of butterfly shape. *Reprinted from* [126], *Copyright 2021, with permission from Elsevier*

3 AIMS OF THESIS

1. Finding thermodynamic variables governing nanoparticle spatial organization in polymer solutions.
2. Preparing two-component polymer blend nanocomposites with engineered dispersion of nanoparticles.
3. Optimizing preparation protocol for two-component polymer blend copolymer nanocomposite foams using chemical foaming agents employing 3D printing technology.
4. Analyzing structural-mechanical property relationships in cellular nanocomposites and identifying the role of individual structural variables in these relationships.

4 MATERIALS, PREPARATION PROTOCOL, AND METHODS

4.1 Materials

4.1.1 Polymer matrices

4.1.1.1 Polymer glasses

Homopolymeric amorphous polymer glasses were used for the preparation of polymer nanocomposites to establish a principle of governing dispersion state of nanoparticles in matrice via the solvent-casting method, specifically PS (Sigma Aldrich), PC (Makrolon 2407 C, Bayer AG), PMMA (Plexiglass P8N, Evonik) and PVAc Sigma Aldrich). Molecular weight M_w and polydispersity D (determined from gel permeation chromatography, GPC), T_g (determined from differential scanning calorimetry, DSC, with the heating rate 10 °C·min^{-1}) and Hildebrant solubility parameters δ_polymer [149] of these polymers are shown in Table 1.

Table 1: Polymer glasses used for the preparation of nanocomposites.

Polymer	Molecular weight M_w (kg·mol^{-1})	Polydispersity D (-)	Glass transition temperature T_g (°C)	Solubility parameter δ_polymer (MPa$^{0.5}$)
PS	201	2.4	104.5	18.7
PC	42	2.2	143.3	19.6
PMMA	100	2.1	115.1	19.0
PVAc	500	2.2	43.0	19.5

4.1.1.2 High impact polystyrene (HIPS)

Commercial grade HIPS PS HI 336M (Synthos Kralupy, Czech Republic) was used. It is a thermoplastic material designed for injection molding with very easy flow and good processability and also very suitable for 3D printing. The input raw material had a form of lens granules of diameter 2.5–4 mm. [150] The structure of HIPS with discrete sphere particles is shown in Figure 28. It was determined by infrared spectroscopy (FTIR) that it contains styrene-butadiene copolymer. The size of rubber particles varied from 10 μm (large occluded particles) to hundreds of nanometers (small solid particles). The density of HIPS was determined pycnometrically in water to 1.03 g·cm^{-3}. The molecular mass of the PS matrix was approximately determined by dynamic light scattering (DLS) to 150 kg·mol^{-1}. Glass transition temperature of the PS matrix was 88.3 °C (determined by DSC, heating rate 10 °C·min^{-1}). Thermal decomposition of PS HI 336M started at 217 °C (determined by thermogravimetric analysis – TGA, heating rate 10 °C·min^{-1}).

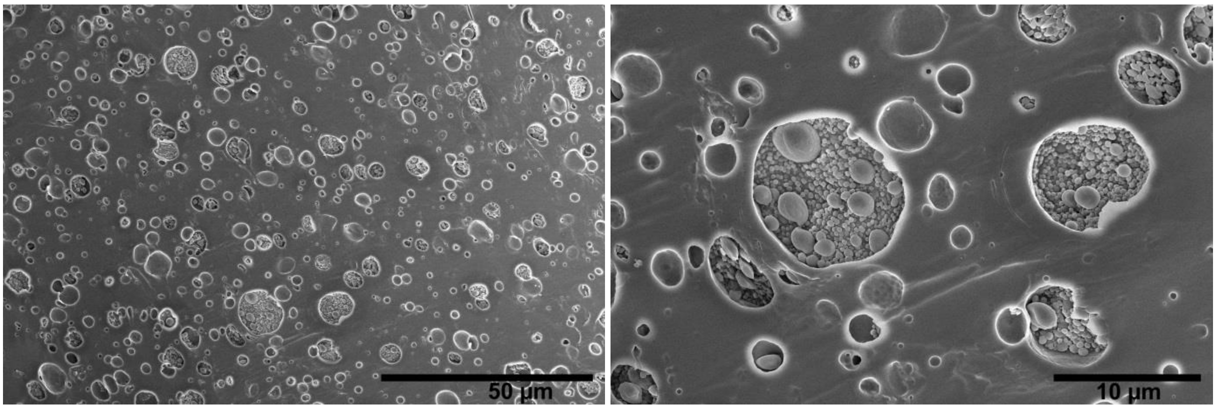

Figure 28: Scanning electron microscope (SEM) image of neat PS HI 336M etched in an acid permanganate mixture for 20 minutes – overview photo (**left**) and detail of occluded and solid particles (**right**).

4.1.2 Nanoparticles

Three types of nanoparticles were used – spherical silica pre-dispersed as a colloidal solution in 30.6 wt. % solution in isopropanol (IPA-ST) or 30.1 wt. % solution in MEK (MEK-ST). Both types of colloidal silica had the same particle diameter (20 nm) and were purchased from Nissan Chemicals. It is important to highlight that it is silica with an untreated surface, so all experiments guarantee direct interaction of silica surface with polymer segments. The second type of nanoparticles was powdered fumed silica (Sigma Aldrich) formed by 7 nm particles sintered together into larger aggregates (about 70 nm) as a result of production protocol. The last type of nanoparticles were functional semiconductive zinc oxide particles doped with 2 wt. % of aluminum oxide (AZO, US Research Nanomaterials) with 15 nm size.

4.1.3 Foaming agent – azodicarbonamide

Azodicarbonamide (1,1′-azobisformamide) is a foaming agent frequently used in the production of thermoplastic (e.g. PP or PVC) and rubber profiles foams because its decomposition liberates a high volume of gas, which is trapped in the melt. [151; 152]

When azodicarbonamide is heated to 165–195 °C an exothermic decomposition without melting to yield a gas is observed and a white solid deposit of a sublimed substance (sublimate, formed in the cooler parts of reaction space) and a white residue are formed. During decomposition at 190 °C is produced 32 wt. % of gasses, 41 wt. % of solid residue and 27 wt. % of sublimate. [153]

The foaming effective gas consists mainly of nitrogen and a smaller but significant quantity of carbon monoxide together with a third component, which is isocyanic acid at lower and ammonia at higher temperatures. The sublimate consists of cyanuric acid, cyamelide, and urea, and the residue is a mixture of biurea, cyanuric acid, and urazole. Two main primary reactions appear to take place concurrently during decomposition:

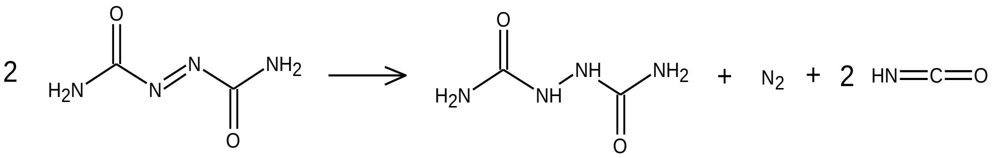

(15)

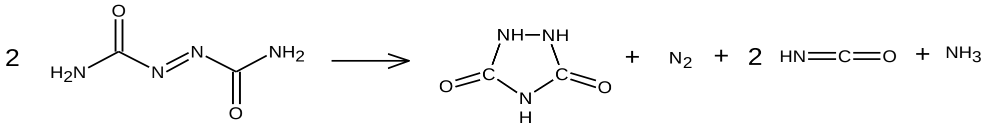

(16)

In the first reaction, two molecules of azodicarbonamide decompose to form biurea, nitrogen, and isocyanic acid. In the second reaction urazole, nitrogen, isocyanic acid, and ammonium are formed. Reaction (16) is basically reaction (17), in which urea is formed:

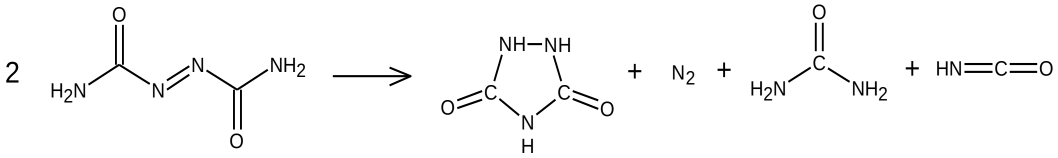

(17)

but at the temperature at which azodicarbonamide decomposes, urea itself is unstable and dissociates to form ammonia and isocyanide acid:

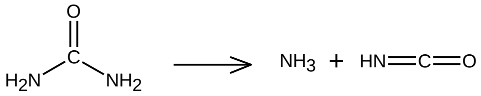

(18)

Anyway, the urea is present in the sublimate due to the recombination of ammonia and isocyanic acid in the cooler parts of the reaction space. Carbon monoxide is formed as a result of the reduction of isocyanic acid by undecomposed azodicarbonamide.

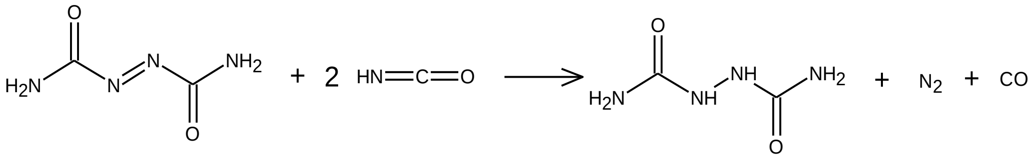

(19)

As a result of being produced by this secondary process, carbon monoxide does not appear initially but only once appreciable isocyanic acid has been formed. Reaction (19) competes with oligomerization of isocyanic acid to form cyclic trimer cyanuric acid and cyamelide $(HNCO)_x$. [153]

In the experimental part of this thesis, a commercial blowing agent Unicell D200A (Tramaco) based on azodicarbonamide of the appearance of yellow powder was used. According to its datasheet [152], the decomposition temperature is about 210 °C, gas yield at 220 °C is about 240 $cm^3 \cdot g^{-1}$ and its average particle size is 5.3 μm. TGA of the pure foaming agent was measured to verify the accuracy of the data.

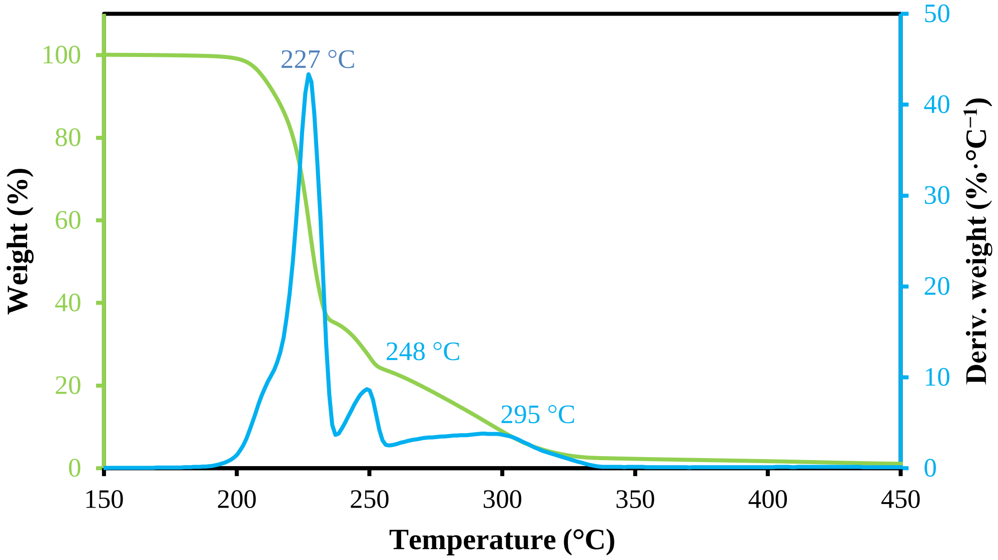

Figure 29: TGA curve of foaming agent Unicell D200A – percentual loss of mass (red) and derivation of loss of mass (blue). Measured in a nitrogen atmosphere with temperature ramp 10 °C·min^{-1}.

The decomposition of the foaming agent accompanied by a loss of mass was observable from 187 °C. The widely accepted scheme of decomposition of azodicarbonamide described above is not capable of explaining the three peaks observed in the TGA curve determining three decomposition steps – the first one with the fastest loss of mass at 227 °C, the second one at 248 °C, and the third one at 295 °C. Since competitive reactions such as reactions described above cannot yield separated or independent peaks and consequently, these reactions could only be associated with the first peak. Therefore, the whole complex thermal decomposition includes reactions (15–19) corresponding to the first peak and two degradations of the corresponding solid products: $H_6N_4C_2O_2$ (biurea) in reaction (20) and $H_3N_3C_2O_2$ (urazole) in reaction (21). According to DSC measurement, decomposing reactions (15–19) are exothermic and reactions (20) and (21) are endothermic. It has to be also considered the possibility of the formation of an intermediate compound (adsorption reaction) between the HNCO and the azodicarbonamide. [151]

$$H_3N_3C_2O_2 \textit{ (solid state)} \rightarrow \text{volatile products} \tag{20}$$

$$H_6N_4C_2O_2 \textit{ (solid state)} \rightarrow \text{volatile products} \tag{21}$$

4.1.4 Solvents

All solvents used during the preparation of nanocomposites via the solvent-casting method were analytical purity quality (p.a. quality). A list of all solvents with important characteristics (boiling point T_B and Hildebrandt solubility parameter $\delta_{solvent}$ calculated from Hansen solubility parameters [154]) is shown in Table 2. The acetone-toluene mixture was used in a volume ratio of 1:1.

Table 2: Solvents used for nanocomposite preparation.

Solvent	Boiling point T_B (°C)	Solubility parameter $\delta_{solvent}$ ($MPa^{0.5}$)
tetrahydrofuran (THF)	66	18.6
acetonitrile	82	24.3
ethyl acetate	77	18.6
anisole	154	19.5
cyclohexanone	156	20.3
dichloromethane (DCM)	40	19.8
dimethylacetamide (DMAC)	165	22.1
dimethylformamide (DMF)	153	24.8
acetone	56	20.3
toluene	111	18.2
acetone-toluene mixture	69	19.3
dioxane	101	20.5
water*	100	47.9
isopropanol (IPA)*	83	23.5
ethyl methyl ketone (MEK)*	80	19.0
xylene*	139	18.0

*Water, IPA, MEK, and xylene were not used for nanocomposite preparation, it was used just for ζ-potential determination.

4.2 Preparation protocol

4.2.1 Solvent-casting

The appropriate solvent was poured into a glass flask, heated under reflux to 50 °C, and stirred with a magnetic stirrer. When the solvent was heated, the polymer beads were added in the ratio of 150 cm^3 of solvent to 10 g of polymer (corresponds to 6.0 vol. % for solution of PS, 5.2 vol. % for PC, and 5.3 vol. % for PMMA and PVAc), which is in the semi-diluted region of a polymer solution. After the complete dissolving of polymer beads, nanoparticles were added. The mixtures were first ultrasonicated with an ultrasonic homogenizer with titanium tip (Sonopuls, Bandelin) to break aggregates formed during particle storage. Spherical colloidal silica was dispersed in its storage solvent (IPA or MEK) and powdered fumed silica and AZO particles were dispersed in a small amount of solvent used for nanocomposite preparation.

After 60 minutes of stirring solvent-polymer-nanoparticle system, the solution was poured onto a preheated aluminum sheet in an atmospheric drier with a forced airflow to ensure the most rapid evaporation of the majority solvent and fixing the obtained nanocomposite structure with no additional nanoparticle aggregation caused by sedimentation. The nanocomposite was dried in the atmospheric dryer for 24 hours. The temperature of evaporation was always above the boiling point of the appropriate solvent and above the glass temperature of an appropriate polymer matrix. After drying in the atmospheric drier, the nanocomposite was minced and dried again in a vacuum drier for 6 days to remove residual solvent. The absence of residual solvent and particle loading was checked by TGA.

4.2.2 Foams preparation

The preparation protocol of polymer nanocomposite foams is schematically described in Figure 30. Masterbatch of foaming agent (33.3 wt. %), i.e. polymer granules with concentrated azodicarbonamide, were prepared first. Masterbatch was prepared in laboratory mixer (Plastograph EC plus W 50 EHT, Brabender), where HIPS was heated to 130 °C (actual melt temperature due to shear friction was 150 °C), this temperature was sufficiently high to melt and process HIPS and also sufficiently low that no thermal decomposition of the foaming agent occurred. After melting of HIPS, foaming agent Unicell D200A was added and the compound was blended for 5 minutes with 60 rpm. After colling down, the masterbatch was minced into granules.

Due to the considerable requirement on the fumed nanosilica melt homogenization, the HIPS with fumed nanosilica was not processed in the form of a concentrated masterbatch but was directly pre-mixed at the final concentration of nanoparticles intended for sample preparation in Brabender mixer. To compare nanocomposite structures achieved by different processing methods, the colloidal spherical silica (MEK-ST) was also incorporated into samples by the solvent-casting method described above. Nanocomposites with silica (melt-blended fumed or solvent-casted spherical) were also minced.

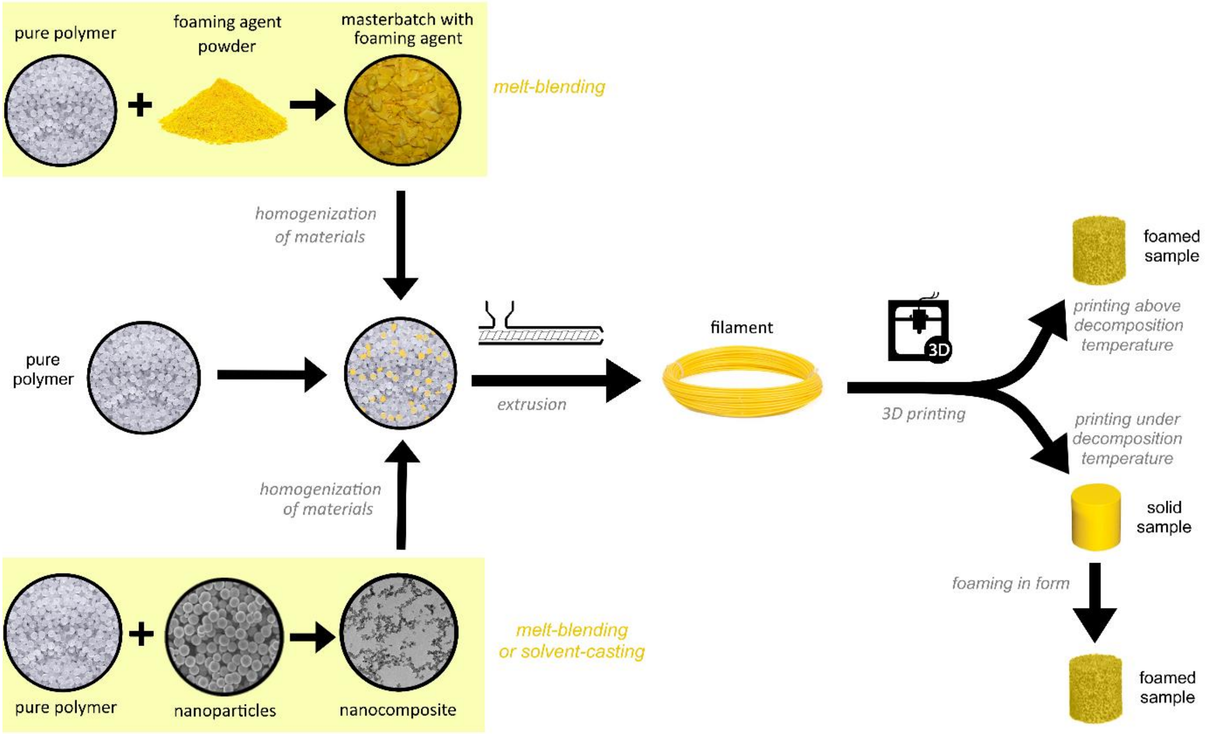

Figure 30: Polymer nanocomposite foam preparation scheme.

Pure HIPS granules (for preparation of pure foams without nanoparticles) or pre-mixed nanocomposite (for preparation of nanocomposite foams) were mixed with the appropriate amount of foaming agent masterbatch in a single-screw extruder (HAAKE PolyLab OS system with HAAKE Rheomex OS, Thermo Scientific) at 180 °C (actual melt temperature 170 °C). The overview of prepared filaments is shown in Table 3.

Table 3: List of nanocomposite filaments with the blowing agent.

Sample identification	Unicell content (wt. %)	Nanosilica content (wt. %)	Method of nanosilica mixing
pure HIPS	–	–	–
without nanoparticles	2.0	–	–
fumed silica	2.0	0.25	melt-blending
	2.0	1.0	melt-blending
	2.0	2.5	melt-blending
	2.0	5.0	melt-blending
	2.0	10.0	melt-blending
spherical silica	2.0	1.0	solvent-casting

All filaments analyzed in this dissertation thesis were extruded at the same conditions (rotation of extruder 25 rpm and drawing-off device 60 rpm) to ensure the same conditions for pore formation. Only nanocomposite filaments for 3D printing (Figure 31C, D) were extruded at slightly different conditions to reach a filament diameter of 1.75 mm suitable for 3D printing. Nanoparticles caused an increase in melt viscosity and thus nanocomposite filaments had to be drawed-off with higher speed (80 rpm) to reach the same diameter as 3D printing filaments without nanoparticles. The structure and mechanical properties of these 3D printing nanocomposite filaments (see appendix) were very close to the properties of nanocomposite filaments pulled with extruder rotation 25 rpm and drawing-off device 60 rpm.

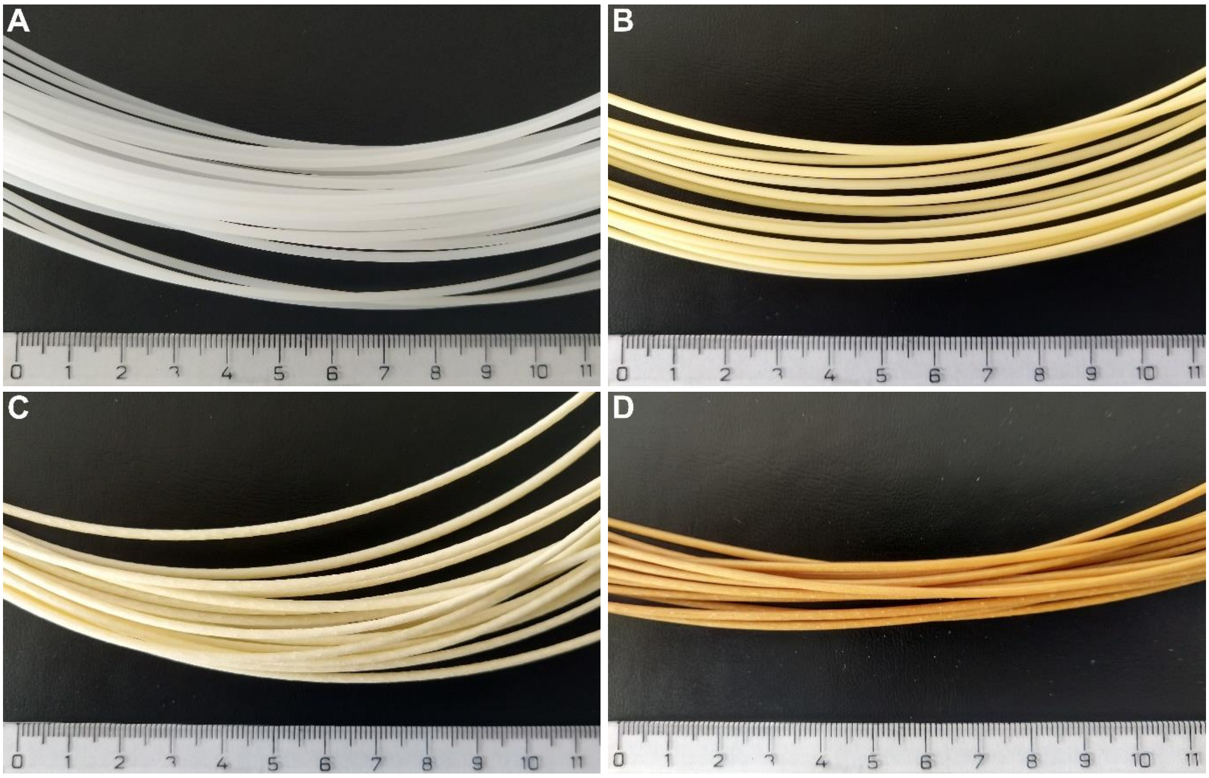

Figure 31: Filaments for 3D printing. **A** – Pure HIPS filament without additives. **B** – HIPS with 2 wt. % of azodicarbonamide and without nanoparticles. **C** – HIPS with 2 wt. % of azodicarbonamide and 1 wt. % of melt-blended fumed nanosilica. **D** – HIPS with 2 wt. % of azodicarbonamide and 1 wt. % of solvent-casted spherical nanosilica.

3D printing of test bodies was performed with Reach 3D Printer or Rebel 3D Printer using slicer software Repetier-Host. Bed temperature was set to 75 °C, the diameter of the nozzle was 0.4 mm. Two different nozzle temperatures were chosen, namely 180 °C for printing below the decomposition temperature of the chemical blowing agent and 220 °C for printing above the decomposition temperature of the foaming agent. Quality of the printing, i.e. height of one printed layer varied according to temperature conditions – 0.1 mm layer for printing at 180 °C to reach high quality printed body and 0.3 mm layer for printing at 220 °C to not overpress bubbles formed by the decomposition of blowing agent at the higher temperature.

If the sample was printed above the decomposition temperature of the foaming agent, it was no further treated, the foam was tested directly in the printed state (Figure 32C). When 3D printing occurred above decomposition of the temperature of the foaming agent, the gas was released, bubbles were formed and the printed material expanded. To neglected possible overflows, the flow of filament material through the printer extruder was reduced, e.g. for 80 %. Then a high-quality undeformed body was achieved even when printing the foaming material. The value of the flow reduction was set experimentally.

If the sample was printed under the decomposition temperature of the foaming agent, the entire processing was carefully thermally balanced to allow the polymer to process well, but the blowing agent did not foam. For example, during 3D printing, the temperature processing range was very narrow. At 170 °C, the melt had too high viscosity, did not pass through the nozzle and 3D printing was not possible. Thermal decomposition of the foaming agent occurred at 190 °C, causing undesirable foaming during processing. The products printed under the decomposition temperature of the foaming agent were tested directly after 3D printing or finally foamed at 200 °C in an atmospheric oven (post-processing foaming). Time of post-processing foaming varied according to nanosilica presence – 30 min for samples without nanoparticles, 10 min for samples with 1 wt. % of fumed nanosilica and 5 min for 1 wt. % of spherical nanosilica (explanation in paragraph 5.2.2). This was followed by rapid cooling to room temperature to stabilize the foam structure (Figure 32B). The foaming process (Figure 32A) was carried out in a form, its circumference was made of aluminum and the bases were made of glass. The form diameter d_f was 120 % compared to the diameter of the printed sample d_s. The form height was the same as that of the printed sample $h_f = h_s$. The entire form was carefully heated before sample placement to allow more efficient heat transfer to the bulk of the sample. After foaming, the sample was cooled down to room temperature to fix the formed porous structure.

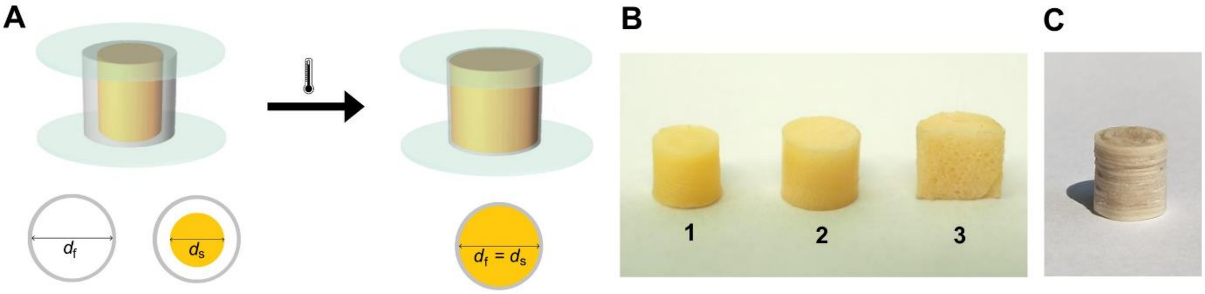

Figure 32: A – Post-processing foaming scheme. **B** – Photo of HIPS samples with 2 wt. % of Unicell D200A. Unfoamed cylinder after 3D printing at 180 °C (1), cylinder foamed to 120 % of diameter at 200 °C for 30 minutes (2) and the foamed cylinder cut in half (3). **C** – Photo of HIPS sample with 2 wt. % of Unicell D200A after 3D printing at 220 °C.

4.3 Methods

4.3.1 Structural analysis

Scanning electron microscopy (SEM)

Neat HIPS sample for SEM observation was etched in an acid permanganate mixture (10 ml of 85 wt. % H_3PO_4, 15 ml of 96 wt. % H_2SO_4 with 0.5 wt. % of $KMnO_4$) for 20 minutes. The other samples were broken in liquid nitrogen and their fracture surface was observed. A 10 nm layer of Au was deposited by sputtering on all samples to ensure better surface conductivity (Coater Leica EM ACE 600). SEM observation was done on a high-resolution microscope Verios 460L (FEI) in secondary electrons mode (SE).

Transmission electron microscopy (TEM)

Samples for TEM or scanning transmission electron microscopy (STEM) observation were broken in liquid nitrogen first and then 50 nm ultramicrotome cuts were made. Most of the samples were measured by the high-resolution microscope Verios 460L (FEI) in STEM mode, the remaining samples were measured by TEM microscope Morgagni 268D (FEI) and by SEM microscope MIRA3 (Tescan) in STEM mode. Observations were made in both bright field (BF) and dark field (DF) modes.

The average nanoparticle element diameter d_w in polymer nanocomposites was calculated via image analysis from binarized TEM and STEM images containing a sufficient number of elements by approximating projections of individual elements – nanoparticles, clusters, and aggregates – to an ideal sphere (an example of the binarization procedure is provided in Figure 33).

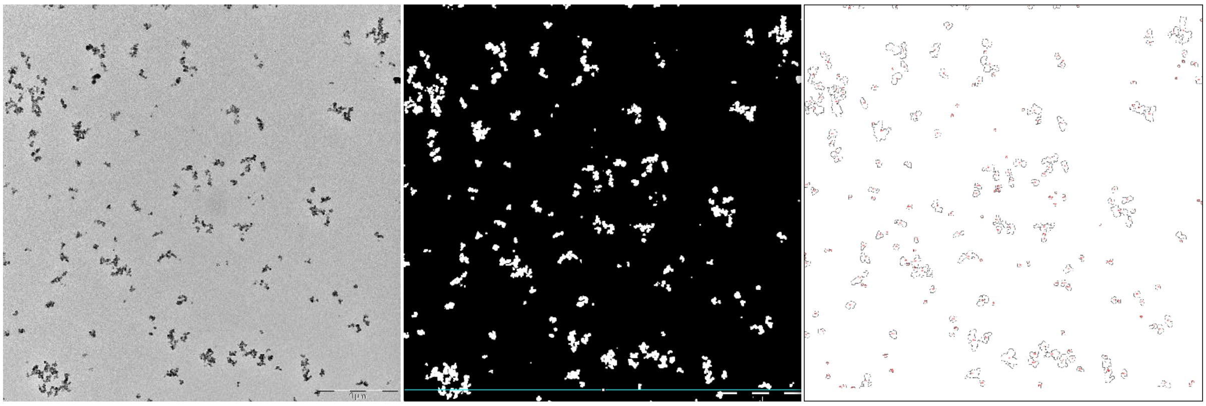

Figure 33: Example of binarization for PMMA nanocomposite with 1 vol. % of fumed silica prepared in acetone. **Left** – Original TEM image. **Middle** – Binarization of agglomerates by ImageJ® software (area without scale bar was selected to avoid distortion of results). **Right** – Particle elements (agglomerates) detected by the automatic function of the ImageJ®. The area of each element was approximated to an ideal sphere and the mass average agglomerate diameter was calculated.

Confocal laser scanning microscopy (CLSM)

Samples for CLSM observation were broken in liquid nitrogen and observed on Olympus Lext OLS 4000 confocal laser microscope in the range 2.5–100 of magnification. The images were taken from different parts of the sample to verify the homogeneity of the porous structure.

The average pore size and pore density per unit volume were evaluated from CLSM images. The average size was determined using ImageJ® software as measuring of the diameter of each pore in the horizontal and diagonal direction, the average diameter of all pores was then estimated. Cell population density N_0 was calculated based on the equation (cell·cm^{-3}) [155]:

$$N_0 = \left(\frac{n_\mathrm{p} \cdot M^2}{A}\right)^{\frac{3}{2}} \cdot \frac{1}{1 - V_\mathrm{f}}, \tag{22}$$

where n_p is the number of the pores in the micrograph, M is the magnification factor of the micrograph, A is the area of the micrograph (cm^2), and V_f is the void fraction calculated as

$$V_\mathrm{f} = 1 - \frac{\rho_\mathrm{f}}{\rho_\mathrm{s}}, \tag{23}$$

where ρ_f is the mass density of the sample with pores which was experimentally measured and ρ_s is the mass density of the sample without pores which was calculated theoretically based on the composition of the system. The experimental mass density determination was done both pycnometrically and by weight to volume measurements. Void fraction V_f was recalculated to percentual porosity P (%):

$$P = V_{\mathrm{f}} \cdot 100 = \left(1 - \frac{\rho_{\mathrm{f}}}{\rho_{\mathrm{s}}}\right) \cdot 100. \tag{24}$$

Dynamical light scattering (DLS)

Sizes (hydrodynamic diameter) of the expanded polymer coils in different solvents were measured by DLS (DynaPro Nanostar, Wyatt Technology Corporation).

4.3.2 Thermal analysis

Thermogravimetric analysis (TGA)

Approximate determination of the thermal stability of the polymers, verification of residual solvent, filler loading, and blowing agent decomposition TGA measurements were done on TGA Discovery (TA Instruments). Temperature ramp 10 °C·min^{-1} to 650 °C in nitrogen atmosphere was followed by a switch to an oxidative atmosphere with an isothermal hold for 20 min.

The foaming process of azodicarbonamide blowing agent (pure or 2 wt. % incorporated in HIPS) was simulated from the beginning in an oxidative atmosphere - jump heating to the appropriate temperature (160–250 °C) with a 60 min hold followed by temperature ramp of 10 °C·min^{-1} to 650 °C and hold for 20 min to burn the rest of the sample.

Differential scanning calorimetry (DSC)

DSC of polymer nanocomposites was made by DSC Discovery (TA Instruments) to determine T_{g} and activation energy of glass transition $E_{\mathrm{A,\,Tg}}$ in heating-cooling cycles with temperature ramp 5, 7.5, 10, 15, 20, 35 and 50 °C·min^{-1} in the temperature range 30–200 °C for PS samples, 50–260 °C for PC, 30–200 °C for PMMA and 0–80 °C for PVAc.

4.3.3 Zeta potential

Zeta potential (ζ-potential) of colloidal spherical nanosilica was measured in 1 wt. % concentration in a series of solvents (all solvents listed in Table 2) at Zetasizer instrument (Malvern Panalytical).

4.3.4 Mechanical properties

Mechanical tensile testing of filaments

Tensile tests were performed on Zwick Roell Z10 device. Filament specimens had a round shape with a gauge length of 100 mm. 5 specimens were measured for each sample batch. The conditions of the test were set to:

- Test speed: 2 mm·min^{-1}.
- Load cell: 10 kN.
- Pre-load: 0.25 N.
- End of the test: force shutdown threshold 80 % of maximal force (F_{max}) or maximum extension 300 %.
- Room temperature.

From tensile mechanical tests were evaluated:

- Tensile modulus: the maximum of the peak of the first derivation from the stress-strain curve.
- Offset yield strength: stress at which line parallel to the initial linear regime of the stress-strain curve offset by 0.2 % of strain from the origin intersects the original stress-strain curve.
- Tensile strength: stress at the break.
- Elongation: deformation at the break.
- Specific properties were determined by dividing certain property measured value by the mass density of the material.

Mechanical compression testing of 3D printed materials

Compression tests were performed on Zwick Roell Z10 device. Directly 3D printed specimens had a cylindric shape with a high of 6 mm and a diameter of 6 mm. Specimens treated by post-processing foaming after 3D printing had a cylindric shape with a high of 6 mm and a diameter of 7.2 mm. 5 specimens were measured for each sample batch. The conditions of the test were set to:

- Test speed: 1 mm·min^{-1}.
- Load cell: 1 kN.
- Pre-load: 5 N.
- End of the test: force shutdown threshold 50 % of $F_{\max}$ or minimum tool separation 2 mm.
- Room temperature.

From compression mechanical tests were evaluated:

- Compression modulus: the maximum of the peak of the first derivation from the stress-strain curve.
- Offset yield strength: stress at which line parallel to the initial linear regime of the stress-strain curve offset by 0.2 % of strain from the origin intersects the original stress-strain curve.
- Specific properties were determined by dividing certain property measured value by the mass density of the material.

Three series of 3D printed cylinders were distinguished for compression measurements:

1) Cylinders 3D printed below the decomposition temperature of the blowing agent (printing temperature 180 °C).
2) Cylinders 3D printed above the decomposition temperature of the blowing agent (printing temperature 220 °C).
3) Cylinders 3D printed below the decomposition temperature and then treated by post-processing foaming in the pre-heated oven (foaming temperature 200 °C) in the mold with 120 % of the diameter of original cylinders.

5 RESULTS AND DISCUSSION

5.1 Controlling nanocomposite structure

5.1.1 Nanocomposites with homopolymer matrices

This chapter Nanocomposites with homopolymer matrices is based on the published article *Thermodynamic parameters controlling nanoparticle spatial packing in polymer solutions* from authors K. Zarybnicka, F. Ondreas, P. Lepcio, M. Kalina, M. Zboncak, and J. Jancar (*Macromolecules*. 2020, **53**(19), 8704-8713. ISSN 0024-9297. Available at: doi:10.1021/acs.macromol.0c00698). The text is reproduced with permission from [156]. Copyright 2020 American Chemical Society.

5.1.1.1 ξ-potential of spherical nanosilica in solvents

The spatial organization of colloidal silica, fumed silica, and AZO nanoparticles was investigated in PMMA, PC, PVAc, and PS matrices to determine the role of polymer-solvent-particle interactions in different systems and generalize the preparation protocol-structure function described previously in the PMMA-silica system in [25]. The solid-state organization of polymer nanocomposites was inherited from the thermodynamically driven organization state in the nanosuspension, which was controlled by the selection of solvent and supposedly in equilibrium. This state was preserved through rapid evaporation far above the matrix glass transition temperature and solvent boiling point. Therefore, a wide range of solvents was used to prepare polymer nanocomposites and examine their structure. The spherical colloidal nanosilica was selected as the reference model nanofiller because of its spherical shape and well-defined chemical composition – amorphous silicon dioxide with silanol Si-OH groups on its surface.

The ζ-potential was measured to quantify the charge on the silica surface in the presence of various solvents. The ζ-potential was negative in almost all solvents (the only exception was dioxane – explanation below), which means that the silica surface was negatively charged and solvents preferred electron donor behaviour. [30] It was found that the amount of charge depends approximately linearly on the polarity index (*PI*, constant readily accessible in the literature [157]) of the solvent (Figure 34) – a more polar solvent produced a greater negative ζ-potential on the silica surface. Protons were probably cleaved from silanol groups, which made the silica behave as an acid (proton donor). Solvents in the vicinity of the silica surface (except dioxane), on the other hand, acted as bases (proton acceptor).

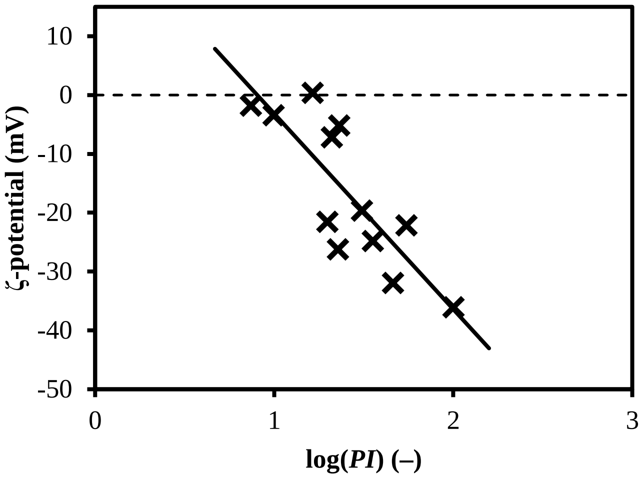

Figure 34: Charge on silica surface in organic solution represented by the ζ-potential as the dependence of logarithm of the polarity index of solvents. Raw data are available in the appendix.

Dioxane, acting as an acid causing slightly positive ξ-potential on the silica surface, demonstrated the ambivalent character of the silica surface, which acted as a base in this case, and led to a formation of spherical silica nanoparticles into anisotropic microfibers (Figure 35). This topic of anisotropic microfibers formation from spherical nanoparticles via self-assembly process was largely described in another work of the dissertation thesis author [158]. Theaverage fiber size in the longitudinal direction was 5 μm and in the transverse direction 470 nm.

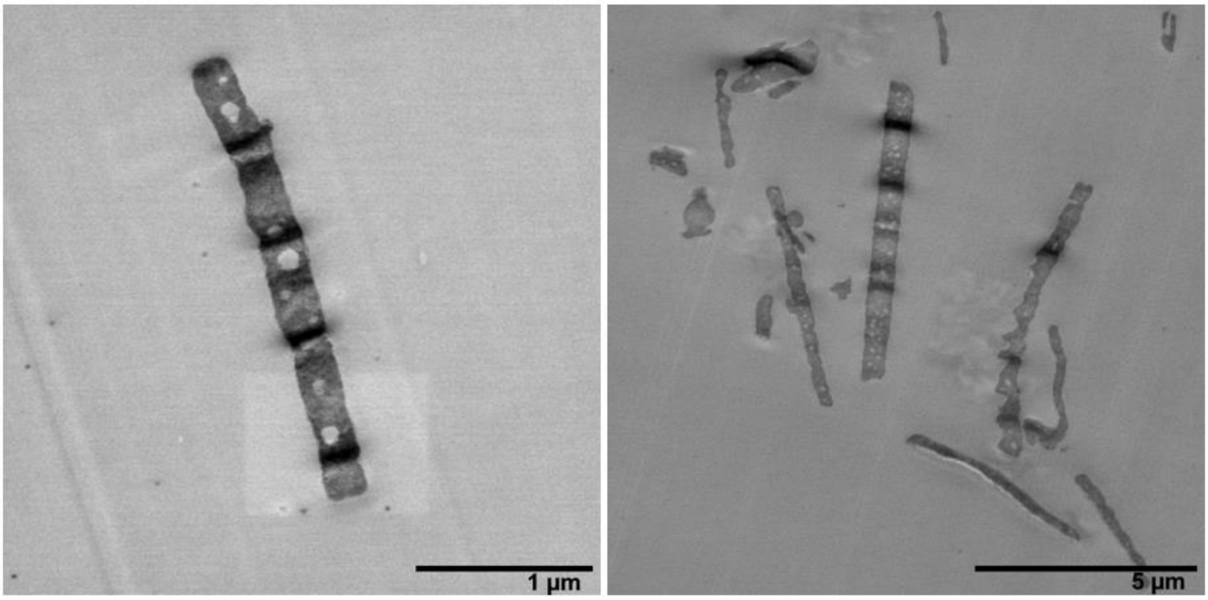

Figure 35: STEM images of nanocomposites with anisotropic microfibers composed of PC and 1 vol. % of spherical silica prepared in dioxane with positive ζ-potential.

5.1.1.2 Nanocomposite with spherical nanosilica

The choice of polymer matrix had an essential effect on the resulting nanocomposite structure and properties. The nanocomposites prepared in THF with 1 vol. % loading of spherical nanosilica were prepared using four different glassy homopolymer matrices – non-polar PS, PC with sterically hindered ester polar groups in its backbone chain, and polar PMMA and PVAc, both having polar ester groups on short side branches. In the case of PMMA, ester groups at short branches protrude out, but in the case of PVAc, the polar groups are bonded on the backbone chain.

THF was the only investigated solvent that dissolved all four matrices. Hence, it could serve as a case example to investigate the role of polymer on nanoparticle dispersion. In the nanocomposites prepared in THF, solvent-particle interactions remained unchanged, but silica-polymer and solvent-polymer interactions varied depending on the polarity and location of the groups in the polymer chains. Nanocomposites prepared in THF with different nanoparticle organizations are depicted in Figure 36.

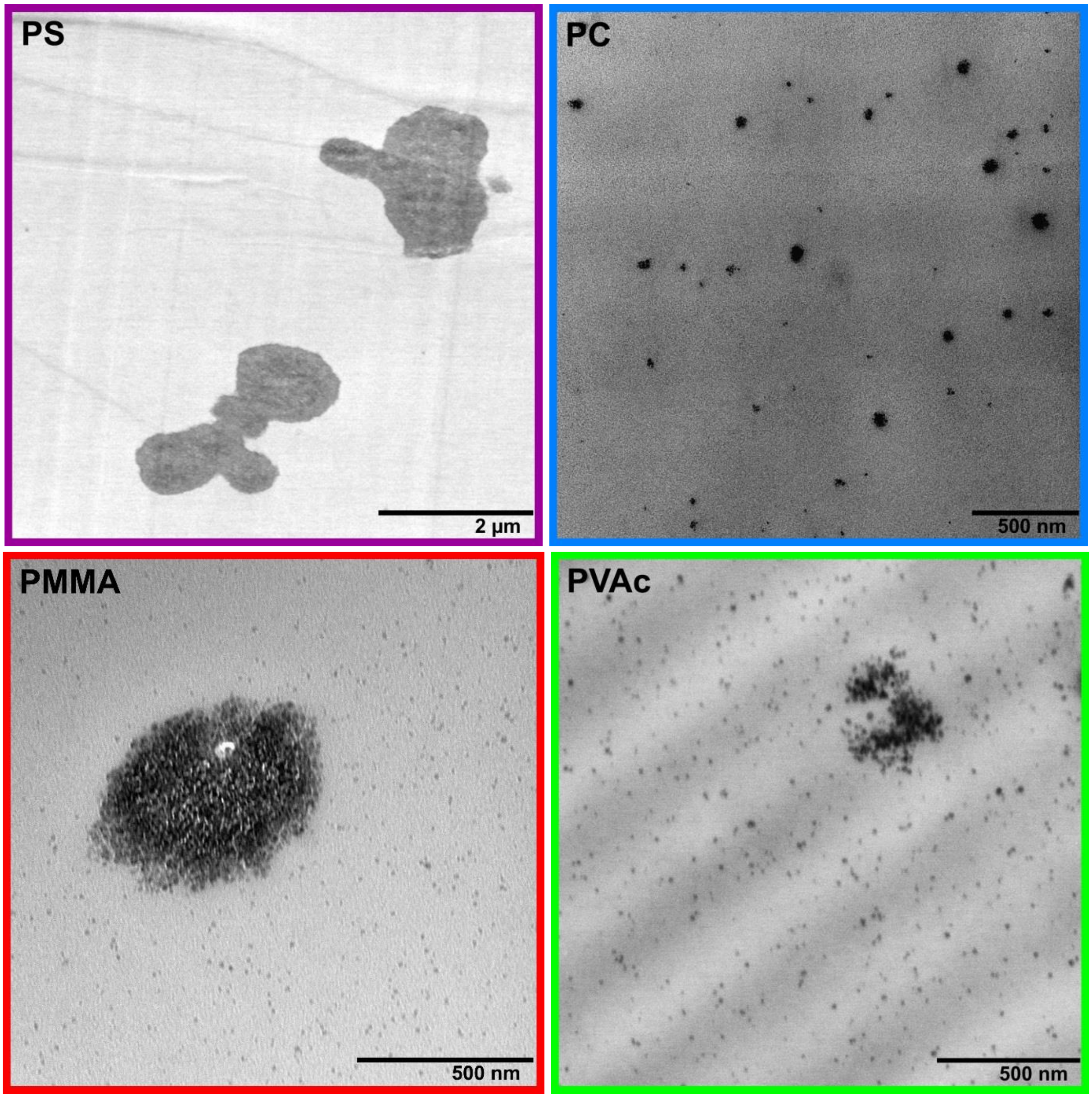

Figure 36: TEM images of nanocomposites with 1 vol. % of spherical silica prepared in THF with four different matrices – PS (purple), PC (blue), PMMA (red), and PVAc (green).

For quantitative estimation of the nanocomposite structure, the size of agglomerates d_w (individual particles, clusters, or aggregates) formed in the nanocomposite was calculated. It was basically the diameter of the agglomerates projected into an ideal sphere – detail of calculation is described in paragraph 4.3.1.

Non-polar PS had a poor affinity to polar silica and large silica aggregates with a size of approximately 2 281 nm were formed exclusively. No individually dispersed nanoparticles were observed. Since the PS chains did not interact with silica effectively, silica preferred interactions with the solvent molecules forming the solvation shell around the silica surface. When the solvent was evaporating, the thickness of the solvation shell decreased to the point, where particles started to interact directly with each other and contact aggregation occurred.

In the PC matrix, there was a good dispersion of very small silica aggregates containing 2–20 particles (average aggregate diameter ~62 nm). Polar groups in the PC were capable to interact with the silica surface and portions of its chains were absorbed onto the silica surface. When the solvation shell was disrupted during evaporation, the absorbed chains prevented massive aggregation of particles limiting direct contact between silica particles. Due to the steric hindrance of PC chain segmental mobility, this process was not efficient enough to lead to dispersion of individual particles.

In the case of PMMA and PVAc matrices, two parallel populations of nanoparticle spatial organization were formed – individually dispersed particles and aggregated nanoparticles. Individually dispersed nanoparticles were quasi-homogenously distributed throughout both matrices. Polar groups of PMMA and PVAc were easily available for silica surface and, thus, the absorption of polymer chains on the particle surface was sufficiently effective to ensure good dispersion of nanoparticles. When the THF was used as a solvent, the depletion attraction occurred and nanoparticle aggregates were formed. [25] Depletion attraction is facilitated by solvents with very strong attractive interaction to silica. Because of the weak adsorption of the polymer chains on the silica surface, a solvation shell was formed around nanoparticles. The polymer segments were, therefore, displaced by the solvent and did not adsorb onto certain particles. Nanoparticles onto which polymer chains were not adsorbed could become in contact with other nanoparticles and formed aggregates upon evaporation of the solvent. Nanoparticle aggregates formed in the PMMA matrix had a spherical shape with an average size of 664 nm. Nanoparticle aggregates in the PVAc were rarer and smaller (227 nm). Individual particles in PMMA had an average size of 17 nm and in PVAc 31 nm.

Additionally nanocomposites of PS, PC, PMMA, and PVC with 1 vol. % of spherical nanosilica were prepared in a variety of other solvents depending on the need of structure diversity and solubility of each matrix individually.

PS nanocomposites were prepared from DMAC, DMF, cyclohexanone, and toluene (Figure 37). In the first three solvents, small chain-bound clusters were formed containing from a few to tens of nanoparticles. The average size of the clusters was very similar in all the systems – 37 nm in DMAC, 44 nm in DMF, and 40 nm in cyclohexanone. On the other hand, PS nanocomposite made in toluene contained only aggregates about 403 nm in diameter. Toluene was the only non-polar solvent of these four, thus toluene preferable interact with non-polar PS rather than with polar silica. There was an abundance of toluene in the polymer-solvent-particle solution, it was possible that due to the attractive interaction between toluene and PS, PS chains were surrounded by solvent molecules and no longer interacted with silica becoming unable to prevent contact nanoparticle aggregation efficiently.

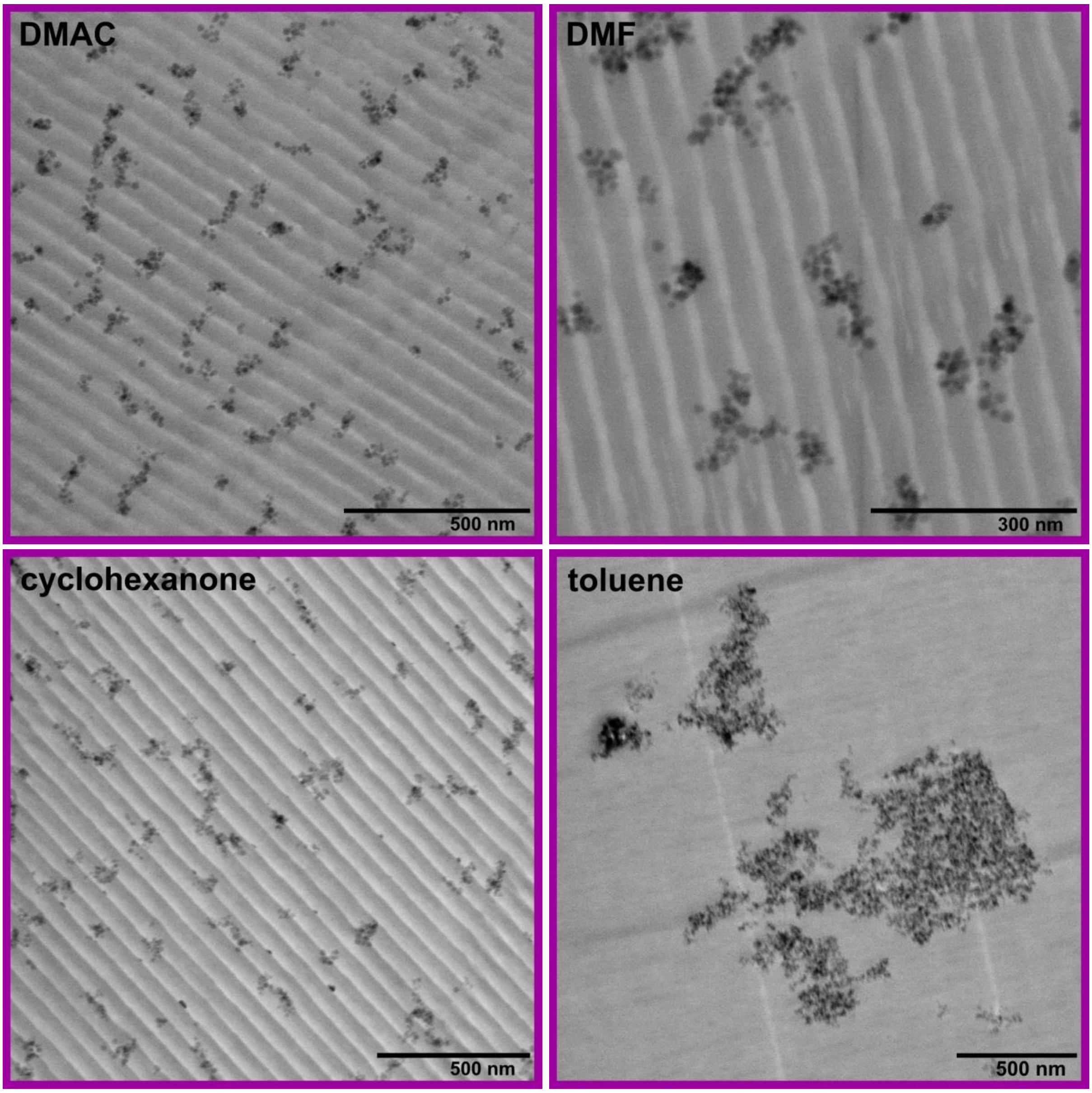

Figure 37: TEM images of PS nanocomposites with 1 vol. % of spherical silica prepared in different solvents – DMAC, DMF, cyclohexanone, and toluene. The stripes in the images are artifacts after cutting with a vibrating ultramicrotome knife.

PC nanocomposite was also made in the DCM (Figure 38), which had two acidic hydrogens in its molecule. Despite the fact that silica behaved like a weak acid in the DCM, DCM remained acidic for polycarbonate. The solvent was in the system in an abundance in comparison with silica, hence, in the competition between acidic DCM and acidic silica for alkaline PC, the DCM prevailed. PC adsorption onto silica was inhibited resulting in a contact aggregation. In the PC nanocomposite, aggregates ranging in size from 100 nm to several micrometers were observed, with an average aggregate size of approximately 1 395 nm.

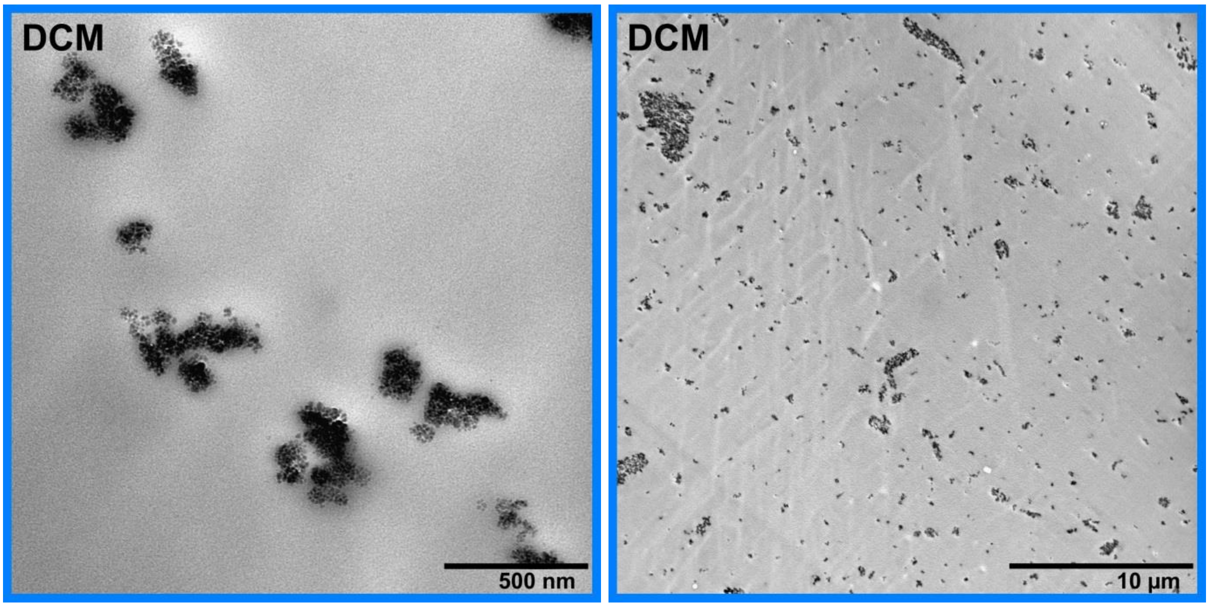

Figure 38: TEM images of PC nanocomposite with 1 vol. % of spherical silica prepared in DCM – the detail on aggregates (**left**), overview image (**right**).

Obtaining good dispersion of silica was easier in polar polymers with well-accessible functional groups, such as PMMA and PVAc. PMMA nanocomposites prepared in cyclohexanone, acetonitrile, and anisole are depicted in Figure 39. PMMA systems from the previous work [25] (see Figure 6 above) prepared in ethyl acetate, acetone, acetone-toluene mixture, and toluene were also included in the evaluation. All of the solvents were basic, thus, they competed with PMMA for the interaction with the silica surface. However, the attraction between silica and PMMA was strong enough to let PMMA absorb onto the silica surface and stabilized the good dispersion after solvent evaporation. There was an excellent dispersion of individual nanoparticles in cyclohexanone, acetonitrile, ethyl acetate, and acetone accompanied by the presence of very small aggregates/clusters consisting of 2–5 particles with an average size of 30–34 nm. Poorer dispersion was observed in toluene and anisole. There were detected two populations of aggregates in PMMA prepared in toluene – smaller aggregates had an average size of 34 nm and a larger size of 244 nm. The size of nanoparticle aggregates in anisole was 320 nm. Acetone-toluene mixture (1:1 volume ratio) provided nanoparticle dispersion qualitatively fitting between the individual nanoparticle dispersion in acetone and nanoparticle aggregation in toluene yielding chain bound clusters with the size of approximately 70 nm.

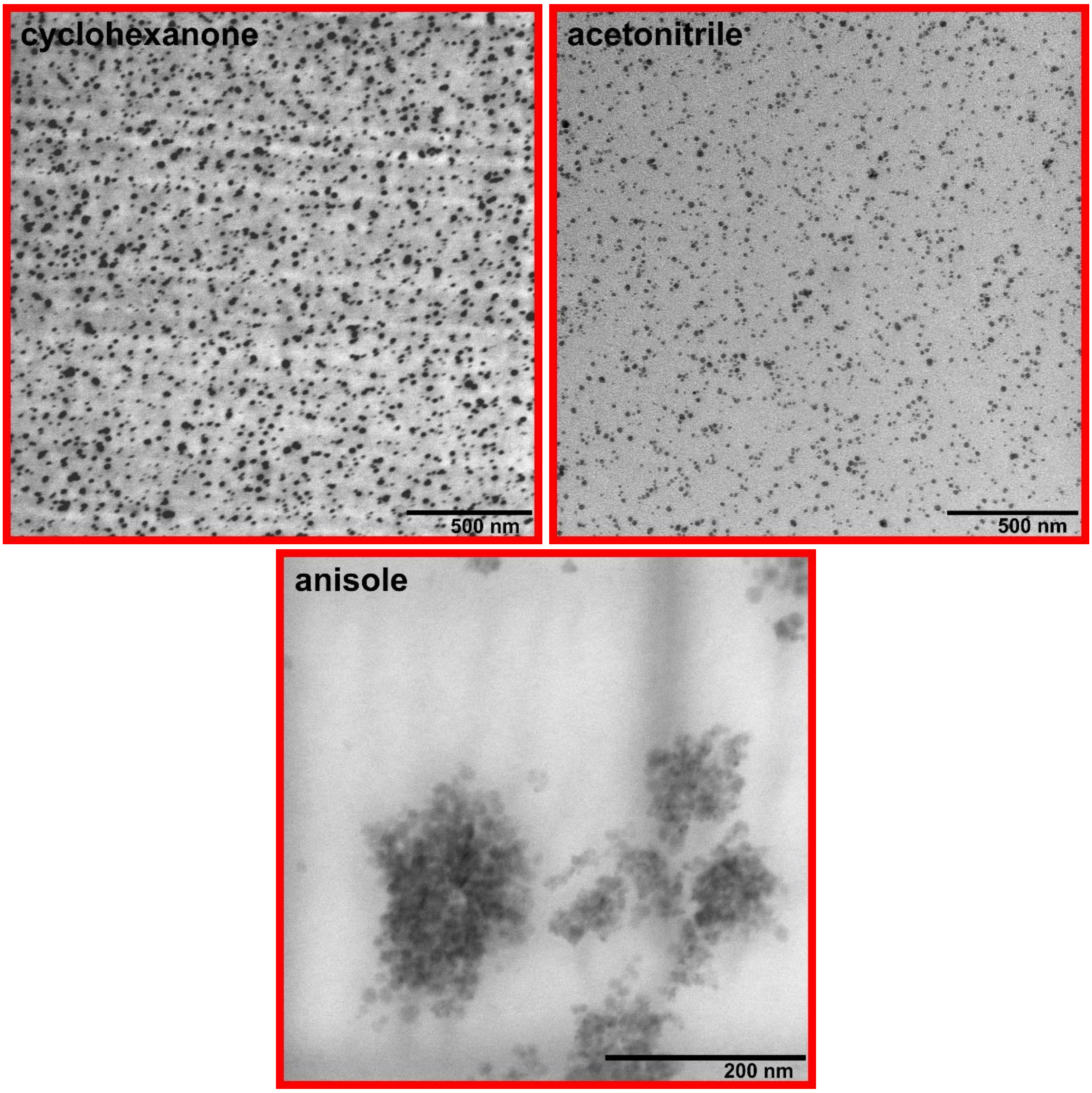

Figure 39: TEM images of PMMA nanocomposites with 1 vol. % of spherical silica prepared in different solvents – cyclohexanone, acetonitrile, and anisole.

In the case of PVAc samples (Figure 40) prepared in acetone, acetone-toluene mixture, and toluene, good dispersion of individually dispersed particles was fixed with accompanying by small chain bound clusters. The average size of agglomerates varied from 33 to 49 nm in these samples. PVAc chains were more rigid than PMMA samples (Kuhn length of PVAc chains was 2.5 nm, Kuhn length of PMMA chains was 2.1 nm [159]), thus PVAc chains were probably a stiffer hindrance for particles preventing massive contact aggregation and thus aggregates formed in PVAc were smaller than in PMMA at the same solvent conditions.

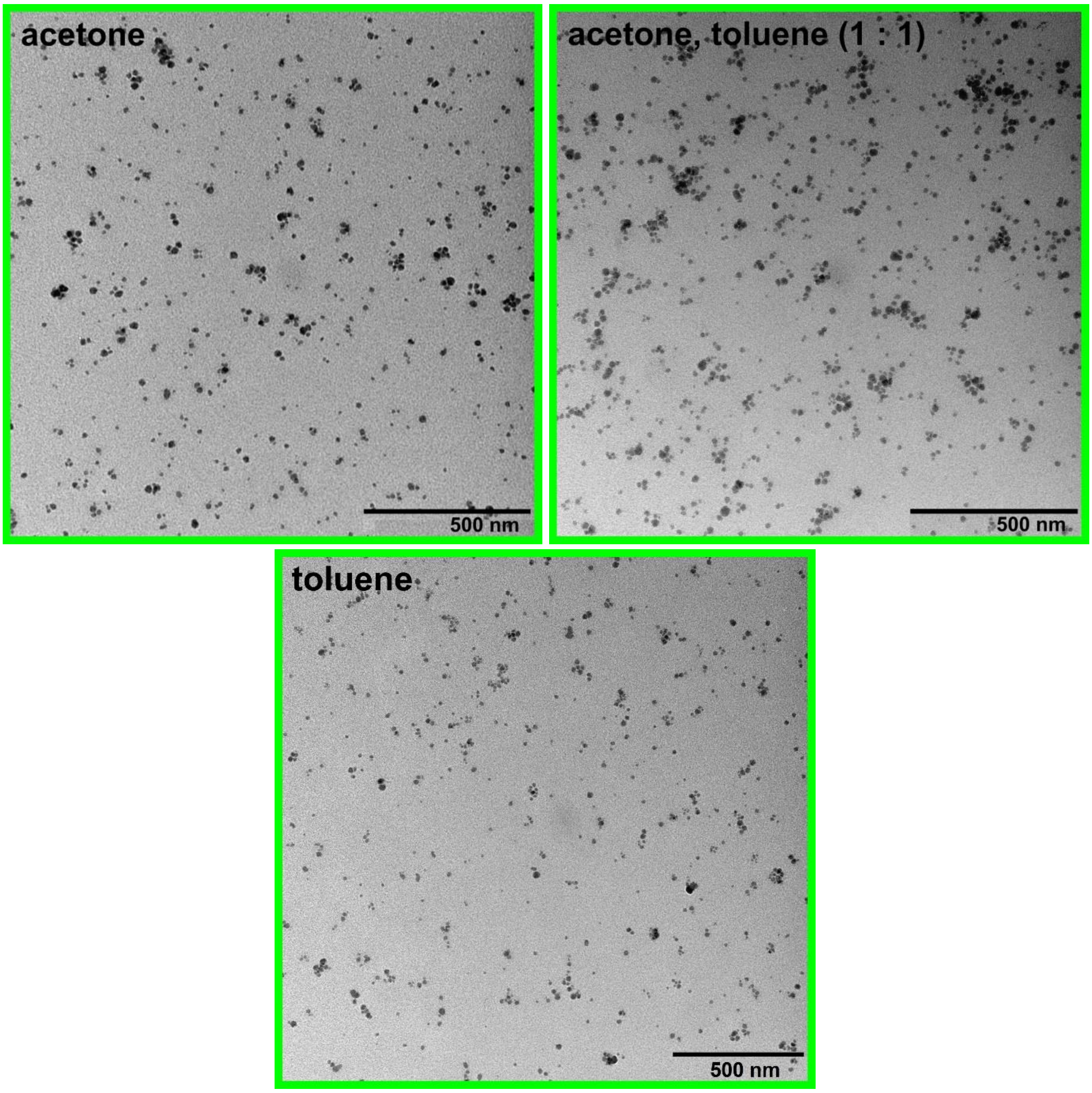

Figure 40: TEM images of PVAc nanocomposites with 1 vol. % of spherical silica prepared in different solvents – acetone, acetone-toluene mixture (1:1 volume ratio), and toluene.

5.1.1.3 General laws controlling morphogenesis in glassy nanocomposites

The only heteroatom present in the polymers investigated in this thesis (PC, PMMA, and PVAc except for PS with no heteroatom) was oxygen, which interacted with its free electron pairs as a proton acceptor (base). Hence, polymer chains and solvent molecules competed with each other over the acidic silica surface. The polymer-solvent interaction seemed to be one of the dominant parameters in the determination of the nanoparticle organization as will be shown below. Nevertheless, when nanoparticle-solvent interaction was weak, particle-particle and polymer-particle interaction strengths started to play a decisive role in the nanoparticle aggregation process.

The surface chemistry of nanoparticles was recognized as an important parameter influencing the polymer-particle interaction and, consequently, the quality of polymer nanocomposite dispersion. The solubility parameter δ of a particle relates to its surface properties rather than its bulk chemistry. Jouault et al. [30] suggested δ to be one possible criterion for the determination of nanoparticle dispersion in solvent cast polymer nanocomposites. They hypothesized that better solvent for polymer (i.e. difference of solubility parameter between solvent and polymer is very low) reduces dielectric constant $\varepsilon \rightarrow$ lowers dissociation of silanol groups (lowers ζ-potential) $\rightarrow$ lowers solvation shell and repulsive barrier around particles and contact aggregation may occur.

Nanosilica used in the current experiments contained bare particles with no surface modification. Therefore, the values for bulk silica were used to predict the nanoparticle dispersion state. Lepcio [41; 156] estimated Hansen solubility parameters [160] of silica from the critical concentration of a displacer co-solvent [161] to $(18.8 \pm 1.0)\ (\mathrm{J{\cdot}cm^{-3}})^{0.5}$, $(5.7 \pm 0.8)\ (\mathrm{J{\cdot}cm^{-3}})^{0.5}$, and $(6.3 \pm 0.8)\ (\mathrm{J{\cdot}cm^{-3}})^{0.5}$ for dispersive (energy from dispersion forces between molecules), polar (energy from the dipolar intermolecular force between molecule), and hydrogen bonding (energy from hydrogen bonds between molecules) partial solubility parameter, respectively. Hildebrant solubility parameter of bare silica δ_{silica} (spherical colloidal silica) could be then calculated as:

$$\delta_{\mathrm{silica}} = \sqrt{4 \cdot \delta_{\mathrm{D}} + \delta_{\mathrm{P}} + \delta_{\mathrm{H}}} = 20.6\ \mathrm{MPa}^{0.5}. \qquad (25)$$

According to this δ_{silica} value, the affinity of polymers to silica scales in the order PC > PVAc > PMMA > PS as determined by the difference in the solubility parameters of silica and appropriate polymer ($1 < 1.1 < 1.6 < 1.9\ \mathrm{MPa}^{0.5}$).

Following the acid-base competition theory, the polarity of the particles and the polymer must be taken into account. While the polarity of particles was fixed for all samples using the same silica nanoparticles, the polymer dipole moments were evaluated according to the dipole moments of their monomers. Methyl methacrylate monomer (PMMA) has a dipole moment of 1.67 D, vinyl acetate (PVAc) has a dipole moment of 1.79 D, styrene (PS) has a dipole moment of 0.12 D and the average of carbon acid and Bisphenol A (PC) dipole moment is 0.50 D. It has been previously reported [25; 30] that the dispersing solvent can control the nanoparticle spatial organization in polymer nanocomposites. Nevertheless, the current data of this work shows that the type of polymer matrix also had an essential effect on the resulting nanoparticle organization and the relative change in nanocomposite properties induced by nanoparticles. Therefore, all interactions between polymer-solvent-particle should be considered.

For the purpose of quantitative analysis, individually dispersed particles, aggregates, and clusters were considered as basic elements characterizing the actual nanoparticle dispersion. The size of all organization types formed in the structure of nanocomposites (individually dispersed particles, chain bound clusters, and agglomerates) was collectively called the size of the agglomerates d_{w} (calculation of d_{w} is described in paragraph 4.3.1). Size of elements d_{w} was divided by single nanoparticle diameter d_{sp} and related to the polymer-solvent interaction strength evaluated by the reciprocal absolute difference in the Hildebrand solubility parameters δ of solvent and polymer $1/|\delta_{\mathrm{solvent}} - \delta_{\mathrm{polymer}}|$ as shown in Figure 41.

There are at least two main regimes of nanoparticle organizational states as indicated by the two auxiliary solid lines in Figure 41. The systems with very low reciprocal absolute difference between the Hildebrand solubility parameters of solvent and polymer $1/|\delta_{\mathrm{solvent}}-\delta_{\mathrm{polymer}}|$ could be possibly attributed to the third independent mechanism as will be discussed later. In this region (bottom left corner in Figure 41), dispersion of individual particles is expected. At around $1/|\delta_{\mathrm{solvent}}-\delta_{\mathrm{polymer}}|$ of 0.6 MPa$^{-0.5}$, the dependence splits into two independent regimes. Systems on the lower curve keep a relatively good dispersion of individual nanoparticles, very small aggregates of approximately 2–8 nanoparticles or chain bound clusters (i.e. good dispersion in global), while the systems on the upper curve show a large systematic increase of element size with increasing $1/|\delta_{\mathrm{solvent}}-\delta_{\mathrm{polymer}}|$. A detailed characterization of the different nanoparticle self-assembly regimes will follow.

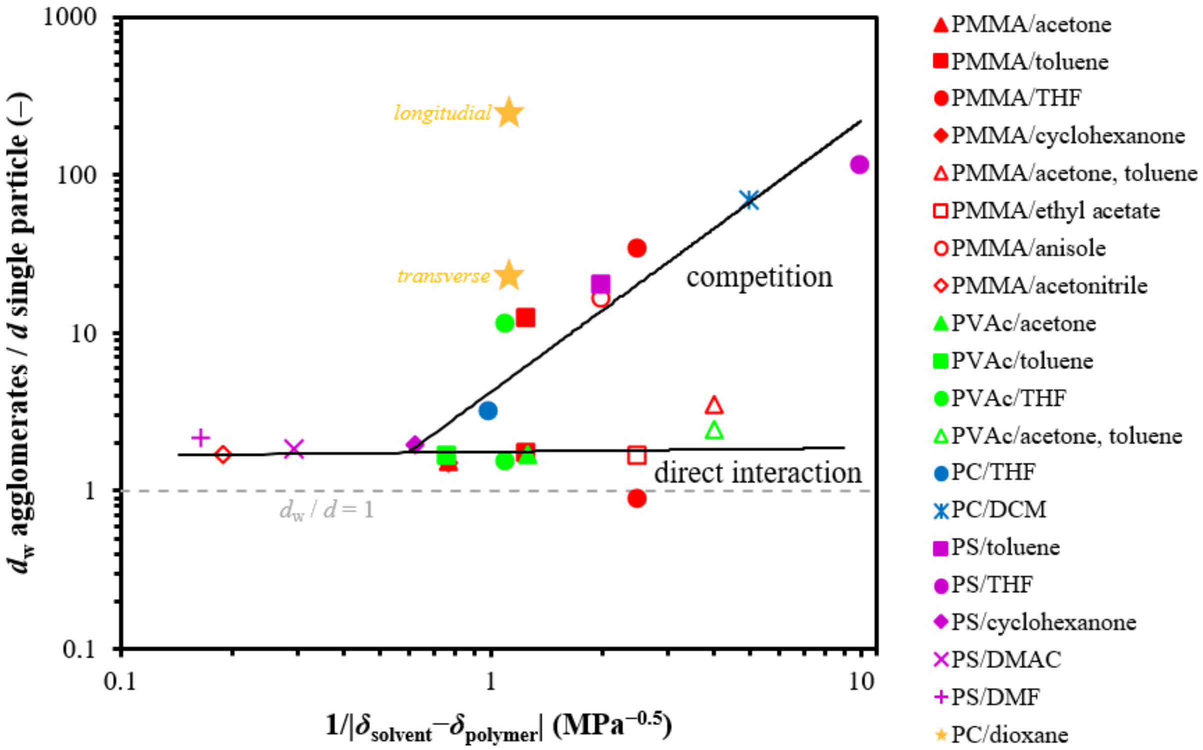

Figure 41: The ratio of agglomerate size d_w to the single-particle diameter d_{sp} for spherical nanosilica nanocomposites depicted as the dependence on the reciprocal absolute difference in the Hildebrand solubility parameters of solvent and polymer. The two populations of dispersed individual particles and aggregated populations in PMMA-THF and PVAc-THF and the two populations of small and larger aggregates in PMMA-toluene composites were plotted separately as two points for each system. The anisotropic microfibrous structure formed in PC-dioxane was a specific case and thus was not included in the trends defined by the solid lines. Raw data are available in the appendix.

It is supposed that the high negative charge on silica manifested by the high negative value of ζ-potential is caused by strong solvation. Therefore, in such systems, solvent-nanoparticle interaction won the competition against the polymer-nanoparticle counterpart for the particle surface and almost no polymer segments could adsorb. The current results are consistent with the previous study [25] which correlated the effective hydrodynamic volume of nanoparticles in a polymer solution and the enthalpy of the acid-base interaction between solvent and particle with the nanoparticle organization. Good dispersion was observed at intermediate solvent-particle interaction strength altogether with little to no traces of polymer adsorption shell as evidenced by the effective hydrodynamic volume. Suggestively, the dispersion stability could be attributed to the combination of the solvation shell and weakly absorbed polymer shell around the particles. This hypothesis is supported by many systems in the bottom left corner of Figure 41. All these systems showed a relatively low ζ-potential of less than –20 mV which corresponds to weak electrorepulsive stability as the threshold of incipient electrorepulsive stability of colloidal solutions is considered about ±10 mV. [162]

Strong particle-solvent interaction would normally provide a strong solvation shell and a good electrorepulsive stability, the solvent would act as a displacer preventing polymer adsorption on the nanoparticle surface. [30] However, in the presence of polymer, it reportedly caused a depletion attraction which could compromise the otherwise good dispersion of nanoparticles [25] as it can be seen on PC-DCM-silica system where large aggregates were found (Figure 41). PC had the strongest interaction strength with the silica surface of the investigated polymers, and yet, the aggregation tendency was imposed by an appropriate solvent. Hence, it is apparent that the polymer-particle interaction could be equaled or even outweighed by the role of solvent and the strong polymer-particle interaction alone is not always a sufficient condition to obtain a good dispersion of nanoparticles. The difference between the solubility properties of the competing polymer and solvent is the key parameter that, together with the particle-particle interaction assessed by ζ-potential, governs the nanocomposite structure. This finding is consistent with the seemingly superior importance of the solvent and the known significance of the polymer matrix.

Moreover, stabilization of good dispersion possibly relies also on the chain conformation rather than the surface interaction strength alone. With a larger difference in solubility parameters between solvent and polymer (or its small reciprocal value), the polymer coil was more packed, the radius of polymer coil r_{polymer} decreased (Figure 42A), as verified by DLS measurement (Figure 42C). Unlike other polymers, PS had an approximately constant coil radius in the investigated range of solvents. It could be possibly caused by its low polarity, relatively high molecular weight, chain rigidity, and polydispersity.

In the solution state, when the compact coil adsorbs on the surface of the silica, a stiffer layer of the modified matrix will be created around the particle and therefore another particle cannot access the first particle. The packed coil in a poor solvent adsorbs to one particle surface and forms a compact polymer shield layer which prevents direct particle-particle contact. Thus, a layer of an adsorbed polymer is formed around the particle, followed by a polymer bulk, thereby stabilizing good dispersion. Similar behaviour was observed by Jouault et al. [30] when they described the adsorption of poly(2-vinyl pyridine) (P2VP) onto nanosilica surface in MEK. The resulting “hairy” particles were sterically stabilized against agglomeration.

On the other hand, expanded coil (Figure 42B) in a good solvent (the small difference in solubility parameter or its large reciprocal value) can more readily act as bridging molecules and thus promote a couple of the particles over short distances and hold the particles together, creating clusters. Furthermore, more flexible expanded coil adsorbed on one particle is not such a difficulty to another particle to approach and create contact aggregation.

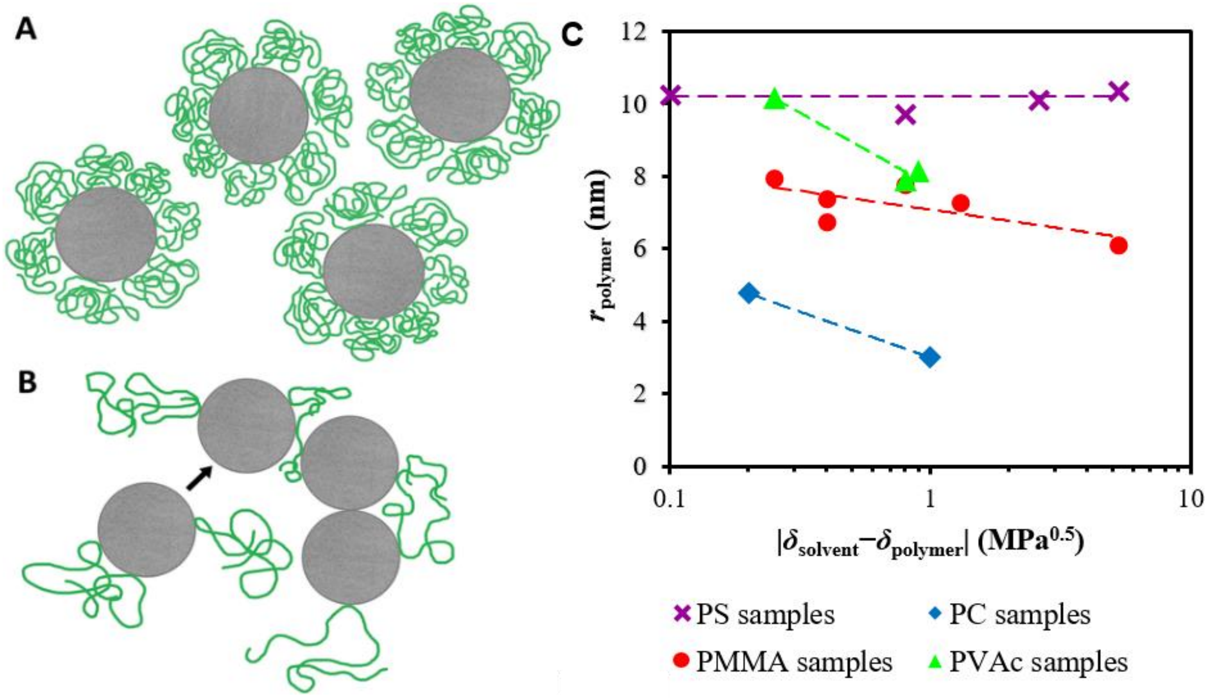

Figure 42: **A** – Nanoparticles with an adsorbed layer of compact polymer coils formed in a poor solvent. **B** – Nanoparticles with adsorbed flexible expanded polymer coils formed in a good solvent. Graph **C** – Radius of polymer coils in solutions of various solvents (determined by DLS) dependence on the difference of solubility parameter between solvent and polymer. Dashed lines are for eye guidance.

Low negative values of ζ-potential above −5 mV and below approximately −10 mV, which is the threshold for incipient electro-repulsive stability [162], allow for both particle-particle agglomeration and acid-base adsorption of polymer onto silica taking place simultaneously. The latter process led to a formation of an adsorbed polymer shell which could stabilize a relatively good dispersion while the former yielded large aggregates. Unlike the previous case, particle-polymer interactions seem to have an important role in this mechanism of nanoparticle assembly.

The stability of silica in toluene was such low (ζ-potential of −3.3 mV) that the polymer adsorption was competed by rapid nanoparticle contact aggregation. While this process was of a completely different nature than the depletion attraction, as was shown in the previous study [25], the formed nanocomposite structures followed in both cases a similar dependence on $1/|\delta_{solvent}-\delta_{polymer}|$ (Figure 41), though it is not clear whether this was a coincidence or a systematic behaviour.

Contact aggregates observed in toluene nanocomposites showed less symmetric and more chaotic organization which was possibly attributed to their kinetic origin compared to the thermodynamic one of the aggregates formed due to the depletion attraction. [25] Large aggregates were observed for PS-toluene system, which showed the lowest particle-polymer interaction strength and the greatest $1/|\delta_{solvent}-\delta_{polymer}|$ values of all the toluene samples. Two populations of aggregates were found in the PMMA-toluene system suggesting that lessened coil swelling and increased strength of surface interaction helped to prevent nanoparticle aggregation. Finally, polymer adsorption stabilized dispersion of individual nanoparticles and very small clusters/aggregates were formed in PVAc-toluene, where the matrix showed the lowest coil expansion and the strongest nanoparticle-polymer interaction.

Finally, dioxane was a special case since it was the only investigated solvent that acted as an acid towards the silica (ζ-potential of +0.4 mV), which means that dioxane and silica should compete together for the basic active sites of the polymer. Moreover, positively charged silica could catalyze the decomposition of dioxane to acetaldehyde and subsequent polymerization of acetaldehyde to oligomeric or polymeric (POE) chains which possibly leads to the exceptionally large nanoparticle assemblies. In silica-PC-dioxane nanocomposite, the 20 nm spherical nanosilica was assembled into 5 μm long microfibres with an aspect ratio of 11 and d_w/d_{sp} of about 250 and 23.5 for longitudinal and transverse direction, respectively. [158]

The solubility parameters represent the enthalpic parameters in the polymer nanocomposite solutions. It should be taken into account that the dispersion of nanoparticles in a nanocomposite system is also affected by entropic parameters, such as the molecular weight of the polymer matrix. The conclusion of this thesis is based on experimental data, thus the variation of molecular weight across all systems would be beyond the scope. Hashemi et al. [23] observed that the stability of a good dispersion increases with increasing molecular weight. Due to the larger number of entanglements on the longer chains, the nanoparticles do not have such an opportunity to diffuse freely through the system, and their aggregation is thus to some extent more suppressed. Jouault et al. [30] stated that in the case of really strong adsorption of polymer chains onto nanoparticles surface (e.g. due to strong hydrogen bonds between the silanol groups on the nanoparticle surface and the functional nitrogen groups in P2VP), the good dispersion in polymer nanocomposites is always achieved, independent of matrix molecular weight.

5.1.1.4 Nanocomposites with functional nanoparticles

The concept of the dependence of the size of the agglomerates on the solubility parameter was verified on systems with other nanoparticles (1 vol. % filling). The first one was fumed silica, having the same chemical composition as spherical colloidal silica, carried silanol groups on its surface so the same interactions occurred. The fumed silica varied from the spherical silica in size, geometry, and particle distribution – small 7 nm particles in fumed silica are rigidly sintered together to 70 nm large aggregates of irregular shape because of a fabrication process. Though the chemistry of colloidal and fumed silica was similar, their physical properties were very different to such an extent that these two types of particles often exhibited a completely different organizational behaviour. The second type of particles was functional semiconductive AZO particles having a similar particle size as spherical silica but they were slightly flattened, not strictly rounded. Basically, it differed in chemical composition (AZO particles are made of ZnO and 2 wt. % of Al_2O_3).

Nanocomposites filled with fumed silica prepared from PMMA in acetone and THF and from PVAc prepared in acetone are depicted in Figure 43. The best dispersion was reached in PMMA in acetone, it could be said, there were a lot of individually dispersed fumed silica particles with a few small aggregates, the average size of agglomerates was 112 nm. In PMMA-THF and PVAc-acetone, there were good dispersion of small aggregates of size 204 nm in PMMA and 183 nm in PVAc.

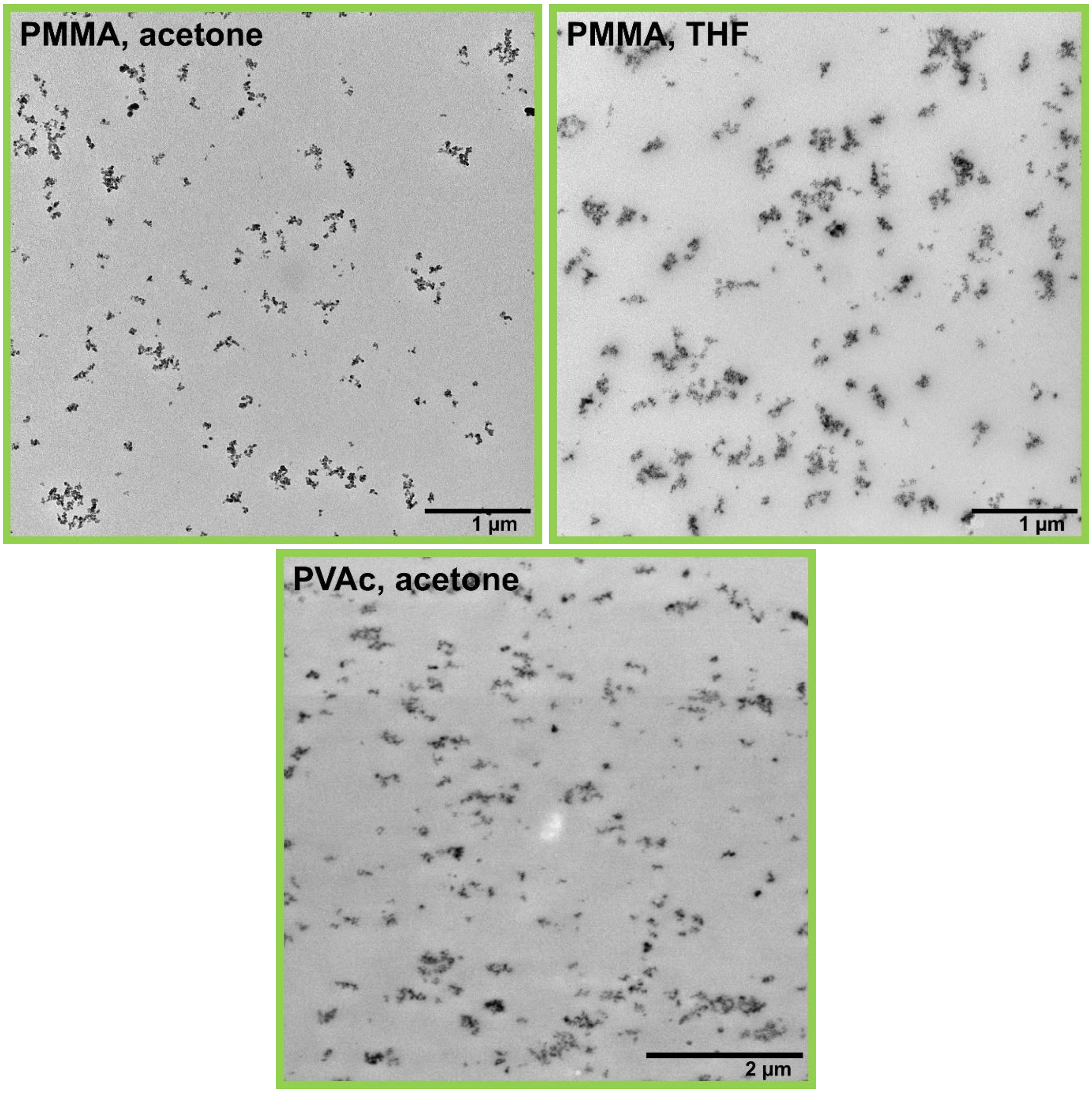

Figure 43: TEM images of nanocomposites with 1 vol. % of fumed silica in PMMA prepared in acetone and THF and PVAc prepared in acetone.

Nanocomposites with semiconductive AZO particles are depicted in Figure 44. AZO particles had a higher density than silica (density of silica is 2.2 g·cm^{-3}, the density of AZO particles is 5.6 g·cm^{-3}) so they were harder to disperse in solution and they tended to aggregate. Despite this fact, the particles were well dispersed in PMMA when acetone was used as a solvent. In addition to small aggregates, a large number of individual particles could be also recorded, an average size of agglomerates was 143 nm. Poor dispersion occurred in samples made of PMMA in toluene (size of aggregates 526 nm) and in PC made in THF (395 nm).

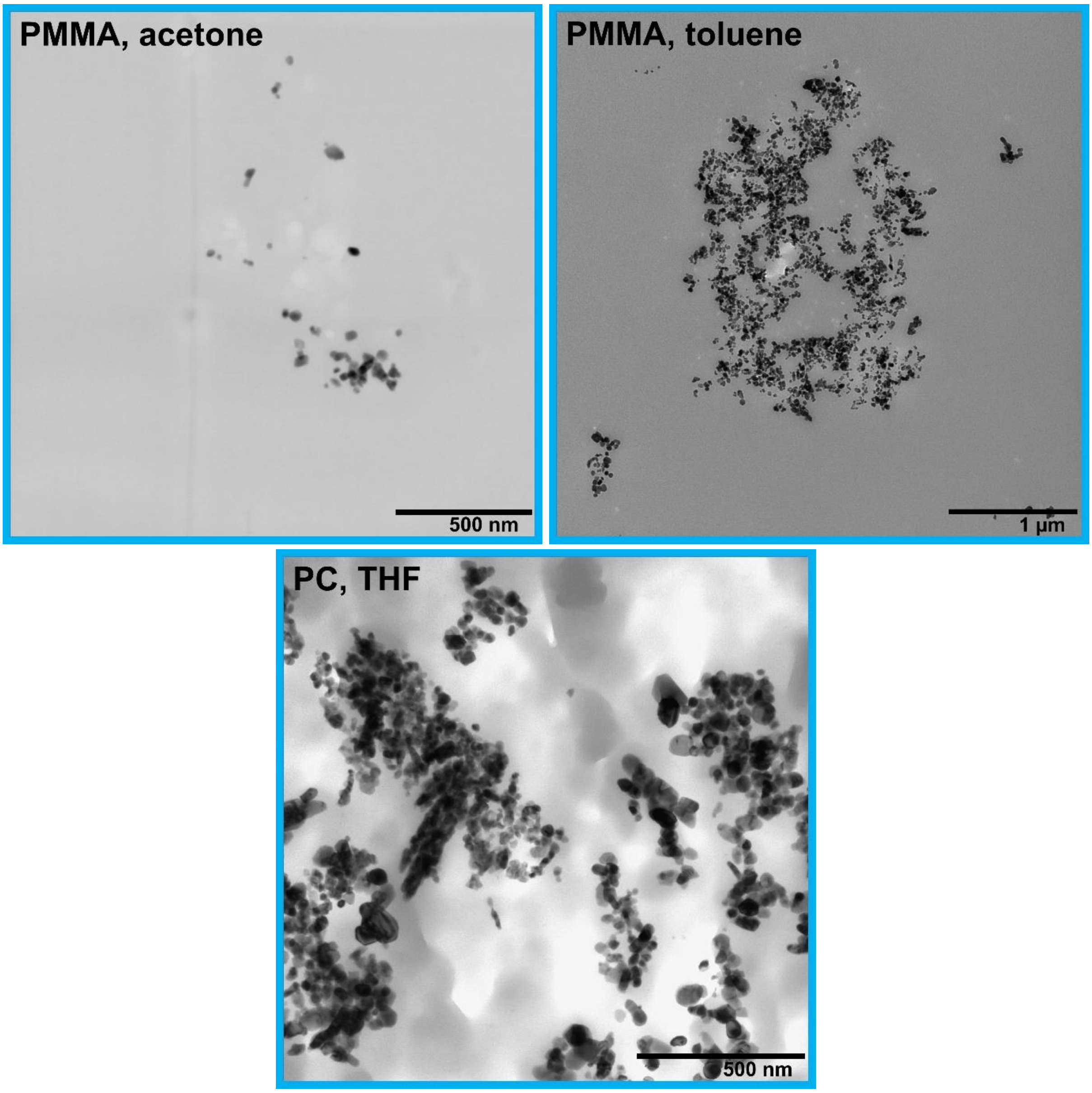

Figure 44: TEM images of nanocomposites with 1 vol. % of AZO in PMMA prepared in acetone and toluene and PC prepared in THF.

Fumed silica and AZO nanoparticles followed principally the same behaviour as colloidal silica (Figure 41). However, coherence with the proposed nanoparticle self-assembly mechanisms was observed. They fit into the dependence of agglomerate size divided by nanoparticle size $d_{\mathrm{w}}/d_{\mathrm{sp}}$ on the reciprocal value of the difference of Hildebrant solubility parameter between solvent and polymer $1/|\delta_{\mathrm{solvent}}-\delta_{\mathrm{polymer}}|$ previously shown for spherical nanosilica and the same trend was observed (Figure 45). The semi-empirical principle of governing the structure of nanocomposites in polymer glasses with different chemical compositions and different polarities was proved independently of the geometry and chemical composition of the nanoparticles.

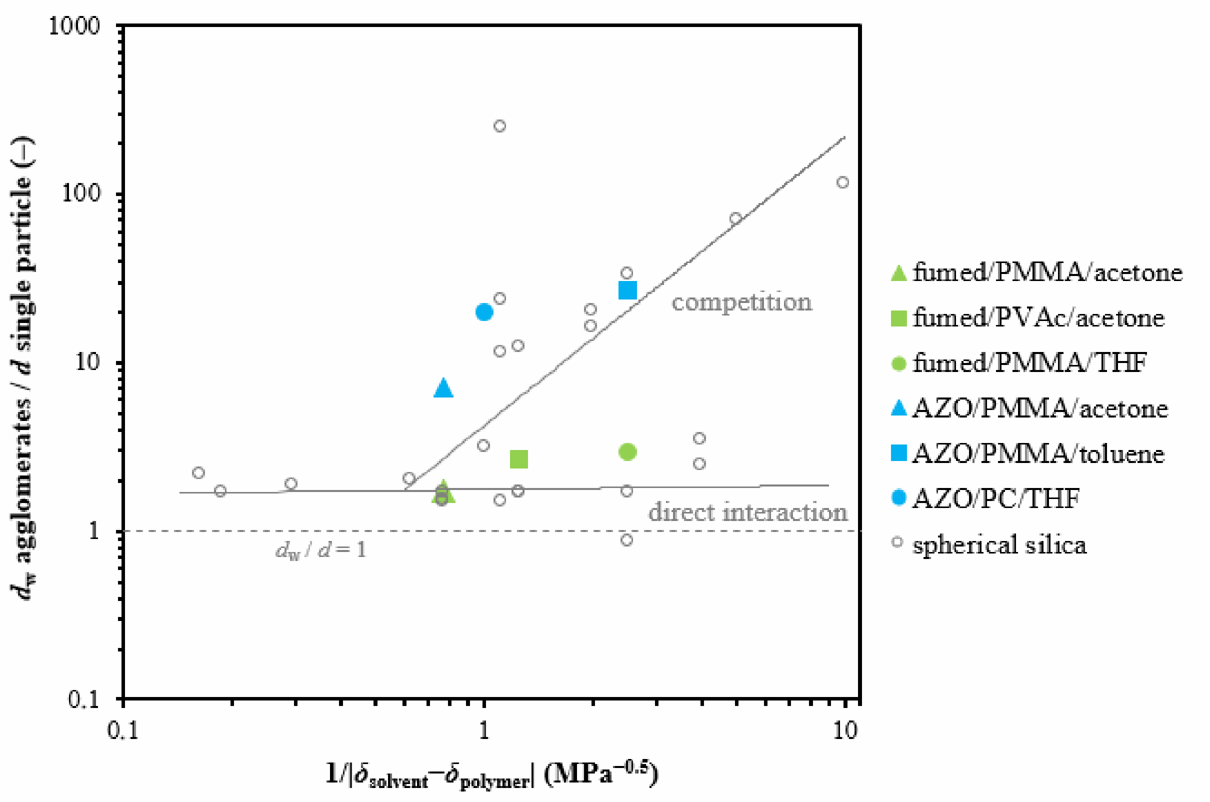

Figure 45: The ratio of agglomerate size d_w to the single-particle diameter d_{sp} for fumed nanosilica and AZO nanoparticles composites depicted as the dependence on the reciprocal absolute difference in the Hildebrand solubility parameters of solvent and polymer. Raw data are available in the appendix.

5.1.1.5 Relaxation properties of polymer nanocomposites

The different strengths of the nanoparticle-polymer and the solvent-polymer interaction also affected the thermomechanical properties of the investigated nanocomposites. The T_g of the nanocomposites prepared in the THF was determined employing the DSC (10 °C·min^{-1}) and compared to the glass transition temperature of the neat polymer matrices, $T_{g,\,matrix}$. The change of nanocomposite T_g from the $T_{g,\,matrix}$ was determined as:

$$\Delta T_g = T_g - T_{g,\,matrix}. \tag{26}$$

In agreement with the existing models, the T_g increased with increasing heating rates. Modified Arrhenius equation [163] can then be used for calculation of the activation energy of glass transition, $E_{A,\,Tg}$:

$$\ln q = \ln q_0 - \frac{E_{A,\,Tg}}{R} \cdot \frac{1000}{T_g}, \tag{27}$$

where q is the heating rate (K·min^{-1}), q_0 is the preexponential factor with the same unit as the unit of heating rate, R is the universal gas constant (J·K^{-1}·mol^{-1}). The $E_{A,\,Tg}$ (kJ) can be calculated from the slope of the linear dependence of the ln$q$ vs. $1/T_g$ plot. The relative $E_{A,\,Tg}$

was calculated by dividing $E_{A,\,Tg}$ of nanocomposite by activation energy of neat polymer matrix, $E_{A,\,Tg\,\mathrm{matrix}}$:

$$\mathrm{rel.}\ E_{A,\,Tg} = \frac{E_{A,\,Tg}}{E_{A,\,Tg\,\mathrm{matrix}}}. \tag{28}$$

Rel. E_A and ΔT_g were related to the absolute difference between the solubility parameters of solvent and polymer $|\delta_{\mathrm{solvent}}-\delta_{\mathrm{polymer}}|$ (Figure 47A). The increase of $|\delta_{\mathrm{solvent}}-\delta_{\mathrm{polymer}}|$ directly correlates with the decrease of the size of aggregates d_w as shown in Figure 41 and Figure 45. The function of rel. E_A, and ΔT_g on size of agglomerates d_w (Figure 46) was consistent with this finding. Therefore, further in the text, it is inherently considered that the increase of $|\delta_{\mathrm{solvent}}-\delta_{\mathrm{polymer}}|$ includes the decrease of d_w.

Although the individual particles in the PVAc-THF and PMMA-THF samples exceeded the aggregate population in frequency, a large number of primary particles with the inaccessible surface area were concentrated in the aggregates reducing the overall available active particle surface. Since this reduction had a significant effect on relaxation behaviour, the d_w values for PMMA and PVAc were taken from the larger of the two populations present in these systems.

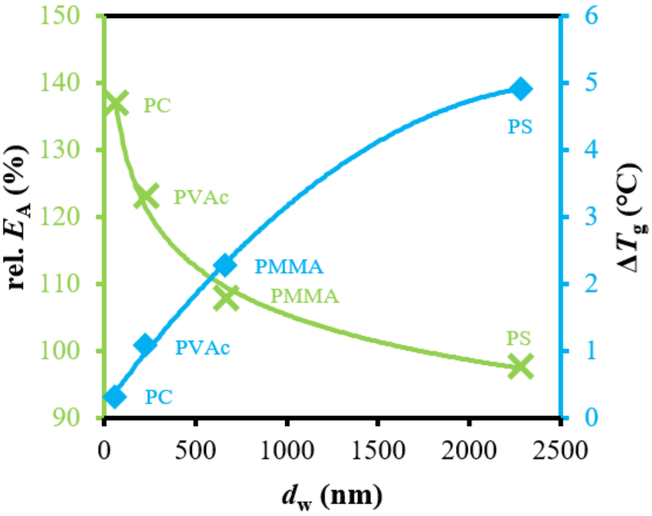

Figure 46: Dependence of the relative glass transition activation energy (E_A) and the increase of glass transition temperature (ΔT_g) on the element size d_w.

A gradual increase in rel. E_A accompanied the increasing $|\delta_{\mathrm{solvent}}-\delta_{\mathrm{polymer}}|$, i.e., decreasing element size d_w as expected. Polymer chains formed an affected polymer layer with retarded molecular packing and dynamics around the solid surface of particles due to the attractive interactions. [11; 25] The effective interfacial surface increases with increasing $|\delta_{\mathrm{solvent}}-\delta_{\mathrm{polymer}}|$ (decreasing d_w); therefore, the number of polymer chains with retarded dynamics also increased for smaller particles and so did the energy expenditure required for the release of chain segmental scale movement. However, ΔT_g grew with decreasing $|\delta_{\mathrm{solvent}}-\delta_{\mathrm{polymer}}|$ (increasing d_w) despite it was expected that ΔT_g should follow the same trend as rel. E_A and increase with increasing the effective interfacial area. [11; 25; 164; 165; 166; 167; 168; 169]

Nevertheless, the previous investigations were performed on a system with constant chemical composition and the interfacial area controlled via nanoparticle concentration. Therefore, the strength of the silica-polymer interactions expressed by the solubility parameters (Figure 47B) was investigated. It was expected that the attraction between the particle surface and the polymer chains was stronger for lower values of the absolute difference $|\delta_{\mathrm{silica}}-\delta_{\mathrm{polymer}}|$. PC had the strongest attraction to the nanosilica surface while PS had the weakest. Rel. E_{A} increased with the increasing interaction strength in accordance with expectations; however, ΔT_{g} followed the opposite trend again.

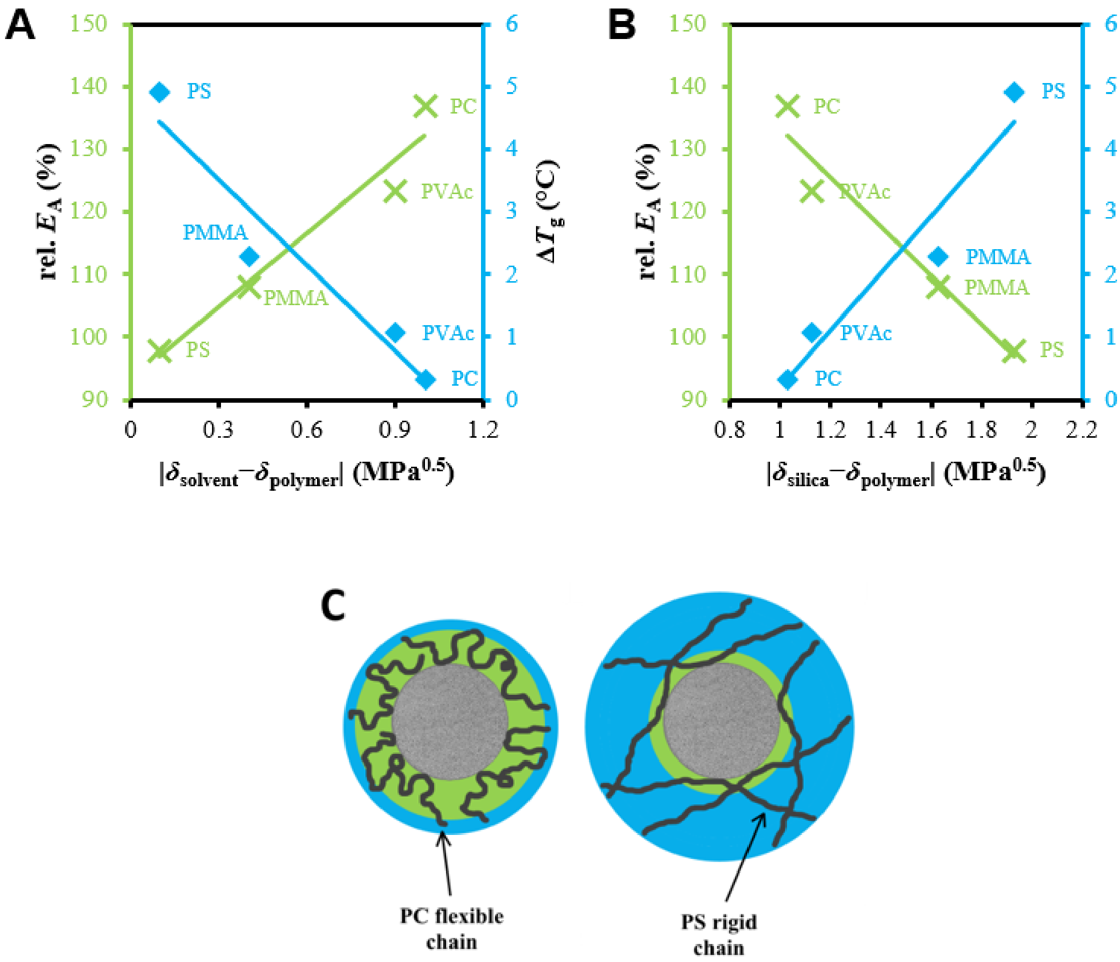

Figure 47: **A** – Dependence of the relative activation energy of glass transition (E_{A}) and glass transition temperature (ΔT_{g}) on the absolute difference in solubility parameters of solvent and polymer and **B** – on the difference in Hildebrand's solubility parameters of silica and polymer. Raw data are available in the appendix. **C** – An illustrative picture shows the difference between the adsorption of flexible PC chains and rigid PS chains onto nanoparticle surface, green color represents the immobilized layer, blue color represents the frustrated layer.

Before further interpretation, it would be useful to recall the detailed physicochemical situation of the affected polymer layer [11; 25; 164] (Figure 47C) and the mechanisms of chain interaction with nanoparticle surface [170; 171; 172; 173; 174]. It is assumed that the affected polymer layer around nanoparticles consists of the immobilized and frustrated polymer layer. The immobilized polymer layer consists of tightly adsorbed polymer segments that directly adheres to the surface of the nanoparticle with greatly retarded chain dynamics and a typical thickness of 1–3 nm [59; 175; 176; 177] while the frustrated layer is formed by chains interacting with the immobilized polymer layer via intramolecular (chain connectivity) or intermolecular (entanglements) interaction. [11; 178] The packing of the frustrated layer is also influenced, and its dynamics retarded, but to a much lesser extent compared to the immobilized layer. On the other hand, the thickness of the frustrated layer is larger (10–20 nm) [28; 164; 177; 179], thus, it occupies a larger overall volume of the material.

Tannenbaum and Ciprari et al. [170; 171] assumed that polymers with a strong attraction to the particles tend to adsorb with a larger number of their segments, possibly forming trains on the nanoparticle surface. Subsequently, they form short loops and do not affect a large number of surrounding chains due to short effective length and a frustrated layer. Weakly binding polymers prefer the adsorption of only one or a very few segments and form long loops with long effective length forming a large frustrated layer.

Cheng et al. [172] investigated the dependence of the thickness of the interfacial layer between the polymer matrix and the polymer rigidity defined through the characteristic ratio C_∞. They revealed that the thickness of the interfacial layer and length scale of dynamic heterogeneity in polymer nanocomposites increased with increasing polymer C_∞. Jouault et al. [173] determined a greater amount of bound polymer for weakly interacting PS than for attractively interacting PMMA matrix in a series of nanosilica filled nanocomposites.

Generalizing the results of this dissertation work altogether with the other available data, it was assumed that the interaction strength and chain conformation (stiffness) control the size of the affected polymer layer and the thickness ratio between the immobilized and the frustrated layers within it. Moreover, it was suggested that glass transition temperature T_g and activation energy E_A are susceptible to individual layers in different ways. Rel. E_A is assumed to be susceptible mainly by the properties of the immobilized layer formed by adsorbed polymer segments that directly adhere to the nanoparticle surface. The stronger the interaction between polymer and silica was, the thicker the immobilized layer with more retarded dynamics was formed. In turn, more energy was required to release the chain conformations. The rel. E_A scaled in the following order: PC > PVAc > PMMA > PS which agrees well with the proposed hypothesis. ΔT_g is expected to be primarily dependent on the properties of the frustrated layer. [164] Flexible chains (like PC) did not transfer the immobilization retardation over long distances; hence, the frustration layer was rather thin. In contrast, the rigid PS chains transferred the retardation furthest to the bulk polymer more effectively and the frustration layer around the nanoparticles was thicker, shifting the glass transition to the higher temperature. Confirming the hypothesis, chain flexibility, and interaction strength decreased while ΔT_g increased in the following order: PC > PVAc ≥ PMMA > PS. PC had the most flexible chains, which characteristic ratio C_∞ is 2.4, the characteristic ratio of PVAc and PS is 8.9 and 10.2, respectively. PMMA's C_∞ is dependent on the chain tacticity – isotactic PMMA has $C_\infty = 9.2–10.7$, syndiotactic 7.3–8.4 and atactic PMMA is assumed to have the greatest stiffness. [180] The PMMA used in this study was atactic with a high portion of syndiotactic chains. [181] In the light of the presented evidence, the widespread simple expectation that strong polymer-particle interactions yield the best possible enhancement of all thermo-mechanical properties seems no longer valid. More likely, the complex interplay of several mechanisms operating at the nano-scale has to be considered. This complex situation can be easily solved by taking the various thicknesses of immobilized and frustrated layers into account.

5.1.2 Nanocomposites with HIPS matrix

5.1.2.1 Solvent-casted HIPS nanocomposites

For the preparation of HIPS nanocomposites, the cyclohexanone, DMAC, and DMF solvents were used (in these solvents, the best dispersion of small silica clusters in the glassy PS phase was achieved.). The solubility of HIPS in these three solvents was different. Cyclohexanone dissolved both, the PS matrix and rubber particles, but DMAC and DMF dissolved just the PS matrix selectively. The different behaviour of the HIPS in the solvents was examined by DLS (Figure 48). Particle size in each solution was measured. In every solution, there were two populations of particles – small polymer coils of the size of tens of nanometers and larger undissolved rubber particles of micrometer size.

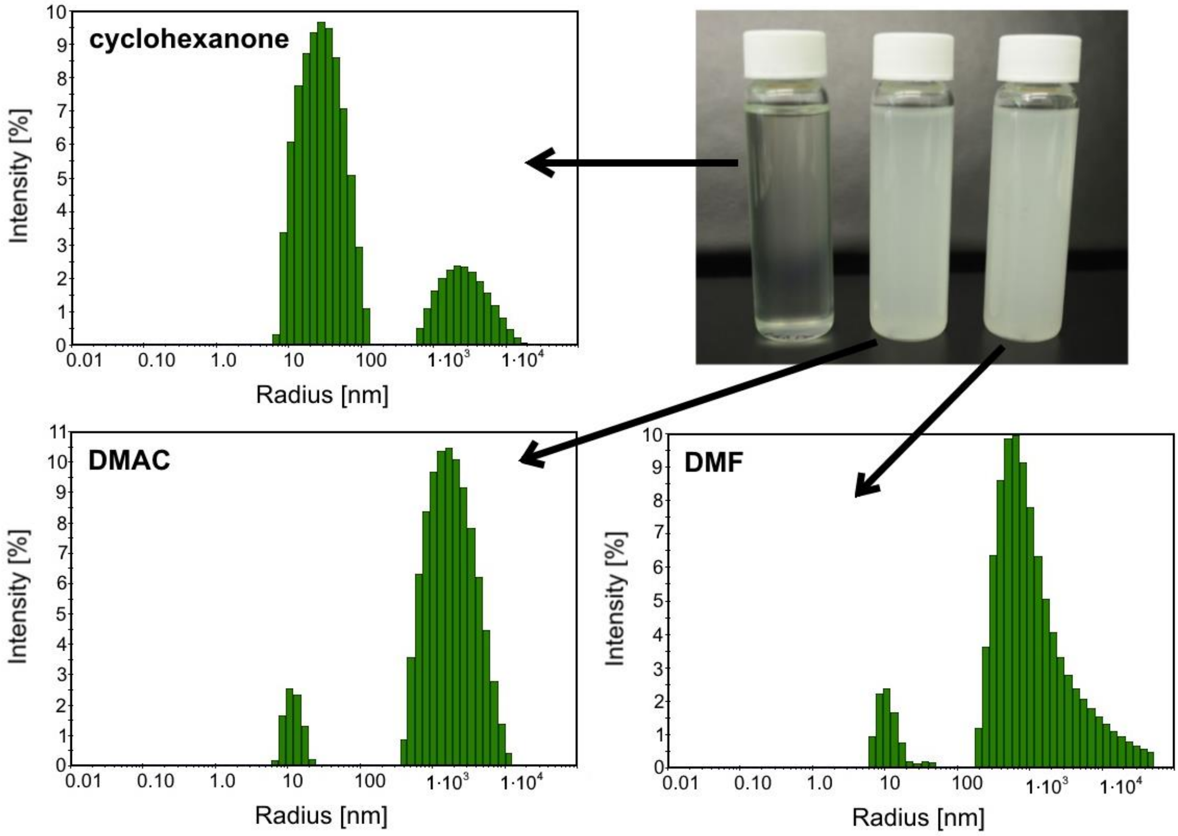

Figure 48: Representative DLS histograms of the size of HIPS components in solutions of three different solvents – cyclohexanone, DMAC, and DMF, supplemented with a photo of each solution.

The cyclohexanone solution was clear when viewed with the naked eye. From DLS histogram, it is evident that the ratio of the intensity representing polymer coils significantly exceeded that of the rubber particles. Thus, most rubber particles were dissolved into individual polymer chains dispersed homogeneously in colloidal solution. The average gyration radius of polymer coils was 31.7 nm (corresponding to molecular weight 1 078 kg·mol^{-1}) which points to the released large crosslinked rubber macromolecules. The average radius of rubber particles was 3.5 μm.

The HIPS solutions in DMAC and DMF were white turbid when viewed with the naked eye. Thus, there were undissolved micrometer particles in the solutions. The average gyration radius of polymer coils measured by DLS was 11.2 nm ($M_w \approx 164$ kg·mol^{-1}) in DMAC and 10.2 nm ($M_w \approx 140$ kg·mol^{-1}) in DMF, which was significantly smaller compared to the cyclohexanone. In the DMAC and DMF, only lower molecular weight PS was dissolved, but in cyclohexane, both the PS and PBR, which had a higher molecular weight due to crosslinking, were released into solution. The average rubber particle size was 2.5 μm in DMAC and 3.0 μm in DMF.

HIPS with 1 vol. % of spherical silica was prepared using these three solvents and the effect of selective solubility of rubber domains during solvent-casting was investigated (Figure 49 to 51). In general, a homogeneous dispersion of small clusters was achieved in all three types of solvents. The structure of the HIPS copolymer itself did not change, retaining both solid and occluded particles of the same size as in pure HIPS. Differences occurred in the deposition of nanoparticles at the polymer interface and within the rubber particles.

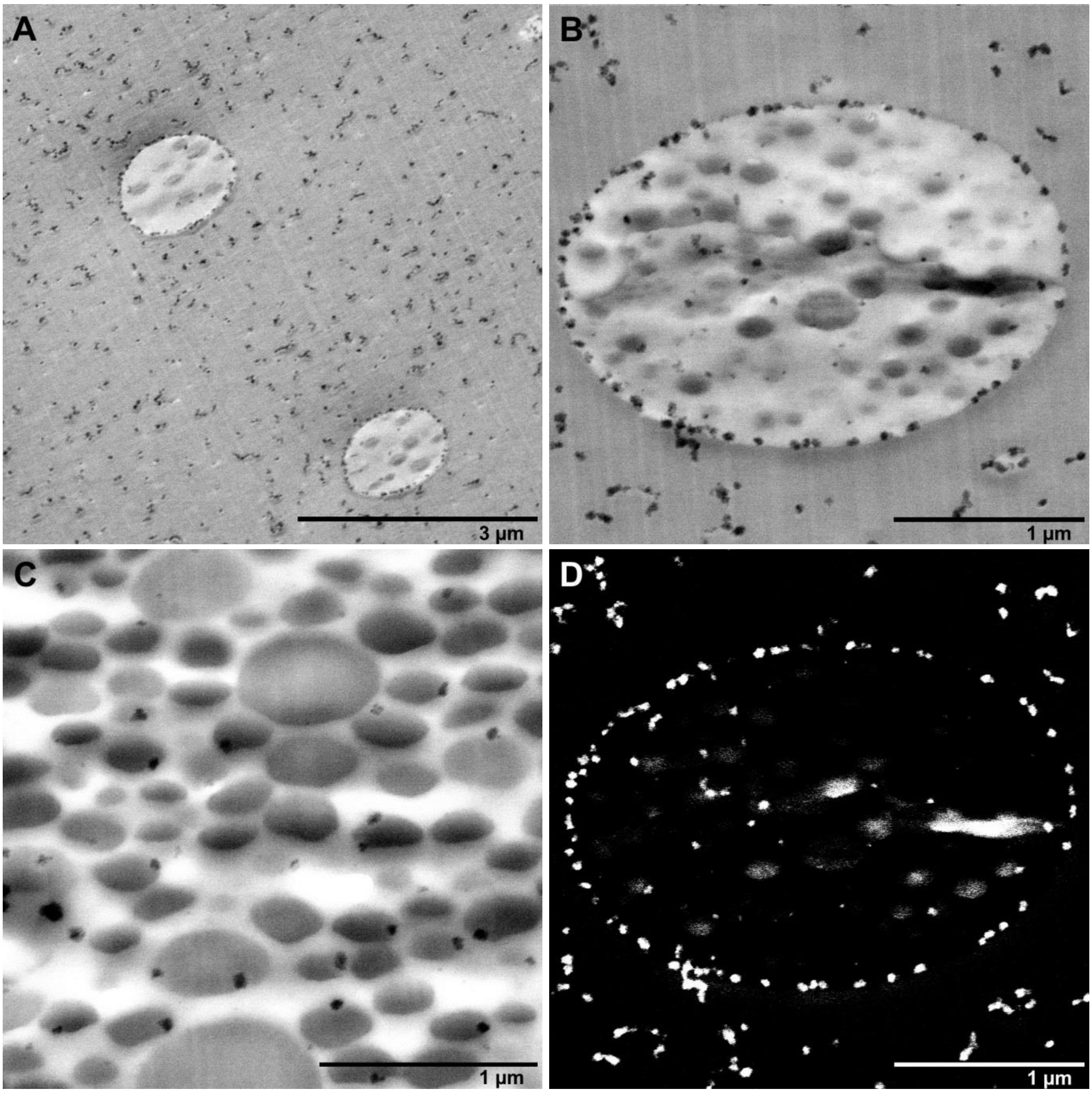

Figure 49: TEM images of HIPS nanocomposite prepared in cyclohexanone with 1 vol. % of spherical silica. **A** – Overview of good dispersion. **B** – Occluded particle detected in BF mode. **C** – Detail inside of occluded particle. **D** – Occluded particle detected in DF mode.

Very good dispersion of nanosilica was achieved in cyclohexanone. Small clusters containing less than 10 particles accompanied by individually dispersed particles were formed and homogeneously distributed in the PS matrix (Figure 49A). Furthermore, small spherical silica individual particles were deployed at the PS-rubber interface of solid (pure rubber domains) and occluded (larger rubber particles with incorporated smaller PS domains) particles (Figure 49B, D). Silica was deposited at the interface as a monolayer. In the case of cyclohexanone, nanosilica also penetrated into the rubbery domains, where it was arranged mainly at the interface of rubber and PS occlusions. Within rubbery domains, only individual nanoparticles were observed with no clusters. Particles did not penetrate into solid rubber particles. Hence, silica was preferentially deposited in the PS parts of the copolymer rather than in rubber parts. This may be due to the fact that the rubber was partially crosslinked and therefore the particles were more difficult to diffuse between the PBR network. PS and rubber are both non-polar with no heteroatoms so their miscibility with silica should be at a similar level but they differ in solubility parameter values – δ for PBR is 17.0 MPa$^{0.5}$ and for PS is 18.7 MPa$^{0.5}$ which is closer to silica 20.6 MPa$^{0.5}$.

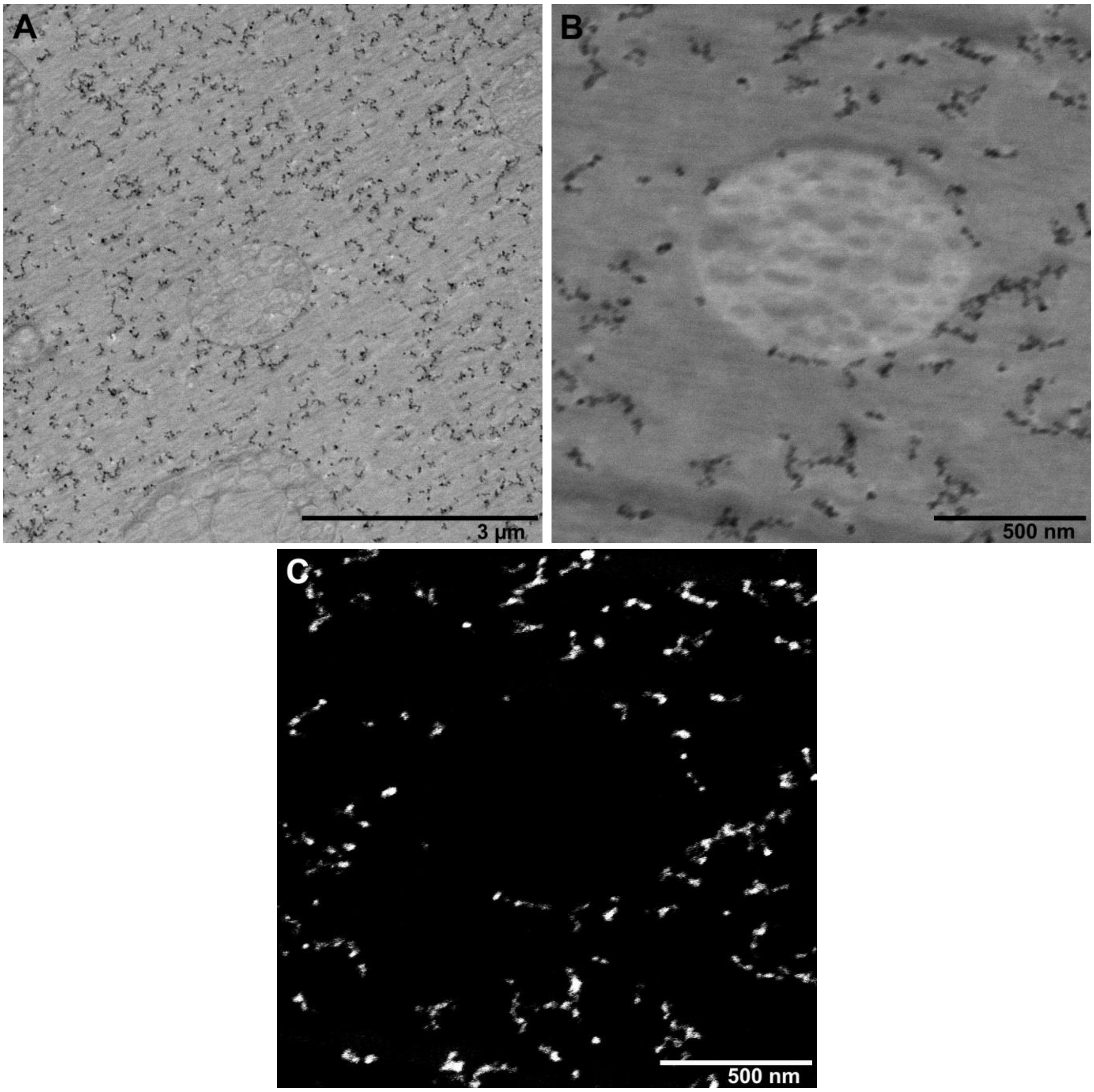

Figure 50: TEM images of HIPS nanocomposite prepared in DMAC with 1 vol. % of spherical silica. **A** – Overview of good dispersion. **B** – Occluded particle detected in BF mode. **C** – Occluded particle detected in DF mode.

HIPS nanocomposites with spherical silica prepared in DMAC (Figure 50) and in DMF (Figure 51) exhibited very similar morphologies. Both were prepared in solvents that dissolve PS matrix selectively and did not dissolve rubber particles. Thus, the state of nanosilica dispersion in the PS matrix was equal to cyclohexanone – good homogenous dispersion of small clusters, just in the case of DMAC and DMF the clusters were slightly larger (containing up to 20 particles) and no individually dispersed particles were observed. Unlike cyclohexanone, no silica particles were able to penetrate into undissolved rubber particles, neither solid nor occluded. Furthermore, there was no coherent adjoining layer of nanoparticles on the PS-rubber interface. The rubber particles became inaccessible for nanosilica assembling in a selective solvent.

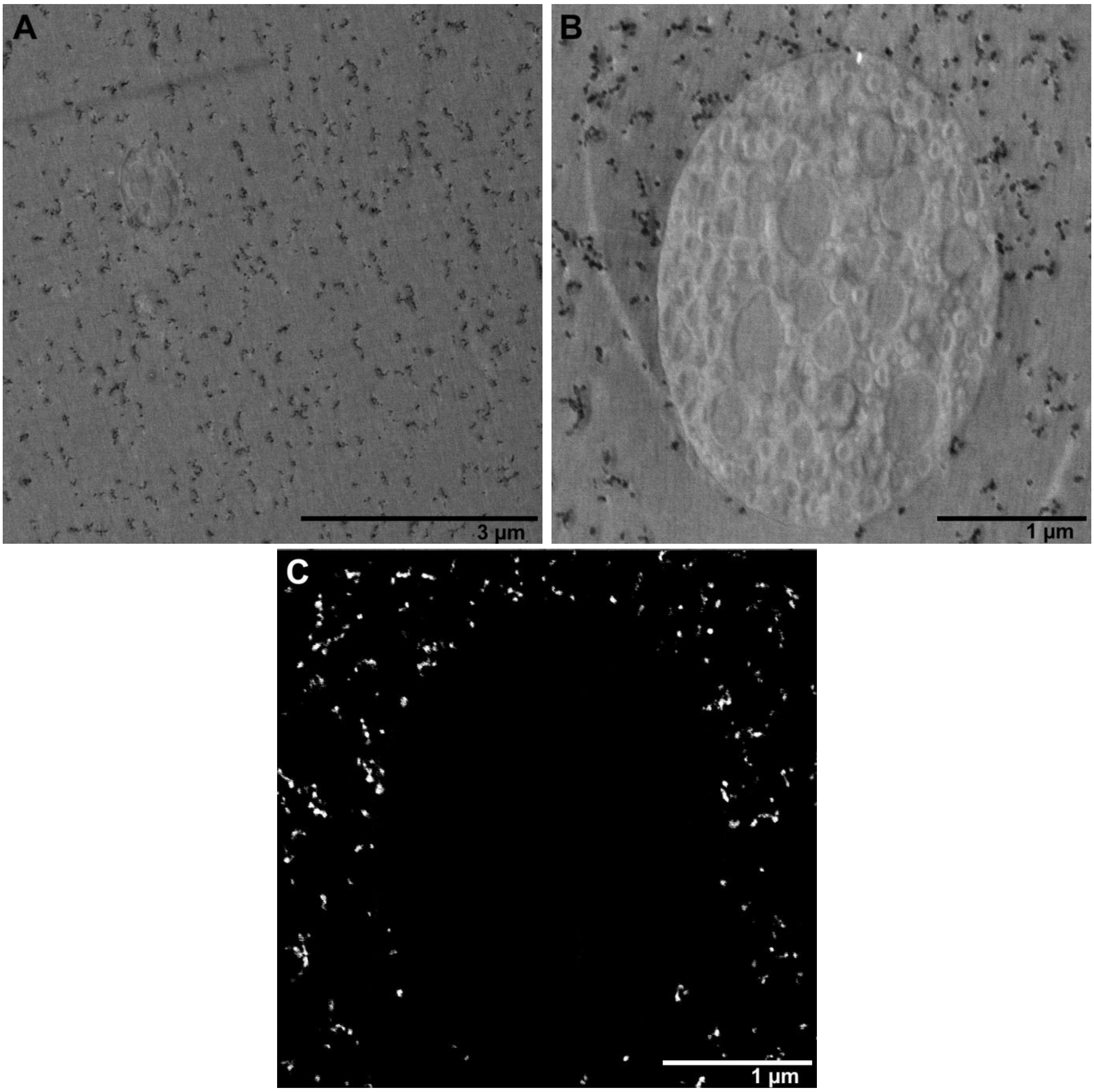

Figure 51: TEM images of HIPS nanocomposite prepared in DMF with 1 vol. % of spherical silica. **A** – Overview of good dispersion. **B** – Occluded particle detected in BF mode. **C** – Occluded particle detected in DF mode.

Spherical silica was relatively small (10–15 nm) and with its rounded shape had a prerequisite for easy incorporation even in the worse accessible copolymer particles. Fumed silica (70 nm) with its irregular shape was also examined to compare the potency of non-selective solvent (cyclohexanone) to incorporate silica nanoparticles into rubber particles. Nanocomposite series prepared in cyclohexanone, DMAC, and DMF were investigated again. All HIPS nanocomposites with fumed silica are shown in Figure 52. Not in one case larger fumed silica penetrated into rubber particles. Also, the state of nanoparticle dispersion changed. In cyclohexanone, there stayed homogenous dispersion of small aggregates. But in DMAC and DMF, there was spotted more extensive aggregation and inhomogenous spacing of particles in the samples leading to the formation of particle-rich areas with aggregates and particle-poor areas with no silica. It could be considered, that sufficiently small particles with spherical geometry and non-selective solvent are needed to incorporate silica into the rubber particles of PS-rubber copolymer.

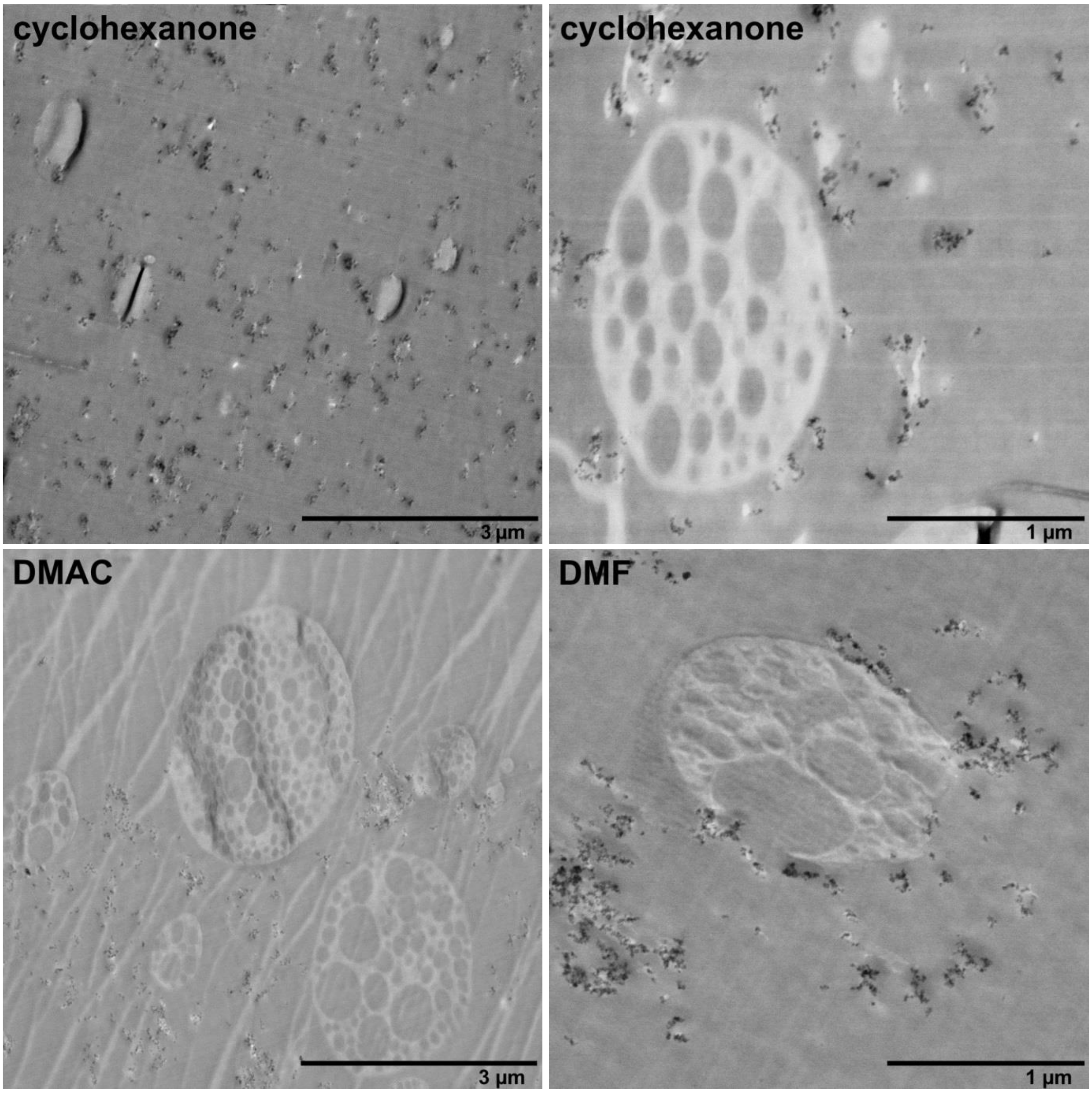

Figure 52: TEM images of HIPS nanocomposites with 1 vol. % of fumed silica prepared in cyclohexanone (**upper left** – overview of good dispersion, **upper right** – detail of occluded particle), in DMAC (**bottom left**), and in DMF (**bottom right**).

5.1.2.2 Melt-blended HIPS and PS nanocomposites

To simplify the preparation protocol, many experiments were first performed with fumed silica particles incorporated into the HIPS using melt-blending. Powdered fumed silica was first mixed with molten HIPS in a mixer (melt temperature 150 °C, 60 rpm) and then processed to form a filament employing a single-screw extruder (melt temperature 170 °C, 25 rpm). The direct mixing of the silica powder and HIPS in the single-screw extruder did not homogenize the materials sufficiently and the silica aggregation was noticeable to the naked eye, therefore, it was necessary to pre-homogenized materials in the mixer. The structure of the resulting sufficiently homogenized nanocomposite is shown in Figure 53. The dispersion of nanoparticles in the melt-blended systems was significantly impaired compared to the samples prepared by solvent-casting. The sample contained homogeneously dispersed small contact aggregates, which were occasionally accompanied by large spherical aggregates with a diameter of several microns. By simple melt-blending, the nanoparticles were not effectively separated and aggregates were still present, but to observe the effect of nanoparticles on the structure of the nanocomposite foam, in which the pores were in the order of tens to hundreds of micrometers, the dispersion prepared by the melt-blending method was sufficiently fine and homogeneous. The rubber particles in HIPS were often torn out and left a hole when melt-blended samples were cut at ultramicrotome (preparation of samples for STEM or TEM observation). This was inappropriate for some image analysis because it was not clear, if the hole was made by thorning out the rubber particle or if it was a pore made by the foaming agent. The melt-blended nanocomposite from homopolymer PS without rubber particles with fumed silica was made for the accuracy of image analyses described in paragraph 5.2.5 in detail.

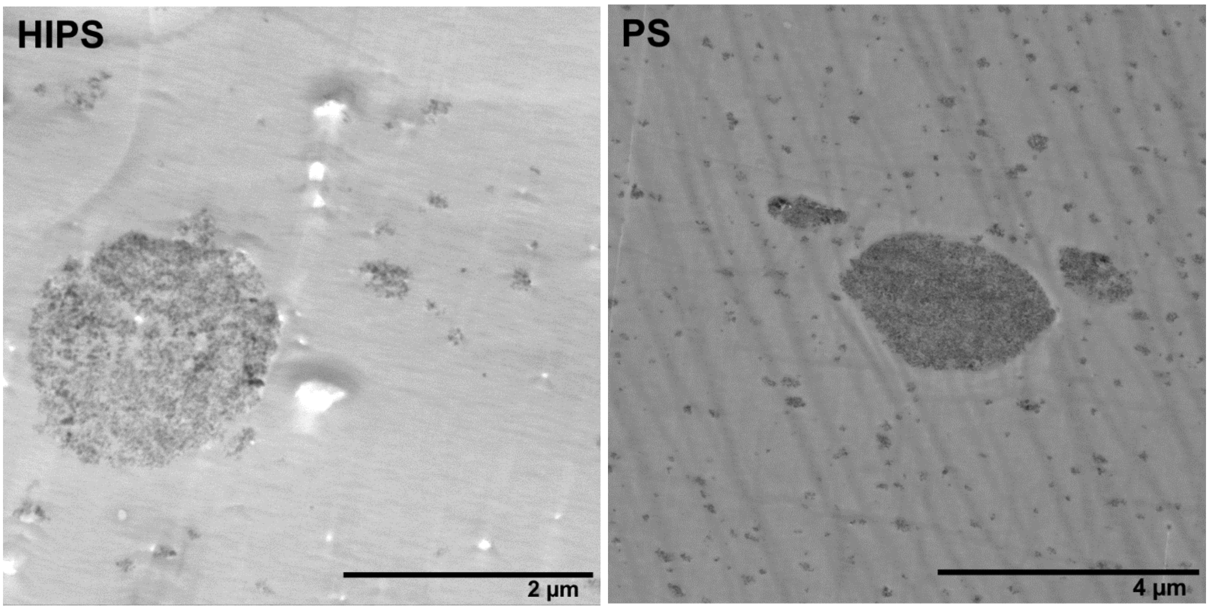

Figure 53: TEM image of nanocomposite with 1 vol. % of fumed silica prepared by the melt-blending method. **Left** –HIPS sample with the holes caused by the rupture of the rubber particles during ultramicrotome cutting. **Right** – Homopolymer PS.

5.2 Structural and thermal analysis of foams

5.2.1 Structure evolution during preparation

To precisely control the preparation process, the structure of the prepared materials was monitored after each step. The analysis was performed for the neat HIPS filled with 2 wt. % of azodicarbonamide. The dispersion of the blowing agent particles after extrusion is shown in Figure 54. The monoclinic crystals of azodicarbonamide were more or less uniformly distributed in the HIPS matrix.

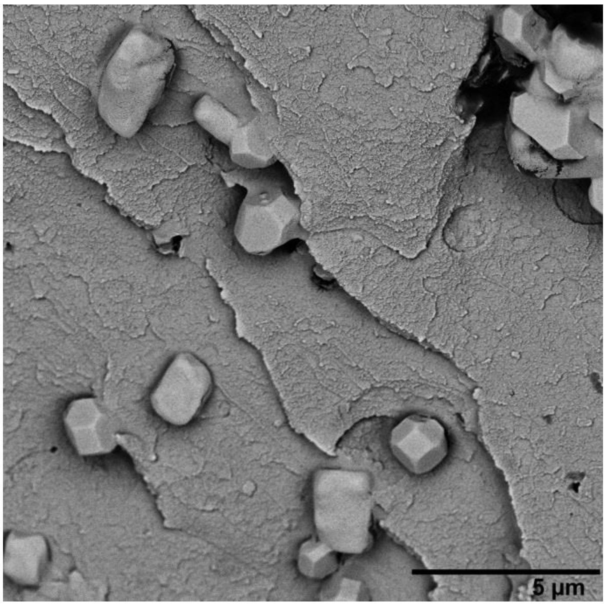

Figure 54: Dispersion of 2 wt. % of foaming agent azodicarbonamide in the HIPS matrix. SEM photo.

Due to local overheating caused by shear friction during the single-screw extrusion of a filament for the 3D printing, local thermal decomposition of the blowing agent particles occurred at a lesser extent, even though the average melt temperature (~170 °C) was below the decomposition temperature of the blowing agent (it starts at 187 °C). Gas released during melt processing led to the formation of a small number of closed pores as depicted in Figure 55. The average diameter of these pores was within the interval of 20 to 50 micrometers. Macroscopically, the extruded filament appeared smooth and, therefore, it was perfectly suited for further processing by 3D printing.

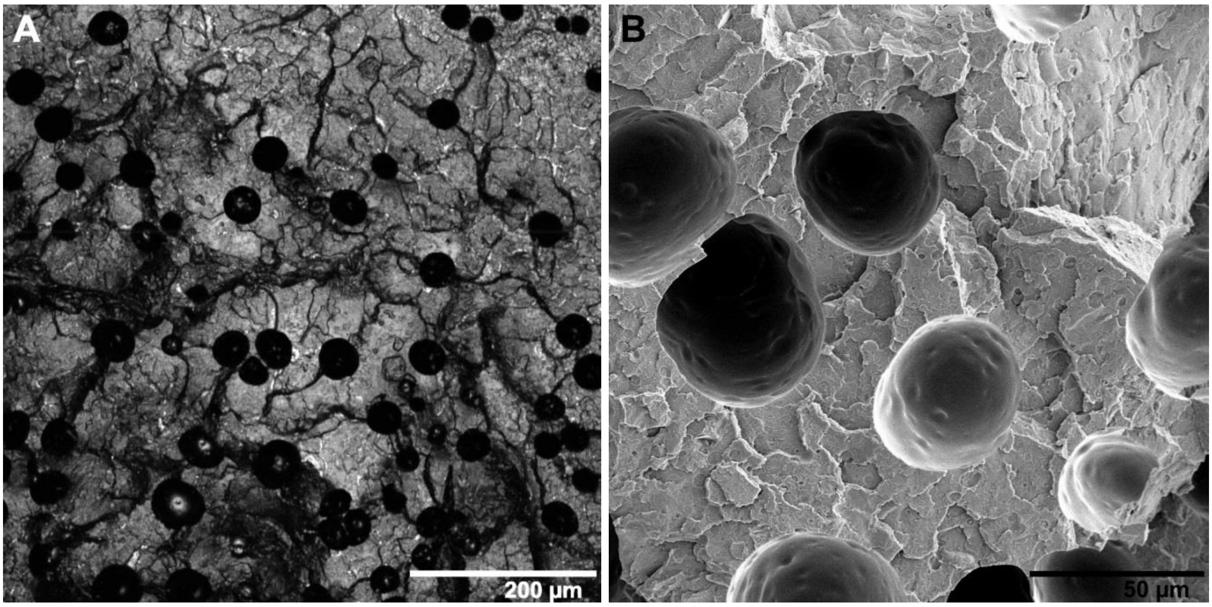

Figure 55: Structure of HIPS with 2 wt. % of foaming agent, filament after extrusion in the single-screw extruder. **A** – Overview, CLSM photo. **B** – Detail of hollow cells, SEM photo.

When the temperature used in the 3D printing was higher than the decomposition temperature of the foaming agent (printing temperature 220 °C), the decomposition of azodicarbonamide occurred and a foamed nanocomposite filament was deposited directly. Small pores with sizes up to 30 µm (Figure 56) were formed without the need for any thermal post-processing foaming after 3D printing.

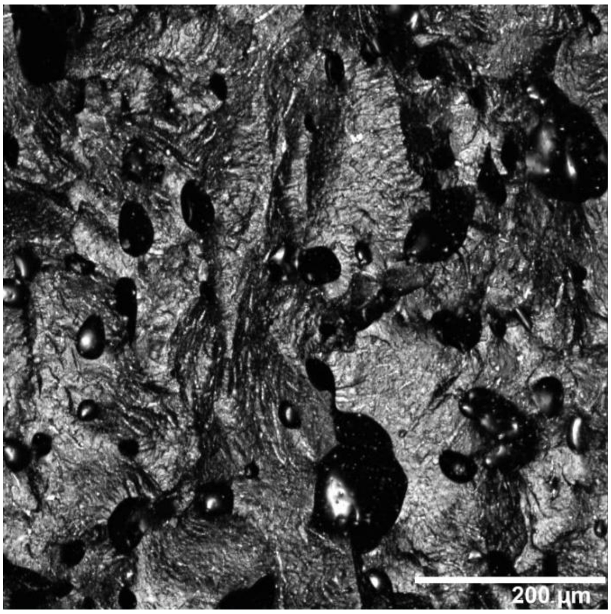

Figure 56: Structure of HIPS with 2 wt. % of foaming agent, porous sample after 3D printing above the decomposition temperature of foaming agent, CLSM photo.

During the 3D printing below the decomposition temperature of azodicarbonamide (printing temperature 180 °C), the closed-cell pores formed in the filament after single-screw extrusion were eliminated by pressure generated by the 3D printer nozzle, and due to the rapidly decreasing temperature of the deposited melt, the heat in the system was no longer sufficient to create new pores. Also, during 3D printing, there was no noticeable shear stress that could overheat the sample locally. The result was a completely non-porous 3D printed sample with precisely defined shapes that were generated by the design software. It was shown that the polymer with the thermal blowing agent could be processed using 3D printing to avoid early foaming and the structure of the 3D printed body was homogeneous, accurate, and pore-free. The evidence is shown in Figure 57, which shows the pore-free fracture surface of the cylindrical sample after printing.

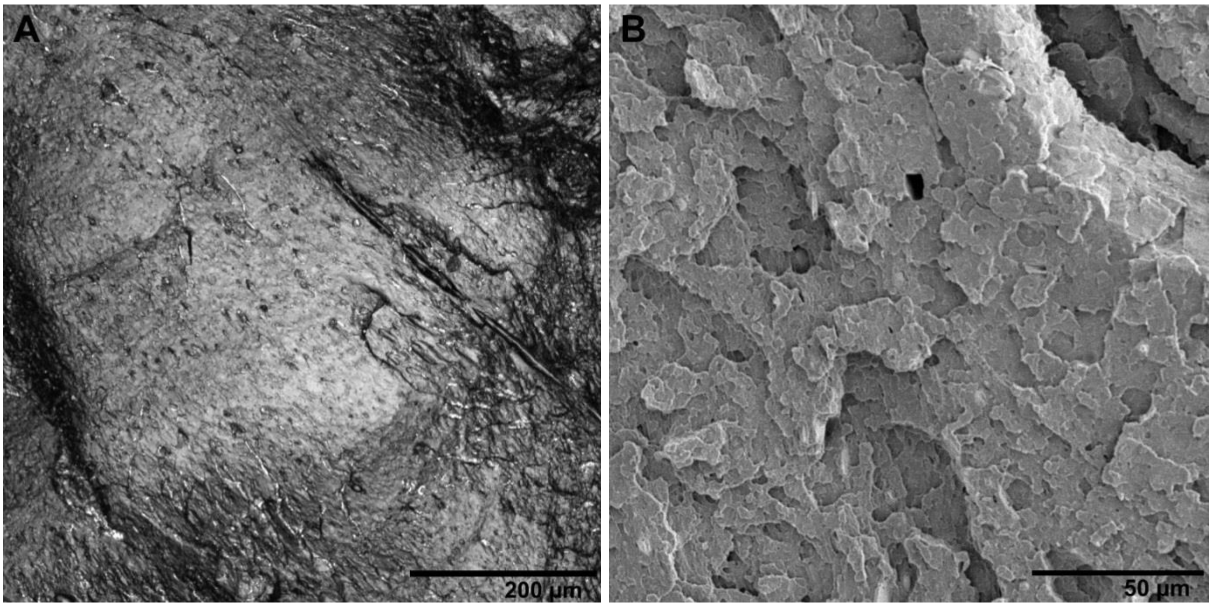

Figure 57: Structure of HIPS with 2 wt. % of foaming agent, sample after 3D printing below the decomposition temperature of foaming agent. **A** – Overview, CLSM photo. **B** – Detail of pore-free fracture surface, SEM photo.

The cylinder 3D printed below the decomposition temperature of the blowing agent was foamed in glass-aluminum mold shaped to form the final body – cylinder with the same high and 120 % diameter as the printed body. The accurate foaming temperature and time were determined experimentally to 200 °C and 30 min. At lower temperatures, the foam was unable to fill the entire mold space well even after a long foaming time. On the other hand, at higher temperatures or time, there was an apparent degradation of the polymer, large inhomogeneous bubbles were formed or the sample overflowed from the mold. In general, the trend was that the higher the temperature or the longer foaming time, the larger pores were formed, overflows occurred and the density decreased.

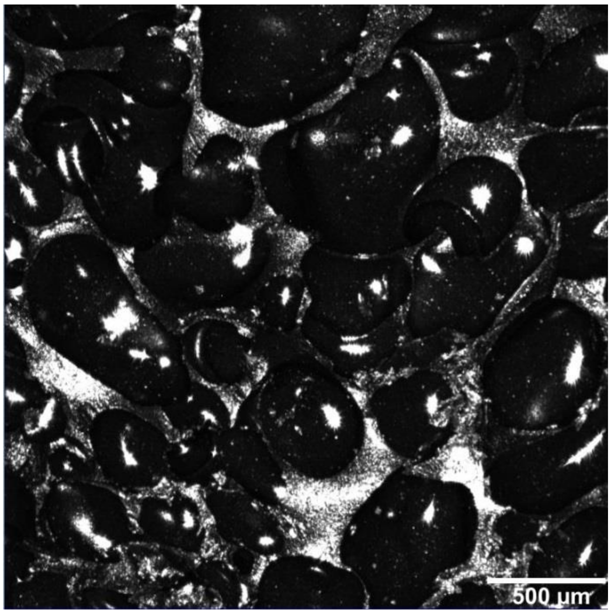

Figure 58: Structure of HIPS with 2 wt. % of foaming agent foamed at 200 °C for 30 minutes (post-processing foaming), CLSM photo.

The structure of the sample foamed at 200 °C for 30 min is captured in Figure 58. Irregularly shaped pores of average size 340 μm were visible in the foam structure, the pore density was $2.8 \cdot 10^{6}$ cells·cm^{-3}. The porosity of the sample appeared to be closed-cell, but a minority of the pores were seen to merge to form a structure with open porosity locally.

5.2.2 Thermal decomposition of the foaming agent

The optimum foaming temperature and time were determined employing the TGA, in which the foaming process in the air was simulated. One-hour isothermal hold of pure azodicarbonamide or HIPS with 2 wt. % of azodicarbonamide at constant temperature is shown in Figure 59. The temperature range for individual measurements was 160–250 °C in 10 °C steps. It seems clear, that significant decomposition of the pure blowing agent and gas release occurred at temperatures above 200 °C. In the case of HIPS with 2 wt. % of the foaming agent, degradation of the polymer matrix in an oxidative atmosphere at elevated temperatures was observed. The dashed line in the graph represents 2 wt. %, i.e. the limit at which the whole amount of the foaming agent would theoretically decompose while maintaining all the polymer matrix. As can be seen, when the sample was foaming at higher temperatures, there was a massive degradation of the HIPS matrix, so the high temperature was undesirable.

Pure foaming agent (azodicarbonamide):

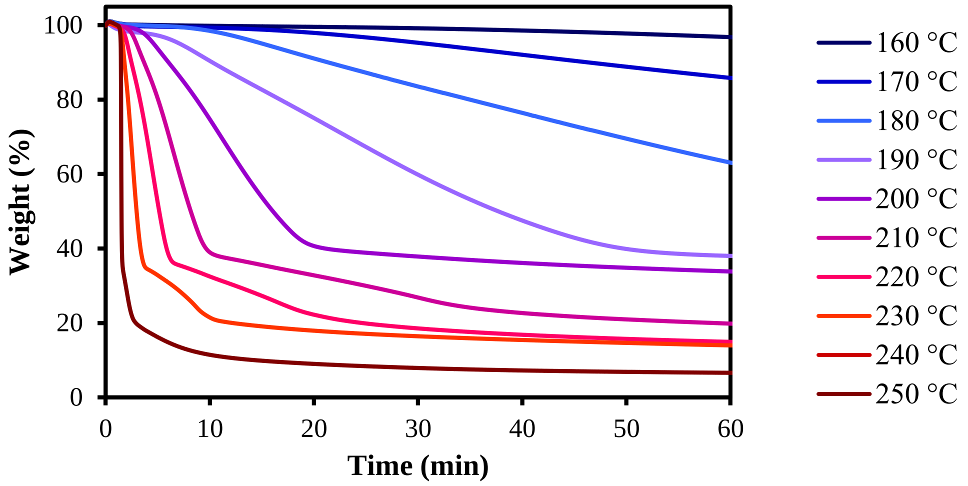

2 wt. % of foaming agent in HIPS:

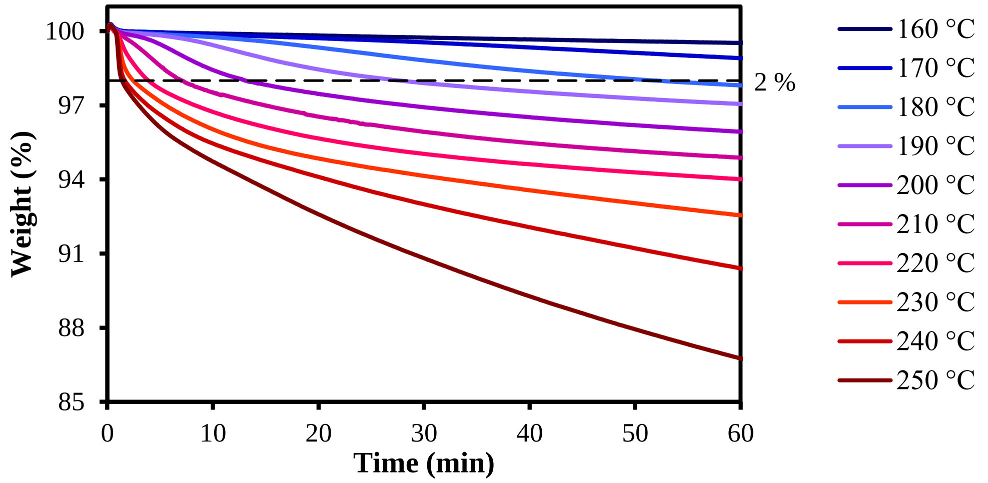

Figure 59: TGA simulation of foaming process in air atmosphere – isothermal hold of the material at different temperatures for 60 minutes. The upper graph shows the decomposition of the pure foaming agent (azodicarbonamide). The lower graph shows the thermal decomposition of the HIPS sample with 2 wt. % of foaming agent. The dashed line defines the content of the foaming agent in the sample.

When HIPS with the blowing agent was extruded from the 3D printer at 180 °C, almost no blowing agent decomposed, because decomposition of azodicarbonamide at this temperature was very slow, and the stay of the polymer in the heated printer extruder and nozzle was short. At 220 °C, the probability of HIPS degradation was faster, however, the stay of melted polymer in the printer and the heated nozzle was short but the time was sufficient for the blowing agent to decompose and cause foaming.

Hence, foaming at 200 °C for 30 min after 3D printing at 180 °C was, found to provide optimal conditions – azodicarbonamide decomposition was fast enough for a sufficiently long time to produce the desired foam structure while minimizing HIPS degradation. With shorter foaming times, the HIPS degradation was even more suppressed.

5.2.3 Effect of nanoparticles on the foaming process

Thermogravimetric analysis (TGA) was performed using filaments to investigate the effect of nanoparticles on the thermal behaviour of the thermal blowing agent and thus on the behaviour of the entire polymer system during processing. Description of the TGA measurements is provided in paragraph 4.3.2.

Complete TGA curves:

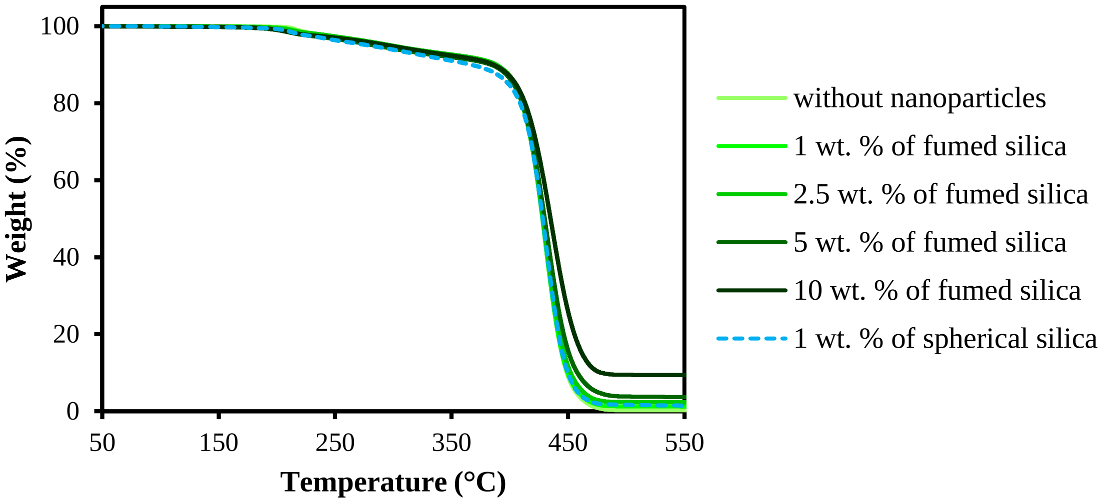

Detail of blowing agent decomposition area:

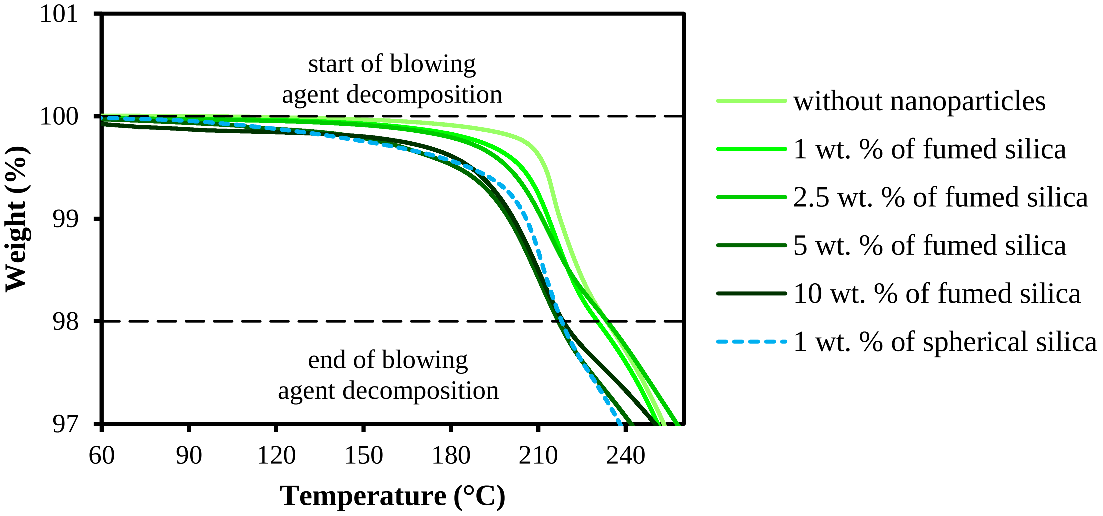

Figure 60: TGA curves of extruded filaments. **Top** – complete curves. **Bottom** – detail of area when the blowing agent was decomposed to gaseous products and causing foaming.

Figure 60 depicts the results of the TGA measurements. The TGA curves showed a similar shape for all the systems investigated differing more significantly only above approximately 450 °C. Here, the curves deviated from each other due to different amounts of nanosilica. However, magnifying the area in which the blowing agent decomposed, the significant effect of silica on this process was observed. Increasing silica content, the decomposition behaviour deviated more and more from the sample without nanoparticles. The sample with 1 wt. % of solvent-casted spherical silica deviated more than the sample with 1 wt. % of melt-blended fumed silica. To numerically compare this trend, the decomposition temperature of the blowing agent was determined (Figure 61) – the peak value from the first derivation of the TGA curves. The blowing agent was the first component that decomposed in the system, so it was determined from the first peak value in the temperature range of 180–240 °C. Since it was a peak of derivation, it was more precisely the temperature at which the decomposition of the blowing agent had the fastest rate.

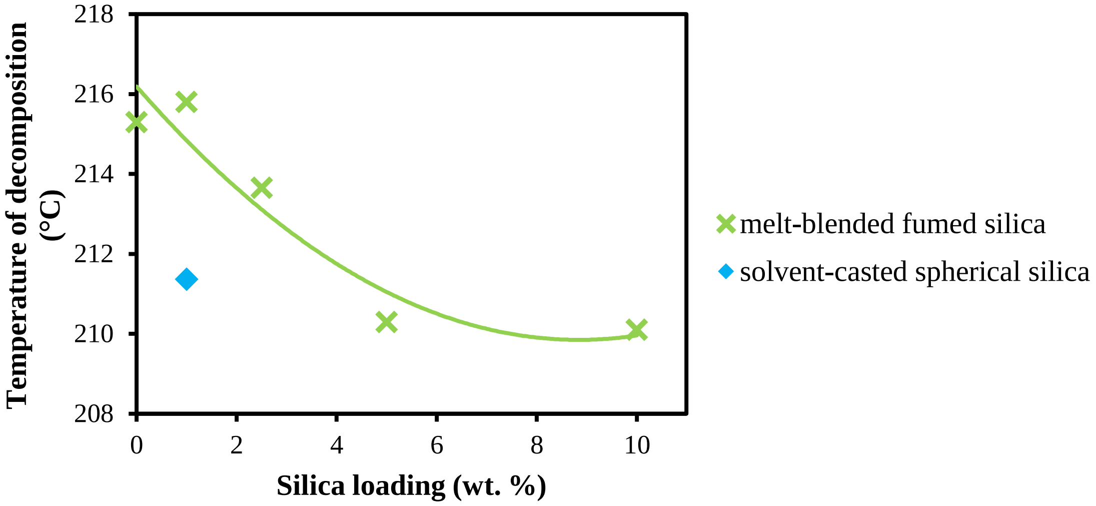

Figure 61: Dependence of blowing agent decomposition temperature on nanosilica loading.

Results in Figure 61 confirmed, that the decomposition temperature of the blowing agent decreased with an increasing amount of nanoparticles. During processing, decomposition of blowing agent in nanocomposites occurred at lower temperatures and the system was able to foam in a shorter time under the same temperature conditions. For spherical silica, this effect proved to be much more enhanced than for fumed silica. This was observed in practical terms in later experiments (paragraph 5.2.6) when 3D printed cylinders were foamed in a glass-aluminum mold at elevated temperatures. The system without nanoparticles needed 30 minutes to fill the mold. The sample with melt-blended fumed silica reduced this foaming time to 10 minutes and the sample with solvent-casted spherical silica to 5 minutes. Since the solvent-casted spherical nanosilica was distributed in the polymer matrix in the form of individual particles and its distribution homogeneity was on the nanoscale, it had a more significant effect on the surface energy of the blowing agent than large isolated aggregates of melt-blended fumed silica.

We ascribe this effect to the lowering the surface energy azodicarbonamide grains by silica nanoparticles making it easier to release gaseous products. A similar effect was observed by Zakiyan et. al [143] on the PS system but with a physical blowing agent (CO_2) because the nanoparticles reduced Gibb’s free nucleation energy. Saha et al. [144] observed three different types of nanoparticles in PU foams and, conversely, observed an increase in thermal stability with the addition of nanoparticles. However, this could be due to the influence of nanoparticles on the synthesis of the PU polymer itself, when in their presence the polymer could crosslink more and thus cause an increase in thermal stability.

5.2.4 Effect of silica content on the foam porosity

The presence of nanoparticles had a major influence on the porosity, pore size, and spatial pore distribution of the resulting foam. In Figure 62, foamed HIPS with 2 wt. % of the foaming agent after single-screw extrusion is depicted. Samples had different nanosilica content – the first sample was without nanoparticles and then with 0.25, 1, 2.5, 5, and 10 wt. % of melt-blended fumed silica. All samples were prepared under the same conditions (temperature, rpm) to ensure the same foaming conditions and reproducibility. All samples showed a relatively uniform distribution of closed cells.

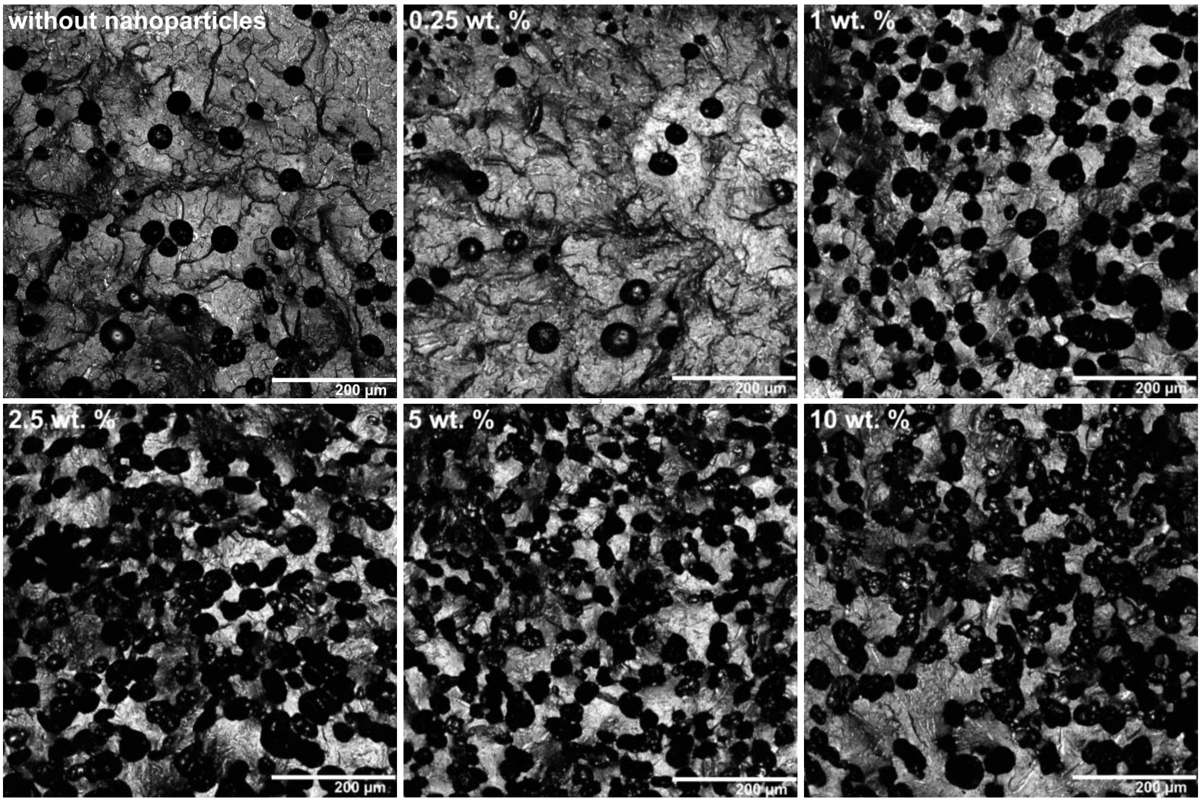

Figure 62: CLSM images of extruded filaments – HIPS with 2 wt. % of blowing agent after single-screw extrusion with different amounts of melt-blended fumed silica (without nanoparticles, with 0.25, 1, 2.5, 5, and 10 wt. % of fumed nanosilica).

It was clearly observable, that with higher silica content, the porosity of foams increased. It was shown that nanoparticles served as nucleating agents when a thermal chemical blowing agent was used. Bubble growth was facilitated on the surface of nanoparticles, creating more stable nucleation centers leading to a structure with a larger number of smaller pores.

Samples without nanoparticles and with 0.25 wt. % of fumed silica had discrete individual pores. In the sample with 1 wt. %, the number of pores highly raised and they slightly started to connect, but most of the pores were still separated. From the 2.5 to 10 wt. % of nanoparticles, the foam structure did not change significantly – all three samples showed the structure of a larger amount of mostly coalesced pores. All samples passed through the extruder at the same time, so they had also the same time for pore formation. Thus, the individual pores are all approximately the same size. Large pores were observed due to the connection of several of these individual pores, which grew close together. In the case of 10 wt. % of nanosilica, the ratio of connected bubbles seemed to be so high, that the start of open porosity could be almost considered, but these large connected bubbles were not connected from a macroscopical point of view.

One sample with solvent-casted spherical silica was also extruded (Figure 63). The whole concentration series was not made due to the large demands on solvent material consumption, which represent an increased burden in financial and environmental points and due to more difficult way of solvent-casted samples preparation also time burden. Solvent-casted spherical silica sample showed the structure of a large number of individual pores and unlike 1 wt. % of fumed silica showed no coalescence of pores.

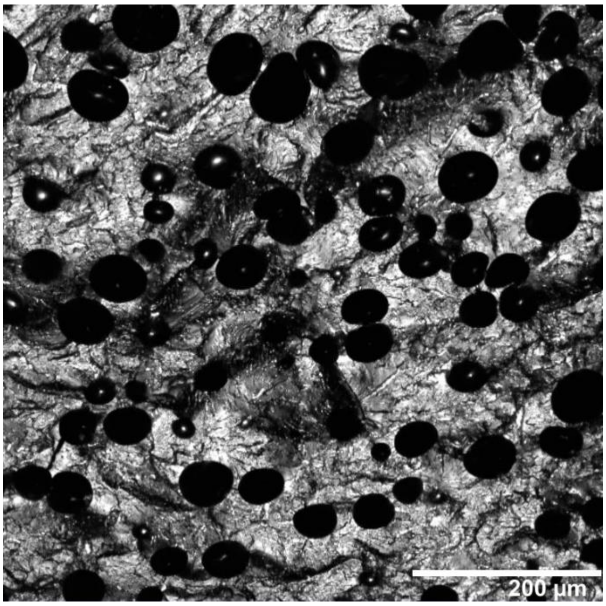

Figure 63: CLSM image of extruded filament – HIPS with 2 wt. % of blowing agent after single-screw extrusion with 1 wt. % of solvent-casted spherical nanosilica.

For the exact quantification of pore structure, four parameters were measured – average pore size, cell density, porosity, and mass density of filaments. Description of the measurement methods is provided in paragraph 4.3.1. These parameters were related to the content of nanosilica (Figure 64). As the particle content increased, the structure approximately stabilized at constant values, as could be concluded from porosity and density measurement. Cell density (number of pores per volume unit) sharply increased when 1 wt. % of nanoparticles was added and started to decrease due to coalescence of pores in larger pore aggregates – one aggregate was counted as one pore. This went hand in hand with a steady increase in average pore size.

Sample with solvent-casted spherical silica showed structural properties closer to the sample without nanoparticles than the sample with melt-blended fumed silica. This was also observed experimentally during the extruding of the filament – fumed silica filaments tended to foam and expand more (but still not significantly), while spherical silica filament was extruded without a naked eye visible surface porosity with a smooth surface, as well as filament without nanoparticles.

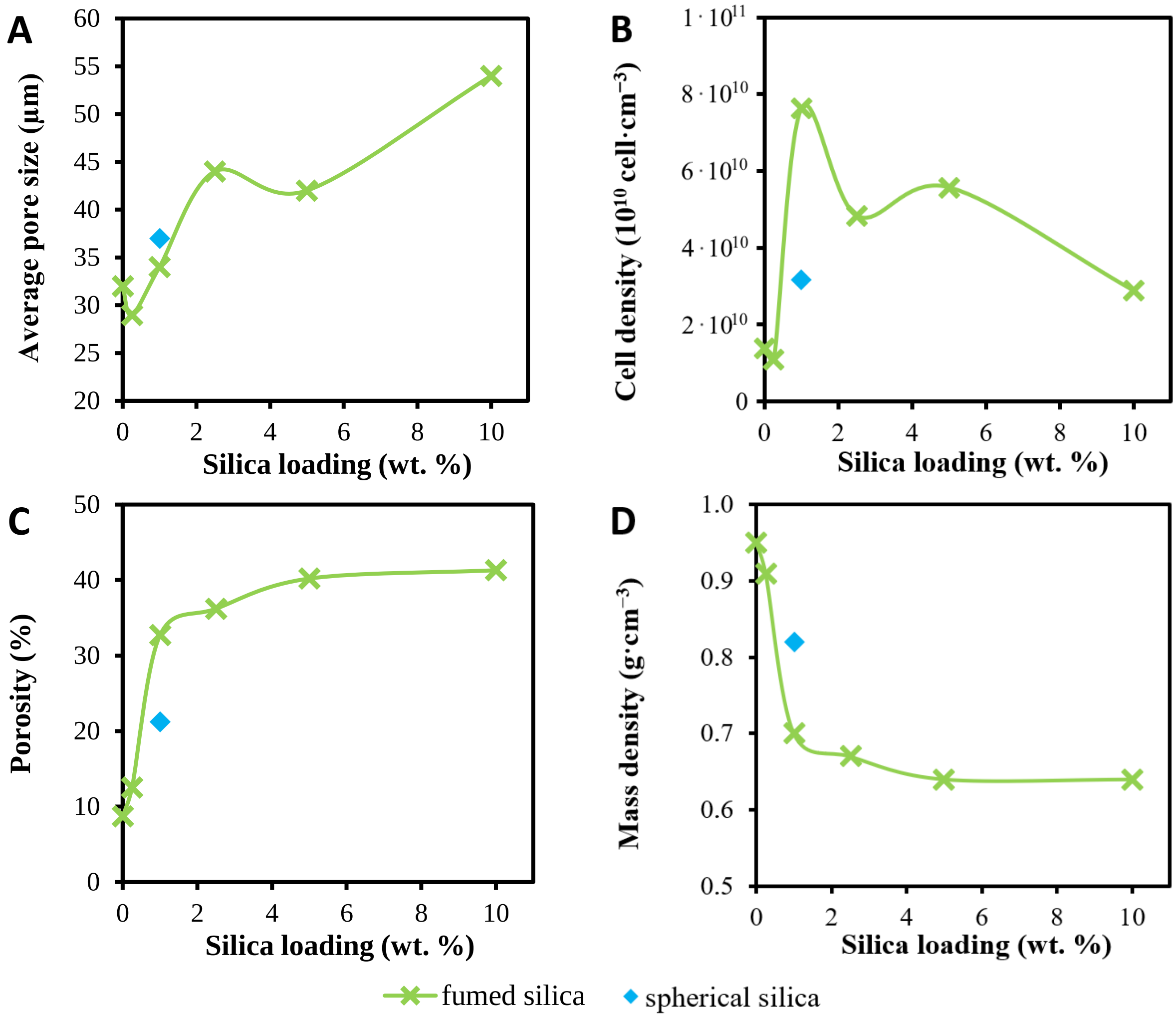

Figure 64: Graphical evaluation of structural properties of extruded filaments dependent on silica content. **A** – average pore size, **B** – cell density, **C** – porosity, and **D** – density. Raw data are available in the appendix.

The polydispersity index (*PDI*) was also analyzed to assess the homogeneity of the resulting porous structure:

$$PDI = \frac{P_{\mathrm{p,w}}}{P_{\mathrm{p,n}}} = \frac{\sum n \cdot d_{\mathrm{p}}^2}{\sum n \cdot d_{\mathrm{p}}}, \tag{29}$$

where $P_{\mathrm{p,w}}$ is average pore size (number average), $P_{\mathrm{p,n}}$ is average pore size (weight average), n is a number of pores and d_{p} is spore size (pore diameter). Calculated values of PDI were 1.07 for the sample without nanoparticles, 1.22, 1.16, 1.21, 1.33, and 1.22 for samples with melt-blended fumed silica (0.25, 1, 2.5, 5, and 10 wt. %, respectively) and 1.12 for the sample with 1 wt. % of solvent-casted spherical silica. Since the values were in a relatively narrow range of 1.07–1.33, it can be said that the homogeneity of the porous structure did not deteriorate with the addition of nanoparticles. Sample with solvent-casted spherical silica showed a slightly closer homogeneity value to sample without nanoparticles than samples with melt-blended fumed silica.

5.2.5 Spatial distribution of nanoparticles within the foam structure

To understand the role of nanoparticles during pore growth, the spatial arrangement of the particles in the foam structure was observed, in particular their arrangement near the interface of the formed pores and the polymer matrix. Three systems of extruded filaments were compared – neat polymer, polymer with 1 wt. % of melt-blended fumed silica and polymer with 1 wt. % of solvent-casted spherical silica, all of them contained 2 wt. % of the foaming agent.

Originally, this experiment was performed using nanocomposites with the HIPS matrix. After cutting the filament into ultrathin sheets for the STEM observation, some rubber particles were removed from the sheets during cutting. Hence, it was impossible to distinguish whether the observed pores were formed by the decomposition of the foaming agent or by removed rubbery inclusions during specimen preparation. For this reason, the HIPS matrix was replaced by a pure PS matrix for these experiments. The structure of pure PS nanocomposites was presented in paragraphs 5.1.1.2 and 5.1.2.2. PS systems were processed in the same way as the HIPS ones.

Microscopic images of the interface between polystyrene and the pore are shown in Figure 65. It was assumed, that during the growth of the bubble, the nanoparticles were concentrated at the pore surface, effectively reinforcing it, and, during the growth of the pore, more energy was needed. However, this hypothesis was not confirmed, as evidence by Figure 65. The particles were not located at the interface, hence, the hypothesized interface reinforcement was not confirmed.

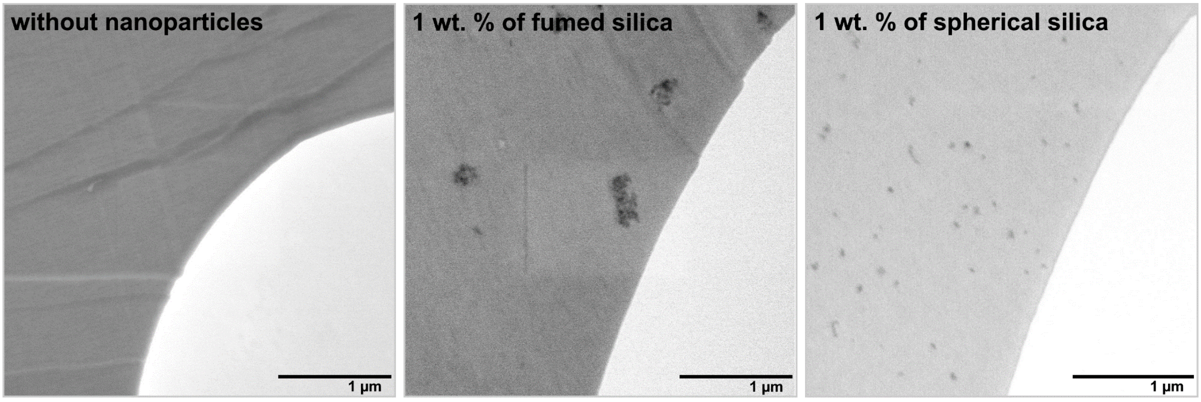

Figure 65: Detail of the pore interface structure formed during filament extrusion. All samples were made of PS matrix and contained 2 wt. % of foaming agent. **Left –** without nanoparticles; **middle –** with 1 wt. % of melt-blended fumed silica; **right –** with 1 wt. % of solvent-casted spherical silica. (STEM)

5.2.6 Structure of the 3D printed foams

All of the 3D printed foams tested were of a cylindrical shape. Three types of samples were prepared according to the processing conditions:

1) Cylinders printed below the decomposition temperature of the blowing agent (printing temperature 180 °C).
2) Cylinders printed above the decomposition temperature of the blowing agent (printing temperature 220 °C).
3) Cylinders by post-processing foaming in the pre-heated oven (foaming temperature 200 °C).

When HIPS with the blowing agent was 3D printed below the decomposition temperature of azodicarbonamide, a very precise 3D printed structure was reached. No macroscopically observable porosity was produced. This property is an important premise e.g. for multi-material 3D printing, where the printing of the next material follows directly on the previous material to produce for example sandwich or gradient structures, where the foamable filament could be effectively used.

The microscopical structure of cylinders printed below the decomposition temperature of the blowing agent is depicted in Figure 66 (upper line). In the case of the sample without nanoparticles, it was possible to print a solid body without pores. When nanoparticles were added, the bubble formation occurred even below the standard decomposition temperature of azodicarbonamide. As was explained in paragraph 5.2.2, the presence of nanoparticles lowered the decomposition temperature of the blowing agent probably due to lowering surface energy around blowing agent grains, and thus gaseous decomposition products were released easier. Thus, it was possible to achieve porous structure even when 3D printing occurred at low-temperature conditions. During 3D printing, there was no shear stress as in the extruder, so the local overheating caused by shear friction could not be considered.

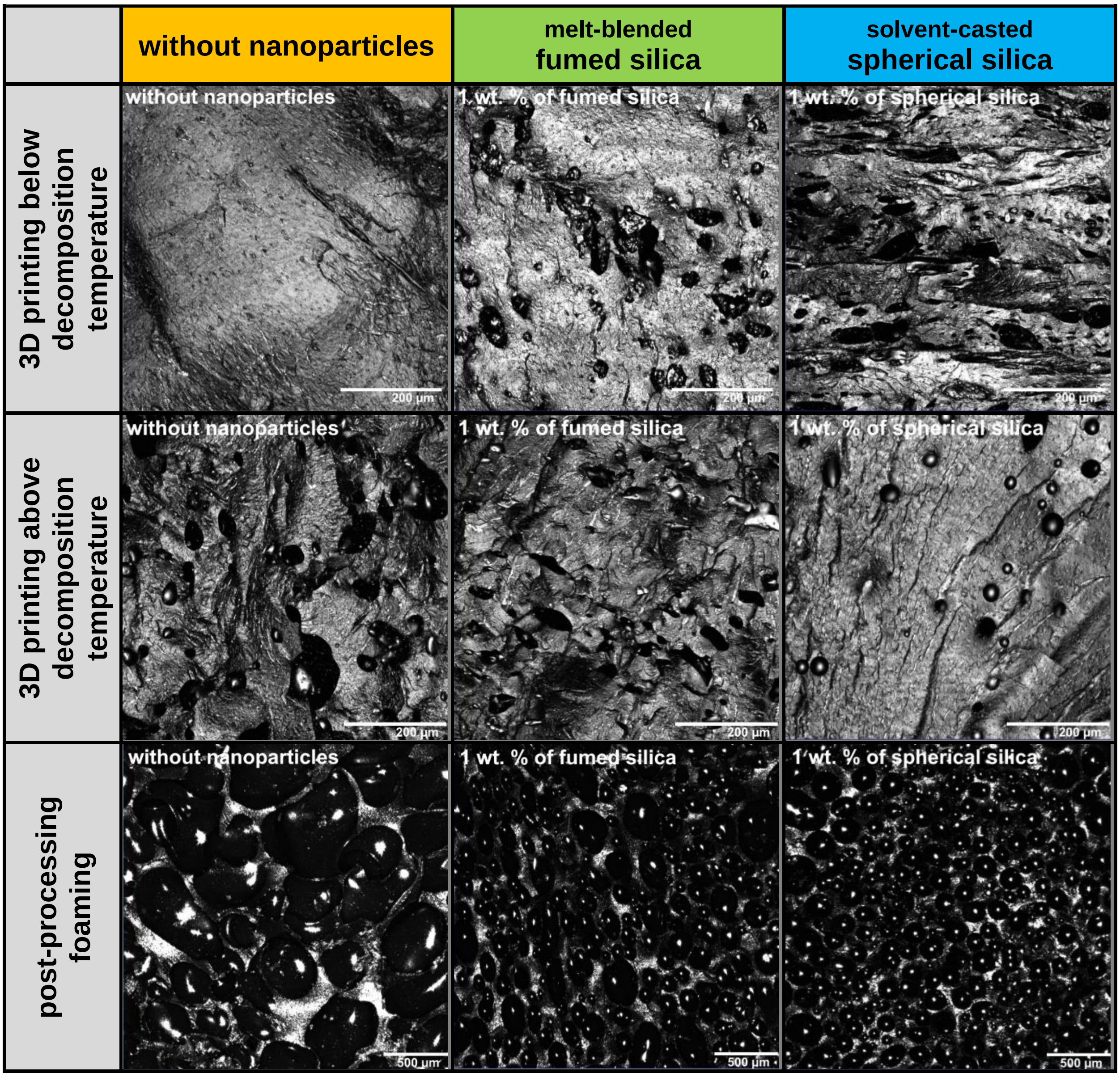

Figure 66: CLSM images of 3D printed cylinders based on HIPS and azodicarbonamide without nanoparticles (left column), with 1 wt. % of melt-blended fumed silica (middle column), and with 1 wt. % of solvent-casted spherical silica (right column). **Upper line** – after 3D printing below the decomposition temperature of the blowing agent (180 °C, scale bar 200 μm). **Middle line** – after 3D printing above the decomposition temperature of the blowing agent (220 °C, scale bar 200 μm). **Bottom line** – after post-processing in the pre-heated oven (200 °C, scale bar 500 μm).

When HIPS with the blowing agent was 3D printed above the decomposition temperature of azodicarbonamide with 100 % flow of the material through the printer, the expanding material took up more space than the compact unfoamed solid material and therefore overflows on the printed body arose. This inconvenience was suppressed by reducing the flow of material into the printer. The degree of this reduction was set experimentally so that the printed bodies had a shape precisely defined by the design, i.e. with no overflows or unprinted areas. The flow reduction was about 80 % in all three cases. The microscopical structure of cylinders printed above the decomposition temperature of the blowing agent is depicted in Figure 66 (middle line). The homogenous microporosity was formed in all three cases (without nanoparticles, with melt-blended fumed silica, and with solvent-casted spherical silica). Printing above the decomposition temperature of azodicarbonamide allowed producing of directly foamed bodies with a precise outer structure designed by software without any post-processing treatment. Needless to say, that the resulting pores were slightly compressed by the printer nozzle during the deposition of the newly printed layer, i.e. they were reduced in size.

Cylinders, which were 3D printed below the decomposition temperature of the blowing agent, were then thermally treated in a pre-heated oven – they were subjected to post-processing foaming. 3D printed cylinders were closed in the aluminum mold with glass bases with a diameter of 120 % compared to the diameter of the original cylinders and foamed in the oven at 200 °C. Foaming time was set experimentally so that the cylinder was perfectly foamed, i.e. it just took its place in the mold without overflows or unfilled spots. Foaming time varied significantly depending on the material. Without nanoparticles, the foaming time was 30 minutes. With fumed silica distributed in the material in the form of micro aggregates, the foaming time was 10 minutes, i.e. it was reduced by 66.7 %. In the case of spherical silica distributed in the material in the form of individual nanoparticles, the foaming time was 5 minutes, i.e. reduced by 83.3 %. Another fact that contributed to the more rapid foaming was that the samples with nanoparticles had small pores already immediately after 3D printing, unlike the sample without nanoparticles. These pores then served as precursors for post-process foaming and facilitated the formation of larger pores. Post-processing foaming after 3D printing allowed the production of material with even larger pores, i.e. with even lower density. It allowed to print small objects and then foam them into larger ones with little material consumption. The microscopical structure of cylinders after post-processing foaming is depicted in Figure 66 (bottom line). The effect of nanoparticles was striking in this case. Large pores were formed in the sample without nanoparticles. The size of the pores was significantly decreased and the number of pores was increased when nanoparticles were added. Nanoparticles served as heterogeneous nucleation centers during bubble growth and thus support growing large amounts of smaller pores. In the case of solvent-casted spherical silica, pores seemed to be smaller and more homogenous than in the case of melt-blended fumed silica.

Quantification of structural properties (pore size, cell density, porosity, and density) was calculated for cylindrical 3D printed samples (Figure 67) in the same way as in the case of extruded filaments. Due to the large variance of values in cell density, the *y*-axis of the graph is with a logarithmic scale. The sample without nanoparticles printed below the decomposition temperature of the azodicarbonamide appeared to be pore-free upon microscopic observation, but its measured density was lower than the theoretical density, which this material should have completely without pores (solid material). Therefore, this sample is missing in the graphs with the pore size and cell density, but it is plotted in the graphs with the evaluated porosity and density. Its density was highest and the porosity lowest compared to other samples, where the pores were observed microscopically. In terms of pore sizes, the cylinders after 3D printing showed a more or less uniform pore size. The increase in pore size was evident in the samples after post-processing foaming, while the sample without nanoparticles had significantly larger pores. The cell population density was larger in the case of directly 3D printed samples. In post-processed samples, the time for pore growing and pore coalescence caused the growth of a smaller amount of larger pores, and thus cell density dropped. In the case of porosity and mass density, the group printed above the decomposition temperature of the blowing agent had almost uniform porosity and density, as did the group after post-processing foaming. Sample with spherical nanosilica had slightly lower porosity and slightly higher density. The difference was observable in the group printed below the decomposition temperature of the blowing agent – the densest sample without pores was without nanoparticles and the lightest sample with the highest porosity was the one with fumed silica.

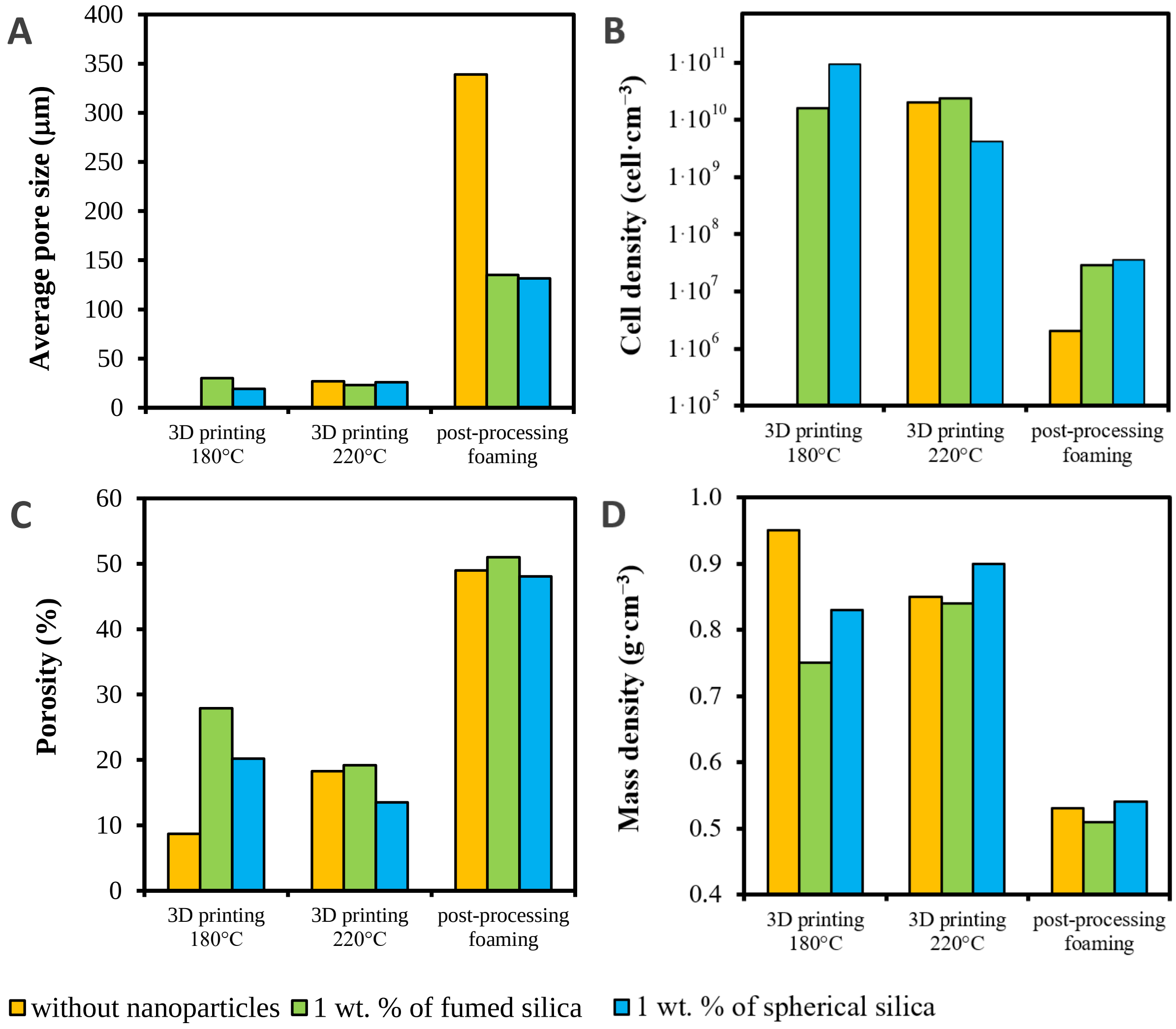

Figure 67: Graphical evaluation of structural properties of 3D printed cylinders (printed below and above the decomposition temperature of the blowing agent and after post-processing foaming). **A** – average pore size, **B** – cell density, **C** – porosity, and **D** – density. Raw data are available in the appendix.

5.3 Mechanical properties of foams

This chapter is mainly intended to characterize the properties of prepared filaments and 3D printed structures.

5.3.1 Tensile properties of filaments

Stress-strain curves of the materials investigated are shown in Figure 68. Tensile behaviour with high deformations was observable in the pure HIPS sample, sample without nanoparticles or only with a small nanoparticle loading (0.25 wt. % of fumed silica). A further increase of nanoparticle content led to embrittlement and a decrease in the stress plateau region and elongation. Pure HIPS, sample without nanoparticles, and sample with 0.25 wt. % of fumed silica had significant overshoot in yield point area with strain softening region. On the other hand, this overshoot disappeared and the yield point was followed only by gradual strain hardening in samples with higher nanoparticle content. The sample with 10 wt. % of fumed silica showed such a brittle behaviour, that not all of the test specimens reached the yield point and their failure occurred immediately after the linear region of elastic deformation.

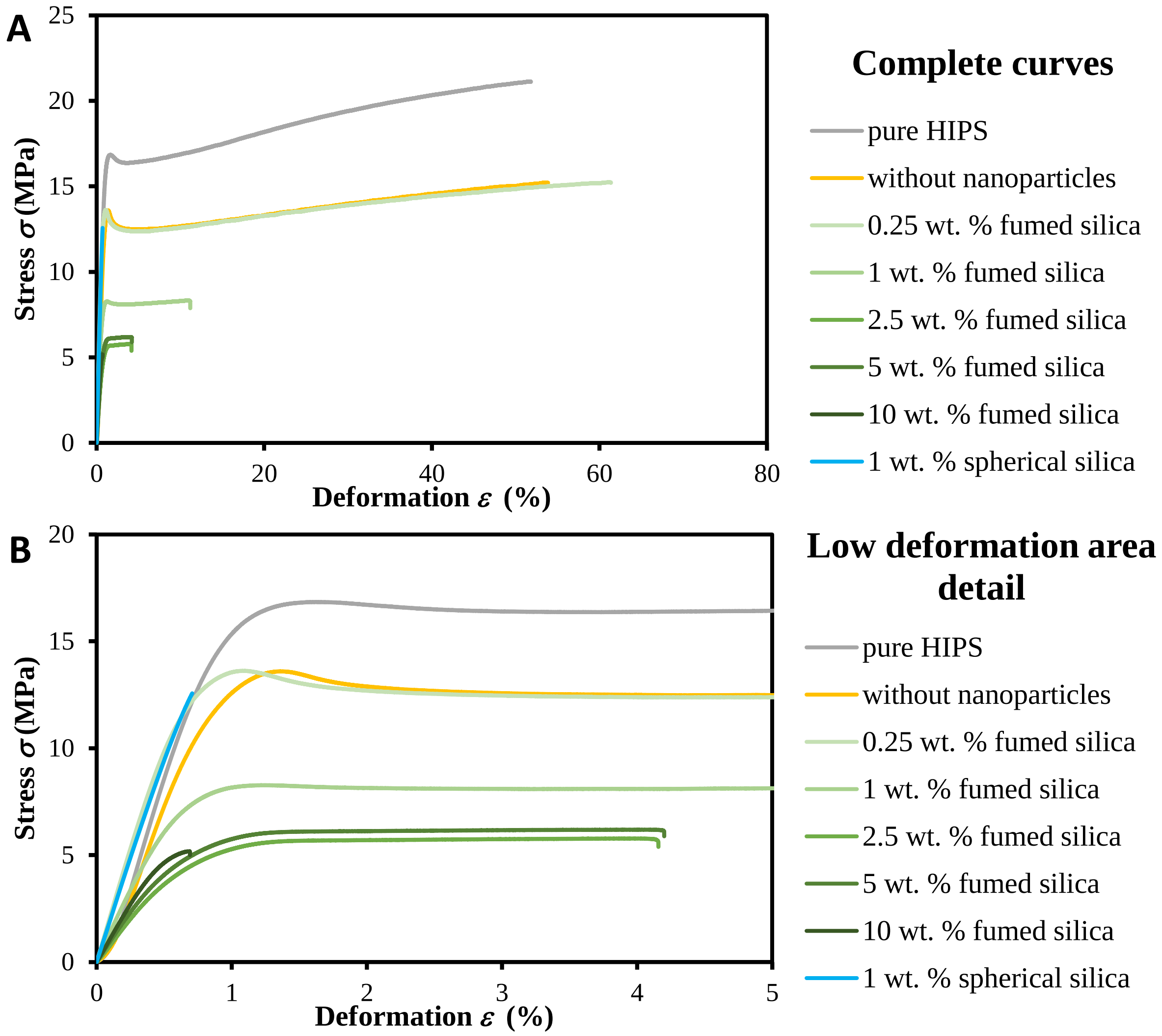

Figure 68: Representative tensile stress-strain curves of extruded filaments. **Top** – complete curves. **Bottom** – detail of low deformation area. All curves of specimens are in the appendix.

Very significant differences in the mechanical response were observed between samples with 1 wt. % of the different silica. Sample with 1 wt. % of melt-blended fumed silica showed still ductile behaviour, although it reached maximally half deformations than pure HIPS. In contrast, the sample with 1 wt. % of solvent-casted spherical silica was the most brittle of all the filaments but was able to achieve higher stress than other silica samples.

The composition dependences of the elastic modulus, yield strength, maximal strength, and elongation are shown in Figure 69. Each property was also divided by the density to express specific properties of the compositions reflecting variations in density.

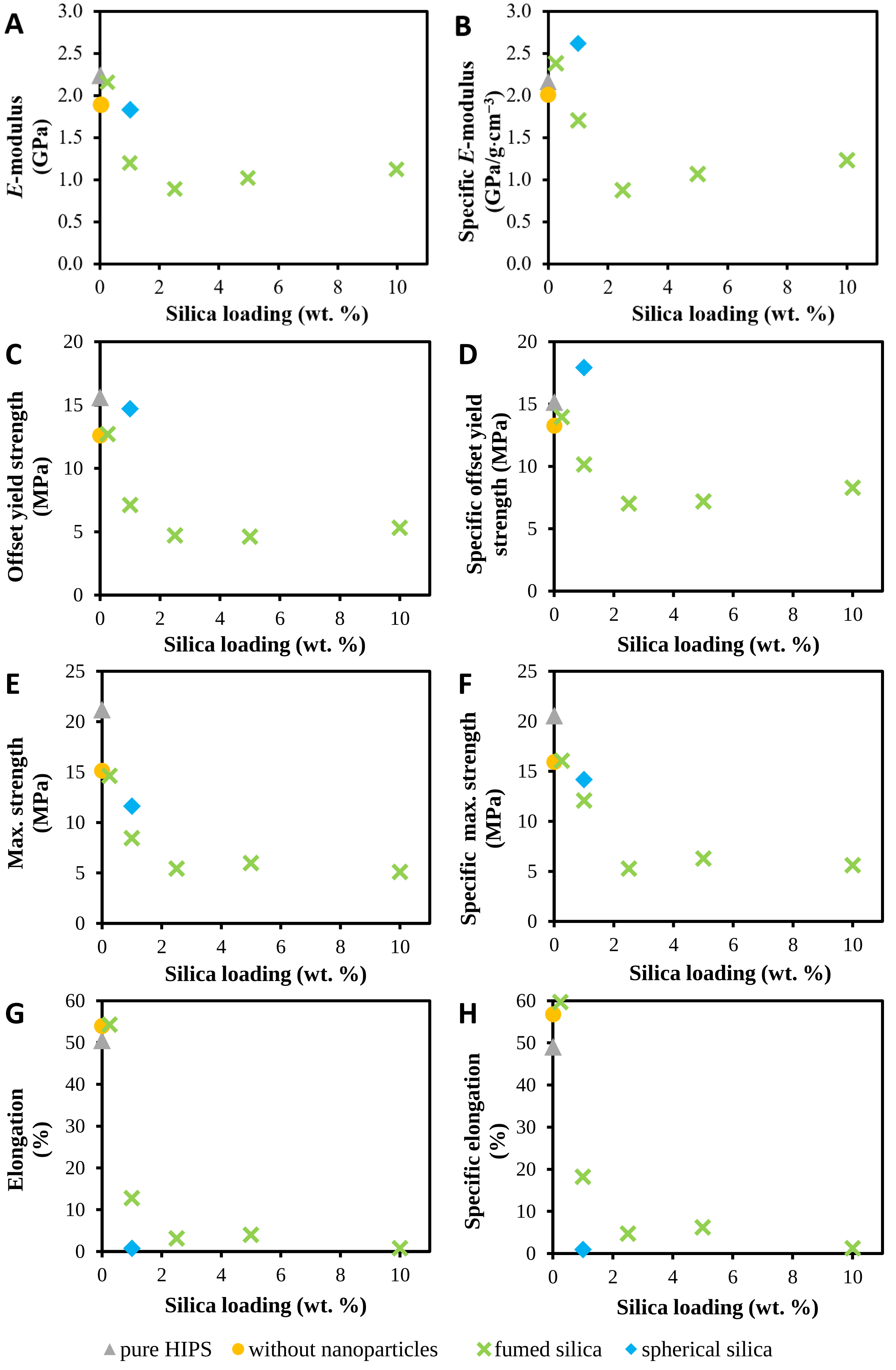

Figure 69: Graphical evaluation of tensile properties of extruded filaments. **A** – measured modulus, **B** – specific modulus, **C** – measured offset yield strength, **D** – specific yield strength, **E** – measured maximum strength, **F** – specific maximum strength, **G** – measured elongation, **H** – specific elongation. Raw data are available in the appendix.

The different behaviour of samples with 1 wt. % of silica (solvent-casted spherical silica or melt-blended fumed silica) was due to how nanoparticles were incorporated into the polymer matrix. While fumed nanosilica particles remained exclusively in the polystyrene matrix (Figure 53), spherical nanosilica was also incorporated at the interface of the PS-rubber particles and in the occluded rubber particles themselves (Figure 49). Disruption of the PS-rubber phase interface and reinforcement of the rubber particles themselves leaded to a loss of the toughening rubber effect. During deformation, there was no effective interface extraction of rubber fibrils, on which energy dissipation would occur. The sample with spherical silica thus shifted its mechanical properties towards the properties of pure PS away from the properties of rubber – it lost ductility but was able to withstand higher stresses.

In the case of of modulus of elasticity, the highest measured value was reached by pure HIPS. As the silica content increased, the modulus gradually decreased as the porosity increased in the structure of these samples. From the sample of 2.5 wt. % of fumed silica, the modulus was already approximately constant, which fully corresponded to the result of the structural analysis when the measured porosity stabilized at approximately a constant value with increasing particle content. The spherical silica sample achieved a greater modulus of elasticity than the fumed silica sample due to the above-mentioned suppression of the rubber effect. When comparing the specific modulus of elasticity, this effect was further enhanced and the filament with 1 wt. % of spherical silica achieved higher tensile modulus than pure HIPS, as did the sample with 0.25 wt. % of fumed silica.

Yield strength was evaluated as 0.2 % offset strength because not all samples had a significant overshoot, from which could be deducted yield point as the maximum of the peak. In some fragile samples, the failure occurred in the linear elastic region, so it could not be evaluated even offset strength – in the sample with 10 wt. % of fumed silica, the yield was determined only on the basis of 3 values, in the sample with 1 wt. % of spherical silica was then successfully evaluated only a single value. Yield strength showed a very similar trend as the modulus – the highest measured value was reached by pure HIPS, with increasing silica content the yield strength value decreased. The sample with 1 wt. % of spherical silica was equal to pure HIPS in terms of the measured yield point, and its specific value even exceeded pure HIPS (but there was not a statistically sufficient amount of data for reliable conclusions with spherical silica). The maximum achieved strength (tensile strength at the break) was again achieved by pure HIPS. With the increasing content of additives (whether blowing agents or nanosilica), the strength decreased significantly.

In the case of elongation, the decrease of nanocomposite samples compared to pure HIPS was more pronounced than in the case of maximum strength. With the addition of nanoparticles, the elongation decreased sharply, for samples with 1 wt. % of spherical silica and 10 wt. % of fumed silica, the elongation was at a minimum value. Interestingly, despite the addition of rigid particles into the polymer matrix, the sample without nanoparticles (but with blowing agent particles) and with 0.25 wt. % of fumed silica had a higher measured elongation than pure HIPS, in the case of comparing specific properties more significantly higher.

Only a small amount of nanoparticles was sufficient enough to effectively modify the mechanical properties. A higher content worsened the mechanical properties in an undesirable way and made the cost of the material more expensive. Xu et al. [182]

concluded during their research of PU foams with organoclay nanofiller, that compressive and tensile strength was maximized at 2 phr (≈ 1.96 %) of the nanofiller. Up to this value, the nanoclay filler increased the strength, at higher contents the strength decreased. They also observed that the average pore size decreased to 2 phr and increased when exceeded. Zhang et al. [73] observed very similar behaviour directly on the HIPS system with TiO_2 nanoparticles. They observed maximized notched impact strength, tensile strength, and tensile elastic modulus at 2 % of nanofiller. The conclusions of these independent researches are practically identical to the conclusions of this dissertation work. As for the practical observation of the filaments examined in this work, filaments with a higher silica content (2.5 wt. % and higher) were no longer suitable for 3D printing – filaments diameter fluctuated and the surface roughness of the filament increased.

5.3.2 Compressive behaviour of 3D printed foams

Compressive stress-strain curves of the cylinders are in Figure 70, while the top graph shows the deformation response of cylinders printed below the decomposition temperature of the blowing agent, the middle graph shows the deformation response of cylinders printed above the decomposition temperature and the bottom graph shows cylinders after post-processing foaming. For comparison, one representative curve of each sample was plotted in one graph in Figure 71.

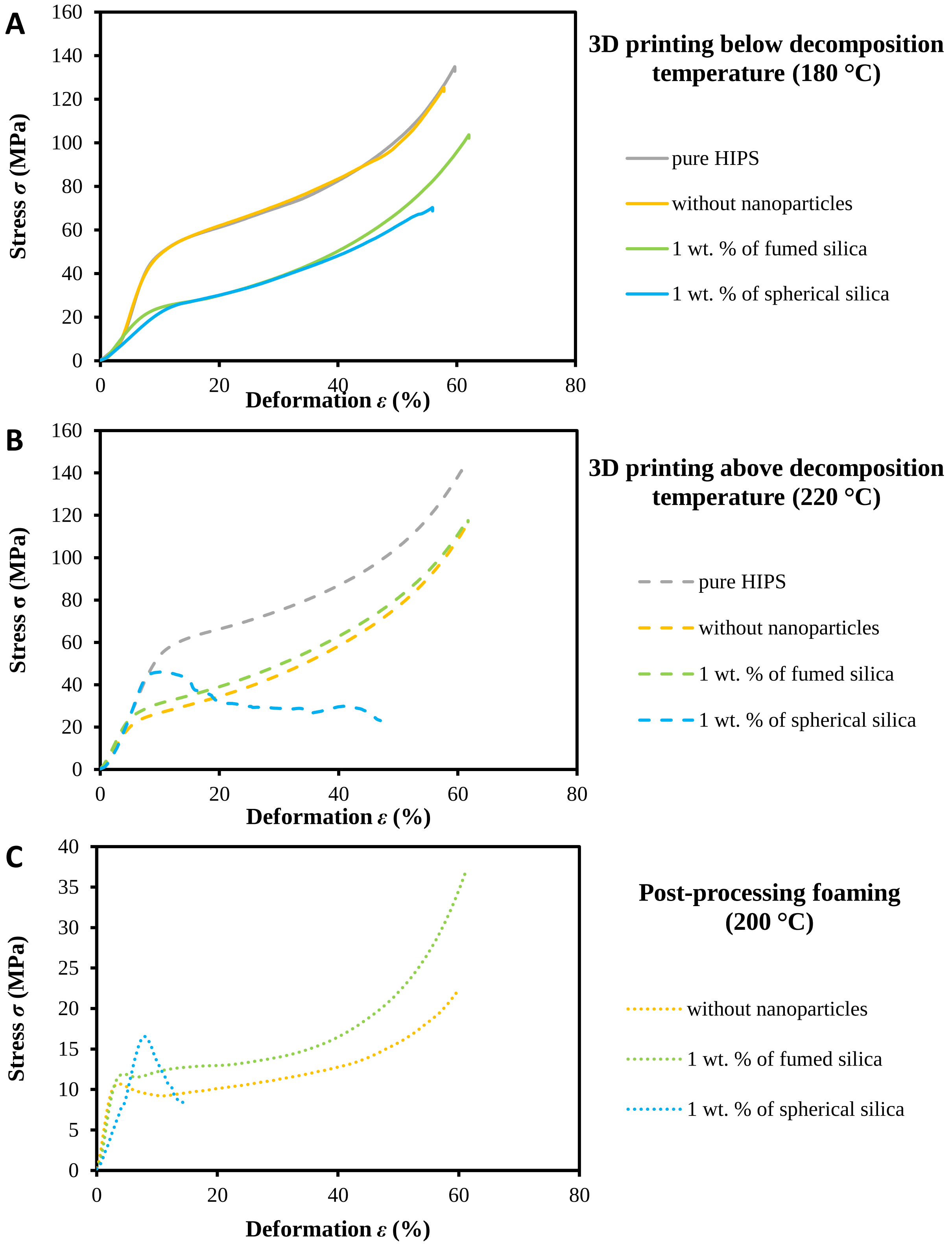

Figure 70: Representative compressive stress-strain curves of 3D printed cylinders. **Top** – Cylinders printed below the decomposition temperature of the blowing agent. **Middle** – Cylinders printed above the decomposition temperature of the blowing agent. **Bottom** – Cylinders after post-processing foaming. All curves of all specimens are in the appendix.

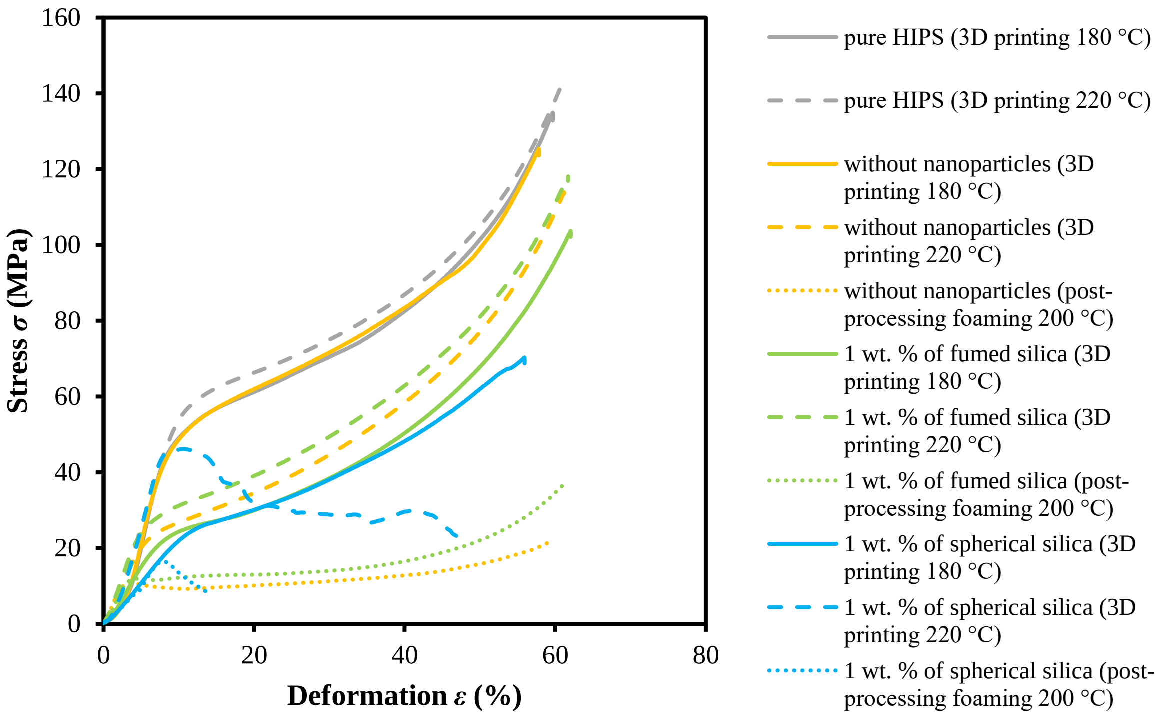

Figure 71: Compressive stress-strain curves 3D printed cylinders – comparison of a representative curve of each material together.

In the case of samples 3D printed below the decomposition temperature of the blowing agent, the results fully corresponded to the structure of the samples. Samples without pores (pure HIPS and HIPS without nanoparticles) could withstand higher compressive stresses. In contrast, samples with nanoparticles that contained microscopically observable porosity showed after linear elastic regime lower plastic collapse stress. For all samples printed below the decomposition temperature, continuous strain hardening occurred after the linear regime without overshoot at yield point and without constant plateau regime. Pure HIPS, HIPS without nanoparticles, and sample with fumed silica showed a perfectly plastic gradual deformation when the original cylinder was deformed into a perfect compressed cylinder with a lower height and a larger diameter after the mechanical test. Sample with spherical silica was also deformed into a compressed cylinder, but there was a slight fracturing on the surface of the cylinder constitute of small cracks.

In the case of samples 3D printed above the decomposition temperature of the blowing agent, the highest stress was again withstood by pure HIPS without porosity. Porous samples without nanoparticles and with fumed silica showed lower plastic collapse stress after the elastic region with gradual strain hardening without overshoot on yield point. On the other hand, the sample with spherical silica reached higher stresses within the linear elastic region than other porous samples, its elastic region was followed by a significant overshoot on yield and some of its specimens switched to a constant plateau mode, some specimens collapsed before the plateau regimen. Pure HIPS, HIPS without nanoparticles, and the sample with fumed silica were again deformed into a perfect cylinder, but test specimens of the sample with spherical silica crashed during loading by axial splitting, so there was a complete failure material before reaching set up maximum deformation.

Pure HIPS was not included among the samples after post-process foaming, because as the only sample it did not contain a blowing agent, it was not possible to foam it and the post-processing thermal treatment did not make sense for this sample. All other samples had approximately the same porosity and density, but the sample without nanoparticles had significantly larger pores and significantly lower cell density. This difference in structure was well reflected in the deformation response when due to the finer pore structure of the samples with nanoparticles, higher plastic collapse stress was achieved than in the case of samples without nanoparticles. All samples showed a significant overshoot in the yield region after the elastic region followed by a plateau regime. Only the sample with spherical silica failed before the plateau regimen, but this sample showed the highest yield point peak. The sample without nanoparticles was deformed into a compressed cylinder, but the surface was damaged by small cracks along the edges. The fumed silica sample deformed into a perfect cylinder without disturbing the surface. Samples with spherical silica showed multiple fracturing before reaching set up maximum deformation.

The quantification of compressive properties (elastic modulus and offset yield strength) of cylinders after 3D printing and post-processing foaming was performed and is graphically shown in Figure 72. Both properties were also evaluated as specific property. More about the data evaluation could be found in paragraph 4.3.4.

In the case of 3D printing below the decomposition temperature of the blowing agent, samples without porosity (pure HIPS and HIPS without nanoparticles) surpassed the samples with visible pores formed due to the presence of nanoparticles both in the modulus value and in the yield strength value, even in the case of evaluation of specific properties. The sample without nanoparticles had a slightly higher modulus than pure HIPS due to reinforcement by undecomposed blowing agent particles. In the case of 3D printing above the decomposition temperature of the blowing agent, the sample with spherical silica surpassed all other samples – it had the highest value of modulus and yield strength if the specific properties were taken into account, then even a higher yield strength than pure HIPS without additives. The sample without nanoparticles and with fumed silica had equal values significantly lower than pure HIPS and the sample with spherical silica. In the case of post-processing foaming, both samples with nanoparticles exceeded the properties of the sample without nanoparticles as to the value of modulus and yield strength.

The effective improvement of mechanical properties by nanoparticles was demonstrated especially in samples where nanoparticles were allowed to fully manifest during porosity formation, i.e. post-processing foaming because the system was not limited by the short time or limited space for foaming. Unlike samples directly after 3D printing, when porosity formation was significantly affected by the deposition of individual printed layers and the forming pores were spread with an extruder nozzle. Samples with solvent-casted spherical silica were more brittle due to the disruption of the rubber effect by nanoparticles.

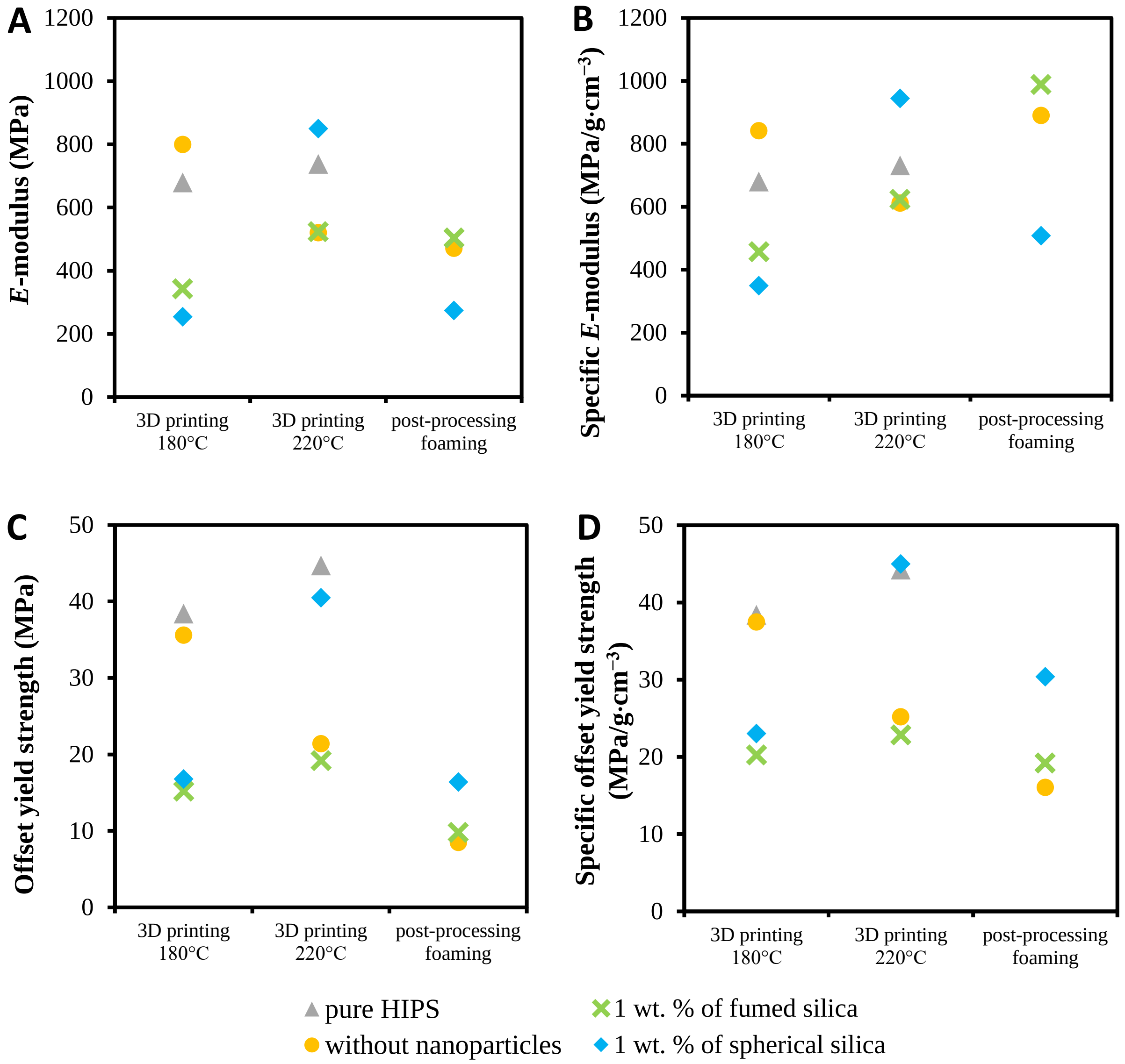

Figure 72: Graphical evaluation of compressive properties of 3D printed cylinders. **A** – measured elastic modulus, **B** – specific elastic modulus, **C** – measured offset yield strength, **D** – specific offset yield strength. Raw data are available in the appendix.

To incorporate new 3D printed materials produced using foamable filament based on HIPS, azodicarbonamide, and nanosilica particles into a wide range of material options, the results of mechanical tests (compression modulus) and structural tests (density, therefore porosity) were entered in the Asby diagram presented in paragraph 2.2.6. The samples created in this dissertation thesis were drawn in the graph with red dots (Figure 73). 3D printed foams with a hierarchical structure designed from nano to macro scale were shifted from the area of foams to the area of natural materials (dark green envelop) and some with a higher modulus of elasticity and higher density also extend into the area of solid polymer materials (dark blue envelop).

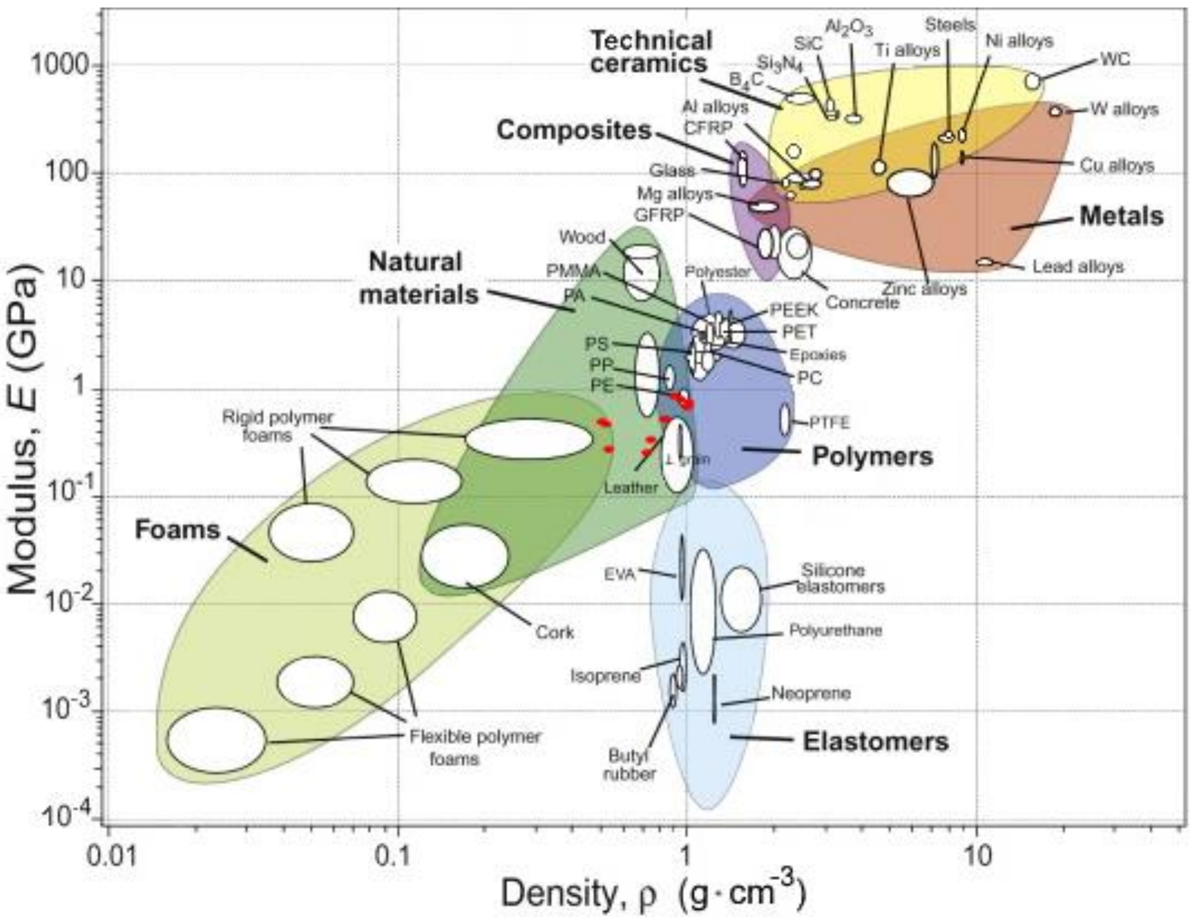

Figure 73: 3D printed HIPS foams with a chemical blowing agent and nanosilica plotted in Ashby diagram. Red points represent foams prepared in this work. *Original figure reuse from* [139].

Generally summarized, post-processing foaming samples were in the lower density and lower modulus regions, while samples printed above the decomposition temperature of the blowing agent were in the higher density and higher modulus regions. Samples with nanoparticles printed below the decomposition temperature of the blowing agent showed a slightly higher density and low modulus and samples with pure HIPS and without nanoparticles were in the region of higher density and higher modulus.

6 CONCLUSION

Cellular nanocomposites with structure organized on multiple hierarchical levels were prepared using the additive manufacturing technique. The principle governing the self-assembly of silica in glassy polymer nanocomposites prepared by solvent-casting was found. The difference in the Hildebrand solubility parameter between the polymer and the solvent was proved to be the decisive parameter. In the case of a small difference between the solubility parameters, the particles were coated with an adsorbed layer of compact polymer coils which stabilized good dispersion. If the difference between the parameters was large, the polymer chains adsorbed on one particle were more expanded and flexible and therefore did not form a steric barrier for another particle, and contact aggregation occurred. The expanded coil could act as bridging molecules within a cluster. Another important parameter was the ζ-potential of nanoparticles in a given solvent, which represented the charge on the silica surface and the ability of the solvent to create a solvation shell around the particles.

Three solvents producing very good dispersion of nanoparticles in glassy PS were also investigated in systems with two-component polymer blend HIPS. Cyclohexanone dissolved both components of the HIPS – PS matrix and rubber particles. Thus, small spherical nanosilica was capable to penetrate into occluded rubber particles and assembled in the PS-rubber interface. DMAC and DMF dissolved selectively PS and did not dissolve PBR particles. Therefore, silica was unable to enter the rubber particles and remained only in the PS matrix. Sufficiently small particles with spherical geometry and non-selective solvent were needed for the efficient incorporation of silica into the rubber particles of the HIPS.

HIPS nanocomposite with solvent-casted spherical silica (prepared in cyclohexanone) and melt-blended fumed nanosilica were used for the preparation of foamable filaments for 3D printing using azodicarbonamide as the blowing agent. Azodicarbonamide had a sufficiently high decomposition temperature to prevent its unwanted foaming during processing (filament extrusion, 3D printing), but at the same time, its decomposition temperature was low enough to avoid excessive HIPS degradation.

It has been shown that nanoparticles behaved as nucleating agents for the pores. Pore growth was facilitated on the surface of the nanoparticles, creating more stable nucleation centers leading to foams with a larger amount with smaller pores. The formed pores were always closed. Nanoparticles were the most effective at low concentrations below 1 wt. % to create foams with small pores.

The presented foamable HIPS-nanoparticle material for 3D printing offered a huge variability of possibilities – a non-foamed solid sample was printed, a porous sample was directly printed as well or the sample was foamed to large dimensions after printing by post-processing foaming in the oven. And all of this was done using one filament by a simple variation of printer settings.

Mechanical properties of the cellular foamable materials were also analyzed to characterize prepared systems. Despite the used additives forming a small microscopically observable porosity in the filaments themselves, the quality of the foamable filaments for 3D printing was comparable to the pure HIPS standardly used for 3D printing as was shown by tensile tests. In the case of compressive properties of 3D printed samples, the addition of nanoparticles in many cases even improved the properties of the material compared to pure HIPS.

The solvent-casted spherical silica system was more similar to the nanoparticle-free system (in terms of density, cell density, porosity and did not form observable porosity during extrusion, the filaments were smooth), which was advantageous for processing. At the same time, it had more modified properties than a fumed silica system after 3D printing. The only disadvantage of this system was the higher brittleness due to the suppression of the rubber effect in HIPS by the presence of nanoparticles at the PS-rubber interface and in the rubber particles. But despite this embrittlement, the 3D material was printable and showed, for example, an increase in the modulus of elasticity.

The material based on HIPS and azodicarbonamide with the possible addition of nanoparticles developed in this dissertation was essentially a finished and characterized product that could contribute to the satisfaction of the growing demand for 3D printing materials with enhanced specialized properties.

7 APPENDIX – RAW DATA

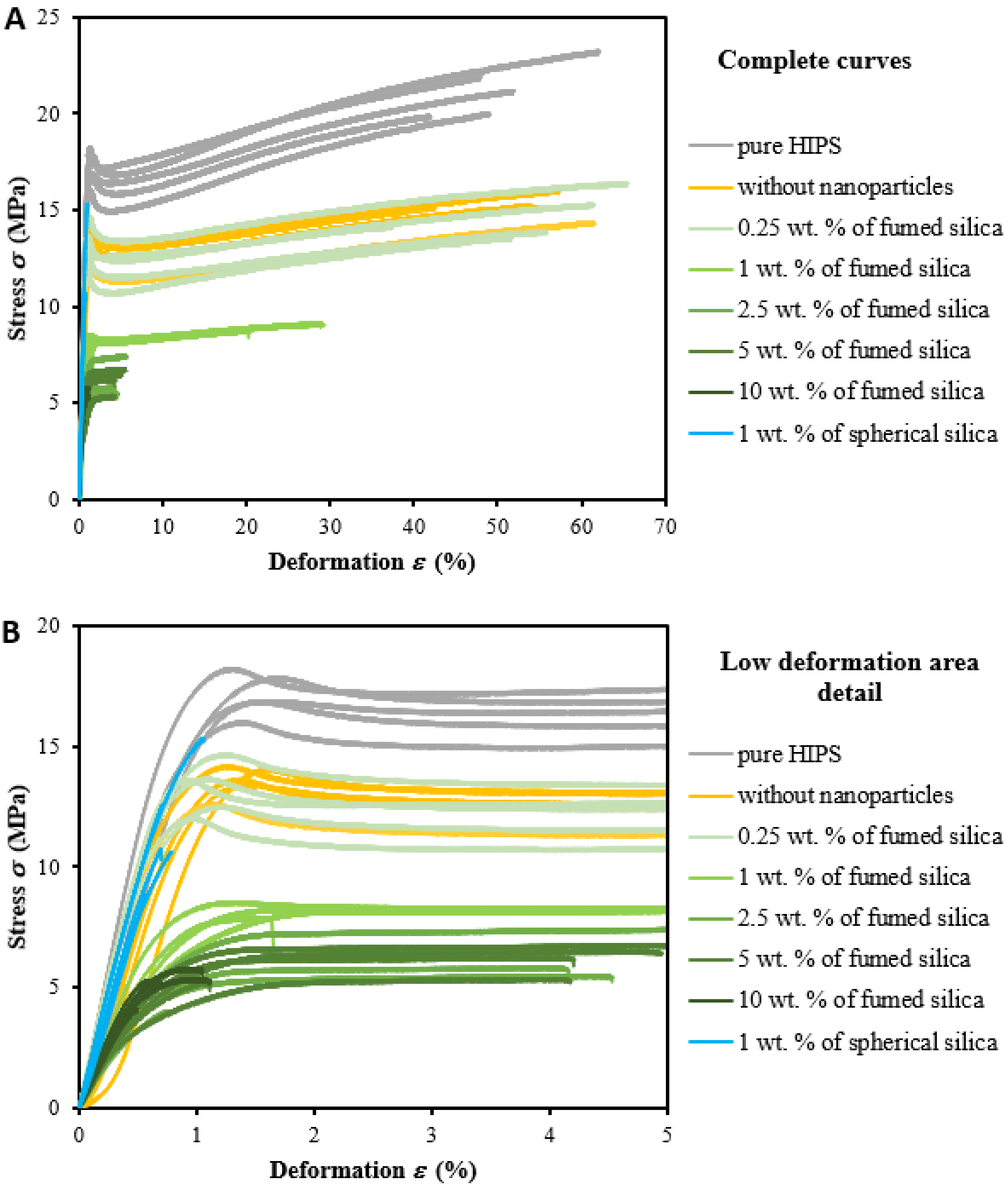

Figure 74: All tensile stress-strain curves of extruded filaments. **Top** – complete curves. **Bottom** – detail of low deformation area.

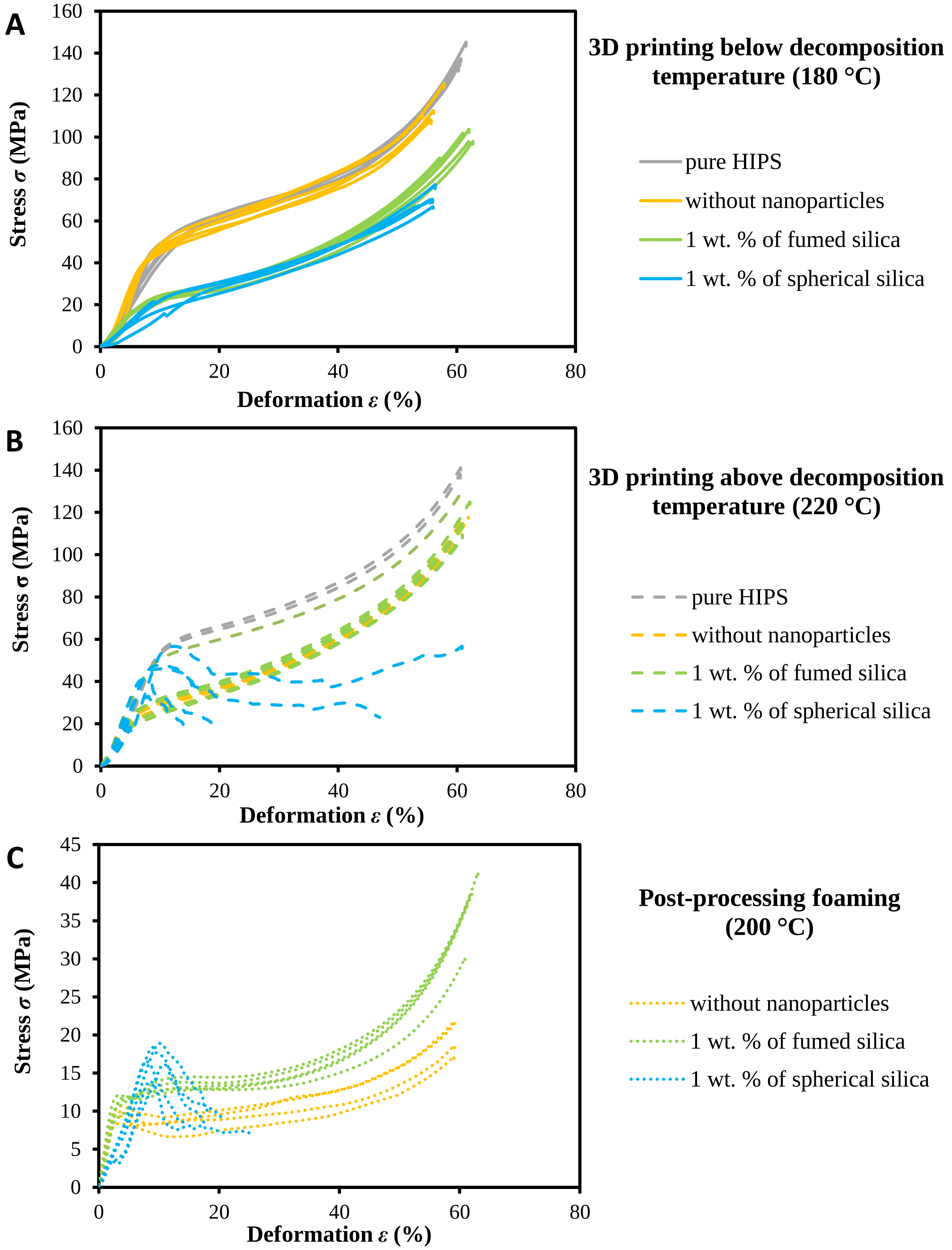

Figure 75: All compressive stress-strain curves of 3D printed cylinders. **Top** – Cylinders printed below the decomposition temperature of the blowing agent. **Middle** – Cylinders printed above the decomposition temperature of the blowing agent. **Bottom** – Cylinders after post-processing foaming.

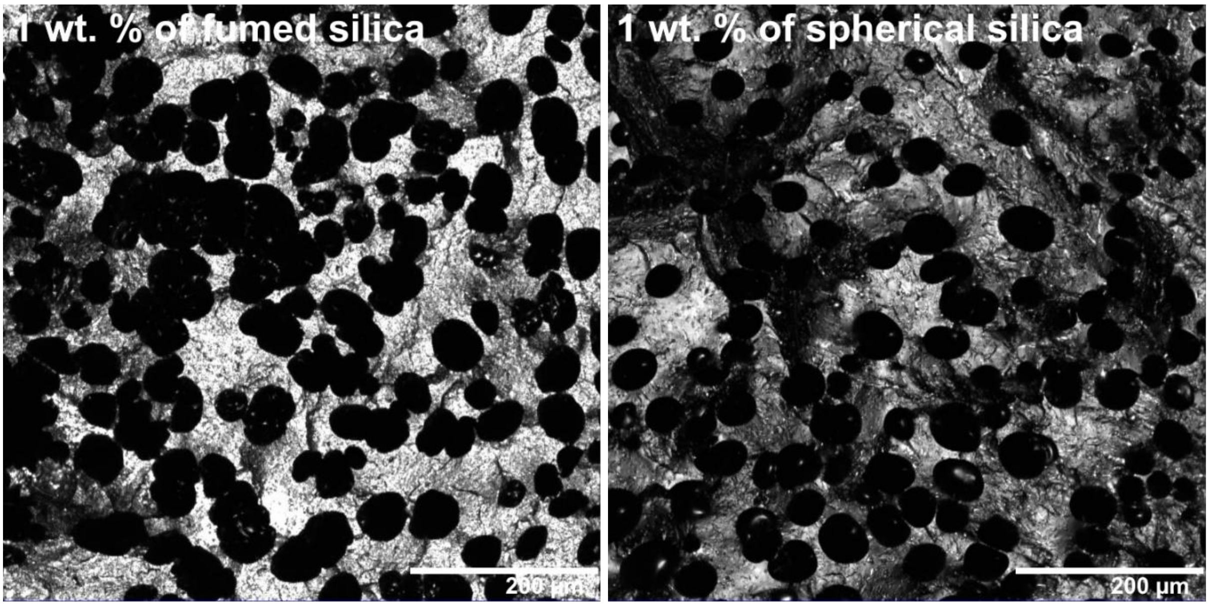

Figure 76: CLSM images of filaments for 3D printing – HIPS with 2 wt. % of blowing agent. With 1 wt. % of melt-blended fumed silica (**left**) and with 1 wt. % of solvent-casted spherical silica (**right**).

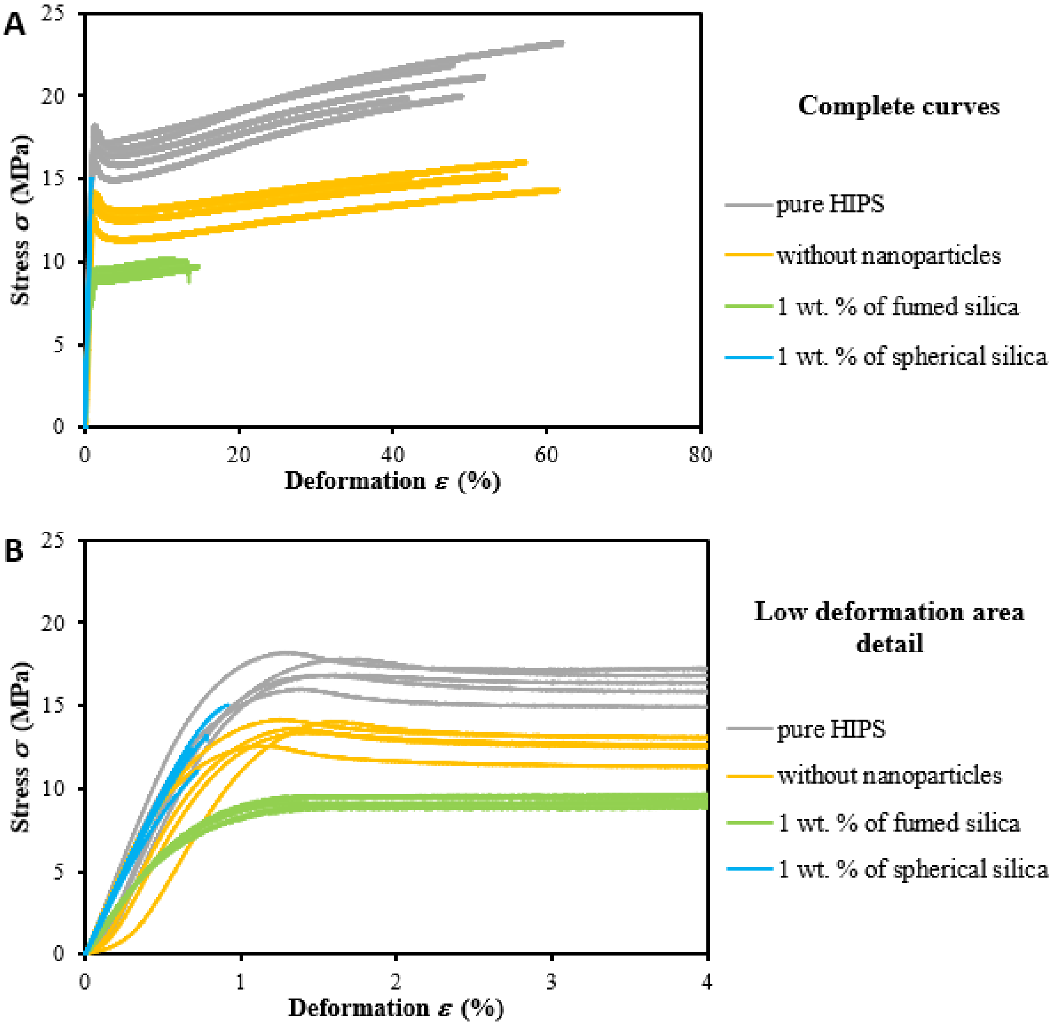

Figure 77: Tensile stress-strain curves of filaments for 3D printing. **Top** – complete curves. **Bottom** – detail of low deformation area.

Table 4: *ζ*-potential of spherical colloidal silica in a variety of solvents and their polarity index.

Solvent	*ζ*-potential (mV)	Polarity index *PI* [157] (–)	log(*PI*) (–)
acetone	−24.1	35.5	1.55
acetone – toluene (1:1)	−30.4	22.7	1.36
toluene	−4.8	9.9	1.00
acetonitrile	−25.9	46	1.66
THF	−8.5	21	1.32
DCM	−23.2	30.9	1.49
dioxane	0.6	16.4	1.21
xylene	−2.5	7.4	0.87
anisole	−27.3	19.8	1.30
isopropanol	−24.7	54.6	1.74
ethyl acetate	−6.1	23	1.36
DMAC	−34.5	40.1	1.60
water	−29.2	100	2.00

Table 5: Reciprocal absolute difference of Hildebrand solubility parameter between solvent and polymer and size of agglomerates of polymer nanocomposites filled with spherical silica with the size of single-particle d_{sp} = 20 nm.

Polymer	Solvent	$1/\lvert\delta_p - \delta_s\rvert$ (MPa$^{-0.5}$)	Size of agglomerates d_w (nm)	d_w/d_{sp} (–)
PVAc	acetone	1.3	34	1.70
	acetone, toluene (1:1)	4	49	2.45
	toluene	0.8	33	1.67
	THF (individual particles)	1.1	31	1.50
	THF (aggregates)	1.1	227	11.35
PMMA	acetone	0.8	31	1.54
	acetone, toluene (1:1)	4	70	3.49
	toluene (small aggregates)	1.3	34	1.70
	toluene (larger aggregates	1.3	244	12.20
	THF (individual particles)	2.5	17	0.87
	THF (aggregates)	2.5	664	33.20
	acetonitrile	0.2	34	1.68
	ethyl acetate	2.5	33	1.67
	anisole	2	320	16.00
	cyclohexanone	0.8	30	1.51
PC	THF	1	62	3.12
	DCM	5	1395	69.75
	dioxane (longitudial)	1.1	5000	250.00
	dioxane (transverse)	1.1	470	23.50
PS	THF	10	2281	114.05
	DMAC	0.3	37	1.87
	DMF	0.2	44	2.19
	cyclohexanone	0.6	40	2.00
	toluene (aggregates)	2	403	20.15

Table 5: Reciprocal values of the difference of Hildebrand solubility parameter between solvent and polymer and size of agglomerates of polymer nanocomposites filled with fumed silica with the size of single-particle d_{sp} = 70 nm or AZO particles with the size of single-particle d_{sp} = 20 nm.

Particles	Polymer	Solvent	$1/\lvert\delta_p – \delta_s\rvert$ ($MPa^{–0.5}$)	Size of agglomerates d_w (nm)	d_w/d_{sp} (–)
Fumed silica	PMMA	acetone	0.8	112	1.73
		THF	2.5	204	2.92
	PVAc	acetone	1.3	183	2.62
AZO particles	PMMA	acetone	0.8	143	7.14
		toluene	2.5	526	26.31
	PC	THF	1.0	395	19.74

Table 6: Raw data of T_g and E_A of pure polymers without nanoparticles (matrix) and polymer nanocomposites with 1 vol. % of nanosilica prepared in THF. Calculated values of ΔT_g and rel. E_A.

	Pure polymer without nanoparticles		NC with 1 vol. % of nanosilica		Shift of glass transition temperature	Relative activation energy of glass transition
	$T_{g,\ matrix}$ (°C)	$E_{A,\ matrix}$ (kJ)	$T_{g,\ NC}$ (°C)	$E_{A,\ NC}$ (kJ)	ΔT_g (°C)	rel. E_A (%)
PVAc	41.1	271.3	42.2	334.4	1.1	123.3
PMMA	115.6	462.5	117.9	499.6	2.3	108.0
PC	143.9	494.3	144.2	676.8	0.3	136.9
PS	87.5	374.3	92.5	366.5	4.9	97.9

Table 6: Raw data of structure parameters of extruded filaments.

Filament	Theoretical density of solid material ($g\cdot cm^{–3}$)	Measured density of foam material ($g\cdot cm^{–3}$)	Porosity (%)	Average pore size (μm)	Cell density ($cells\cdot cm^{–3}$)
pure HIPS	1.03	N/A	0	N/A	N/A
without nanoparticles	1.04	0.95	8.7	32	$1.38\cdot 10^{10}$
0.25 wt. % of fumed silica	1.04	0.91	12.5	29	$1.08\cdot 10^{10}$
1 wt. % of fumed silica	1.04	0.70	32.7	34	$7.63\cdot 10^{10}$
2.5 wt. % of fumed silica	1.05	0.67	36.2	44	$4.83\cdot 10^{10}$
5 wt. % of fumed silica	1.07	0.64	40.2	42	$5.57\cdot 10^{10}$
10 wt. % of fumed silica	1.09	0.64	41.3	54	$2.88\cdot 10^{10}$
1 wt. % of spherical silica	1.04	0.82	21.2	37	$3.16\cdot 10^{10}$

Table 6: Raw data of structure parameters of cylinders 3D printed below the decomposition temperature of blowing agent.

Filament	Theoretical density of solid material	Measured density of foam material	Porosity	Average pore size	Cell density
	($g \cdot cm^{-3}$)	($g \cdot cm^{-3}$)	(%)	(μm)	($cells \cdot cm^{-3}$)
without nanoparticles	1.04	0.95	8.7	N/A	N/A
1 wt. % of fumed silica	1.04	0.75	27.9	30	$2.20 \cdot 10^{10}$
1 wt. % of spherical silica	1.04	0.83	20.2	19	$1.29 \cdot 10^{11}$

Table 6: Raw data of structure parameters of cylinders 3D printed above the decomposition temperature of blowing agent.

Filament	Theoretical density of solid material	Measured density of foam material	Porosity	Average pore size	Cell density
	($g \cdot cm^{-3}$)	($g \cdot cm^{-3}$)	(%)	(μm)	($cells \cdot cm^{-3}$)
without nanoparticles	1.04	0.85	18.3	27	$2.85 \cdot 10^{10}$
1 wt. % of fumed silica	1.04	0.84	19.2	23	$3.32 \cdot 10^{10}$
1 wt. % of spherical silica	1.04	0.90	13.5	26	$5.87 \cdot 10^{9}$

Table 6: Raw data of structure parameters of post-processing foamed cylinders.

Filament	Theoretical density of solid material	Measured density of foam material	Porosity	Average pore size	Cell density
	($g \cdot cm^{-3}$)	($g \cdot cm^{-3}$)	(%)	(μm)	($cells \cdot cm^{-3}$)
without nanoparticles	1.04	0.53	49.0	339	$2.84 \cdot 10^{6}$
1 wt. % of fumed silica	1.04	0.51	51.0	135	$3.98 \cdot 10^{7}$
1 wt. % of spherical silica	1.04	0.54	48.1	132	$4.97 \cdot 10^{7}$

Table 6: Raw data of tensile properties of extruded filaments.

Filament	Measured values								Density	Specific values							
	E	S.D.	$\sigma_{0.2}$	S.D.	σ_{max}	S.D.	ε_{max}	S.D.		E	S.D.	$\sigma_{0.2}$	S.D.	σ_{max}	S.D.	ε_{max}	S.D.
	(MPa)		(MPa)		(MPa)		(%)		($g \cdot cm^{-3}$)	(MPa)		(MPa)		(MPa)		(%)	
pure HIPS	2.23	0.12	15.6	0.9	21.2	1.4	50.5	7.4	1.03	2.17	0.12	15.1	0.9	20.6	1.4	49.1	7.2
without nanoparticles	1.91	0.24	12.6	0.7	15.1	0.6	53.9	7.1	0.95	2.01	0.25	13.3	0.7	15.9	0.6	56.8	7.5
0.25 wt. % of fumed silica	2.17	0.09	12.7	1.0	14.6	1.2	54.3	10.8	0.91	2.38	0.10	14.0	1.1	16.1	1.3	59.7	11.9
1 wt. % of fumed silica	1.19	0.17	7.1	0.7	8.4	0.5	12.7	12.0	0.70	1.70	0.24	10.1	1.0	12.1	0.7	18.2	17.2
2.5 wt. % of fumed silica	0.90	0.08	4.7	0.7	5.4	1.3	3.1	2.2	0.67	0.88	0.08	7.0	1.0	5.3	1.3	4.7	3.4
5 wt. % of fumed silica	1.02	0.07	4.6	0.7	6.0	0.7	4.0	1.7	0.64	1.07	0.08	7.2	1.1	6.3	0.7	6.2	2.6
10 wt. % of fumed silica	1.12	0.09	5.3*	0.4	5.1	0.6	0.8	0.3	0.64	1.24	0.10	8.3*	0.6	5.6	0.7	1.2	0.4
1 wt. % of spherical silica	1.83	0.16	14.7**	N/A	11.6	2.5	0.8	0.2	0.82	2.62	0.23	17.9**	N/A	14.2	3.5	0.9	0.2

*Offset yield strength was determined from 3 values.

**Offset yield strength was determined from 1 value.

Table 7: Raw data of compression properties of cylinders 3D printed below the decomposition temperature of blowing agent.

3D printed cylinder	Measured values				Density	Specific values			
	E	S.D.	$\sigma_{0.2}$	S.D.		E	S.D.	$\sigma_{0.2}$	S.D.
	(MPa)		(MPa)		(g·cm^{-3})	(MPa)		(MPa)	
pure HIPS	680	188	38.4	2.3	1.00	680	188	38.4	2.3
without nanoparticles	800	68	35.6	1.7	0.95	843	71	37.5	1.8
1 wt. % of fumed silica	344	39	15.2	1.5	0.75	458	52	20.3	2.0
1 wt. % of spherical silica	255	28	16.8	4.3	0.73	350	39	23.0	5.9

Table 8: Raw data of compression properties of cylinders 3D printed above the decomposition temperature of blowing agent.

3D printed cylinder	Measured values				Density	Specific values			
	E	S.D.	$\sigma_{0.2}$	S.D.		E	S.D.	$\sigma_{0.2}$	S.D.
	(MPa)		(MPa)		(g·cm^{-3})	(MPa)		(MPa)	
pure HIPS	739	49	44.7	7.4	1.01	731.7	49	44.3	7.3
without nanoparticles	521	64	21.4	1.3	0.85	612.5	76	25.2	1.5
1 wt. % of fumed silica	524	40	19.2	3.4	0.84	623.7	48	22.9	4.0
1 wt. % of spherical silica	850	99	40.5	8.4	0.90	944.9	110	45.0	9.3

Table 9: Raw data of compression properties of post-processing foamed cylinders.

3D printed cylinder	Measured values				Density	Specific values			
	E	S.D.	$\sigma_{0.2}$	S.D.		E	S.D.	$\sigma_{0.2}$	S.D.
	(MPa)		(MPa)		(g·cm^{-3})	(MPa)		(MPa)	
without nanoparticles	472	39	8.5	0.9	0.53	891	73	16.0	1.7
1 wt. % of fumed silica	504	44	9.8	0.9	0.51	989	86	19.2	1.8
1 wt. % of spherical silica	275	30	16.4	1.9	0.54	508	56	30.4	3.5

8 BIBLIOGRAPHY

[1] WEGST, Ulrike, Hao BAI, Eduardo SAIZ, Antoni TOMSIA and Robert RITCHIE. Bioinspired structural materials. *Nature Materials*. 2015, **14**(1), 23-36. ISSN 1476-1122. Available at: doi:10.1038/nmat4089

[2] GIBSON, Lorna. Biomechanics of cellular solids. *Journal of Biomechanics*. 2005, **38**(3), 377-399. ISSN 00219290. Available at: doi:10.1016/j.jbiomech.2004.09.027

[3] FRATZL, Peter and Richard WEINKAMER. Nature's hierarchical materials. *Progress in Materials Science*. 2007, **52**(8), 1263-1334. ISSN 00796425. Available at: doi:10.1016/j.pmatsci.2007.06.001

[4] DIXON, P. and L. GIBSON. The structure and mechanics of Moso bamboo material. *Journal of The Royal Society Interface*. 2014, **11**(99), 20140321-20140321. ISSN 1742-5689. Available at: doi:10.1098/rsif.2014.0321

[5] WOESZ, Alexander, James WEAVER, Murat KAZANCI, Yannicke DAUPHIN, Joanna AIZENBERG, Daniel MORSE and Peter FRATZL. Micromechanical properties of biological silica in skeletons of deep-sea sponges. *Journal of Materials Research*. 2006, **21**(08), 2068-2078. ISSN 0884-2914. Available at: doi:10.1557/jmr.2006.0251

[6] KAO, Joseph, Kari THORKELSSON, Peter BAI, Benjamin RANCATORE and Ting XU. Toward functional nanocomposites: taking the best of nanoparticles, polymers, and small molecules. *Chem. Soc. Rev*. 2013, **42**(7), 2654-2678. ISSN 0306-0012. Available at: doi:10.1039/C2CS35375J

[7] FENG, Jiawei, Jianzhong FU, Ce SHANG, Zhiwei LIN, Xiaomiao NIU and Bin LI. Efficient generation strategy for hierarchical porous scaffolds with freeform external geometries. *Additive Manufacturing*. 2020, **31**. ISSN 22148604. Available at: doi:10.1016/j.addma.2019.100943

[8] YANG, Xiao-Yu, Li-Hua CHEN, Yu LI, Joanna ROOKE, Clément SANCHEZ and Bao-Lian SU. Hierarchically porous materials: synthesis strategies and structure design. *Chemical Society Reviews*. 2017, **46**(2), 481-558. ISSN 0306-0012. Available at: doi:10.1039/C6CS00829A

[9] ZENG, C., X. HAN, L.J. LEE, K.W. KOELLING and D.L. TOMASKO. Polymer–Clay Nanocomposite Foams Prepared Using Carbon Dioxide. *Advanced Materials*. 2003, **15**(20), 1743–1747. ISSN 0935-9648. Available at: doi:10.1002/adma.200305065

[10] LEE, L, C ZENG, X CAO, X HAN, J SHEN and G XU. Polymer nanocomposite foams. *Composites Science and Technology*. 2005, **65**(15-16), 2344-2363. ISSN 02663538. Available at: doi:10.1016/j.compscitech.2005.06.016

[11] JANCAR, J., J.F. DOUGLAS, F.W. STARR, S.K. KUMAR, P. CASSAGNAU, A.J. LESSER, S.S. STERNSTEIN and M.J. BUEHLER. Current issues in research on structure–property relationships in polymer nanocomposites. *Polymer*. 2010, **51**(15), 3321-3343. ISSN 00323861. Available at: doi:10.1016/j.polymer.2010.04.074

[12] AKSIT, Merve, Chunjing ZHAO, Bastian KLOSE, Klaus KREGER, Hans-Werner SCHMIDT and Volker ALTSTÄDT. Extruded Polystyrene Foams with Enhanced Insulation and Mechanical Properties by a Benzene-Trisamide-Based Additive. *Polymers*. 2019, **11**(2), 1–10. ISSN 2073-4360. Available at: doi:10.3390/polym11020268

[13] LOBOS, Juan and Sachin VELANKAR. How much do nanoparticle fillers improve the modulus and strength of polymer foams?. *Journal of Cellular Plastics*. 2016, **52**(1), 57-88. ISSN 0021-955X. Available at: doi:10.1177/0021955X14546015

[14] WICKLEIN, Bernd, Andraž KOCJAN, German SALAZAR-ALVAREZ, Federico CAROSIO and Giovanni CAMINO. Thermally insulating and fire-retardant lightweight anisotropic foams based on nanocellulose and graphene oxide. *Nature Nanotechnology*. 2015, **10**(3), 277–283. ISSN 1748-3387. Available at: doi:10.1038/NNANO.2014.248

[15] JIANG, Yanhui and Qiming WANG. Highly-stretchable 3D-architected Mechanical Metamaterials. *Scientific Reports*. 2016, **6**(1). ISSN 2045-2322. Available at: doi:10.1038/srep34147

[16] LUONG, Dung. Structure and Compressive Properties of Invar-Cenosphere Syntactic Foams. *Materials*. 2016, **9**(2), 1–16. ISSN 1996-1944. Available at: doi:10.3390/ma9020115

[17] SALLEH, Zulzamri, Md MAINUL ISLAM, Jayantha ANANDA EPAARACHCHI and Haibin SU. Mechanical properties of sandwich composite made of syntactic foam core and GFRP skins. *AIMS Materials Science*. 2016, **3**(4), 1704-1727. ISSN 2372-0484. Available at: doi:10.3934/matersci.2016.4.1704

[18] GUPTA, Nikhil, Dinesh PINISETTY and Vasanth SHUNMUGASAMY. *Reinforced polymer matrix syntactic foams*. 1. New York: Springer, 2013. ISBN 978-3-319-01242-1.

[19] KIM, Hyunwoo, Ahmed ABDALA and Christopher MACOSKO. Graphene/Polymer Nanocomposites. *Macromolecules*. 2010, **43**(16), 6515-6530. ISSN 0024-9297. Available at: doi:10.1021/ma100572e

[20] ALEXANDRE, Michael and Philippe DUBOIS. Polymer-layered silicate nanocomposites: preparation, properties and uses of a new class of materials. *Material Science and Enfineering*. 2000, **28**, 1–63.

[21] MONIRUZZAMAN, Mohammad and Karen WINEY. Polymer Nanocomposites Containing Carbon Nanotubes. *Macromolecules*. 2006, **39**(16), 5194-5205. ISSN 0024-9297. Available at: doi:10.1021/ma060733p

[22] AZIZI SAMIR, My, Fannie ALLOIN and Alain DUFRESNE. Review of Recent Research into Cellulosic Whiskers, Their Properties and Their Application in Nanocomposite Field. *Biomacromolecules*. 2005, **6**(2), 612-626. ISSN 1525-7797. Available at: doi:10.1021/bm0493685

[23] HASHEMI, Amir, Nicolas JOUAULT, Gregory WILLIAMS, Dan ZHAO, Kevin CHENG, Jeffrey KYSAR, Zhibin GUAN and Sanat KUMAR. Enhanced Glassy State Mechanical Properties of Polymer Nanocomposites via Supramolecular Interactions. *Nano Letters*. 2015, **15**(8), 5465-5471. ISSN 1530-6984. Available at: doi:10.1021/acs.nanolett.5b01859

[24] HOTZE, Ernest, Tanapon PHENRAT and Gregory LOWRY. Nanoparticle Aggregation: Challenges to Understanding Transport and Reactivity in the Environment. *Journal of Environment Quality*. 2010, **39**(6), 1909–1924. ISSN 1537-2537. Available at: doi:10.2134/jeq2009.0462

[25] LEPCIO, Petr, Frantisek ONDREAS, Klara ZARYBNICKA, Marek ZBONCAK, Ondrej CAHA and Josef JANCAR. Bulk polymer nanocomposites with preparation protocol governed nanostructure: the origin and properties of aggregates and polymer bound clusters. *Soft Matter*. 2018, **14**(11), 2094-2103. ISSN 1744-683X. Available at: doi:10.1039/C8SM00150B

[26] DLAMINI, D.S., S.B. MISHRA, A.K. MISHRA and B.B. MAMBA. Comparative studies of the morphological and thermal properties of clay/polymer nanocomposites synthesized via melt blending and modified solution blending methods. *Journal of Composite Materials*. 2011, **45**(21), 2211-2216. ISSN 0021-9983. Available at: doi:10.1177/0021998311401074

[27] WAHIT, M., A. HASSAN, A. RAHMAT and Z. ISHAK. Morphological and Mechanical Properties of Rubber-toughened Polyamide 6/Polypropylene Nanocomposites Prepared by Different Methods of Compounding. *Journal of Elastomers and Plastics*. 2016, **38**(3), 231-247. ISSN 0095-2443. Available at: doi:10.1177/0095244306063852

[28] KUMAR, Sanat, Nicolas JOUAULT, Brian BENICEWICZ and Tony NEELY. Nanocomposites with Polymer Grafted Nanoparticles. *Macromolecules*. 2013, **46**(9), 3199-3214. ISSN 0024-9297. Available at: doi:10.1021/ma4001385

[29] LIN, Jia-Horng, Yi-Jun PAN, Chien-Teng HSIEH, Chen-Hung HUANG, Zheng-Ian LIN, Yueh-Sheng CHEN, Kuan-Hua SU and Ching-Wen LOU. Using multiple melt blending to improve the dispersion of montmorillonite in polyamide 6 nanocomposites. *Polymer Testing*. 2016, **56**, 74-82. ISSN 01429418. Available at: doi:10.1016/j.polymertesting.2016.09.016

[30] JOUAULT, Nicolas, Dan ZHAO and Sanat KUMAR. Role of Casting Solvent on Nanoparticle Dispersion in Polymer Nanocomposites. *Macromolecules*. 2014, **47**(15), 5246-5255. ISSN 0024-9297. Available at: doi:10.1021/ma500619g

[31] JOUAULT, Nicolas, Perrine VALLAT, Florent DALMAS, Sylvère SAID, Jacques JESTIN and François BOUÉ. Well-Dispersed Fractal Aggregates as Filler in Polymer−Silica Nanocomposites: Long-Range Effects in Rheology. *Macromolecules*. 2009, **42**(6), 2031-2040. ISSN 0024-9297. Available at: doi:10.1021/ma801908u

[32] ABBASIAN, Mojtaba and Robab MAHI. In-situ synthesis of polymer – silica nanocomposites by living radical polymerisation using TEMPO initiator. *Journal of Experimental Nanoscience*. 2012, **9**(8), 785-798. ISSN 1745-8080. Available at: doi:10.1080/17458080.2012.714482

[33] HOOPER, Justin and Kenneth SCHWEIZER. Contact Aggregation, Bridging, and Steric Stabilization in Dense Polymer−Particle Mixtures. *Macromolecules*. 2005, **38**(21), 8858-8869. ISSN 0024-9297. Available at: doi:10.1021/ma051318k

[34] HOOPER, Justin and Kenneth SCHWEIZER. Theory of Phase Separation in Polymer Nanocomposites. *Macromolecules*. 2006, **39**(15), 5133-5142. ISSN 0024-9297. Available at: doi:10.1021/ma060577m

[35] HOOPER, Justin and Kenneth SCHWEIZER. Real Space Structure and Scattering Patterns of Model Polymer Nanocomposites. *Macromolecules*. 2007, **40**(19), 6998-7008. ISSN 0024-9297. Available at: doi:10.1021/ma071147e

[36] MACKAY, M. General Strategies for Nanoparticle Dispersion. *Science*. 2006, **311**(5768), 1740-1743. ISSN 0036-8075. Available at: doi:10.1126/science.1122225

[37] MARMO, Michael, Mohamed MOSTAFA, Hideo JINNAL, Frederick FOWKES and John MANSON. Acid-Base Interaction in Filler-Matrix Systems. *Industrial & Engineering Chemistry Product Research and Development*. 1976, **15**(3), 206–211.

[38] FOWKES, Frederick and Mohamed MOSTAFA. Acid-Base Interaction in Polymer Adsorption. *Industrial & Engineering Chemistry Product Research and Development*. 1978, **17**(1), 3–7.

[39] FOWKES, Frederick. Quantitative characterization of the acid-base properties of solvents, polymers, and inorganic surfaces. *Journal of Adhesion Science and Technology*. 1990, **4**(8), 669–691.

[40] DRAGO, Russell, Glenn VOGEL and Terence NEEDHAM. A Four-Parameter Equation for Predicting Enthalpies of Adduct Formation. *Journal of the American Chemical Society*. 1971, **93**(23), 6014–6026.

[41] LEPCIO, Petr. *Effect of sub-mictometer sctructural features on rheology of polymer nanocomposites*. Brno, 2018. Doctoral thesis. Brno University of Technology.

[42] ONDREAS, Frantisek. *Thermomechanical response of polymer nanocomposites with preparation protocol controlled nanoparticle dispersion*. Brno, 2018. Doctoral thesis. Brno University of Technology.

[43] LEDNICKÝ, František. *Mikroskopie a morfologie polymerů: Díl 1. Mikroskopie polymerů a preparačních technik*. Vyd. 1. V Liberci: Technická univerzita, 2009. ISBN 978-80-7372-486-3.

[44] LEDNICKÝ, František. *Mikroskopie a morfologie polymerů: Díl 2. Morfologie polymerů*. Vyd. 1. V Liberci: Technická univerzita, 2009. ISBN 978-80-7372-487-0.

[45] BALAZS, A., T. EMRICK and T. RUSSELL. Nanoparticle Polymer Composites: Where Two Small Worlds Meet. *Science*. 2006, **314**(5802), 1107-1110. ISSN 0036-8075. Available at: doi:10.1126/science.1130557

[46] SUDEEP, P. and Todd EMRICK. Pearls of Wisdom: Stringing Nanoparticles and Polymers into New Assemblies and Materials. *ACS Nano*. 2009, **3**(10), 2870-2875. ISSN 1936-0851. Available at: doi:10.1021/nn901358a

[47] LI, Qifang, Jinbo HE, Elizabeth GLOGOWSKI, Xuefa LI, Jin WANG, Todd EMRICK and Thomas RUSSELL. Responsive Assemblies: Gold Nanoparticles with Mixed Ligands in Microphase Separated Block Copolymers. *Advanced Materials*. 2008, **20**(8), 1462-1466. ISSN 09359648. Available at: doi:10.1002/adma.200702004

[48] LO, Chieh-Tsung, Byeongdu LEE, Mong-Wei GAO and Po-Wei CHOU. Ordering of block copolymer/nanoparticle composite thin films. *Polymer International*. 2013, **62**(1), 99-105. ISSN 09598103. Available at: doi:10.1002/pi.4303

[49] HUH, June, Valeriy GINZBURG and Anna BALAZS. Thermodynamic Behavior of Particle/Diblock Copolymer Mixtures: Simulation and Theory. *Macromolecules*. 2000, **33**(21), 8085-8096. ISSN 0024-9297. Available at: doi:10.1021/ma000708y

[50] LEE, Jae, Russell THOMPSON, David JASNOW and Anna BALAZS. Self-assembly of a binary mixture of particles and diblock copolymers. *Faraday Discussions*. 2003, **123**, 121-131. ISSN 13596640. Available at: doi:10.1039/b205023b

[51] ŠŇUPÁREK, Jaromír. *Makromolekulární chemie: úvod do chemie a technologie polymerů*. 1. Pardubice: Univerzita Pardubice, 2006. ISBN 80-719-4863-2.

[52] POUCHLÝ, Julius. *Fyzikální chemie makromolekulárních a koloidních soustav*. 3. Praha: Vydavatelství VŠCHT, 2008. ISBN 978-80-7080-674-6.

[53] STROBL, Gert. *The physics of polymers: concepts for understanding their structures and behavior*. 2nd corr. ed. New York: Springer, 1997. ISBN 35-406-3203-4.

[54] RUBINSTEIN, Michael and Ralph COLBY. *Polymer physics*. 1. New York: Oxford University Press, 2003. ISBN 978-0198520597.

[55] BARTOVSKÁ, Lidmila and Marie ŠIŠKOVÁ. *Fyzikální chemie povrchů a koloidních soustav*. 4. Praha: Vysoká škola chemicko-technologická v Praze, 2002. ISBN 80-708-0475-0.

[56] FERNÁNDEZ-BARBERO, A., M. CABRERIZO-VÍLCHEZ and R. MARTÍNEZ-GARCÍA, C. SOLANS, M. INFANTE, M. GARCÍA-CELMA. *Trends in Colloid and Interface Science X: Progress in colloid and polymer science*. 100. New York: Springer, 1996. ISBN 37-985-1056-3.

[57] BAGWE, Rahul, Lisa HILLIARD and Weihong TAN. Surface Modification of Silica Nanoparticles to Reduce Aggregation and Nonspecific Binding. *Langmuir*. 2006, **22**(9), 4357-4362. ISSN 0743-7463. Available at: doi:10.1021/la052797j

[58] BUTT, Hans-Jürgen, Kh GRAF and Michael KAPPL. *Physics and chemistry of interfaces*. 1. Weinheim: Wiley-VCH, 2003. ISBN 35-274-0413-9.

[59] KIM, So and Charles ZUKOSKI. Role of Polymer Segment–Particle Surface Interactions in Controlling Nanoparticle Dispersions in Concentrated Polymer Solutions. *Langmuir*. 2011, **27**(17), 10455-10463. ISSN 0743-7463. Available at: doi:10.1021/la201704u

[60] ŽÍDEK, Jan, Jiří KUČERA and Josef JANČÁŘ. Model of randomly distributed set of non-intersecting particles with controlled macroscopic homogeneity. *CMC-Computers Materials & Continua*. 2010, **450**(1), 1–23.

[61] DONALD, Athene and Edward KRAMER. Internal structure of rubber particles and craze break-down in high-impact polystyrene (HIPS). *Journal of Materials Science*. 1982, (17), 2351–2358.

[62] PAUL, Donald and C. BUCKNALL. *Polymer blends: Volume 2: Performace*. 1. New York: Wiley, 2000. ISBN 04-713-5280-2.

[63] KESKKULA, H., M. SCHWARZ and D.R. PAUL. Examination of failure in rubber toughened polystyrene. *Polymer*. 1986, **27**(2), 211-216. ISSN 00323861. Available at: doi:10.1016/0032-3861(86)90328-9

[64] SORIANO-CORRAL, Florentino, Graciela MORALES, Pablo ACUñA and Enrique DÍAZ-BARRIGA. Synthesis and Characterization of High Impact Polystyrene from a Heterogenous Styrene-Rubber-Polystyrene Solution: Influence of PS Concentration on the Phase Inversion, Morphology and Impact Strength. *Macromolecular Symposia*. 2013, **325-326**(1), 177–183. ISSN 10221360. Available at: doi:10.1002/masy.201200059

[65] SVOBODA, Luboš. *Stavební hmoty*. 1st. Bratislava: Jaga, 2004. ISBN 80-807-6007-1.

[66] TJONG, S.C. Structural and mechanical properties of polymer nanocomposites. *Materials Science and Engineering: R: Reports*. 2006, **53**(3-4), 73-197. ISSN 0927796X. Available at: doi:10.1016/j.mser.2006.06.001

[67] JANCAR, J. and L. RECMAN. Particle size dependence of the elastic modulus of particulate filled PMMA near its Tg. *Polymer*. 2010, **51**(17), 3826-3828. ISSN 00323861. Available at: doi:10.1016/j.polymer.2010.06.041

[68] JANČÁŘ, Josef. *Úvod do materiálového inženýrství polymerních kompozitů*. 1. Brno: Vysoké učení technické v Brně, 2003. ISBN 80-214-2443-5.

[69] MO, Yu and Jia XU. Studies on Mechanical Properties and Optimization Model of PI/SiO₂ Nanocomposite Based on Materials Studio. *Advanced Materials Research*. 2014, **1049-1050**(2014), 54-57. ISSN 1662-8985. Available at: doi:10.4028/www.scientific.net/AMR.1049-1050.54

[70] YANG, Feng and Gordon NELSON. Polymer/silica nanocomposites prepared via extrusion. *Polymers for Advanced Technologies*. 2006, **17**(4), 320-326. ISSN 1042-7147. Available at: doi:10.1002/pat.695

[71] JANCAR, Josef, Robert HOY, Alan LESSER, Ema JANCAROVA and Jan ZIDEK. Effect of Particle Size, Temperature, and Deformation Rate on the Plastic Flow and Strain Hardening Response of PMMA Composites. *Macromolecules*. 2013, **46**(23), 9409-9426. ISSN 0024-9297. Available at: doi:10.1021/ma400965c

[72] ZUIDERDUIN, W.C.J, C WESTZAAN, J HUÉTINK and R.J GAYMANS. Toughening of polypropylene with calcium carbonate particles. *Polymer*. 2003, **44**(1), 261-275. ISSN 00323861. Available at: doi:10.1016/S0032-3861(02)00769-3

[73] ZHANG, Jinzhu, Xin WANG, Lude LU, Dan LI and Xujie YANG. Preparation and performance of high-impact polystyrene (HIPS)/nano-TiO2 nanocomposites. *Journal of Applied Polymer Science*. 2003, **87**(3), 381-385. ISSN 0021-8995. Available at: doi:10.1002/app.11302

[74] ŠVEC, P., L. ROSÍK, Z. HORÁK and F. VEČERKA. *Polystyren a jeho modifikace*. 1st. Prague: Státní nakladatelství technické literatury, 1985.

[75] DUCHÁČEK, Vratislav. *Polymery: výroba, vlastnosti, zpracování, použití*. 1st. Praha: Vysoká škola chemicko-technologická, 1995. ISBN 80-708-0241-3.

[76] GIBSON, Lorna, M. ASHBY and Brendan HARLEY. *Cellular materials in nature and medicine*. 1st. New York: Cambridge University Press, 2010. ISBN 978-0-521-19544-7.

[77] LOKENSGARD, Erik. *Industrial plastics: theory and application*. 5th ed. Clifton Park, NY: Delmar Cengage Learning, 2010. ISBN 14283-6070-0.

[78] MILLS, N., C. FITZGERALD, A. GILCHRIST and R. VERDEJO. Polymer foams for personal protection: cushions, shoes and helmets. *Composites Science and Technology*. 2003, **63**(16), 2389-2400. ISSN 02663538. Available at: doi:10.1016/S0266-3538(03)00272-0

[79] CHRISTENSEN, Richard. A comparison of open cell and closed cell properties for low-density materials. *Journal of Mechanics of Materials and Structures*. 2007, **2**(7), 1299-1307. ISSN 1559-3959. Available at: doi:10.2140/jomms.2007.2.1299

[80] CAVASIN, M., S. GIANNIS, M. SALVO, V. CASALEGNO and M. SANGERMANO. Mechanical and thermal characterization of an epoxy foam as thermal layer insulation for a glass fiber reinforced polymer. *Journal of Applied Polymer Science*. 2018, **135**(47). ISSN 00218995. Available at: doi:10.1002/app.46864

[81] OLIVIERO, Maria, Letizia VERDOLOTTI, Mariamelia STANZIONE, Marino LAVORGNA, Salvatore IANNACE, Maurizio TARELLO and Andrea SORRENTINO. Bio-based flexible polyurethane foams derived from succinic polyol: Mechanical and acoustic performances. *Journal of Applied Polymer Science*. 2017, **134**(45). ISSN 00218995. Available at: doi:10.1002/app.45113

[82] ARAM, Elham and Shahram MEHDIPOUR-ATAEI. A review on the micro- and nanoporous polymeric foams: Preparation and properties. *International Journal of Polymeric Materials and Polymeric*

Biomaterials. 2016, **65**(7), 358-375. ISSN 0091-4037. Available at: doi:10.1080/00914037.2015.1129948

[83] FORSTER, Jason, Heeso NOH, Seng LIEW et al. Biomimetic Isotropic Nanostructures for Structural Coloration. *Advanced Materials*. 2010, **22**(26-27), 2939-2944. ISSN 09359648. Available at: doi:10.1002/adma.200903693

[84] OTSUKA, Tetsuo, Kentaro TAKI and Masahiro OHSHIMA. Nanocellular Foams of PS/PMMA Polymer Blends. *Macromolecular Materials and Engineering*. 2008, **293**(1), 78-82. ISSN 14387492. Available at: doi:10.1002/mame.200700257

[85] YOKOYAMA, Hideaki and Kenji SUGIYAMA. Nanocellular Structures in Block Copolymers with CO 2 -philic Blocks Using CO 2 as a Blowing Agent: Crossover from Micro- to Nanocellular Structures with Depressurization Temperature. *Macromolecules*. 2005, **38**(25), 10516-10522. ISSN 0024-9297. Available at: doi:10.1021/ma051757j

[86] LI, L., H. YOKOYAMA, T. NEMOTO and K. SUGIYAMA. Facile Fabrication of Nanocellular Block Copolymer Thin Films Using Supercritical Carbon Dioxide. *Advanced Materials*. 2004, **16**(14), 1226-1229. ISSN 0935-9648. Available at: doi:10.1002/adma.200400264

[87] WIRPSZA, Zygmunt. *Polyurethanes: chemistry, technology and applications*. 1st. Chichester: Ellis Horwood, 1992. ISBN 01-368-3186-9.

[88] WOLDENSENBET, Eyassu and Narendra SANKELLA. Flexural Properties of Nanoclay Syntactic Foam Sandwich Structures. *Journal of Sandwich Structures and Materials*. 2009, **11**(5), 425-444. ISSN 1099-6362. Available at: doi:10.1177/1099636209104095

[89] GUAN, Jianjun, Kazuro FUJIMOTO, Michael SACKS and William WAGNER. Preparation and characterization of highly porous, biodegradable polyurethane scaffolds for soft tissue applications. *Biomaterials*. 2005, **26**(18), 3961-3971. ISSN 01429612. Available at: doi:10.1016/j.biomaterials.2004.10.018

[90] CAI, Qing, Jian YANG, Jianzhong BEI and Shenguo WANG. A novel porous cells scaffold made of polylactide–dextran blend by combining phase-separation and particle-leaching techniques. *Biomaterials*. 2002, **23**(23), 4483-4492. ISSN 01429612. Available at: doi:10.1016/S0142-9612(02)00168-0

[91] LI, Jianhua, Zhongjie DU, Hangquan LI and Chen ZHANG. Porous epoxy monolith prepared via chemically induced phase separation. *Polymer*. 2009, **50**(6), 1526-1532. ISSN 00323861. Available at: doi:10.1016/j.polymer.2009.01.049

[92] MOSADEGH-SEDGHI, Sanaz, Denis RODRIGUE, Josée BRISSON and Maria ILIUTA. Highly hydrophobic microporous low-density polyethylene hollow fiber membranes by melt-extrusion coupled with salt-leaching technique. *Polymers for Advanced Technologies*. 2013, **24**(6), 584-592. ISSN 10427147. Available at: doi:10.1002/pat.3122

[93] REIGNIER, Joël and Michel HUNEAULT. Preparation of interconnected poly(ε-caprolactone) porous scaffolds by a combination of polymer and salt particulate leaching. *Polymer*. 2006, **47**(13), 4703-4717. ISSN 00323861. Available at: doi:10.1016/j.polymer.2006.04.029

[94] APEL, P.Yu., I.V. BLONSKAYA, S.N. DMITRIEV, T.I. MAMONOVA, O.L. ORELOVITCH, B. SARTOWSKA and Yu. YAMAUCHI. Surfactant-controlled etching of ion track nanopores and its practical applications in membrane technology. *Radiation Measurements*. 2008, **43**, 552-559. ISSN 13504487. Available at: doi:10.1016/j.radmeas.2008.04.057

[95] YAMAUCHI, Yu. and P. APEL. The effect of surfactants on chemical development of ion track nanopores in polymer. *Journal of Physics: Conference Series*. 2010, **248**. ISSN 1742-6596. Available at: doi:10.1088/1742-6596/248/1/012060

[96] NGUYEN, Thi-Hiep, Young-Hee KIM, Ho-Yeon SONG and Byong-Taek LEE. Nano Ag loaded PVA nano-fibrous mats for skin applications. *Journal of Biomedical Materials Research Part B: Applied Biomaterials*. 2011, **96**(2), 225-233. ISSN 15524973. Available at: doi:10.1002/jbm.b.31756

[97] LIU, Wanjun, Lei ZHU, Chen HUANG and Xiangyu JIN. Direct Electrospinning of Ultrafine Fibers with Interconnected Macropores Enabled by in Situ Mixing Microfluidics. *Applied Materials and Interfacec*. 2016, **8**(50), 34870-34878. ISSN 1944-8244. Available at: doi:10.1021/acsami.6b11362

[98] MCCANN, Jesse, Manuel MARQUEZ and Younan XIA. Highly Porous Fibers by Electrospinning into a Cryogenic Liquid. *Journal of the American Chemical Society*. 2006, **128**(5), 1436-1437. ISSN 0002-7863. Available at: doi:10.1021/ja056810y

[99] POP-ILIEV, Remon, Ning DONG, Donglai XU and Chul PARK. Visualization of the foaming mechanism of polyethylene blown by chemical blowing agents under ambient pressure. *Advances in Polymer Technology*. 2007, **26**(4), 213-222. ISSN 07306679. Available at: doi:10.1002/adv.20102

[100] ATAEI, Mohammadmehdi, Vahid SHAAYEGAN, Chongda WANG, Franco COSTA, Sejin HAN, Chul PARK and Markus BUSSMANN. Numerical analysis of the effect of the local variation of viscosity on bubble growth and deformation in polymer foaming. *Journal of Rheology*. 2019, **63**(6), 895-903. ISSN 0148-6055. Available at: doi:10.1122/1.5113802

[101] WONG, Anson and Chul PARK. A Modified Classical Nucleation Theory for Plastic Foam Processing. In: *Advances in Multidisciplinary Engineering*. ASME Press, 2016, s. 179-190. ISBN 9780791861080. Available at: doi:10.1115/1.861080_ch20

[102] WANG, C., S. LEUNG, M. BUSSMANN, W. ZHAI and C. PARK. Numerical Investigation of Nucleating-Agent-Enhanced Heterogeneous Nucleation. *Industrial & Engineering Chemistry Research*. 2010, **49**(24), 12783-12792. ISSN 0888-5885. Available at: doi:10.1021/ie1017207

[103] FENG, James and Christopher BERTELO. Prediction of bubble growth and size distribution in polymer foaming based on a new heterogeneous nucleation model. *Journal of Rheology*. 2004, **48**(2), 439-462. ISSN 0148-6055. Available at: doi:10.1122/1.1645518

[104] LENSKY, Nadav, Vladimir LYAKHOVSKY and Oded NAVON. Radial variations of melt viscosity around growing bubbles and gas overpressure in vesiculating magmas. *Earth and Planetary Science Letters*. 2001, **186**(1), 1-6. ISSN 0012821X. Available at: doi:10.1021/ma971811z

[105] MOON, Yongrak and Sung CHA. Study on viscosity changes with talc in microcellular foaming process. *Fibers and Polymers*. 2007, **8**(4), 393-398. ISSN 1229-9197. Available at: doi:10.1007/BF02875828

[106] ARORA, Kelyn, Alan LESSER and Thomas MCCARTHY. Preparation and Characterization of Microcellular Polystyrene Foams Processed in Supercritical Carbon Dioxide. *Macromolecules*. 1998, **31**(14), 4614-4620. ISSN 0024-9297. Available at: doi:10.1021/ma971811z

[107] SALERNO, Aurelio and Concepción DOMINGO. Polycaprolactone foams prepared by supercritical CO2 batch foaming of polymer/organic solvent solutions. *The Journal of Supercritical Fluids*. 2019, **143**, 146-156. ISSN 08968446. Available at: doi:10.1016/j.supflu.2018.08.006

[108] LIU, Jie, Shengxue QIN, Giulong WANG, Hongbin ZHANG, Haiping ZHOU and Yang GAO. Batch foaming of ultra-high molecular weight polyethylene with supercritical carbon dioxide: Influence of temperature and pressure. *Polymer Testing*. 2021, **93**. ISSN 01429418. Available at: doi:10.1016/j.polymertesting.2020.106974

[109] SHI, Shaozhe, Yuan ZHANG, Yong LUO et al. Reinforcement of Mechanical Properties of Silicone Rubber Foam by Functionalized Graphene Using Supercritical CO 2 Foaming Technology. *Industrial & Engineering Chemistry Research*. 2020, **59**(51), 22132-22143. ISSN 0888-5885. Available at: doi:10.1021/acs.iecr.0c04677

[110] SANZ-HORTA, Raúl, Enrique MARTINEZ-CAMPOS, Carolina GARCÍA, Helmut REINECKE, Alberto GALLARDO, Juan RODRIGUEZ-HERNANDEZ and Carlos ELVIRA. Breath figures makes porous the “so-called” skin layer obtained in polymer foams prepared by supercritical CO2 treatments. *The Journal of Supercritical Fluids*. 2021, **167**. ISSN 08968446. Available at: doi:10.1016/j.supflu.2020.105051

[111] KRAUSE, Katharina, Thomas NEUMEYER, Christin BAUMGART and Volker ALTSTAEDT. Influence of low heat conductive inserts on morphology of foam injection molded parts. In: *AIP*

Conference Proceedings. American Institute of Physics, 2019, s. 030047-. Available at: doi:10.1063/1.5088305

[112] WU, H., G. ZHAO, J. WANG, G. WANG and W. ZHANG. Effects of process parameters on core-back foam injection molding process. *Express Polymer Letters*. 2019, **13**(4), 390-405. ISSN 1788618X. Available at: doi:10.3144/expresspolymlett.2019.32

[113] MuCell Processes. *Trexel* [online]. Wilmington: Trexel, Inc., 2017 [cit. 2019-06-24]. Available at: https://www.trexel.com/en/mucell-injection-molding/the-process

[114] ZHAO, Jinchuan, Yongna QIAO, Guilong WANG, Chongda WANG and Chul PARK. Lightweight and tough PP/talc composite foam with bimodal nanoporous structure achieved by microcellular injection molding. *Materials and Design*. 2020, **195**. ISSN 02641275. Available at: doi:10.1016/j.matdes.2020.109051

[115] WANG, Guilong, Guoqun ZHAO, Guiwei DONG, Libin SONG and Chul PARK. Lightweight, thermally insulating, and low dielectric microcellular high-impact polystyrene (HIPS) foams fabricated by high-pressure foam injection molding with mold opening. *Journal of Materials Chemistry C*. 2018, **6**(45), 12294-12305. ISSN 2050-7526. Available at: doi:10.1039/C8TC04248A

[116] HAN, HyukSu, Hyun NAM, Youngkee EUN, Su LEE, Jeongho NAM, Jeong RYU, Sung LEE and Jungin KIM. Numerical analysis on foam reaction injection molding of polyurethane, part B: Parametric study and real application. *Journal of the Korean Crystal Growth and Crystal Technology*. 2016, **26**(6), 258-262. ISSN 1225-1429. Available at: doi:10.6111/JKCGCT.2016.26.6.258

[117] GARBACZ, Tomasz, Aneta TOR-ŚWIąTEK and Tomasz JACHOWICZ. Effect of Chemical Blowing Agent on the PVC Cellular Coating Extrusion. *Materials*. 2020, **13**(24). ISSN 1996-1944. Available at: doi:10.3390/ma13245752

[118] XU, Zhijuan, Ping XUE, Fuhua ZHU and Jimin HE. Effects of Formulations and Processing Parameters on Foam Morphologies in the Direct Extrusion Foaming of Polypropylene using a Single-screw Extruder. *Journal of Cellular Plastics*. 2005, **41**(2), 169-185. ISSN 0021-955X. Available at: doi:10.1177/0021955X05051740

[119] DEMIRTAş, Emre, Hakan ÖZKAN and Mohammadreza NOFAR. Continuous foam extrusion of high impact polystyrene (HIPS): Effects of processing parameters and blowing agent type and content. In: DEMIRTAS, Erme, Hakan ÖZKAN and Mohammadreza NOFAR. *Proceedings of the Europe/Africa Conference Dresden 2017 - Polymer Processing Society PPS*. Dresden: AIP Publishing, 2019, s. 060011-. ISBN 978-0-7354-1783-0. Available at: doi:10.1063/1.5084843

[120] SAHAGÚN, C., R. GONZÁLEZ-NÚñEZ and D. RODRIGUE. Morphology of Extruded PP/HDPE Foam Blends. *Journal of Cellular Plastics*. 2016, **42**(6), 469-485. ISSN 0021-955X. Available at: doi:10.1177/0021955X06063521

[121] SVATÍK, Juraj. *Functional fomas with density gradient*. Brno, 2019. Diploma thesis. Brno University of Technology.

[122] MILOJEVIć, Marko, Lidija GRADIŠNIK, Janja STERGAR et al. Development of multifunctional 3D printed bioscaffolds from polysaccharides and NiCu nanoparticles and their application. *Applied Surface Science*. 2019, **488**, 836-852. ISSN 01694332. Available at: doi:10.1016/j.apsusc.2019.05.283

[123] HUANG, Li, Xiaoyu DU, Suna FAN et al. Bacterial cellulose nanofibers promote stress and fidelity of 3D-printed silk based hydrogel scaffold with hierarchical pores. *Carbohydrate Polymers*. 2019, **221**, 146-156. ISSN 01448617. Available at: doi:10.1016/j.carbpol.2019.05.080

[124] LAHTINEN, Elmeri, Esa KUKKONEN, Joonas JOKIVARTIO, Joni PARKKONEN, Jussi VIRKAJÄRVI, Lauri KIVIJÄRVI, Markus AHLSKOG and Matti HAUKKA. Preparation of Highly Porous Carbonous Electrodes by Selective Laser Sintering. *ACS Applied Energy Materials*. 2019, **2**(2), 1314-1318. ISSN 2574-0962. Available at: doi:10.1021/acsaem.8b01881

[125] WAGNER, A., A.M. KREUZER, L. GÖPPERL, L. SCHRANZHOFER and C. PAULIK. Foamable acrylic based ink for the production of light weight parts by inkjet-based 3D printing. *European Polymer Journal*. 2019, **115**, 325-334. ISSN 00143057. Available at: doi:10.1016/j.eurpolymj.2019.03.031

[126] LEE, Hwarueon, Sunga KIM, Sungchul SHIN and Jinho HYUN. 3D structure of lightweight, conductive cellulose nanofiber foam. *Carbohydrate Polymers*. 2021, **253**. ISSN 01448617. Available at: doi:10.1016/j.carbpol.2020.117238

[127] MU, X., T. BERTRON, C. DUNN, H. QIAO, J. WU, Z. ZHAO, C. SALDANA and H. QI. Porous polymeric materials by 3D printing of photocurable resin. *Materials Horizons*. 2017, **4**(3), 442-449. ISSN 2051-6347. Available at: doi:10.1039/C7MH00084G

[128] WIRTH, David, Anna JAQUEZ, Sofia GANDARILLA, Justin HOCHBERG, Derek CHURCH and Jonathan POKORSKI. Highly Expandable Foam for Lithographic 3D Printing. *Applied Materials and Interfaces*. 2020, **12**(16), 19033-19043. ISSN 1944-8244. Available at: doi:10.1021/acsami.0c02683

[129] GAMA, N., A. FERREIRA and A. BARROS-TIMMONS. 3D printed cork/polyurethane composite foams. *Materials and Design*. 2019, **179**. ISSN 02641275. Available at: doi:10.1016/j.matdes.2019.107905

[130] Preparation and characterization of 3D printed filament from post-used styrofoam. In: YUEN NG, Tze, Seong CHUN KOAY, Ming YENG CHAN, Huo LENG CHOO and Thai KIAT ONG. *13TH INTERNATIONAL ENGINEERING RESEARCH CONFERENCE*. AIP Publishing, 2020. ISBN 978-0-7354-1992-6. Available at: doi:doi.org/10.1063/5.0001340

[131] H S, Bharath, Dileep BONTHU, Pavana PRABHAKAR and Mrityunjay DODDAMANI. Three-Dimensional Printed Lightweight Composite Foams. *ACS Omega*. 2020, **5**(35), 22536-22550. ISSN 2470-1343. Available at: doi:10.1021/acsomega.0c03174

[132] PATIL, Balu, B.R. BHARATH KUMAR, Srikanth BONTHA, Vamsi BALLA, Satvasheel POWAR, V. HEMANTH KUMAR, S.N. SURESHA and Mrityunjay DODDAMANI. Eco-friendly lightweight filament synthesis and mechanical characterization of additively manufactured closed cell foams. *Composites Science and Technology*. 2019, **183**. ISSN 02663538. Available at: doi:10.1016/j.compscitech.2019.107816

[133] YOO, C.J., B.S. SHIN, B.S. KANG, C.Y. GWAK, C. PARK, Y.W. MA and S.M. HONG. A Study on a New 3D Porous Polymer Printing Based on EPP Beads Containing CO 2 Gas. *Procedia Engineering*. 2017, **184**, 10-15. ISSN 18777058. Available at: doi:10.1016/j.proeng.2017.04.064

[134] YOO, C, B SHIN, B KANG, D YUN, D YOU and S HONG. Manufacturing a Porous Structure According to the Process Parameters of Functional 3D Porous Polymer Printing Technology Based on and Chemical Blowing Agent. *IOP Conference Series: Materials Science and Engineering*. 2017, **229**. ISSN 1757-8981. Available at: doi:10.1088/1757-899X/229/1/012027

[135] CHOI, Won, Ki HWANG, Hyuk KWON et al. Rapid development of dual porous poly(lactic acid) foam using fused deposition modeling (FDM) 3D printing for medical scaffold application. *Materials Science and Engineering: C*. 2020, **110**. ISSN 09284931. Available at: doi:10.1016/j.msec.2020.110693

[136] KADER, M.A., P.J. HAZELL, A.D. BROWN, M. TAHTALI, S. AHMED, J.P. ESCOBEDO and M. SAADATFAR. Novel design of closed-cell foam structures for property enhancement. *Additive Manufacturing*. 2020, **31**. ISSN 22148604. Available at: doi:10.1016/j.addma.2019.100976

[137] GIBSON, L. and M. ASHBY. The mechanics of three-dimensional cellular materials. *Proceedings of the Royal Society of London. A. Mathematical and Physical Sciences*. 1982, **382**(1782), 43-59. ISSN 2053-9169. Available at: doi:10.1098/rspa.1982.0088

[138] MENGES, G. and F. KNIPSCHILD. Estimation of Machanical Properties for Rigid Polyurethane Foams. *Polymer Engineering and Science*. 1975, **15**(8), 623–627.

[139] ASHBY, Michael F. Material selection strategies. *Materials and the environment: Eco-informed material choice*. 2nd ed. Waltham: Butterworth-Heinemann, 2013, s. 227–273. ISBN 978-0-12-385971-6.

[140] FLECK, N., V. DESHPANDE and M. ASHBY. Micro-architectured materials: past, present and future. *Proceedings of the Royal Society A: Mathematical, Physical and Engineering Sciences*. 2010, **466**(2121), 2495-2516. ISSN 1364-5021. Available at: doi:10.1098/rspa.2010.0215

[141] CHAUDHARY, Amit and Krishnamurthy JAYARAMAN. Extrusion of linear polypropylene-clay nanocomposite foams. *Polymer Engineering and Science*. 2011, **51**(9), 1749-1756. ISSN 00323888. Available at: doi:10.1002/pen.21961

[142] CHEN, Limeng, Deniz RENDE, Linda SCHADLER and Rahmi OZISIK. Polymer nanocomposite foams. *Journal of Materials Chemistry A*. 2013, **1**(12). ISSN 2050-7488. Available at: doi:10.1039/c2ta00086e

[143] ZAKIYAN, Seyed, Mohamad FAMILI and Mohammad AKO. Controlling foam morphology of polystyrene via surface chemistry, size and concentration of nanosilica particles. *Journal of Materials Science*. 2014, **49**(18), 6225-6239. ISSN 0022-2461. Available at: doi:10.1007/s10853-014-8347-4

[144] SAHA, M.C., Md.E. KABIR and S. JEELANI. Enhancement in thermal and mechanical properties of polyurethane foam infused with nanoparticles. *Materials Science and Engineering: A*. 2008, **479**(1-2), 213-222. ISSN 09215093. Available at: doi:10.1016/j.msea.2007.06.060

[145] LING, Jianqiang, Wentao ZHAI, Weiwei FENG, Bin SHEN, Jianfeng ZHANG and Wen ZHENG. Facile Preparation of Lightweight Microcellular Polyetherimide/Graphene Composite Foams for Electromagnetic Interference Shielding. *Applied Materials & Interfaces*. 2013, **5**(7), 2677-2684. ISSN 1944-8244. Available at: doi:10.1021/am303289m

[146] LEE, Yuan-Jyh, Jieh-Ming HUANG, Shiao-Wei KUO and Feng-Chih CHANG. Low-dielectric, nanoporous polyimide films prepared from PEO–POSS nanoparticles. *Polymer*. 2005, **46**(23), 10056-10065. ISSN 00323861. Available at: doi:10.1016/j.polymer.2005.08.047

[147] HAN, Xiangmin, Changchun ZENG, L. LEE, Kurt KOELLING and David TOMASKO. Extrusion of polystyrene nanocomposite foams with supercritical CO2. *Polymer Engineering and Science*. 2003, **43**(6), 1261-1275. ISSN 0032-3888. Available at: doi:10.1002/pen.10107

[148] ANTUNES, Marcelo, Jose VELASCO, Vera REALINHO and Eusebio SOLÓRZANO. Study of the cellular structure heterogeneity and anisotropy of polypropylene and polypropylene nanocomposite foams. *Society of Plastics Engineers*. 2009, **49**(12), 2400-2413. ISSN 00323888. Available at: doi:10.1002/pen.21488

[149] Prediction of Solubility Parameters: A Comparison of four Group Contribution Methods. *Polymer Database* [online]. Crow, 2015 [cit. 2019-02-18]. Available at: http://polymerdatabase.com/pdf/crow_sol_par_June2015.pdf

[150] Technical Data Sheet Synthos PS HI 336M. *Synthos* [online]. Czech Republic: Synthos Kralupy corp, 2017 [cit. 2019-05-14]. Available at: https://www.synthosps.com/fileadmin/user_files/ps/pdf/2/TDS_HI_336M_EN.pdf

[151] REYES-LABARTA, J. and A. MARCILLA. Kinetic study of the decompositions involved in the thermal degradation of commercial azodicarbonamide. *Journal of Applied Polymer Science*. 2008, **107**(1), 339-346. ISSN 00218995. Available at: doi:10.1039/P29750000046

[152] *Technical Data Sheet Unicell D 200 A (product no. 050039731)*. Germany: Tramaco, 2016.

[153] PRAKASH, A., William SWAM and Alec STRACHAN. The thermal decomposition of azodicarbonamide (1,1′-azobisformamide). *J. Chem. Soc., Perkin Trans. 2*. 1975, (1), 46-50. ISSN 0300-9580. Available at: doi:10.1039/P29750000046

[154] BARTON, Allan. Solubility Parameters. *Chemical Reviews*. 1975, **75**(6), 731–753.

[155] MATUANA, Laurent, Chul PARK and John BALATINECZ. Processing and cell morphology relationships for microcellular foamed PVC/wood-fiber composites. *Polymer Engineering and Science*. 1997, **37**(7), 1137-1147. ISSN 0032-3888. Available at: doi:10.1002/pen.11758

[156] ZARYBNICKA, Klara, Frantisek ONDREAS, Petr LEPCIO, Michal KALINA, Marek ZBONCAK and Josef JANCAR. Thermodynamic Parameters Controlling Nanoparticle Spatial Packing in Polymer Solutions. *Macromolecules*. 2020, **53**(19), 8704-8713. ISSN 0024-9297. Available at: doi:10.1021/acs.macromol.0c00698

[157] SMALLWOOD, Ian M. *Handbook of Organic Solvent Properties*. 1. New York: Halsted Press, 1996. ISBN 978-0-08-052378-1.

[158] ZÁRYBNICKÁ, Klára, František ONDREÁŠ, Petr LEPCIO, Chao CHEN and Josef JANČÁŘ. In-situ self-assembly of silica nanoparticles into microfibers with potential to reinforce polymers. *Nanocon: Proceedings 11th International Conference on Nanomaterials - Research & Application*. 2020, , 673-678. Available at: doi:10.37904/nanocon.2019.8489

[159] Characteristic Ratio of Some Polymers. *Polymer Properties Database* [online]. Crow, 2015 [cit. 2019-05-14]. Available at: http://polymerdatabase.com/polymer%20physics/C%20Table%20.html

[160] HANSEN, Charles M. *Hansen solubility parameters: A user's handbook*. 2nd ed. Boca Raton: CRC Press, 2007. ISBN 978-084-9372-483.

[161] VAN DER BEEK, G., M. STUART, G. FLEER and J. HOFMAN. Segmental adsorption energies for polymers on silica and alumina. *Macromolecules*. 1991, **24**(25), 6600-6611. ISSN 0024-9297. Available at: doi:10.1021/ma00025a009

[162] KUMAR, Ajeet and Chandra DIXIT. Methods for characterization of nanoparticles. *Advances in Nanomedicine for the Delivery of Therapeutic Nucleic Acids*. Elsevier, 2017, , 43-58. ISBN 9780081005576. Available at: doi:10.1016/B978-0-08-100557-6.00003-1

[163] SVOBODA, Roman. How to determine activation energy of glass transition. *Journal of Thermal Analysis and Calorimetry*. 2014, **118**(3), 1721-1732. ISSN 1388-6150. Available at: doi:10.1007/s10973-014-4077-8

[164] ONDREAS, Frantisek, Petr LEPCIO, Marek ZBONCAK, Klara ZARYBNICKA, Leon GOVAERT and Josef JANCAR. Effect of Nanoparticle Organization on Molecular Mobility and Mechanical Properties of Polymer Nanocomposites. *Macromolecules*. 2019, **52**(16), 6250-6259. ISSN 0024-9297. Available at: doi:10.1021/acs.macromol.9b01197

[165] KALFUS, J. and J. JANCAR. Immobilization of polyvinylacetate macromolecules on hydroxyapatite nanoparticles. *Polymer*. 2007, **48**(14), 3935-3937. ISSN 00323861. Available at: doi:10.1016/j.polymer.2007.04.049

[166] BERRIOT, Julien, Hélène MONTES, François LEQUEUX, Didier LONG and Paul SOTTA. Evidence for the Shift of the Glass Transition near the Particles in Silica-Filled Elastomers. *Macromolecules*. 2002, **35**(26), 9756-9762. ISSN 0024-9297. Available at: doi:10.1021/ma0212700

[167] BERRIOT, J., H. MONTES, F. LEQUEUX, D. LONG and P. SOTTA. Gradient of glass transition temperature in filled elastomers. *Europhysics Letters (EPL)*. 2003, **64**(1), 50-56. ISSN 0295-5075. Available at: doi:10.1209/epl/i2003-00124-7

[168] EMAMY, Hamed, Sanat KUMAR and Francis STARR. Diminishing Interfacial Effects with Decreasing Nanoparticle Size in Polymer-Nanoparticle Composites. *Physical Review Letters*. 2018, **121**(20). ISSN 0031-9007. Available at: doi:10.1103/PhysRevLett.121.207801

[169] ZBONCAK, Marek, Frantisek ONDREAS, Vojtech UHLIR, Petr LEPCIO, Jan MICHALICKA and Josef JANCAR. *Translation of segment scale stiffening into macroscale reinforcement in polymer nanocomposites*. 2019. ISSN 0032-3888. Available at: doi:10.1002/pen.25317

[170] TANNENBAUM, Rina, Melissa ZUBRIS, Kasi DAVID, Dan CIPRARI, Karl JACOB, Iwona JASIUK and Nily DAN. FTIR Characterization of the Reactive Interface of Cobalt Oxide Nanoparticles Embedded in Polymeric Matrices. *The Journal of Physical Chemistry B*. 2006, **110**(5), 2227-2232. ISSN 1520-6106. Available at: doi:10.1021/jp054469y

[171] CIPRARI, Dan, Karl JACOB and Rina TANNENBAUM. Characterization of Polymer Nanocomposite Interphase and Its Impact on Mechanical Properties. *Macromolecules*. 2006, **39**(19), 6565-6573. ISSN 0024-9297. Available at: doi:10.1021/ma0602270

[172] CHENG, Shiwang, Bobby CARROLL, Wei LU et al. Interfacial Properties of Polymer Nanocomposites: Role of Chain Rigidity and Dynamic Heterogeneity Length Scale. *Macromolecules*. 2017, **50**(6), 2397-2406. ISSN 0024-9297. Available at: doi:10.1021/acs.macromol.6b02816

[173] JOUAULT, Nicolas, Florent DALMAS, François BOUÉ and Jacques JESTIN. Multiscale characterization of filler dispersion and origins of mechanical reinforcement in model nanocomposites. *Polymer*. 2012, **53**(3), 761-775. ISSN 00323861. Available at: doi:10.1016/j.polymer.2011.12.001

[174] GENIX, Anne-Caroline, Vera BOCHAROVA, Bobby CARROLL et al. Understanding the Static Interfacial Polymer Layer by Exploring the Dispersion States of Nanocomposites. *Applied Materials and Interfaces*. 2019, **11**(19), 17863-17872. ISSN 1944-8244. Available at: doi:10.1021/acsami.9b04553

[175] STERNSTEIN, S. and Ai-Jun ZHU. Reinforcement Mechanism of Nanofilled Polymer Melts As Elucidated by Nonlinear Viscoelastic Behavior. *Macromolecules*. 2002, **35**(19), 7262-7273. ISSN 0024-9297. Available at: doi:10.1021/ma020482u

[176] HARTON, Shane, Sanat KUMAR, Hoichang YANG et al. Immobilized Polymer Layers on Spherical Nanoparticles. *Macromolecules*. 2010, **43**(7), 3415-3421. ISSN 0024-9297. Available at: doi:10.1021/ma902484d

[177] JOUAULT, Nicolas, Joseph MOLL, Dong MENG, Kendra WINDSOR, Stacy RAMCHARAN, Clare KEARNEY and Sanat KUMAR. Bound Polymer Layer in Nanocomposites. *ACS Macro Letters*. 2013, **2**(5), 371-374. ISSN 2161-1653. Available at: doi:10.1021/mz300646a

[178] KALFUS, J. and J. JANCAR. Relaxation processes in PVAc-HA nanocomposites. *Journal of Polymer Science Part B: Polymer Physics*. 2007, **45**(11), 1380-1388. ISSN 08876266. Available at: doi:10.1002/polb.21139

[179] ANDERSON, Benjamin and Charles ZUKOSKI. Rheology and Microstructure of an Unentangled Polymer Nanocomposite Melt. *Macromolecules*. 2008, **41**(23), 9326-9334. ISSN 0024-9297. Available at: doi:10.1021/ma801415e

[180] F. BEHBAHANI, Alireza, S. VAEZ ALLAEI, Ghodratollah H. MOTLAGH, Hossein ESLAMI and Vagelis HARMANDARIS. Structure and dynamics of stereo-regular poly(methyl-methacrylate) melts through atomistic molecular dynamics simulations. *Soft Matter*. 2018, **14**(8), 1449-1464. ISSN 1744-683X. Available at: doi:10.1039/C7SM02008B

[181] ONDREAS, Frantisek and Josef JANCAR. Temperature, Frequency, and Small Static Stress Dependence of the Molecular Mobility in Deformed Amorphous Polymers near Their Glass Transition. *Macromolecules*. 2015, **48**(13), 4702-4716. ISSN 0024-9297. Available at: doi:10.1021/acs.macromol.5b00550

[182] XU, Zhongbin, Xiling TANG, Aijuan GU and Zhengping FANG. Novel preparation and mechanical properties of rigid polyurethane foam/organoclay nanocomposites. *Journal of Applied Polymer Science*. 2007, **106**(1), 439-447. ISSN 00218995. Available at: doi:10.1002/app.26497

9 LIST OF ABBREVIATIONS

3D	three-dimensional
A	area of micrograph
AAAS	American Association for the Advancement of Science
A-block	majority block of diblock copolymer
ABS	acrylonitrile butadiene styrene
Al_2O_3	aluminum oxide
Au	gold
AZO	zinc oxide particles doped with 2 wt. % of aluminum oxide
Å	angstrom (physical unit)
B-block	minority block of diblock copolymer (alternatively B-phase)
BF	bright field mode in transmission electron microscopy
C_{60}	carbon-60 (spherical molecule comprised of 60 carbon atoms)
C_A	susceptibility of an acid functional group to form covalent bonds
C_B	susceptibility of a basic functional group to form covalent bonds
cm	centimeter (physical unit)
CLSM	confocal laser scanning microscopy
CO_2	carbon dioxide
C_∞	characteristic ratio
D	debye (physical unit)
D	polydispersity
d	diameter
DCM	dichloromethane
DF	dark field mode in transmission electron microscopy
DLS	dynamic light scattering
DMAC	dimethylacetamide
DMF	dimethylformamide
d_p	pore size (pore diameter)
DSC	differential scanning calorimetry
d_sp	single particle diameter, nanoparticle diameter
d_w	size of the agglomerates (weight average)
E	Young modulus (tensile or compression)
E_A	susceptibility of an acid functional group to undergo electrostatic interactions
$E_{\mathrm{A},\,T\mathrm{g}}$	activation energy of glass transition
$E_{\mathrm{A},\,T\mathrm{g\,matrix}}$	activation energy of glass transition of matrix
E_B	susceptibility of a basic functional group to undergo electrostatic interactions
E_c	elastic modulus of composite
$E_\mathrm{c,\,GG}$	elastic modulus of composite determined by Guth-Gold model
$E_\mathrm{c,\,KN}$	elastic modulus of composite determined by Kerner-Nielsen model
E_f	elastic modulus of the filler
E_fo	elastic modulus of the foam
E_m	elastic modulus of the matrix
E_m'	energy needed to remove unit of molecules to infinite separation
E_PBR	elastic modulus of polybutadiene rubber
E_PS	elastic modulus of polystyrene
E_s	elastic modulus of the solid material
EVA	poly(ethylene-vinyl acetate)
f	composition of diblock copolymer
FDM	fused deposition modeling

F_{max}	maximum force
FTIR	Fourier-transform infrared spectroscopy
g	gram (physical unit)
GPa	gigapascal (physical unit)
GPC	gel permeation chromatography
H_2SO_4	sulfuric acid
$H_3N_3C_2O_2$	urazole
H_3PO_4	phosphoric acid
$H_6N_4C_2O_4$	biurea
HDPE	high-density polyethylene
HIPS	high impact polystyrene
HNCO	isocyanic acid
$(HNCO)_x$	cyamelide
IPA	isopropanol
IPA-ST	solution of spherical silica in isopropanol
J	joule (physical unit)
K	kelvin (physical unit)
k	Boltzmann constant
kcal	kilocalory (physical unit)
kg	kilogram (physical unit)
kJ	kilojoule (physical unit)
$KMnO_4$	potassium permanganate
m	meter (physical unit)
M	magnification factor of the micrograph
MEK	ethyl methyl ketone
MEK-ST	solution of spherical silica in ethyl methyl ketone
min	minute (physical unit)
ml	milliliter (physical unit)
mm	millimeter (physical unit)
M_m^*	modulus of the matrix in the presence of particles
MMA	methyl methacrylate
mol	mole (physical unit)
MPa	megapascal (physical unit)
mV	millivolt (physical unit)
M_w	molecular weight (weight average)
n	amount of the substance or number of units (e.g. number of pores)
N	Newton (physical unit)
N_0	cell population density per unit volume
N_2	nitrogen
N/A	not available, not applicable
NaCl	sodium chloride
nm	nanometer (physical unit)
n_p	number of pores in micrograph
OsO_4	osmium tetraoxide
P	porosity
P2VP	poly(2-vinyl pyridine)
PA	polyamide
PBR	polybutadiene rubber
PC	polycarbonate
PCL	polycaprolactone

PDI	polydispersity index
PE	polyethylene
PEI	polyetherimide
POE	polyoxyethylene
PET	poly(ethylene terephthalate)
phr	parts per hundred rubber
PI	polyimide
PI	polarity index
PLA	poly(lactic acid)
PMMA	poly(methyl methacrylate)
PP	polypropylene
$P_{\mathrm{p,\,n}}$	average pore size (number average)
$P_{\mathrm{p,\,w}}$	average pore size (weight average)
PRISM	polymer reference interaction site model
PS	polystyrene
PS-PFMA	poly(styrene-*block*-perfluorooctyethyl methacrylate)
PU	polyurethane
PVAc	poly(vinyl acetate)
PVC	polyvinyl chloride
PVP	poly(2-vinyl pyridine)
q	heating rate
q_0	preexponential factor
R	universal gas constant
R_0	size of diblock copolymer (radius)
R_{g}	radius of gyration
RIM	reaction injection molding
rpm	revolutions per minute (physical unit)
r_{polymer}	radius of polymer coil
s	second (physical unit)
S.D.	standard deviation
SDS	sodium dodecyl sulfate
SE	secondary electrons mode in scanning electron microscopy
SEM	scanning electron microscope
S_{f}	specific interface area
Si-OH	silanol group
SLA	stereolithography
SLS	selective laser sintering
STEM	scanning transmission electron microscopy
T	absolute temperature
t	thickness of the immobilized/accelerated layer of chain segments
T_{B}	boiling point
TEM	transmission electron microscopy
T_{g}	glass transition temperature
$T_{\mathrm{g,\,matrix}}$	glass transition temperature of matrix
TGA	thermogravimetric analysis
THF	tetrahydrofuran
TiO_2	titanium dioxide
UV	ultraviolet
V_{f}	void fraction
V_{m}	molar volume

v_m	maximum possible volume fraction of the filler
vol. %	percent by volume (physical unit)
wt. %	percent by weight (physical unit)
x	density exponent of the foam
z	coordination number (number of solvent molecules surrounding one polymer molecule
ZnO	zinc oxide
α	preexponential factor
β	empiric constant for calculation of Florry-Huggins parameter
ΔG_M	Gibbs energy of mixing
ΔH	interfacial interaction enthalpy
$\Delta\varepsilon$	difference in molecular interaction energy
δ	Hildebrant solubility parameter
δ_D	Hansen solubility parameter (energy from dispersion forces between molecules)
δ_H	Hansen solubility parameter (energy from hydrogen bonds between molecules)
δ_P	Hansen solubility parameter (energy from dipolar intermolecular forces between molecules)
$\delta_{polymer}$	Hildebrant solubility parameter of the polymer
δ_{silica}	Hildebrant solubility parameter of the silica
$\delta_{solvent}$	Hildebrant solubility parameter of the solvent
ε	interaction energy
ε	mechanical deformation (strain)
ε	dielectric constant
ε_{11}, ε_{22}	energy of agglomeration of individual systems (1 – solvent, 2 – polymer)
ε_{12}	mixing energy of components (1 – solvent, 2 – polymer)
ε_{AB}	interaction energy between monomer of majority block (A) and monomer of minority block (B) in block copolymer
ε_{max}	elongation
ε_{pc}	attraction force of the polymer segment and the particle
ε_{PA}	interaction energy between monomer of majority block (A) and particle
ζ-potential	electrokinetic potential
µm	micrometer (physical unit)
ν	Poisson ration
ρ_f	mass density of sample with pores (foam)
ρ_s	mass density of sample without pores (solid)
σ	mechanical stress
$\sigma_{0.2}$	offset yield strength
σ_{max}	maximum strength
Φ	volume fraction of the filler
Φ_p	fraction of the polymer contained in the cell struts
φ	volume fraction of the filler
χ	Flory-Huggins parameter (alternatively χ_{AB})
°C	Celsius degree (physical unit)

10 LIST OF FIGURES

Figure 1: Scheme of foam material with multiple hierarchical levels of structural organization. The state of nanoparticle (grey) dispersion in a polymer matrix (green) represents an organization of material on a nano-scale level. An arrangement of domains (blue) in a block copolymer (e.g., rubber particles in the PS matrix) exhibits the organization of structure on a micro-scale. A micro-to-macro-scale organization is determined by a structure of walls and cells forming polymer foam. The final macroscopic shape of a product could be organized via 3D printing.. 7

Figure 2: Schematic depiction of nanoparticles (grey) dispersed in a polymer matrix (green) and the amount of affected polymer matrix (blue). **A** – Individually dispersed particles, **B** – chain bound clusters, and **C** – contact aggregates. 9

Figure 3: Transmission electron microscopy (TEM) images of nanocomposites with solvent-casted silica. **A** – With PVP prepared in MEK. **B** – With PVP prepared in pyridine. *Reprinted with permission from* [30]. *Copyright 2014 American Chemical Society*. **C** – With PS prepared in DMAC. *Reprinted with permission from* [31]. *Copyright 2009 American Chemical Society.* 10

Figure 4: Basic types of nanoparticle organization in polymer melt according to PRISM theory. **A** – Contact aggregation. **B** – Steric stabilization. **C** – Polymer segment level tight particle bridging. **D** – Tele-bridging. *Adapted with permission from* [33]. *Copyright 2005 American Chemical Society.* 11

Figure 5: A polymer radius of gyration to nanoparticle radius phase diagram with the area of miscible systems (good dispersion of nanoparticles) and the area of immiscible systems (aggregates). Each nanocomposite was with PS matrix and with 2 wt. % of nanoparticles. *From* [36]. *Reprinted with permission from AAAS.* 12

Figure 6: Bar diagram of donor-acceptor interaction enthalpies of silanol groups on nanosilica surface (acceptor) and PMMA and various solvents (donors). TEM images of PMMA nanocomposites filled with 1 vol. % of nanosilica prepared in an appropriate solvent. [25]... 13

Figure 7: **A** – Phase separation models in diblock copolymers: spheres (**1**), cylinders (**2**), lamellar (**3**), and gyroid structure (**4**). *Reuse from* [44]. *Copyright 2009 Technical University of Liberec.* **B** – TEM image of the PS-PVP block copolymer with Au particles localized in PVP domains. *Reprinted with permission from* [47]. *Copyright 2008 Wiley Materials.* **C** – Schematic picture showing the microphase separation of neat block copolymer (**1**) and the same copolymer with nanoparticles (**2**). *Reprinted with permission from* [48]. *Copyright 2012 Wiley Materials.* 15

Figure 8: A – Approximate phase diagram for diblock copolymer filled with nanoparticles defining areas of different block structures – disordered (D), spherical (S), cylindrical (C), and lamellar (L). B – Snapshot of diblock copolymer without nanoparticles (cylindric structure). C – Block copolymer with 50 vol. % of small nanoparticles (lamellar). *Reprinted with permission from* [49]. *Copyright 2000 American Chemical Society.* D – Block copolymer with 20 vol. % of larger nanoparticles (lamellar). E – Block copolymer with 20 vol. % of smaller nanoparticles (cylindrical). *Reproduced by permission of The Royal Society of Chemistry from* [50]. 16

Figure 9: Adsorption of polymer chain onto the nanoparticle surface. **A** – Adsorption with one polymer segment and with a series of consecutive segments. **B** – Adsorption with multiple detached segments. **C** – Interconnecting of multiple nanoparticles.. 19

Figure 10: **A** – Attraction polymer-particle force phase diagram. *Reprinted with permission from* [35]. *Copyright 2007 Americal Chemical Society*. **B** – Nanoparticle (grey) with absorbed immobilized/accelerated layer of polymer segments (purple) with adjacent frustrated layer (blue) all incorporated in the original bulk polymer matrix (green). [42] **C** – Comparison of interparticle distance and polymer coil size in the case of microparticles (1) and nanoparticles (2). *Reprinted from* [11], *2010, with permission from Elsevier.*.. 20

Figure 11: TEM images of HIPS structure. **A** – Crazes appearing on rubber particles after applying tension (**B** – detail). Stained with OsO_4. *Reprinted from* [63], *Copyright 1986, with permission from Elsevier.* **C** – Highly occluded particle almost totally engulfed by the surrounding craze. The outer rubber shell at the poles of the particle is highly extended and fibrillated. *Reprinted by permission from Springer Nature:* [61], *Copyright 1982.*......... 21

Figure 12: Dependence of the matrix modulus $M_m^* = E_c/f(\varphi)$ on the logarithm of the specific interface area S_f above T_g using the Guth-Gold model (**left**) and below T_g using Kerner-Lewis model (**right**). *Reprinted from* [67]. *Copyright 2010, with permission from Elsevier.*... 23

Figure 13: **A** – Dependence of relative elastic modulus on silica fraction of nanocomposites in three different matrices – PMMA, PS, and PC. [70] **B** – Dependence of reptation time on silica fraction of PMMA nanocomposites with a different state of nanoparticle dispersion. *Reprinted from* [42]. *Copyright 2018, Brno University of*

Technology. **C** – Scheme of nanoparticle toughening mechanism. *Reprinted from* [72]. *Copyright 2003, with permission from Elsevier*. 24

Figure 14: Morphology of closed-cell poly(ethylene-vinyl acetate) (EVA; **left**) and open-cell PU (**right**) foams. *Reprinted from* [78], *Copyright (2003), with permission from Elsevier*. 25

Figure 15: SEM images of nanocellular PS-PFMA. *Reprinted with permission from* [85]. *Copyright 2005 American Chemical Society*. 27

Figure 16: SEM images. **Left** – Syntactic foam structure composed of glass microballoons and epoxy resin. [88] – *Copyright 2009, Journal of Sandwich Structures and Materials.* **Right** – Phase separated biodegradable poly(ester urethane)urea scaffold. *Reprinted from* [89], *Copyright 2005, with permission from Elsevier*. 29

Figure 17: SEM images. **Left** – Bimodal porous structure of polycaprolactone (PCL) with smaller pores created by leaching NaCl and with two visible larger pores created by leaching POE. *Reprinted from* [93], *Copyright 2006, with permission from Elsevier.* **Right** – Structure of a PC membrane with a skin layer obtained using surfactant-controlled etching, the picture shows nanopores passing through the entire film material. *Reprinted from* [94], *Copyright 2008, with permission from Elsevier.* 30

Figure 18: Highly porous electrospun PS fibers, SEM images. *Reprinted with permission from* [97]. *Copyright 2019, American Chemical Society.* 31

Figure 19: Morphology of extruded foam in longitudinal (**left**) and transverse (**right**) direction. *Reuse from* [120]. 33

Figure 20: SLA 3D printed porous structures. **A** – 3D printed scaffold with computer-designed macropores and micropores generated by salt leaching, SEM images. *Reprinted from* [127], *Copyright 2017, with permission from Royal Society of Chemistry*. **B** – High expansion of 3D printable foaming polymer – photographic time frame images. *Reprinted with permission from* [128]. *Copyright 2020 American Chemical Society.* 35

Figure 21: HDPE syntactic foams for 3D printing. **A** – filament for 3D printing with 20 vol. % of fly ash cenospheres. *Reprinted from* [132], *Copyright 2019, ACS Publications.* **B** – 3D printed body with 60 vol. % of glass hollow fibers with observable raster gabs. *Reprinted from* [131], *Copyright 2020, with permission from Elsevier.* 36

Figure 22: **A** – Porous CO_2 hybrid filament for 3D printing observed by optical microscopy. *Reuse from* [133], *Copyright 2017, Elsevier*. **B** – 3D printed samples from hybrid filament with chemical blowing agent – photo of 3D printed sample (**1**) and an internal cross-section of the foamed structure formed by 3D printing, optical microscopy (**2**). *Reuse from* [134], *Copyright 2017, Institute of Physics*. **C** – Dual porous 3D printed poly-lactic acid) (PLA) foams – detail of 3D printed monofilament (**1**), schematic of 3D printed structure (**2**), detail of dual porous printed porous scaffold (**3**), and green fluorescence staining image of living cells (**4**). *Reprinted from* [135], *Copyright 2020 with permission from Elsevier.* 37

Figure 23: Compressive deformation of 3D printed ABS with elliptical pores. A – Compressive stress-strain curve (comparison of simulation and experimental measurement). B – Real 3D printed specimen during compression. C – Plastic strain contours from the numerical simulations. *Reprinted from* [136], *with permission from Elsevier.* 38

Figure 24: Ashby bubble chart relating elastic modulus and density of engineering materials. *Reuse from* [139]. 40

Figure 25: PS samples foamed with CO_2. **Left** – neat PS without nanoparticles. **Middle** – PS loaded with 0.1 wt. % of nanosilica. **Right** – PS with 2 wt. % of the nanosilica. *Reprinted with permission from Springer Nature*: [143], *Copyright 2014.* 41

Figure 26: Microscopic photos of nanocomposite foams. **A** – PEI with 1 wt. % of graphene (overview). **B** – PEI with 1 wt. % of graphene (detail of cell wall, red arrows point to oriented graphene sheets. *Reprinted with permission from* [145]. *Copyright 2013 American Chemical Society.* **C** – PI with 5 wt. % of POSS particles before thermal treatment. **D** – PI after thermal treatment and decomposition of 5 wt. of POSS nanoparticles. *Reprinted from* [146], *Copyright 2005, with permission from Elsevier.* 42

Figure 27: 3D printing with liquid cellulose nanofiber foam. **A** – Dark-field microscopy image of air bubbles in liquid foam ink. **B** – Distribution of cellulose nanofibers in liquid foam ink. **C** – Pore structure of the solid cellulose nanofiber foam. **D** – 3D printed structure of butterfly shape. *Reprinted from* [126], *Copyright 2021, with permission from Elsevier* 43

Figure 28: Scanning electron microscope (SEM) image of neat PS HI 336M etched in an acid permanganate mixture for 20 minutes – overview photo (**left**) and detail of occluded and solid particles (**right**). 46

Figure 29: TGA curve of foaming agent Unicell D200A – percentual loss of mass (red) and derivation of loss of mass (blue). Measured in a nitrogen atmosphere with temperature ramp 10 °C·min^{-1}. 48

Figure 30: Polymer nanocomposite foam preparation scheme. 50

Figure 31: Filaments for 3D printing. **A** – Pure HIPS filament without additives. **B** – HIPS with 2 wt. % of azodicarbonamide and without nanoparticles. **C** – HIPS with 2 wt. % of azodicarbonamide and 1 wt. % of melt-blended fumed nanosilica. **D** – HIPS with 2 wt. % of azodicarbonamide and 1 wt. % of solvent-casted spherical nanosilica. 52

Figure 32: **A** – Post-processing foaming scheme. **B** – Photo of HIPS samples with 2 wt. % of Unicell D200A. Unfoamed cylinder after 3D printing at 180 °C (1), cylinder foamed to 120 % of diameter at 200 °C for 30 minutes (2) and the foamed cylinder cut in half (3). **C** – Photo of HIPS sample with 2 wt. % of Unicell D200A after 3D printing at 220 °C. 53

Figure 33: Example of binarization for PMMA nanocomposite with 1 vol. % of fumed silica prepared in acetone. Left – Original TEM image. Middle – Binarization of agglomerates by ImageJ® software (area without scale bar was selected to avoid distortion of results). Right – Particle elements (agglomerates) detected by the automatic function of the ImageJ®. The area of each element was approximated to an ideal sphere and the mass average agglomerate diameter was calculated. 54

Figure 34: Charge on silica surface in organic solution represented by the ζ-potential as the dependence of logarithm of the polarity index of solvents. Raw data are available in the appendix. 58

Figure 35: STEM images of nanocomposites with anisotropic microfibers composed of PC and 1 vol. % of spherical silica prepared in dioxane with positive ζ-potential. 58

Figure 36: TEM images of nanocomposites with 1 vol. % of spherical silica prepared in THF with four different matrices – PS (purple), PC (blue), PMMA (red), and PVAc (green). 59

Figure 37: TEM images of PS nanocomposites with 1 vol. % of spherical silica prepared in different solvents – DMAC, DMF, cyclohexanone, and toluene. The stripes in the images are artifacts after cutting with a vibrating ultramicrotome knife. 61

Figure 38: TEM images of PC nanocomposite with 1 vol. % of spherical silica prepared in DCM – the detail on aggregates (**left**), overview image (**right**). 62

Figure 39: TEM images of PMMA nanocomposites with 1 vol. % of spherical silica prepared in different solvents – cyclohexanone, acetonitrile, and anisole. 63

Figure 40: TEM images of PVAc nanocomposites with 1 vol. % of spherical silica prepared in different solvents – acetone, acetone-toluene mixture (1:1 volume ratio), and toluene. 64

Figure 41: The ratio of agglomerate size d_w to the single-particle diameter d_{sp} for spherical nanosilica nanocomposites depicted as the dependence on the reciprocal absolute difference in the Hildebrand solubility parameters of solvent and polymer. The two populations of dispersed individual particles and aggregated populations in PMMA-THF and PVAc-THF and the two populations of small and larger aggregates in PMMA-toluene composites were plotted separately as two points for each system. The anisotropic microfibrous structure formed in PC-dioxane was a specific case and thus was not included in the trends defined by the solid lines. Raw data are available in the appendix. 66

Figure 42: **A** – Nanoparticles with an adsorbed layer of compact polymer coils formed in a poor solvent. **B** – Nanoparticles with adsorbed flexible expanded polymer coils formed in a good solvent. Graph **C** – Radius of polymer coils in solutions of various solvents (determined by DLS) dependence on the difference of solubility parameter between solvent and polymer. Dashed lines are for eye guidance. 68

Figure 43: TEM images of nanocomposites with 1 vol. % of fumed silica in PMMA prepared in acetone and THF and PVAc prepared in acetone. 70

Figure 44: TEM images of nanocomposites with 1 vol. % of AZO in PMMA prepared in acetone and toluene and PC prepared in THF. 71

Figure 45: The ratio of agglomerate size d_w to the single-particle diameter d_{sp} for fumed nanosilica and AZO nanoparticles composites depicted as the dependence on the reciprocal absolute difference in the Hildebrand solubility parameters of solvent and polymer. Raw data are available in the appendix. 72

Figure 46: Dependence of the relative glass transition activation energy (E_A) and the increase of glass transition temperature (ΔT_g) on the element size d_w. 73

Figure 47: **A** – Dependence of the relative activation energy of glass transition (E_A) and glass transition temperature (ΔT_g) on the absolute difference in solubility parameters of solvent and polymer and **B** – on the difference in Hildebrand's solubility parameters of silica and polymer. Raw data are available in the appendix. **C** – An illustrative picture shows the difference between the adsorption of flexible PC chains and rigid PS chains onto nanoparticle surface, green color represents the immobilized layer, blue color represents the frustrated layer. 74

Figure 48: Representative DLS histograms of the size of HIPS components in solutions of three different solvents – cyclohexanone, DMAC, and DMF, supplemented with a photo of each solution. 76

Figure 49: TEM images of HIPS nanocomposite prepared in cyclohexanone with 1 vol. % of spherical silica. **A** – Overview of good dispersion. **B** – Occluded particle detected in BF mode. **C** – Detail inside of occluded particle. **D** – Occluded particle detected in DF mode. 78

Figure 50: TEM images of HIPS nanocomposite prepared in DMAC with 1 vol. % of spherical silica. **A** – Overview of good dispersion. **B** – Occluded particle detected in BF mode. **C** – Occluded particle detected in DF mode. 79

Figure 51: TEM images of HIPS nanocomposite prepared in DMF with 1 vol. % of spherical silica. **A** – Overview of good dispersion. **B** – Occluded particle detected in BF mode. **C** – Occluded particle detected in DF mode. 80

Figure 52: TEM images of HIPS nanocomposites with 1 vol. % of fumed silica prepared in cyclohexanone (**upper left** – overview of good dispersion, **upper right** – detail of occluded particle), in DMAC (**bottom left**), and in DMF (**bottom right**). 81

Figure 53: TEM image of nanocomposite with 1 vol. % of fumed silica prepared by the melt-blending method. **Left** –HIPS sample with the holes caused by the rupture of the rubber particles during ultramicrotome cutting. **Right** – Homopolymer PS. 82

Figure 54: Dispersion of 2 wt. % of foaming agent azodicarbonamide in the HIPS matrix. SEM photo. 83

Figure 55: Structure of HIPS with 2 wt. % of foaming agent, filament after extrusion in the single-screw extruder. **A** – Overview, CLSM photo. **B** – Detail of hollow cells, SEM photo. 84

Figure 56: Structure of HIPS with 2 wt. % of foaming agent, porous sample after 3D printing above the decomposition temperature of foaming agent, CLSM photo. 84

Figure 57: Structure of HIPS with 2 wt. % of foaming agent, sample after 3D printing below the decomposition temperature of foaming agent. **A** – Overview, CLSM photo. **B** – Detail of pore-free fracture surface, SEM photo. 85

Figure 58: Structure of HIPS with 2 wt. % of foaming agent foamed at 200 °C for 30 minutes (post-processing foaming), CLSM photo. 86

Figure 59: TGA simulation of foaming process in air atmosphere – isothermal hold of the material at different temperatures for 60 minutes. The upper graph shows the decomposition of the pure foaming agent (azodicarbonamide). The lower graph shows the thermal decomposition of the HIPS sample with 2 wt. % of foaming agent. The dashed line defines the content of the foaming agent in the sample. 87

Figure 60: TGA curves of extruded filaments. Top – complete curves. Bottom – detail of area when the blowing agent was decomposed to gaseous products and causing foaming. 88

Figure 61: Dependence of blowing agent decomposition temperature on nanosilica loading. 89

Figure 62: CLSM images of extruded filaments – HIPS with 2 wt. % of blowing agent after single-screw extrusion with different amounts of melt-blended fumed silica (without nanoparticles, with 0.25, 1, 2.5, 5, and 10 wt. % of fumed nanosilica). 90

Figure 63: CLSM image of extruded filament – HIPS with 2 wt. % of blowing agent after single-screw extrusion with 1 wt. % of solvent-casted spherical nanosilica. 91

Figure 64: Graphical evaluation of structural properties of extruded filaments dependent on silica content. **A** – average pore size, **B** – cell density, **C** – porosity, and **D** – density. Raw data are available in the appendix. 92

Figure 65: Detail of the pore interface structure formed during filament extrusion. All samples were made of PS matrix and contained 2 wt. % of foaming agent. Left – without nanoparticles; middle – with 1 wt. % of melt-blended fumed silica; right – with 1 wt. % of solvent-casted spherical silica. (STEM) 93

Figure 66: CLSM images of 3D printed cylinders based on HIPS and azodicarbonamide without nanoparticles (left column), with 1 wt. % of melt-blended fumed silica (middle column), and with 1 wt. % of solvent-casted spherical silica (right column). Upper line – after 3D printing below the decomposition temperature of the blowing agent (180 °C, scale bar 200 μm). Middle line – after 3D printing above the decomposition temperature of the blowing agent (220 °C, scale bar 200 μm). Bottom line – after post-processing in the pre-heated oven (200 °C, scale bar 500 μm). 95

Figure 67: Graphical evaluation of structural properties of 3D printed cylinders (printed below and above the decomposition temperature of the blowing agent and after post-processing foaming). **A** – average pore size, **B** – cell density, **C** – porosity, and **D** – density. Raw data are available in the appendix. 97

Figure 68: Representative tensile stress-strain curves of extruded filaments. Top – complete curves. Bottom – detail of low deformation area. All curves of specimens are in the appendix. 98

Figure 69: Graphical evaluation of tensile properties of extruded filaments. A – measured modulus, B – specific modulus, C – measured offset yield strength, D – specific yield strength, E – measured maximum strength, F – specific maximum strength, G – measured elongation, H – specific elongation. Raw data are available in the appendix. 99

Figure 70: Representative compressive stress-strain curves of 3D printed cylinders. Top – Cylinders printed below the decomposition temperature of the blowing agent. Middle – Cylinders printed above the decomposition temperature of the blowing agent. Bottom – Cylinders after post-processing foaming. All curves of all specimens are in the appendix. 102

Figure 71: Compressive stress-strain curves 3D printed cylinders – comparison of a representative curve of each material together. 103

Figure 72: Graphical evaluation of compressive properties of 3D printed cylinders. A – measured elastic modulus, B – specific elastic modulus, C – measured offset yield strength, D – specific offset yield strength. Raw data are available in the appendix. 105

Figure 73: 3D printed HIPS foams with a chemical blowing agent and nanosilica plotted in Ashby diagram. Red points represent foams prepared in this work. *Original figure reuse from* [139]. 106

Figure 74: All tensile stress-strain curves of extruded filaments. Top – complete curves. Bottom – detail of low deformation area. 109

Figure 75: All compressive stress-strain curves of 3D printed cylinders. Top – Cylinders printed below the decomposition temperature of the blowing agent. Middle – Cylinders printed above the decomposition temperature of the blowing agent. Bottom – Cylinders after post-processing foaming. 110

Figure 76: CLSM images of filaments for 3D printing – HIPS with 2 wt. % of blowing agent. With 1 wt. % of melt-blended fumed silica (left) and with 1 wt. % of solvent-casted spherical silica (right). 111

Figure 77: Tensile stress-strain curves of filaments for 3D printing. Top – complete curves. Bottom – detail of low deformation area. 111

11 LIST OF TABLES

Table 1: Polymer glasses used for the preparation of nanocomposites. 45

Table 2: Solvents used for nanocomposite preparation. 49

Table 3: List of nanocomposite filaments with the blowing agent. 51

Table 4: *ζ*-potential of spherical colloidal silica in a variety of solvents and their polarity index. 112

Table 5: Reciprocal absolute difference of Hildebrand solubility parameter between solvent and polymer and size of agglomerates of polymer nanocomposites filled with spherical silica with the size of single-particle d_{sp} = 20 nm. 112

Table 6: Raw data of tensile properties of extruded filaments. 115

Table 7: Raw data of compression properties of cylinders 3D printed below the decomposition temperature of blowing agent. 116

Table 8: Raw data of compression properties of cylinders 3D printed above the decomposition temperature of blowing agent. 116

Table 9: Raw data of compression properties of post-processing foamed cylinders. 116

12 AUTHOR PUBLICATIONS AND OTHER OUTPUTS

12.1 Publications

12.1.1 First author papers

1. Zarybnicka, Klara, Frantisek Ondreas, Petr Lepcio, Michal Kalina, Marek Zboncak and Josef Jancar "Thermodynamic Parameters Controlling Nanoparticle Spatial Packing in Polymer Solutions". *Macromolecules*. 2020, 53 (19), 8704-8713. ISSN 0024-9297. doi: 10.1021/acs.macromol.0c00698
2. Zarybnicka, Klara, Frantisek Ondreas, Petr Lepcio, Chao Chen and Josef Jancar. "In-situ self-assembly of silica nanoparticles into microfibers with potential to reinforce polymers". *Nanocon: Proceeding 11th International Conference on Nanomaterials – Research & Application.* 2020, 673-678. doi: 10.37904/nanocon.2019.8489

12.1.2 Co-author papers

1. Bay, R. Konane, Klara Zarybnicka, Josef Jancar and Alfred J. Crosby. "Mechanical Properties of Ultrathin Polymer Nanocomposites". *ACS Applied Polymer Materials*. 2020, 2 (6), 2220-2227. doi: 10.1021/acsapm.0c00201. ISSN 2637-6105.
2. Jancar, Josef, Frantisek Ondreas, Petr Lepcio, Marek Zboncak and Klara Zarybnicka. "Mechanical properties of glassy polymers with controlled NP spatial organization". *Polymer Testing*. 2020, 90, 1–10. ISSN 01429418. doi: 10.1016/j.polymertesting.2020.106640
3. Jancar, Josef, Klara Zarybnicka, Jan Zidek and Frantisek Kucera. "Effect of Porosity Gradient on Mechanical Properties of Cellular Nano-Composites". Polymers. 2020, 12(3), 1-12. doi: 10.3390/polym12030681. ISSN 2073-4360.
4. Ondreas, Frantisek, Petr Lepcio, Marek Zboncak, Klara Zarybnicka, Leon E. Govaert and Josef Jancar. "Effect on Nanoparticle Organization on Molecular Mobility and Mechanical Properties of Polymer Nanocomposites". *Macromolecules*, 2019, 52 (16): 6250-6259. doi: 10.1021/acs.macromol.9b01197
5. Lepcio, Petr, Frantisek Ondreas, Klara Zarybnicka, Marek Zboncak, Ondrej Caha, and Josef Jancar. "Bulk Polymer Nanocomposites With Preparation Protocol Governed Nanostructure: The Origin And Properties Of Aggregates And Polymer Bound Clusters". *Soft Matter*, 2018, 14 (11): 2094-2103. doi:10.1039/C8SM00150B.

12.1.3 Utility model

1. Zarybnicka, Klara, Frantisek Ondreas, Petr Lepcio, Josef Jancar and Antonin Knob. "Thermoplastic masterbatch for the processing of waste polycarbonates with an increased proportion of recycled material". 2019. Czech Republic. 33803 Utility model. Accorded 27.2.2020. Enrolled 17.12.2019.

12.1.4 First author abstracts

1. Zarybnicka, Klara, Frantisek Ondreas, Petr Lepcio, Juraj Svatik, Martina Staffova and Josef Jancar. "Polymer Nanocomposite foams for 3D printing". *Polyméry 2020 Books of Abstracts*, 2020, Bratislava, p. 46–47. ISBN 978-80-89841-14-1.

2. Zarybnicka, Klara, Frantisek Ondreas, Petr Lepcio, Marek Zboncak and Josef Jancar. “Effects of Structural and Processing Parameters on the Thermomechanical Properties of Polymer Nanocomposites”. *DYFP Conference 2018 Book of Abstracts*, 2018. Eindhoven, p. 304–307.
3. Zarybnicka, Klara, Frantisek Ondreas and Josef Jancar. “Effects of Structural and Processing Parameters on the Properties of Polymer Nanocomposites”. Student conference *Chemistry is Life*, 2017. Brno: Brno University of Technology, Faculty of Chemistry, p. 56. ISBN 978-80-214-5488-0.
4. Zarybnicka, Klara and Tomas Opravil. “Possibilities of Using of Fluid Ash in the Self-Leveling Systems”. 17th Slovakian nationwide student scientific conference *Chemistry and Technology for Life,* 2015. Bratislava: Slovak University of Technology in Bratislava, p. 271–272. ISBN 978-80-227-4480-5.

12.2 Projects

12.2.1 Principal investigator

1. TA6280400 (Technology Agency of Czech Republic, Zeta program) – “Recycling of waste polycarbonates and development of advanced thermoplastic blends with polycarbonate part usable in primary production application” (2018–2019).
2. CEITEC VUT-J-19-5962 (Ceitec Junior specific research) – “Fibers formed by self-leveling process from nanosilica particles with potential to reinforce material on two hierarchical levels” (2019).
3. STI-J-18-5330 (Ceitec Junior specific research) – “General principles predicting organization of nanoparticles in polymer matrix and their influence on mechanical properties applied to systems with functional nanoparticles” (2018).
4. Brno Ph.D. talent (scholarship holder) – “Polymer nanocomposite foams based on impact copolymer” (2018–2020).

12.2.2 Co-investigator

1. LTAUSA19059 (Inter-Excellence, Inter-Action) – “Nature-inspired cellular nanocomposites for structural application” (2020–2022). In cooperation with the University of Massachusetts (USA).

12.2.3 Collaborator

1. 18-17540S (Czech Grant Agency) – “Low-density functional nanocomposites” (2018–2020).